Observation and modelling of disks about young stars with ALMA : implication for planetary formation

Sacha Gavino

THÈSE PRÉSENTÉE PAR

Sacha Gavino

POUR OBTENIR LE GRADE DE

DOCTEUR DE L'UNIVERSITÉ DE BORDEAUX

ÉCOLE DOCTORALE: SCIENCES PHYSIQUES ET DE L'INGÉNIEUR

SPECIALITÉ : ASTROPHYSIQUE

Observation and modelling of disks about young stars with ALMA: implication for planetary formation

---

Sous la direction de: Anne Dutrey

Soutenue le: 20 novembre 2020

MEMBRES DU JURY :

Émilie Habart	Maître de conférence, IAS, Orsay	Rapportrice
Franck Le Petit	Astronome, LERMA, Meudon	Rapporteur
Nathalie Brouillet	Astronome adjoint, Univ. Bordeaux	Examinatrice
Sebastian Wolf	Professeur, Kiel University	Examinateur
Hervé Bouy	Professeur, Univ. Bordeaux	Président du juy
Anne Dutrey	Directrice de recherche, Univ. Bordeaux	Directrice de thèse

"The greatest art in theoretical and practical life consists in changing a problem into a postulate."

Goethe to Zelter

Observation et modélisation des disques de gaz et de poussières autour des étoiles jeunes avec ALMA : implication pour la formation planétaire

Résumé: La formation des étoiles s'accompagne généralement de la présence de disques protoplanétaires. Ces disques contiennent un mélange de 99 % de gaz et de 1 % de particules solides appelées grains de poussière. Initialement de taille sub-micrométrique, ces grains vont progressivement s'agglomérer, grossir, et potentiellement permettre la formation de planètes autour de l'étoile.

L'étude de la composition en molécules et en grains des disques jeunes est fondamentale pour contraindre les conditions physico-chimiques initiales et ainsi comprendre les mécanismes de formation planétaire et l'origine de la composition chimique des planètes.

L'objectif de la thèse a été de construire des modèles sophistiqués de disques jeunes typiques constitués de gaz et d'une population de grains de différentes tailles puis, de manière inédite, de tester par simulations numériques l'implication de cette distribution en taille et en température sur l'évolution chimique.

Pour ce faire, nous avons couplé le code de transfert radiatif 3D Monte-Carlo POLARIS au code de simulation gaz-grain dépendant du temps NAUTILUS. Le code de transfert radiatif nous a permis de calculer finement la température des grains en fonction de leur taille et de leur position ainsi que le flux UV au sein du disque. Le code gaz-grain, quant à lui, a ensuite pu simuler l'évolution des abundances chimiques dans nos modèles de disques. De plus, le calcul du flux UV effectué par POLARIS couplé à l'utilisation de section efficaces moléculaires provenant de bases de données a permis le calcul en fonction de la fréquence des taux de photoabsorption, de photodissociation et de photoionisation des molécules.

Mots-clefs: disques protoplanétaires, formation planétaire, astrochimie, Chimie gaz-grain , transfert radiatif, simulations numériques,

Observation and modelling of disks about young stars with ALMA: implication for planetary formation

Abstract: The star formation process usually proceeds with protoplanetary disks. These disks contain a mixture of gas, accounting for 99 % of the disk mass and of solid particles called dust grains (1 % of the disk mass). These grains, initially at sub-micro metric sizes, gradually coagulate, grow, and potentially allow for the formation of planets about the star.

The study of the dust and molecular composition of young disks is fundamental to constraint the physical and chemical initial conditions and thus to understand the mechanisms of planetary formation and the origins of the chemical composition of the planetary cores.

The goal of this thesis was to build state-of-the-art models of typical young disks consisting of gas and of a population of grains of multiple sizes, then, in a new approach, to test with the use of numerical simulations the implication of the size and temperature distributions on the chemical evolution of disks.

To achieve this, we have coupled the 3D Monte-Carlo radiative transfer code POLARIS to the time-dependent gas-grain code NAUTILUS. The radiative transfer code allowed us to finely compute the grain temperature as a function of the size and location as well as the UV flux within the disk. The gas-grain code was able to simulate the evolution of the chemical abundances in our disk models. Moreover, the computation of the UV flux by POLARIS coupled to a set of molecular cross-sections extracted from a comprehensive database allowed us to compute as a function of the frequency the rates of molecular photoabsorption, photodissociation, and photoionization.

Keywords: protoplanetary disks, planetary formation, astrochemistry, gas-grain code, radiative transfer, numerical simulations

Remerciements

Cette thèse est le résultat d'un travail collaboratif et je tiens à remercier toute personne qui y a contribué.

En tout premier lieu, je remercie Anne Dutrey, ma directrice de thèse. Merci infiniment pour m'avoir fait confiance et m'avoir permis de concrétiser un rêve d'enfance. Merci pour ta disponibilité, ta patience et ta grande bienveillance, qualités rares qui ont permis de créer un cadre de travail propice et permis de mener à bout cette thèse dont le sujet n'était pas mon domaine de formation. Tu as su me comprendre, choses pas toujours facile, et m'aiguiller vers la bonne direction dans les moments flous. Travailler avec toi a été extrêmement enrichissant, humainement comme professionnellement. Je retiendrai ta rigueur, ton esprit de synthèse et ton intuition. J'espère que je saurai utiliser ces qualités dans le futur. Je retiendrai aussi ton enthousiasme, ton énergie et ta passion, trois choses que tu sais transmettre naturellement. Enfin, je retiendrai nos discussions sur la psychologie, l'épistémologie et les Goguettes.

Je remercie également Valentine Wakelam, alliée idéale qui a permis à la thèse de prendre une véritable consistence astrochimique. Merci pour ta bienveillance, ta confiance, tes explications toujours claires et ton esprit fin. À mes yeux tu resteras toujours ma co-directrice.

je remercie ensuite Stephane Guilloteau qui a toujours su porter un regard avisé sur le travail de thèse et mis à profit sa rigueur, sa précision et son érudition avec enthousiasme.

Je remercie plus généralement chaque membre de l'équipe AMOR. Merci à toi Emmanuel Di Folco pour ta bienveillance et tes mails qui remontent le moral. Merci à toi Audrey Coutens pour tous tes conseils. Merci à toi Edwige Chapillon pour m'avoir permis de monter à l'interferomètre du Plateau de Bure.

Merci à Julia Kobus et Sebastian Wolf pour leur collaboration fructueuse, leur écoute et leur disponibilité. Merci à Wasim Iqbal pour avoir permis à NAUTILUS de devenir multi-grain. Sans vous, la thèse ne serait pas ce qu'elle est.

Je remercie également les membres du jury. Merci à Émilie Habart et Franck Le Petit pour avoir accepté d'être rapporteurs et pour vos précieux conseils qui m'ont permis d'améliorer mon manuscript. Merci à Nathalie Brouillet, Sebastian Wolf et Hervé Bouy d'avoir pris part au jury.

Je remercie tout particulièrement Cécile Arnaudin, Annick Capéran, Odile Derouaisné et Nathalie Le Roux pour avoir rendu mon séjour au LAB beaucoup plus agréable.

Je remercie Jack Lissauer pour avoir été un phare rassurant, un soutien permanent, un excellent conseiller, et un ami.

Merci à tous les "jeunes du LAB", doctorants et post-doctorants qui ont rendu mon experience de thèse (trop) plaisant. Je n'oublierai pas les pauses café de 15 minutes transformées en pauses de 45 minutes, ni les afterworks de dernière minute qui durent des heures. Plus particulièrement, merci à Jordan pour m'avoir permis des moments d'évasion. Je n'ai qu'une seule chose à te dire: Apéro ? Merci à Yoann, compagnon de bureau, de pause déjeuner, de café et de pintes pour m'avoir soutenu dans ma "flemme" de cuisiner et d'avoir contribué à améliorer mes pauses le midi. Merci aussi à ce sacré William, qui a toujours le mot pour rire (à lire avec un accent américain). Merci à Baptiste, soutien nocturne de fin de thèse. Merci à Phuong pour toutes ces discussions sur nos pays respectifs. Merci à Cesar pour sa bienveillance (et pour avoir donné mon tout premier TD de "Gravitation" en M1). Merci à Tiziano pour ces conversations totalement absurdes. Merci à Audrey, Aurélien, Anthony, Jean-Paul, Laia, Lars, Maria, Marina, Mélisse (pour avoir partagé ses idées cuisines, en particulier le célèbre banane + raclette), Maxime, Núria, Salomé, Takanori et Yassin.

Je remercie tout naturellement mes parents et ma sœur qui m'ont offert un soutien inconditionnel d'un bout à l'autre, y compris quand je prenais les mauvaises décisions aux yeux des autres. Rien n'aurait été possible sans vous.

Je pense ensuite à toutes les personnes qui ont été sur mon chemin durant cette thèse et qui m'ont enrichi d'une manière ou d'une autre. Merci à toi Sebastien, qui même depuis Leiden a su rendre ma thèse plus agréable et être un guide à part entière. Tu es un peu comme mon chien-guide, ou chien de berger, ou chien de traineau, bref, un vrai ami. On ira se promener, promis. Merci à Tidiane, soutien de très longue date. Merci à Bj, Matthieu, Lauraline, Tessa, Louis, Adeline, Amreen, Claire, Hugo et Ugo, aux Goldeneries et tant d'autres pour avoir embelli ma vie à Bordeaux, sauf bien sûr Alice qui m'a obligé à dire chocolatine. Mais tu m'as permis de voir la plage en 2020 et tu aimes les T-Rex, tu es donc presque pardonnée.

Je pense également à Nicolas, source de motivation sans faille, qui m'a permi de dépasser mes limites durant nos séances de boxe. Ces instants sportifs ont été un véritable exutoire dans les moments difficiles.

Enfin, je pense à toi, Léonie. Ce n'est pas la fin qu'on s'était imaginé, mais saches que tu as été mon pilier et ma force depuis le début. Cette thèse, tu l'as portée et tu l'as vécue, c'est donc aussi la tienne. Je t'en serai pour toujours reconnaissant. Je te dédie ce manuscript.

Contents

List of Figures

List of Tables

List of Acronyms

AGN Active Galactic Nuclei

ALMA Atacama Large Millimeter/Submillimeters Array

AURA Association of Universities for Research in Astronomy

CMB Cosmic Microwave Background

CNM Cold Neutral Medium

COM Complex Organic Molecules

CTTS Classical T Tauri star

DSHARP Disk Substructures at High Angular Resolution Project

ESA European Space Agency

EUV Extreme Ultraviolet

FIR Far-Infrared

FUV Far-Ultraviolet

GMC Giant Molecular Cloud

HAe/Be Herbig Ae/Be

HIM Hot Ionized Medium

IR Infrared

ISM Interstellar Medium

ISRF Interstellar Radiation field

JHU Johns Hopkins University

JPL Jet Propulsion Laboratory

JWST James Webb Space Telescope

MRI Magnetorotational Instability

MHD Magnetohydrodynamic

NASA National Aeronautics and Space Administration

NMGC NAUTILUS Multi-Grain Code

NIR Near-Infrared

NGC New General Catalogue of Nebulae and Clusters of Stars

PDR Photon-Dominated Region

RRK Rice-Ramsperger-Kessel

SED Spectral Energy Distribution

STScI Space Telescope Science Institute

SGW Safronov-Goldreich-Ward instability

SOFIA Stratospheric Observatory for Infrared Astronomy

SRF Stellar Radiation field

TTS T Tauri star

UV Ultraviolet

WIM Warm Ionized Medium

WNM Warm Neutral Medium

YSO Young Stellar Object

Chapter 1

Introduction

Contents

Protoplanetary disks around Sun-like stars are the subject of this thesis. In particular, we question their nature through the lens of their chemical content. Protoplanetary disks are known to be the site where planetary formation occurs. This thesis can thus be considered as a modest contribution to the continuous effort to understand the origin of planets.

This effort has been initiated millennia ago, but the foundations of the modern scenario of the formation of planetary systems were established around the sixteenth century. The first step was to renounce the Medieval organization of the Universe, based on Aristotle[1]. This step was made when Copernicus proposed to re-introduce a heliocentric system[2], in such a way that he could reconcile the Physics of Aristotle with the existence of a predictive geometrical model[3]. It took again almost a century to fully accept this model in the frame of modern physics (and not in that of Aristotle's), because of what A. Koyré calls an *"intellectual inertia"*[4].

This new paradigm, where the Earth is not at the center and where the Universe is not immutable imposed an origin to the Solar system. At this moment, Europe witnessed the emergence of new ideas on the formation of the system. We can mention the Vortex Theory, introduced by Descartes (1596-1650) and described in his *Principia Philosophiae* (1644), later discredited by the Newtonian mechanics, or the idea that planets are cooled former stars proposed by Leibniz (1646-1716). However, two classes of hypotheses will rapidly become successful: the well-known *nebular hypothesis* (or Kant-Laplace hypothesis), proposed independently by Immanuel Kant (1724-1804) and Pierre-Simon Laplace (1749-1827), which claims (in his most modern form) that the Solar system originates from a nebula that collapsed by gravitation, flattened, and finally led to the planets we know. The second hypothesis, proposed by Buffon (1707-1788), suggests that the matter ejected from the collision between the edge of the Sun and an impactor (probably a comet) is the origin of the planets[5]. We note that, although totally wrong, Buffon's hypothesis remained the most populous scenario among astronomers until the late nineteenth century. Whatever scenario is considered, they must all agree, as Laplace states, that *"however arbitrary the elements of the system of the planets may be, there exists between them some very remarkable relations, which may throw light on their origin"*[6]. Laplace, here, refers to the observed approximate coplanarity of the orbits and the unity of the direction of rotation in the Solar system. The Kant-Laplace hypothesis, as we will see, is the closest to the modern description of the formation of planetary systems, corroborated by modern observational tools.

In this chapter, we introduce a brief overview of the formation of planetary systems. To do this, we will present the cycle of matter in our galaxy, from its origin in the interstellar medium to its more complex forms in stars and planets.

[1] Alexandre Koyré, *Études galiléennes*, 1966, Á l'Aube de la Science Classique, Hermann Paris.
[2] Nicolaus Copernicus, *De Revolutionibus orbium coelestium.*
[3] Alexandre Koyré, *The astronomical Revolution*, 1961, *I - Copernicus and the Cosmic Overthrow*, Chap. I.
[4] *ibid.*, *III - Borelli and Celestial Mechanics* Chap. I., p. 632.
[5] Georges Louis Leclerc, comte de Buffon, *Histoire naturelle, générale et particulière - Théorie de la Terre, Tome I*, 1774.
[6] Pierre-Simon Laplace, *The System of the World*, 1830, vol.II, Chap. 6, p. 326.

1.1 The origin of planetary systems

1.1.1 The interstellar medium

We can spontaneously assume the existence of a *stellar medium*, but the seemingly emptiness between stars has made the idea of an interstellar medium a little bit harder to conceive over the ages. Yet, this latter constitutes the building block of stars and planets. Ancient and careful observers were actually able to notice small tenuous white clouds in the night sky but the very first breakthrough characterization only came in the late 19th century, when William Huggins inferred a "luminous gas" from the electromagnetic spectrum of a planetary nebula. What we now call the Interstellar Medium (ISM), is a diverse and complex environment made of gas and dust and is arguably one of the most important constituent in galaxies.

1.1.1.1 Our galaxy

Our galaxy, the Milky Way, is a spiral galaxy with a diameter of about 30 kpc. Most of the baryonic mass is located within the thin galactic disk which has a thickness of about 1 kpc. Stars, responsible for nearly all the energy emission in the galaxy, and the ISM, a diluted mixture of gas and dust, constitute nearly all the baryonic matter. At the present time, most of the baryonic mass is now in the form of stellar matter but the ISM, although extremely tenuous, is so vast that it represents about 10% of the baryonic mass [Draine, 2011]. The same scheme is found in most nearby spiral galaxies. The galaxy NGC 3972, as seen in Figure 1.1 (left), clearly exhibits bright and dark structures within a thin disk. These structures are the signature of the presence of gas and dust.

Even though the ISM spans across the whole galactic plane, the distribution is not homogeneous. Instead, it is fragmented into clouds of very diverse shapes, sizes, mass, densities and temperatures. If we randomly zoom in on a spiral arm of our galaxy and scan across the field of view, we would realize how diverse the ISM is.

Figure 1.1 (right) is an image of the Pillars of Creation, a group of clouds in our galaxy located in the center of the Eagle nebula, taken with the Hubble's Wide Field Camera 3. The image field represents about 5 light-year. The pillar-shaped structures are made of dense dusty gas that absorbs background light, making them dark in the visible spectrum. This kind of dark clouds can be found across the galaxy and is usually associated with stellar formation, which means that beyond these dark surfaces, away from the prying eye, stars are maybe about to be born.

1.1.1.2 The interstellar radiation field

The gas and dust are not exactly the only elements constituting the ISM. Indeed, the ISM is bathed in electromagnetic radiations of all wavelengths, from X-rays to radio waves and undergoes a constant flux of cosmic rays.

The ISRF is a contribution of various sources. In the Near-Infrared (NIR) range, it is dominated by the radiation of stars of the late spectral class. The main contributors to the UV and Far-Ultraviolet (FUV) spectrum range are the hot and blue OB class stars.

Figure 1.1: Left: The galaxy NGC 3972. Credits: NASA, ESA, A. Riess (STScI/JHU); Right: The Pillars of Creation in the Eagle nebula. Credits: NASA, ESA, and the Hubble Heritage Team (STScI/AURA)

The energy density in this range is lower than the one originating from late spectral class stars. The dust of the ISM also contributes to the ISRF. Dust grains also emit thermal radiations. They continuously absorb photons from starlight and re-emit the absorbed energy in the Far-Infrared (FIR) in a quasi-blackbody spectral shape. The blackbody spectrum of the Cosmic Microwave Background (CMB) dominates the ISRF in the microwave range. However, its role is very limited in the energy balance since the temperature of the gas and dust is typically warmer than the CMB.

The cosmic rays, on the other hand, are composed of extremely relativistic charged particles like ions, electrons or protons coming from high-velocity gaseous ejecta of supernovae or other violent events. They usually carry a very large kinetic energy, up to 10^{21} eV [Draine, 2011].

1.1.1.3 Constituents of the interstellar medium

The vast majority of the interstellar gas is composed of hydrogen (H) and helium (He), inherited from the early Universe. As the first generation of stars has allowed for nucleosynthesis to occur, the ISM has been enriched little by little in heavy elements such as carbon (C), nitrogen (N) or Oxygen (O). We note here that, when astrophysicists use the term heavy, that actually includes every elements with $Z \geq 3$.

Although these heavy elements represent a tiny fraction of the interstellar mass ($\sim$ 2 %, Yamamoto [2017]), they affect the chemistry and the ionization state of the gas, they regulate the temperature of the gas via heating and cooling processes which in turn increase the chemical complexity, they influence the fragmentation and condensation of clouds and therefore, the star formation rate.

The advent of radio-astronomy in the second part of the 20th century allowed the observation of emission lines of a very large number of chemical species. In 1963, Weinreb et al. [1963] detected for the first time an interstellar molecule using a radio-telescope: the

hydroxyle group OH via its Σ-type double transition toward Cassiopeia A. Since then, more than 200 molecules have been detected. While the simple diatomic molecules H_2 and CO are by far the most abundant molecules in the ISM, more complex molecules, composed of up to 13 atoms have also been detected. Table 1.1 gives a list of interstellar molecules with two to seven atoms observed as of 2018. The hydrogen still represents about 99 % of all interstellar mass. It is distributed as follows: 60 % is in the form of hydrogen atom (H I), about 20 % is in the form of molecular hydrogen (H_2) and about 20 % is in the form of ionized hydrogen (H II) [Draine, 2011]. The tiny remaining fraction of H is located inside more complex molecules.

Table 1.1: List of detected interstellar molecules with two to seven atoms as of 2018 [McGuire, 2018].

2 atoms		3 atoms		4 atoms	5 atoms	6 atoms	7 atoms
CH	CP	H_2O	N_2O	NH_3	HC_3N	CH_3OH	CH_3CHO
CN	NH	HCO^+	MgCN	H_2CO	HCOOH	CH_3CN	CH_3CCH
CH^+	S_iN	HCN	H_3^+	HNCO	CH_2NH	NH_2CHO	CH_3NH_2
OH	SO^+	OCS	SiCN	H_2CS	NH_2CN	CH_3SH	CH_2CHCN
CO	CO^+	HNC	AlNC	C_2H_2	H_2CCO	C_2H_4	HC_5N
H_2	HF	H_2S	SiNC	C_3N	C_4H	C_5H	C_6H
SiO	N_2	N_2H^+	HCP	HNCS	SiH_4	CH_3NC	c-C_2H_4O
CS	CF^+	C_2H	CCP	$HOCO^+$	c-C_3H_2	HC_2CHO	CH_2CHOH
SO	PO	SO_2	AlOH	C_3O	CH_2CN	H_2C_6	C_6H^-
SiS	O_2	HCO	H_2O^+	l-C_3H	C_5	C_5S	CH_3NCO
NS	AlO	HNO	H_2Cl^+	$HCNH^+$	SiC_4	HC_3NH^+	HC_5O
C_2	CN^-	HCS^+	KCN	H_3O^+	H_2CCC	C_5N	
NO	OH^+	HOC^+	FeCN	C_3S	CH_4	HC_4H	
HCl	SH^+	SiC_2	HO_2	c-C_3H	HCCNC	HC_4N	
N_aCl	HCl^+	C_2S	TiO_2	HC_2N	HNCCC	c-H_2CNH	
AlCl	SH	C_3	CCN	H_2CN	H_2COH^+	CH_2CNH	
KCl	TiO	CO_2	SiCSi	SiC_3	C_4H^-	C_5N^-	
AlF	ArH^+	CH_2	S_2H	CH_3	CNCHO	HNCHCN	
PN	NS^+	C_2O	HCS	C_3N^-	HNCNH	SiH_3CN	
SiC		MgNC	HSC	PH_3	CH_3O		
		NH_2	NCO	HCNO	NH_3D^+		
		NaCN		HOCN	H_2NCO^+		
				HSCN	$NCCNH^+$		
				HOOH	CH_3Cl		
				l-C_3H^+			
				HMgNC			
				HCCO			
				CNCN			

The dust grains, on the other hand, account for about 1 % of the total mass of the ISM. Yet, they are of great importance since they act as catalysts of lots of crucial chemical processes, such as the formation of molecular hydrogen, and they are the fundamental

blocks of planetary embryos. When astrophysicists talk about dust, dust grains or grains, they actually mean sub-microscopic solid particles. The typical size of dust grains is 0.1 μm but some can reach microscopic sizes and even beyond in certain environments like circumstellar disks. Dust grains are formed in the envelop of late phase of star evolution (Red Giant). Depending on the type of progenitors the grain material can have a various composition but the vast majority of grains can be classified into either silicate particles or carbonaceous particles.

1.1.1.4 Phases and densities

The ISM is fragmented into clumps and filaments of various sizes called clouds that are sparsely distributed over the galaxy. They differ in temperature and density. It thus appeared necessary to classify clouds by typical properties. Figure 1.2 [Yamamoto, 2017] represents a diagram which illustrates the relationship between the ISM's temperature versus its density. The clouds can be grouped in several distinct categories. The first category are clouds in pressure equilibrium and lies on a line of constant pressure such as the Coronal gas or the Diffuse clouds. A second category are dense clouds in which gravitational contraction can take place such as Hot cores or Molecular clouds. Let's briefly describe the different phases in view of Figure 1.2.

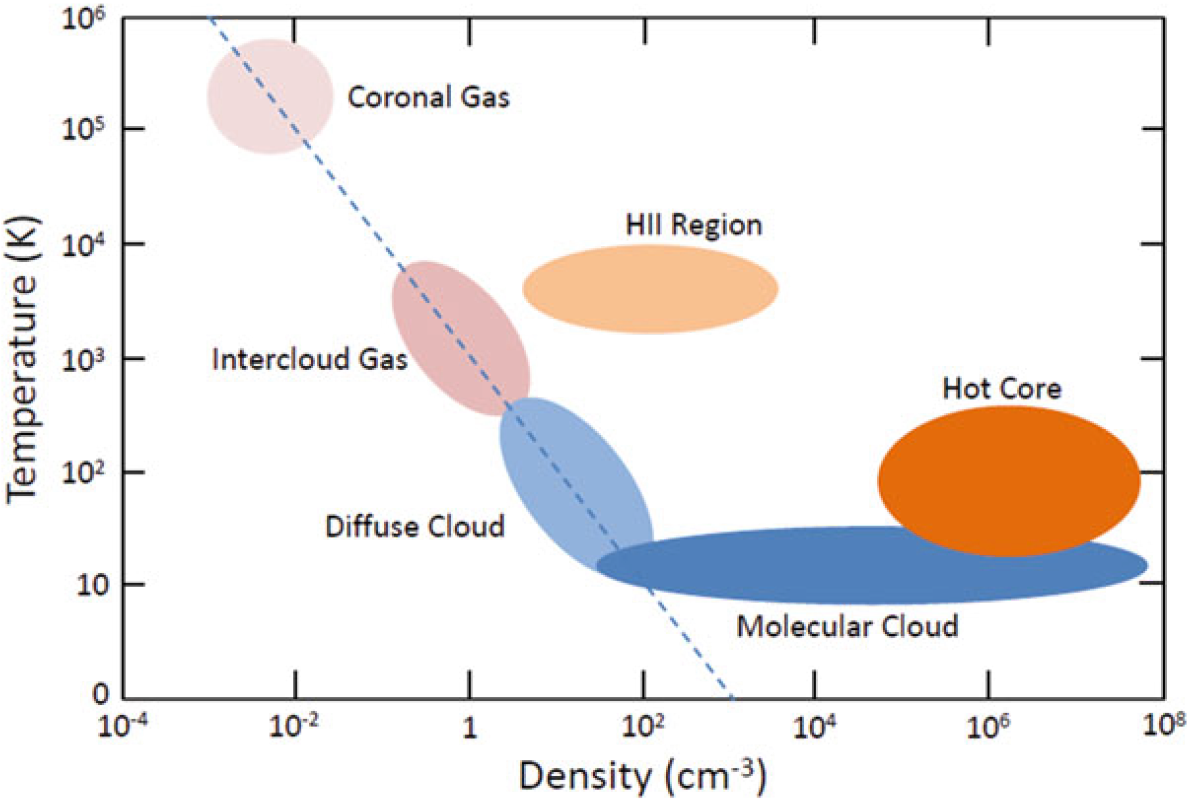

Figure 1.2: Temperature-density diagram of interstellar phases from Yamamoto [2017]. The dashed blue lines represents a contour line of pressure.

The Coronal Gas consist in a hot diffuse cloud with temperature $\geq 10^{5.5}$ K and densities of about 0.004 cm^{-3} [Draine, 2011]. The gas is heated and ionized by shocks with gas ejected from supernovae explosions. It is also referred to as Hot Ionized Medium (HIM).

The Intercloud Gas region combines different typical phases. The very upper left, usually referred to as Warm Ionized Medium (WIM), is a low density medium almost exclusively made of hydrogen that has been photo-ionized by UV flux originating from nearby hot stars. The denser and colder part of the Intercloud Gas is referred to as Warm Neutral Medium (WNM), which is made of atomic hydrogen heated to temperature of a few thousands of Kelvin ($\approx$ 5000 K) and at densities $\approx$ 0.6 cm^{-3} [Draine, 2011]. The warm neutral medium represents about 40 % of the total volume of the galactic disk.

The upper left of the Diffuse Cloud as along with the lower right of the Intercloud Gas represent regions of Cold Neutral Media (CNM). The medium is mostly composed of cool neutral atomic hydrogen at temperature T $\approx$ 100 K and $n_H \approx 30$ cm^{-3}. The lower right of the Diffuse Cloud is usually referred to as diffuse molecular gas. The cloud has similar physical conditions as the cool H I regions (CNM). However, the column densities is large enough so that H_2 self-shielding becomes efficient, leading to large H_2 abundance in the cloud interior.

The Molecular Cloud, often referred as dense molecular gas is a gravitationally bound cloud in which star formation occurs. It is usually cold (a few tens of Kelvin), dark ($A_v \geq 3$) and very dense ($n_H \approx 10^3$-10^6 cm^{-3}). We note here that the word dense is a very relative term as the density inside these clouds is not greater than the density achieved in ultra-high vacuum chambers on Earth.

1.1.2 From clouds to stars

When we look at the night sky, we often notice that stars are gathered together within what we call clusters. This results is not a coincidence and has to see with the very first step of star formation. Indeed, stars are born from the collapse of a nebula. Kant and Laplace's hunch is indeed proven right. But the question remains: how do you obtain a fully working planetary systems out of the ISM? Modern astrophysics is able to quantitatively describe the overall scenario, but we will see that questions are still unanswered.

A Giant Molecular Cloud (GMC) is initially a stable object. The internal kinetic energy counteracts the gravitational energy and prevent the cloud from collapsing. The cloud is said to be in a virial equilibrium. At some point, however, gravity potential has to overcome internal energy. To do so, the cloud must be dense enough to reach a mass limit imposed by the Jeans criteria [Larson, 1985] but this situation cannot happen without external help. It is assumed, for instance, that some nearby events such as supernovae, generate shock waves that break the stability of the cloud. The whole cloud doesn't collapse, instead, various small denser regions form within the cloud, called clumps ($n_H \approx 10^2$-10^4 cm^{-3}), collapsing individually, resulting in the *fragmentation* of the cloud (Fig. 1.3; top right) and potentially multiple star-births (cluster). Each clump keeps

contracting under its own gravity and leads to the formation of a dense core with density $n_H \approx 10^4$-10^6 cm^{-3} (see Williams et al. [2000]) and finally to a Class 0 object: a protostar (Fig. 1.3; right). The latter rapidly accretes the matter of the envelope, becomes more and more massive until the temperature of the core is sufficiently high to trigger the fusion reactions. A star is born.

Back to the initial stage, the clump, prior to the contraction process, was given a certain initial rotation so that the infalling material possesses angular momentum. As the clumps contracts, the radius becomes increasingly smaller, and by conservation of angular momentum's principle, the clumps's rotation becomes increasingly faster. The rotation causes sufficiently strong centrifugal forces to flatten the cloud perpendicularly to its rotational axis. This results in a circumstellar disk or protoplanetary disk. They are usually simply referred to as *disks*.

If the centrifugal force exceeds the gravitational force, the stellar embryo fragments and will never become a main sequence star. This is what is described as the *angular momentum problem* of star formation [Bodenheimer, 1995, Belloche et al., 2002]. To prevent this, the angular momentum must be transferred outward. The redistribution mechanisms are still no fully understood. Observations show that the angular momentum is decreased toward smaller core sizes, although not sufficiently to sustain a solar-mass star [Caselli et al., 2002]. A few dominant models emerged, proposing that the disk is responsible for the angular redistribution, such as the magneto-rotational instability or the magneto-thermal disk winds (see Kratter and Lodato [2016]; Najita and Bergin [2018]). A recent observational studies by Gaudel et al. [2020] also suggests that the disk formation is a direct consequence of angular momentum conservation. Indeed, by studying 16 nearby class 0 protostar, they concluded that the material involved in the stellar formation process has an angular momentum of the order of small T Tauri disks.

During the protostellar phase, the fraction of mass embedded in the core is still smaller than that of the envelope but the accretion rate is relatively high so that the luminosity is mainly due to the flow of matter accreted into the core [Natta, 2000]. After about 10^5 to 10^6 years [Dunham et al., 2014], the pre-main sequence star has accreted most of the infalling material. The residual envelope ultimately dissipates, revealing an optically thick protoplanetary disk and a pre-main sequence star visible at optical wavelengths (Fig. 1.3; bottom). Optically thick here means that the star radiation cannot pass through the disk. The star has acquired most of its final mass and is nearly in a state of hydrostatic equilibrium. However, at this point, the star is still not a main-sequence star and the luminosity is mostly due to gravitational contraction on what is called the Kelvin-Helmoltz time-scale [Natta, 2000]. A pre-main sequence star is either called T Tauri stars (TTSs) when $M_\star \leq 1$ $M_\odot$, or Herbig Ae/Be (HAe/Be) when 2 $M_\odot \leq M_\star \leq$ 8 $M_\odot$. TTSss have a typical isochronal lifetime of ≤ 5 Myr [Mamajek, 2009]. The star finally enters the main-sequence when the contribution of the nuclear reactions to the luminosity becomes predominant.

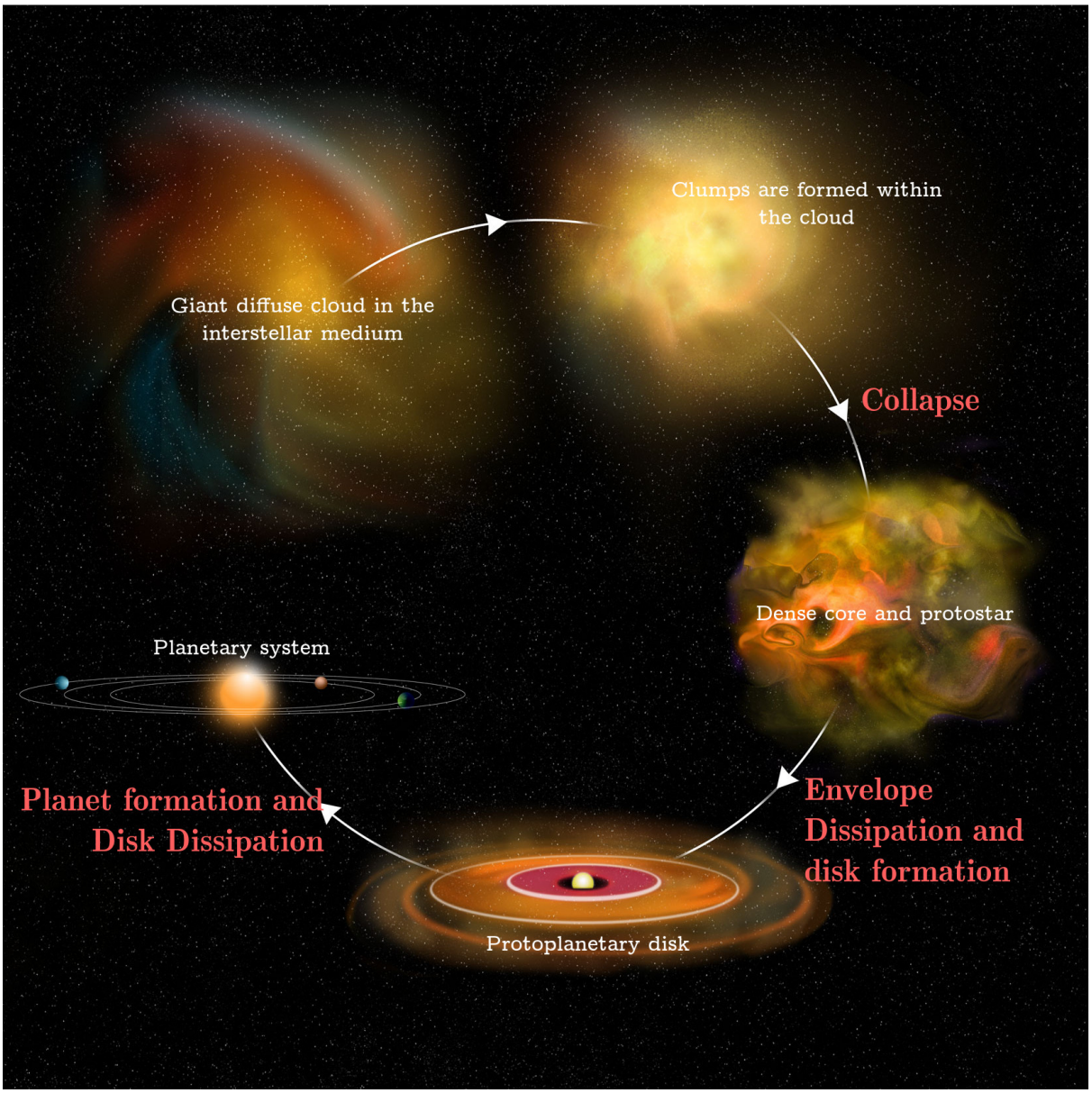

Figure 1.3: Illustration of the star and planet formation cycle. Adapted from Bill Saxton, NRAO/AUI/NSF.

1.1.3 Protoplanetary disks and planet formation

Disks are of particular interest for astronomers as they are the birth-place of planets. During the pre-main sequence phase, where most of the matter of the disk has ended up on the star, the disk is still active and accreted, yet, at a much lower rate than during the protostellar phase [$\sim 10^{-7}$ to 10^{-9} $M_{\odot}yr^{-1}$, Mamajek, 2009], leaving about 10^7 years for planets to form out of the disk's matter before it is fully accreted and evaporated.

We know that the matter constituting the disk is a mixture of surviving interstellar gas and dust grains. However, the physical conditions are different from what is found the ISM. Figure 1.4 illustrates the gas and dust structure of a typical flaring disk about a TTS (black dot) seen edge-on. Whether for the gas or the dust, we see that the vertical structure of protoplanetary disks is layered. The gas' own pressure prevents the disk from becoming infinitely thin and, as a first approximation, can be assumed to be in hydrostatic equilibrium. The disk has a flaring geometry (the scale height depends on the distance from the star) so that the stellar flux also illuminated the disk surface. As illustrated in Fig. 1.4 (right), this results in various conditions depending on the altitude inside the disk [Dullemond et al., 2007].

The dust exhibits a similar vertical structure where grain number density is high in the cold mid-plane and lower at the hot disk's surface. However, dust grain's behavior differs depending on the grain size. Indeed, small grain particles don't *feel* their own pressure but they do *feel* the gas's pressure. Sub-micron sized grains are strongly coupled to the gas while larger grains, such as micron-sized grains tend to be decoupled and sediment toward the disk mid-plane (we ignore turbulence processes). In other words, the disk naturally *collects* the dust and gas material toward the mid-plane where planetary formation is assumed to take place. We will further study this in the next chapter.

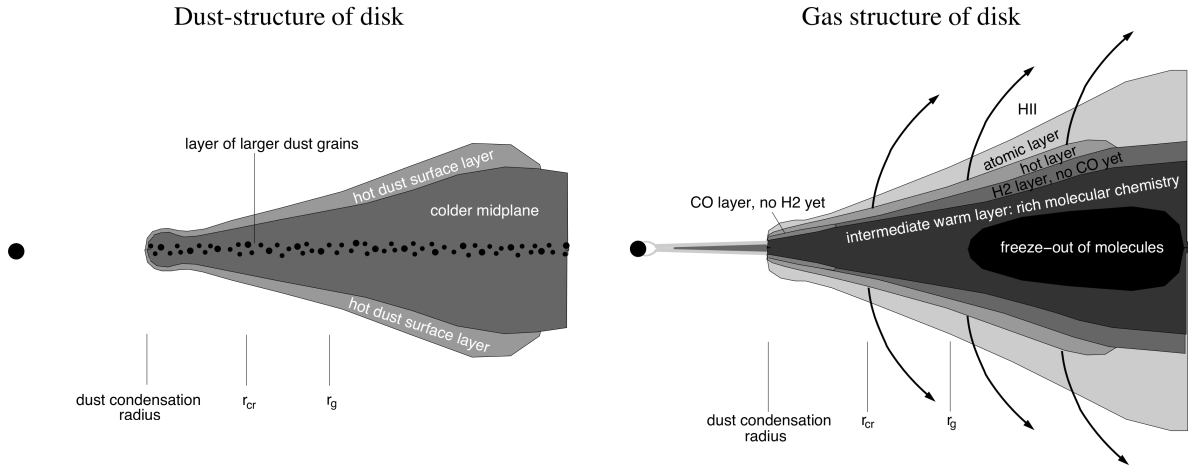

Figure 1.4: Illustration of the structure of a flaring protoplanetary disk seen edge-on. Left: dust structure. Right: gas structure. [Dullemond et al., 2007].

Astronomers know reasonably well the global picture leading to planets in disks: on a timescale of 1-10 Myrs, the coagulation (a process in which small grains collide and stick) of initially sub-micron sized dust particles leads to continued grain growth and ultimately

to the formation of planetesimals, which are the fundamental *blocks* of planets. Then, the molecular gas is dispersed away (Fig. 1.3; bottom left), marking the end of the protoplanetary disk phase and unveiling a newborn planetary system.

However, the purely sequential process described above is very unlikely to be correct. In fact, the quantitative understanding of the mechanisms involved in planetary formation is, even to this day, riddled with many "grey zones". Indeed, scenarios involving coagulation and uninterrupted grain growth fail at efficiently forming planets during the typical disk lifetime. They bump into what we call *barriers* (see Dullemond [2013]), where grain growth cannot exceed certain sizes ($\sim$ centimeter or meter, for instance) without undergoing ineffective or even destructive collision processes. Numerous alternative theoretical models have been developed with the goal to explain how barriers can be overcome. We can mention the gravitational instability models such as the Safronov-Goldreich-Ward instability (SGW) (Goldreich and Ward [1973]; Weidenschilling [1980]) or the streaming instability models (Youdin and Goodman [2005]; Johansen et al. [2007]; Carrera et al. [2015]).

1.2 Aspects of astrochemistry

We have seen in the previous sections the importance of observing chemical species to characterize their influence on astrophysical objects. We can also legitimately wonder how these molecules are formed, excited, or destructed, which chemical processes are at work in space and which routes lead to chemical complexity. The field of science devoted to answering these issues is called astrochemistry or molecular spectroscopy. Although both terms are very often used interchangeably in the astrophysicist community, the latter is more specifically concerned about molecular spectroscopy, a technique dedicated to retrieving the molecular content of a given environment [De Becker, 2013]. Astrochemistry, on the other hand, is interested in all processes forming or breaking chemical bonds in the context of astrophysics and in light of the known molecular population in space given by molecular spectroscopists.

In other words, astrochemistry is, using the words of Dalgarno [2008], the *blending of astronomy and chemistry in which each area enriches the other in a mutually stimulating interaction* (see also van Dishoeck [2018]) and, once inconceivable for astronomers a hundred years ago, is now one the most active field in astrophysics. We present here a brief overview of astrochemistry and the upcoming challenges that the field will face in the 21st century.

1.2.1 Observations

As of 2018, the census reports 204 astromolecules, comprised of 16 different elements [McGuire, 2018] detected in the ISM (see Tab. 1.1) and in circumstellar disks. Their detection depends on the energy required to populate energy levels of molecules. The vast majority was detected using radio astronomy tools (cm and mm/sub-mm ranges) via molecular rotational transitions. The main advantage of radio techniques is that

sources can be detected in emission as well as in absorption (against background continuum) using ground-based observatories. The main disadvantage is that rotational lines are proportional to the square of electric dipole moments, which most purely symmetric molecules hardly possess (e.g. H_2). Therefore, radio techniques have little or no ability to detect symmetric molecules. Infrared astronomy has, to a lesser extent, permitted the detection of molecules via their vibrational lines, which resulting wavelengths fall between NIR to FIR. Infrared tools have been of great help in detecting highly symmetric molecules. A major advantage of infrared astronomy is its ability to detect species in condensed phase (on icy mantles for example) when their rotational lines are not accessible. Visible and UV astronomy has been the least effective in detecting interstellar molecules. Detection in these ranges usually involves electronic transitions between energy levels of molecules or atoms. Since the required energy is very high for these transitions to occur, the detection in the visible and UV is made almost exclusively in absorption.

Progress in astrochemistry is therefore very dependent on new sophisticated observational facilities and data science techniques and we expect progress to continue in the near future. Astrochemistry has been lucky enough so far to benefit from the latest major projects. The case of the Atacama Large Millimeter/Submillimeters Array (ALMA) is a particularly good example. We may also note the Stratospheric Observatory for Infrared Astronomy (SOFIA) and the highly anticipated James Webb Space Telescope (JWST) to be launch in 2021.

1.2.2 Laboratory astrophysics

Conditions under which chemical processes take place in space are somewhat extreme (temperature near absolute zero, extremely low density, cosmic rays...). It is an arduous task to reproduce these conditions in laboratories and in most cases, space itself represents the only *laboratory* accessible to astrochemists. However, laboratories are able to provide basic and fundamental informations which are vital for the practice of astrochemistry.

The first important task is to provide astrochemists with precise atomic and molecular spectroscopic data from UV to mm wavelengths, gathered in databases and catalogs. For instance, the Jet Propulsion Laboratory (JPL) catalog [Pickett et al., 1998] provides transition frequencies and strengths of (sub)mm transitions. The HITRAN [Gordon et al., 2017] and the EXOMOL molecular line lists for exoplanets [Tennyson et al., 2016] are databases for vibrational transitions at infrared wavelengths.

Astrochemists also need the rate coefficients of the thousands of known reactions under space conditions for chemical models. Gas-phase reactions have been summarized and described in the KIDA database [Wakelam et al., 2015]. Photodissociation and photoionization rates of atoms and molecules have been described and updated by Heays et al. [2017]. We note that many rate coefficients have been defined from theoretical calculation of quantum chemistry (e.g. collision rate coefficients for molecular excitation).

The characterization of binding energies (see chapter 3) is a key element for ice astrochemical models. Binding energies are studied using ultra high-vacuum chambers and new modern surface science techniques (see Allodi et al. [2013] for an overview of

techniques used in laboratories).

1.2.3 Astrochemical models

We have seen that *in situ* experiments are, by definition, impossible (except for objets in our solar system) and that laboratory studies cannot cover the entire range of physical conditions found in space. The use of computational chemical kinetics models is required to study the chemistry in space. If kinetic properties from database [e.g., McElroy et al., 2013, Wakelam et al., 2015] and initial abundances (based on observations) are provided, they can be coupled to solve numerical differential equations and compute time-dependent chemical abundances of a given environment. These simulations are performed by gas-grain codes.

Astrochemistry has greatly benefited from advances in high performance computing made over the last two decades and will continue to do in the future. Recently, new machine learning techniques have also started to be used in astrochemistry. For instance, Gratier et al. [2017] used multivariate analysis methods to decompose and interpret the observed signal of the Orion B cloud. We also mention the work of Holdship et al. [2018] who developed Bayesian models to infer reaction rates in molecular clouds.

We will give more details about astrochemical models in chapter 3.

1.3 Chemical modelling of disks

1.3.1 Overview

Physical and chemical processes at stake in disks are numerous. Disks witness dust settling, grain growth, dust drift, accretion processes, turbulence etc. They are subjects to interstellar and intense stellar UV flux that generate multiple chemical layers (PDR, molecular layer, cold mid-plane...). The temperature gradients give rise to radial and vertical snow-lines and to a very rich and complex surface chemistry. Moreover, the detected molecular inventory in disks is small as compared to the ISM (See in Table. 2.1) due to the angular extent of most disks and because many complex molecules are locked on the grains [McGuire, 2018]. Despite the difficulty to detect molecules in disks, it is necessary to do so if one wants to trace the chemical content and retrieve information about the physical environment. in short, disks are very complex systems and still quite poorly understood. Yet, their study is paramount as they are the birthplace of planets. To help astronomers understand the observed physical and chemical complexity of disks, building chemical models is required.

Disks modelling has been a very active topic of research over the last decade and the increasing computation power has allowed to build very sophisticated models. Numerous gas-grain codes have been developed and used. Figure 1.5 provides a small selection of six studies representative of what has been done for disk modelling over the last ten years. Ruaud and Gorti [2019], for instance, built a model of disk using a thermochemical model to study the effect of grain surface reactions on the chemistry. They used a state-of-the-

art 3-phase model that makes the distinction between ice surface layers and icy mantles, as we will see. The 3-phase model is one of the most sophisticated astrochemical model developed so far.

Also, calculating the dust temperature is extremely important to properly study the chemical evolution. In most studies, grain growth and dust settling are properly taken into account. However, the chemistry is usually computed over average optical properties so that only an averaged dust temperature is assumed to account for multiple dust populations. The question of the size-dependent dust temperature effect on the chemistry is yet to be answered.

	Semenov et al. (2010) (ALCHEMIC)	Thi et al. (2013) (PRODIMO)	Akimkin et al. (2013) (ANDES)	Agúndez et al. (2018)	Ruaud&Gorti. (2019)	Gavino et al. (2020)
3-phase model	No	No	No	No	Yes	Yes
Chemical network	osu.2008, RATE06	UMIST database (Wood et al. 2007)	osu.2007 with 2013 Kida updates	UMIST+osu+ Kida	Kida.uva.2014 + modifications	Updated Kida.uva.2014
Dust thermal structure	$T_d = T_g$	Radiative transfer (MCFOST)	radiative transfer in the vertical direction	2D radiative transfer (RADMC)	Radiative transfer (Dullemond et al. 2001)	2D radiative transfer (POLARIS)
Gas temperature	DM Tau parameters (D'Alessio et al. 1999)	Prodimo (Woitke et al. 2009)	Thermal balance (ANDES)	Parametrized following Kamp & Dullemond (2004) $T_d = T_g$	Thermochemical model (Gorti et al. 2015)	Parametrized following Williams & Best (2014)
Photorates	precomputed fits of Van Dishoeck (1988)	Van Dishoeck & Visser (2011)	Van Dishoeck et al. (2006) and the AMOP database	PDR code	Gorti & Hollenbach (2004) (normalised cross-sections)	Using cross-sections following Haeys et al. (2017)
use of PDR code	-	-	-	Meudon PDR code (v 1.4)	-	-
Grain sizes	Single size (0.1micron)	power-law size distribution	Evolution for 2 Myr starting from MRN distrib (growth+fragmentation)	Uniform size distribution	power-law size distribution	size-dependent (Dong et al. 2015)
Settling	-	Settling following Woitke et al. (2009)	vertically integrated kernel (Birnstiel et al. (2010)	Uniform spatial distribution	Settling set by gas turbulence	size-dependent settling (Dong et al. 2015)
temperature-dependent grain size	No	No	No	No	No	YES (per bin)

Figure 1.5: Selection of 5 studies using state-of-the-art protoplanetary disk modelling + the study presented in this thesis (red frame).

1.3.2 Disk model using multiple grain sizes

Heese et al. [2017] studied the effect of a dust temperature spread-out in optically thick disks using a 3D radiative transfer code. They created a disk model using a grain size distribution subdivided into a set of 16 logarithmically distributed intervals and they tested the impact on the thermal properties. The full grain size is ranging from 5 nm to 1 mm. Added to that, they computed the weighted mean dust parameters of the full

range serving as a reference.

Figure 1.6 shows the vertical dust temperature distribution at a radius of 50 au from the star for a selection of five dust sizes and for the reference disk (blue line). Heese et al. [2017] found that in optically thick disks the temperature spread can be as large as 63 %. Of course, this temperature spread is expected to have a dramatic impact on the chemical evolution of disks and defining accurate size-dependent temperatures appears to be vital. This thesis work was dedicated to test this assumption.

Almost simultaneously, was developed by Iqbal and Wakelam [2018] a new version of the gas-grain code NAUTILUS that can account for such size temperature-dependent distributions. This new code is called the Nautilus Multi-Grain Code (NMGC). For the first time we are able to build chemical models of disks composed of realistic multiple grain populations, all of which are chemically-independent.

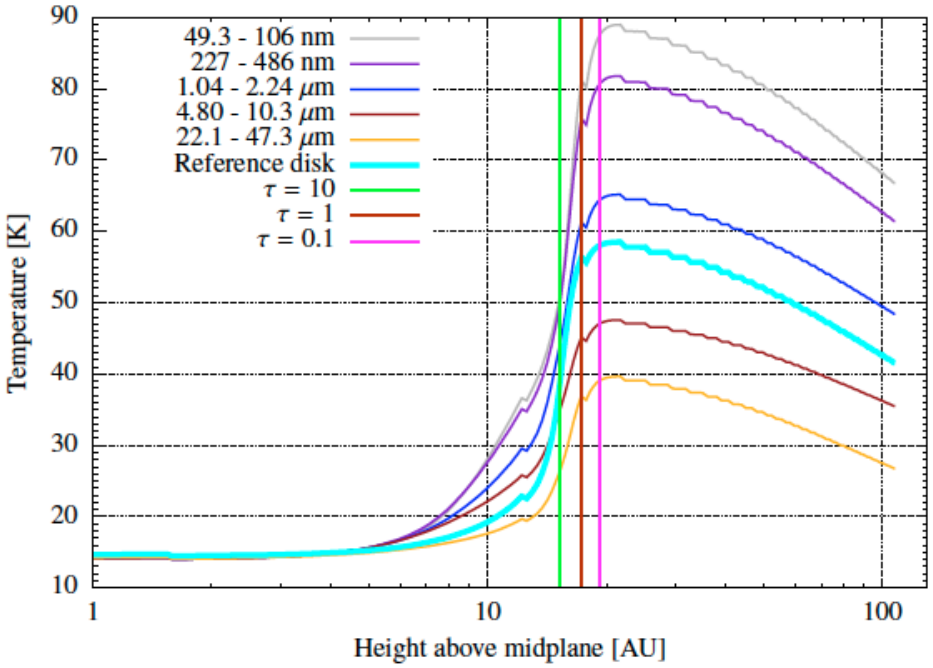

Figure 1.6: Vertical temperature distribution of five grain sizes out of 16 at a radius of 50 au from the star in an optically thick disk. The blue curve represents the reference disk composed of a single grain size [Heese et al., 2017].

1.3.3 The Flying Saucer: an quasi edge-on disk

As we have seen, determining the material content in disks can be challenging. Fortunately, we can take advantage of the random inclinations from which we see disks from the Earth. Some of them are directly observed from the edge, which means that we can characterize their vertical and radial structure in gas and dust and reveal precious information about the physical condition (temperature, density, ionization rate...) and the chemical content.

A very good example of such disks is 2MASS J16281370-2431391, commonly called the *Flying Saucer* (see Fig. 1.7), which is a typical T Tauri disk located in the outskirts of the ρ Oph dark cloud at around 120 pc. Its inclination, estimated at $\sim 87°$ along the line of sight, makes it a nearly purely edge-on disk and a unique observational opportunity. Dutrey et al. [2017] for instance, used ALMA to observe CO J=2-1 and CS J=5-4 in the disk and retrieve the vertical thermal structure of the disk and vertical profile of CO and CS. They shown evidence for a vertical temperature gradient using the CO emission and that CS and CO peak at different altitudes. Also, although the *Flying Saucer* represents a powerful tool to find out more about the vertical and radial structure of T Tauri disks, it still requires powerful instruments with high enough angular resolution.

Given the large number of observationally derived parameters of the *Flying Saucer*, we choose to use them as input to build our disk models for the thesis work. edge-on configuration is perfectly suited for that.

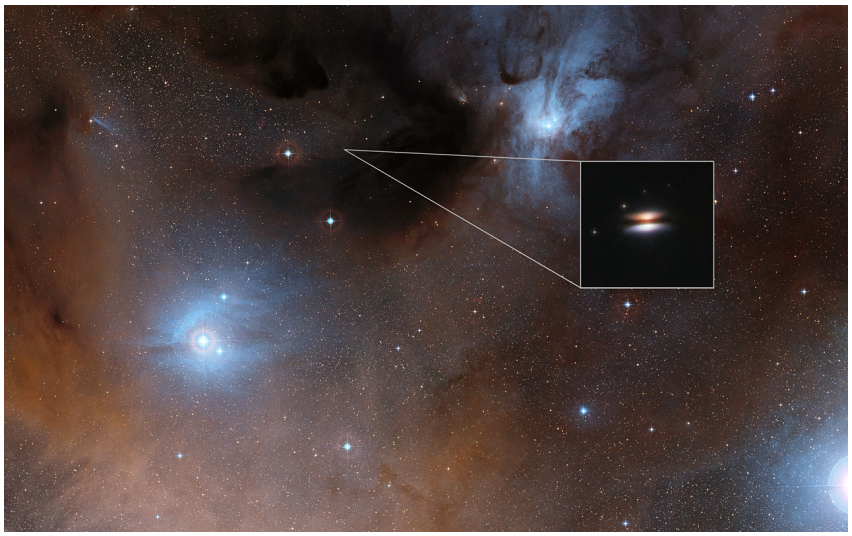

Figure 1.7: The Flying Saucer (2MASS J16281370-2431391), a protoplanetary disk located in the outskirts of the ρ Oph dark cloud L 1688. Credit: Digitized Sky Survey 2/NASA/ESA

1.4 Overview of the thesis

The goal of this thesis is to test the effect of multiple temperature-dependent grain sizes on the chemical evolution of a typical gas-rich T Tauri disk like the *Flying Saucer*. On a large scale, this projects aims to answer broad questions like:

- What is the impact of grain size on the chemical richness?
- How and where complex molecules form inside protoplanetary disks?

The originality of this thesis partially lies in the use of the latest multi-grain version of NAUTILUS (NMGC) hand in hand with the 3D Monte-Carlo continuum radiative

transfer code POLARIS to properly compute dust temperature and then simulate the chemistry on several grain populations. This required to:

1. Build a comprehensive gas and dust disk model composed of properly defined grain populations of independent sizes and temperatures.
2. Use the radiative transfer code POLARIS to have consistent values of grain temperatures as a function of the grain sizes and of the stellar and interstellar radiation field.
3. Make sure to couple the radiative transfer simulations to the chemical models in a consistent manner.
4. Interpret the chemical results in the case of disks consisting of grains with multiple sizes and temperatures.

The special feature of studying the chemical and physical structure of protoplanetary disks is that it requires the expertise of an astronomically (both literally and figuratively) large range of scales and topics, from the nanometer to the astronomical unit and from hydrodynamics to kinetics chemistry. This required to split the thesis in two parts. The first part (Chapters 2 and 3) are here to introduce the necessary technical background that was needed to understand and achieve the thesis work. The second part (Chapters 4, 5 and 6) presents both the conduct of the project and the results.

More specifically, the manuscript is organized as follows:

In chapter 2, we present a detailed description of early protoplanetary disks and their evolution, both from the point of view of theory and observation. The concepts presented in this chapter will serve as a contextual setting and as a basis for the disk modelling performed during this thesis.

The first part of chapter 3 is dedicated to describing the most fundamental chemical processes at stake in protoplanetary disks, in particular those embedded in the chemistry code NAUTILUS. This will serve as a basis to understand the interpretations of the chemistry results. The second part of the chapter describes the working principle of NAUTILUS, more specifically the three-phase model and the multi-grain version of the code. The last part addresses theoretical and observational aspects of H_2 formation in space which will justify the implementation of stochastic formation rates in NAUTILUS.

In chapter 4, we presents the physical disk model built and used during this thesis work, both for the radiative transfer simulations and chemistry simulations. The physical disk structure is derived using the parameters of the *Flying Saucer*.

chapter 5 is a key chapter as it is concerned with describing the coupling between radiative transfer simulations to the chemical code NAUTILUS.

In chapter 6, we presents a bunch of important results both from the radiative transfer simulations and from the chemistry simulations. The first part of the chapter presents the dust temperature and UV flux results in the case of a full grain size and spatial distribution in the disk model. The second part presents chosen substantial results of chemistry from NAUTILUS.

In chapter 7, we give an overview of the main results of the thesis. Then, we briefly describe ongoing projects and future perspectives that are direct follow-up of this work.

Chapter 2

Protoplanetary disks

Contents

2.1 Observable properties of disks

2.1.1 Classifications of Young Stellar Objects

The evolution of a Young Stellar Object (YSO), from its early phase as a protostar to a main-sequence star, is usually described according to the shape of its SED λF_λ (left column of Figure 2.1). A typical SED exhibits an infra-red excess (displayed in red in the SEDs of Fig. 2.1) and an ultra-violet excess (displayed in yellow). The infra-red excess is usually attributed to the presence of hot dust in the disk around the protostar while the ultra-violet excess is attributed to accretion processes of gas onto the stellar surface. The slope of the SED between near-IF and mid-IF is defined as,

$$\alpha_{IR} = \frac{\mathrm{d}\log(\lambda F_\lambda)}{\mathrm{d}\log(\lambda)} \tag{2.1}$$

which is a useful tool to quantify the magnitude of the IR excess and classified the evolution stages of YSO.

The SEDs are observationally classified into four different class detailed in Figure 2.1 and interpreted as different successive evolutionary phases [Adams et al., 1987] of stellar formation.

- **Class 0:** SED peaks in the far-IF and even mm domain of the spectrum without any visual or mid-IF emission. Thus, the slope α_{IR} does not exist. This stage is that of a protostar still collapsing and strongly accreting where the majority of the mass is still embedded in the accreting envelope.
- **Class I:** SED is almost flat (α_{IR}). The SED peaks in the far-IR with a minor rising of the shape into mid-IR characterizing the dust emission of the circumstellar accretion disk. These objects are older than Class 0 objects. Most of the mass is now in the central core.
- **Class II:** SED due to the emission of the disk and of the central pre-main sequence star, falls into mid-IR ($-1.5 < \alpha_{IR} < 0$). The envelope is now dissipated. These objects are called Classical T Tauri star (CTTS)s. An excess of UV due to accreting material is commonly detected.
- **Class III:** Pre-main sequence stars with little or no IR excess ($\alpha_{IR} < -1.5$). These objects have an almost pure stellar photospheric spectrum, meaning that most of the gas disk has almost disappeared and that only a debris disk remains.

2.1.2 Accretion rate

It is first important to point out the distinction between active and passive disks. In active disks, the release of gravitational potential energy as gas flows inward is the main source of energy. Active disks are therefore accreting disks. In passive disks, the internal heat essentially comes from the stellar radiation.

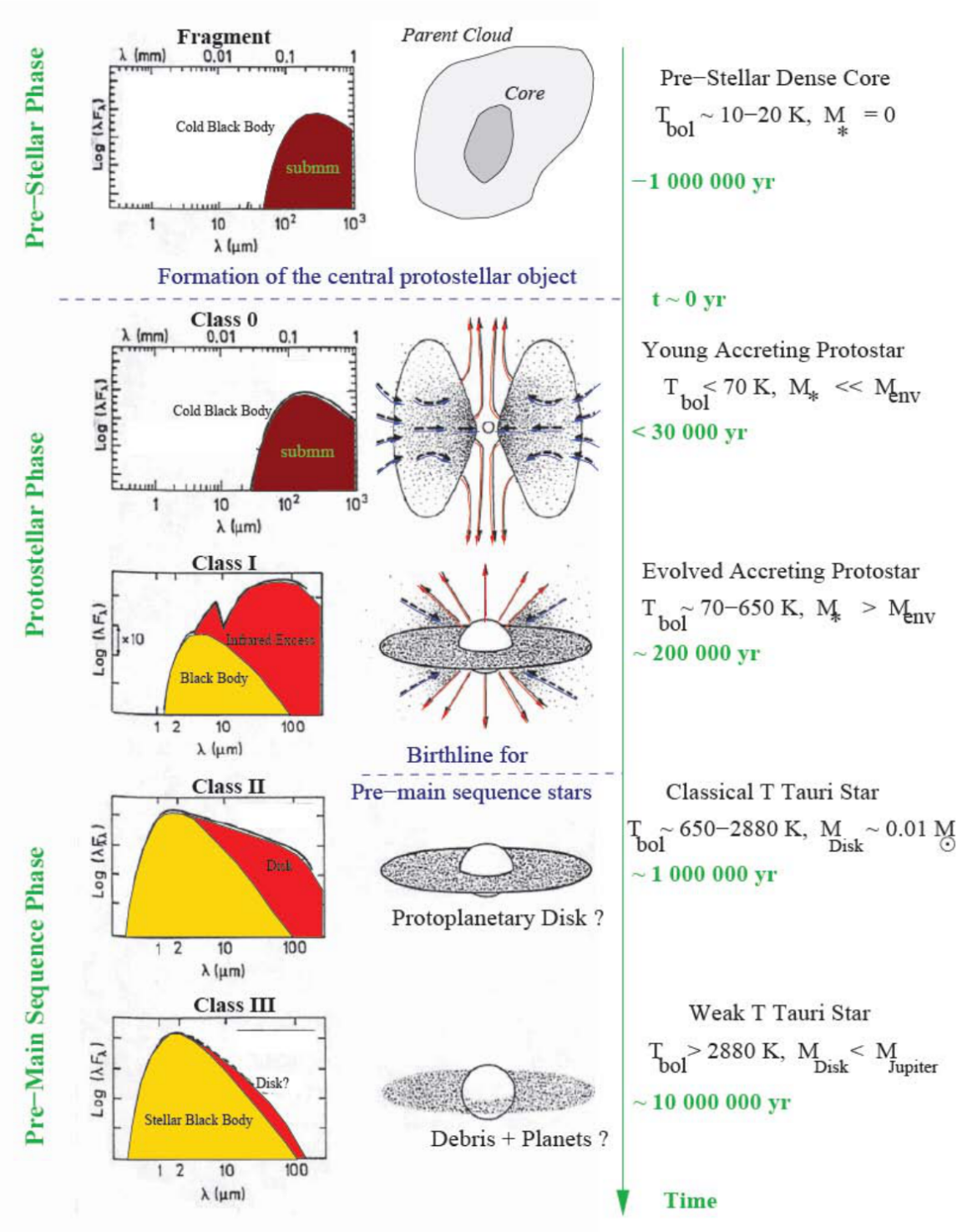

Figure 2.1: The four stages of stellar formation, from class 0 to class III. The IR excess are displayed in red while the UV excess are displayed in yellow. [Extracted from André, 2002]

Let us consider an active disk with an accretion rate through the disk $\dot{M}$. In a steady-state disk, with the radial inward velocity v_r, we can define the accretion rate as:

$$\dot{M} = -2\pi r \Sigma_g v_r = \text{constant} \tag{2.2}$$

where Σ_g is the gas surface density. We will discuss the value of the radial inward velocity in Section. 2.5.3.

However, in practice, the accretion rate is estimated by measuring the stellar and disk luminosity. The luminosity of the disk in the infra-red L_{IR} is the sum of the fraction of intercepted stellar luminosity reprocessed by the disk and half of the accretion luminosity:

$$L_{IR} = fL_* + \frac{1}{2}L_{accr}. \tag{2.3}$$

We can derive L_{accr} and therefore the accretion rate $\dot{M}$ by comparing L_{IR} to the stellar luminosity L_*. In typical CTTSs, the stellar magnetic field disrupts the inner disk at a radius R_m. For a star of mass M_* and radius R_*, the accretion luminosity is written as,

$$L_{accr} \approx GM_*\dot{M}\left(\frac{1}{R_*} - \frac{1}{R_m}\right) \tag{2.4}$$

We note that this implies to know the fraction f with a good approximation but uncertainties can affect the estimation of f. The accretion luminosity is generated by shocks or hotspots on the stellar surface. A typical estimated values of the mass accretion rate around solar mass stars using this method is $\dot{M} \sim 10^{-8} M_\odot$ yr^{-1}.

Lifetime Characterizing the typical disk lifetime is crucial as it gives a maximum timescale to allow for planets to form. Many estimations of disk lifetime are performed via statistical approaches. The idea is to consider the largest unbiased sample possible of T Tauri stars of known age and compare the disk evolution to the age of the star. To do so, we study the IR excess of the T Tauri's SED. For instance, a lack of IR excess at certain wavelengths indicates that a region of the disk has been cleared. Most statistical surveys has shown that disks can live for as long as a few10^7 yr.

2.1.3 Chemical reservoirs in disks

99% of the disk mass content is gas, the other 1% is made of solid dust particles. This is roughly the same ratio as in the molecular cloud matter from which the disk was formed. However, the observed gas-phase chemical content in disks is much more scarce than in the ISM. Table. 2.1 shows a list of detected molecules and isotopologues in disks to date [McGuire, 2018]. This is probably due to several factors that alter the possibility to observe molecules. The first reason is the very small angular apparent size of most disks, as even the nearest objects are only of the order of the arcsecond, contrary to clouds whose size can extend to several degrees. Disks push the limits of observation and challenge even the most powerful instruments like ALMA. The second factor is due to the disk structure itself. Complex molecules are formed and locked on dust grain surfaces in

the cold shielded mid-plane of disk, which drastically decreases the detectability of such molecules. The poor quantity that are liberated to the gas-phase is within very narrow regions of the disk. Gas-phase molecules also tend to reach upper layers of the disk where they meet the intense UV flux resulting in large photo-destruction rates.

Another fundamental question is the chemical inheritance of disks. While the primordial dense molecular clouds are usually already very rich, it is very likely that the stellar formation process modifies the chemical material of the cloud and it is still unknown how much of the chemical content survives the collapse (see for instance Visser+etal2009).

Figure 2.2 illustrates the vertical structure of a disk and the global different chemical layers. The surface layers, subject to intense photo-destructive UV radiation, is a PDR-like region where the chemistry is dominated by atomic ions charge exchange. In particular, the ion C^+ can be found in majority but other ions exist in smaller abundance. As the extinction increases and the A_v reaches ~ 1 deeper in the disk, ions can be recombined with electrons and the chemistry transitions to neutrals and molecules. Atomic hydrogen is mostly transformed into molecular hydrogen H_2. Molecules are then self-shielded and shielded which results in a substantial decrease of the UV radiation penetration and the photodissociation rates. Gas-phase CO, in particular, becomes abundant, along with other molecules such as HCN, H_2CO and CS. The layer is called the "molecular layer. As we go even deeper in the disk, the temperature suddenly drops (down to $\sim$ 5 - 10 K) and the chemistry becomes dominated by icy processes of adsorbed species on grain mantles. The hydrogenation of various icy molecules on surfaces allows to increases the chemical complexity. Only CH_3OH and CH_3CN [Öberg et al., 2015, Walsh et al., 2016] have been detected in the gas-phase, but as mentioned above, observing complex molecules in disks requires extremely powerful instruments using state-of-the-art techniques (velocity stacking or matched-filtering techniques).

Table 2.1: List of molecules detected in protoplanetary disks, with two to six atoms as of 2018 [McGuire, 2018].

2 atoms	**3 atoms**	**4 atoms**	**5 atoms**	**6 atoms**
CN	H_2O	NH_3	HCOOH	CH_3CN
$C^{15}N$	HCO^+	H_2CO	c-C_3H_2	CH_3OH
CH^+	DCO^+	C_2H_2	CH_4	
OH	$H^{13}CO^+$		HC_3N	
CO	HCN			
^{13}CO	DCN			
$C^{18}O$	$H^{13}CN$			
$C^{17}O$	$HC^{15}N$			
H_2	HNC			
HD	H_2S			
CS	N_2H^+			
$C^{34}S$	N_2D^+			
SO	C_2H			
	CO_2			

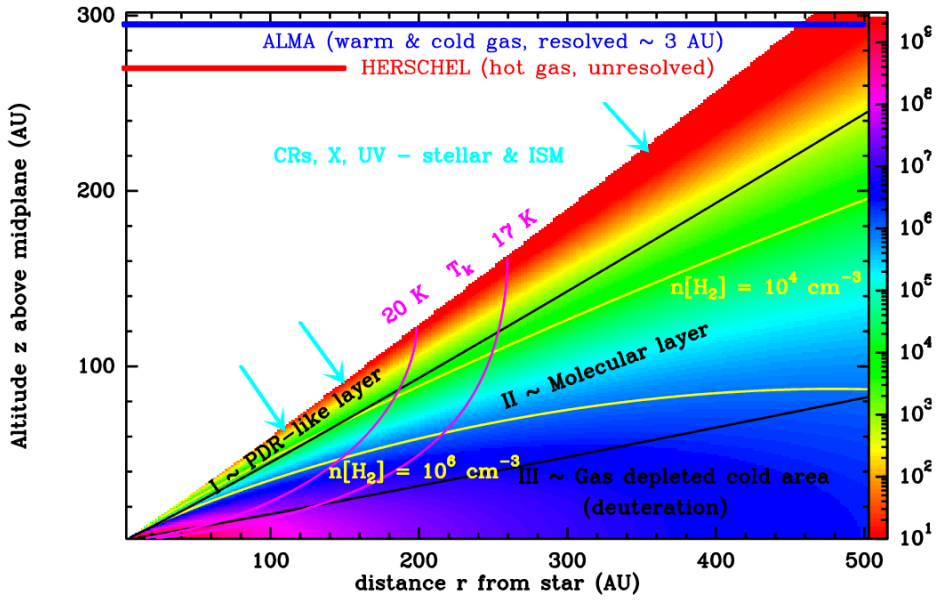

Figure 2.2: Molecular structure for a typical disk orbiting a young solar-mass star: the volume density is shown in color as a function of radius r and altitude z above the mid-plane. The pink lines show the isotherms at 17 and 20 K. The red line gives the area sampled by Herschel observations while the blue line give the area sampled by ALMA. The vertical structure is divided into three layers: I) the PDR-like layer irradiated by the UV stellar and interstellar field, II) the molecular layer and III) the mid-plane where only H_2 and deuterated isotopologues of simple molecules are abundant in the gas-phase (from Dutrey et al. [2014]).

2.1.4 Observation of disks

Observing protoplanetary disks is an extremely challenging task. One reason is that most of their content (dust and gas) is opaque to visible light; another is that disks are very small objects. Their angular size (the apparent size to which they appear on the Celestial sphere) is usually tiny, as we will see, even for the closest disks. In other words, they require very sophisticated observational tools with high resolution and high sensitivity to specific intervals of the electromagnetic spectrum. Fortunately, the 21st century has seen the rise of a new observational era with unprecedented powerful telescopes that has boosted the study of disks over the last decades, such as mm/sub-mm interferometers.

2.1.4.1 Atmospheric transparency

The first observational limitation is the Earth's atmosphere. Figure 2.3 illustrates the atmospheric opacity as a function of wavelength. Visible light is quite well observable from the Earth with minor atmospheric distortions that can be corrected by adaptive optics and by observing at high altitudes. Radiations at shorter wavelengths, such as UV, X-rays and Gamma rays are almost totally blocked by the upper atmosphere and space-based telescopes are required to observe in this electromagnetic domain. Most of

the IR radiations are absorbed by atmospheric gases and are also best observed from space or from air-bone observatories.

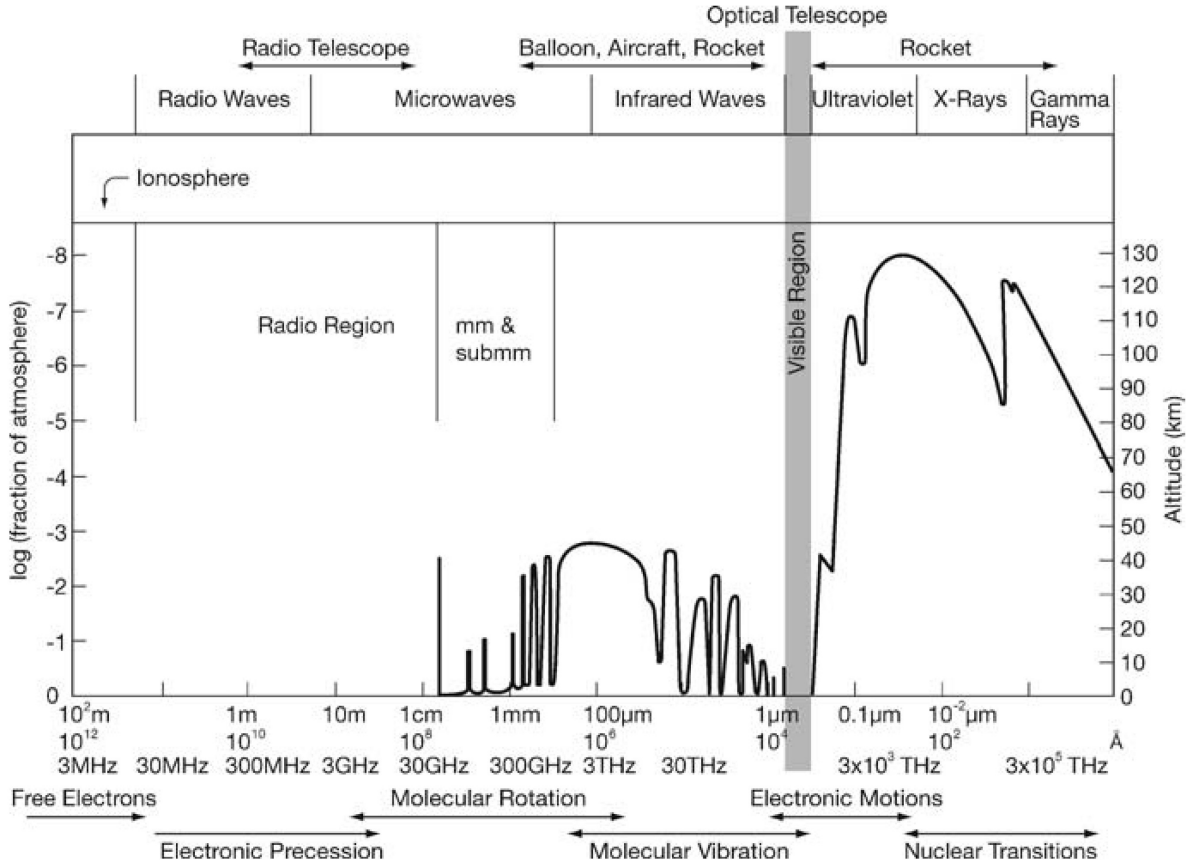

Figure 2.3: Atmospheric electromagnetic transparency (from Wilson et al. [2013]).

There is, on the other hand, a large atmospheric transparency window in the radio wave frequencies, which makes these waves observable with ground-based telescopes. Radio waves are the ideal domain to probe the cold Universe and, lucky for us, disks are relatively cold objects.

2.1.4.2 Resolution

Most nearby known protoplanetary disks are located at about $\sim$ 100 pc from the Sun in the Rho Ophiuchi cloud complex. Even at this relative small distance, a typical disk of 100 au diameter will have an angular size of nearly 1 arcsecond. The Rayleigh criterion shows that a telescope of diameter D, observing at wavelength λ has a resolution of $\theta = 1.22\lambda/D$. The resolution θ is then the minimum observable angular size. We see that the larger the diameter, the better the resolution. But we also see that the resolution goes down for large wavelengths. Let's assume we want to observe the closest known protoplanetary disk, orbiting around TW Hydrae, a $\sim$ 10 Myr old TTS located at a distance of $\sim$ 59.5 pc [Gaia Collaboration et al., 2016]. The apparent size of the disk is about 4 arcseconds. If we use a ground-base telescope of diameter D = 8 m, observing at $\lambda = 3$ μm, the resolution

will be about 0.1 arcseconds, allowing 40 resolution points to observe the whole disk. At $\lambda = 30$ μm, this drops to only 4 resolution points. The relationship between resolution and diameter has motivated the construction of increasingly powerful telescopes.

To counteract the physical constraints imposed by the size, astronomers have developed interferometric techniques, which correlates the received signal from two or more telescopes to simulate the resolution of a larger telescope (its resolution being given by the longer baseline). The late 20th century has seen the construction of many such radio-interferometers.

A significant example is the ALMA interferometer in Chile, the most complex interferometer ever built to date, which is made of 66 state-of-the-art antennas. The baseline can be spread over distances of up to 16 km, achieving a resolution of up to 0.01 arcseconds. Figure 2.4 shows a gallery of 20 high-resolution images of protoplanetary disks observed by ALMA during the large survey program Disk Substructures at High Angular Resolution Project (DSHARP) in 2018 (see Andrews et al. [2018] or Huang et al. [2018]). The survey has revealed substructures and complex patterns that changed our views on these objects.

2.1.4.3 Thermal radiation

One fundamental reason why mm/sub-mm domain is essential is the overall temperature in disks. Indeed, disks are cold objects. This is especially true for the dust. The temperature can be determined via the equilibrium between absorbed energy by the grain and the energy re-emitted. The absorbed energy comes mostly from stellar or diffuse interstellar radiations and from collision with gas particles. The energy is re-emitted at longer wavelengths through thermal radiation in a quasi-black body like shape.

In protoplaneraty disks around T Tauri stars, the radiation field is effectively blocked by the gas and dust of the upper layers. As a consequence, in the mid-plane, where planets form, the grain's equilibrium temperature T_d is expected to be as low as 10 K in the mid-plane. Assuming a black-body, we derive a peak emission wavelength from Wien's law at this temperature of about 290 μm. This shows that the observation at mm wavelengths is necessary.

2.1.4.4 Spectroscopy

Unlike the dust, the gas possesses discrete emission lines. When an atom interacts with electromagnetic radiation, the transition states between the particle's quantized energy levels generate discrete emission lines. Each atom possess a unique emission spectrum. Observing particular spectral transitions is therefore the signature of the presence of particular species.

The spectral structure of molecules is far more complex than that of atoms. For molecules, the discrete spectral lines are not restricted to electronic transitions and we also have to consider energy transitions that are associated with molecular motion i.e. rotation and vibration.

The detection of spectral lines of commonly observed molecules can be used to derive

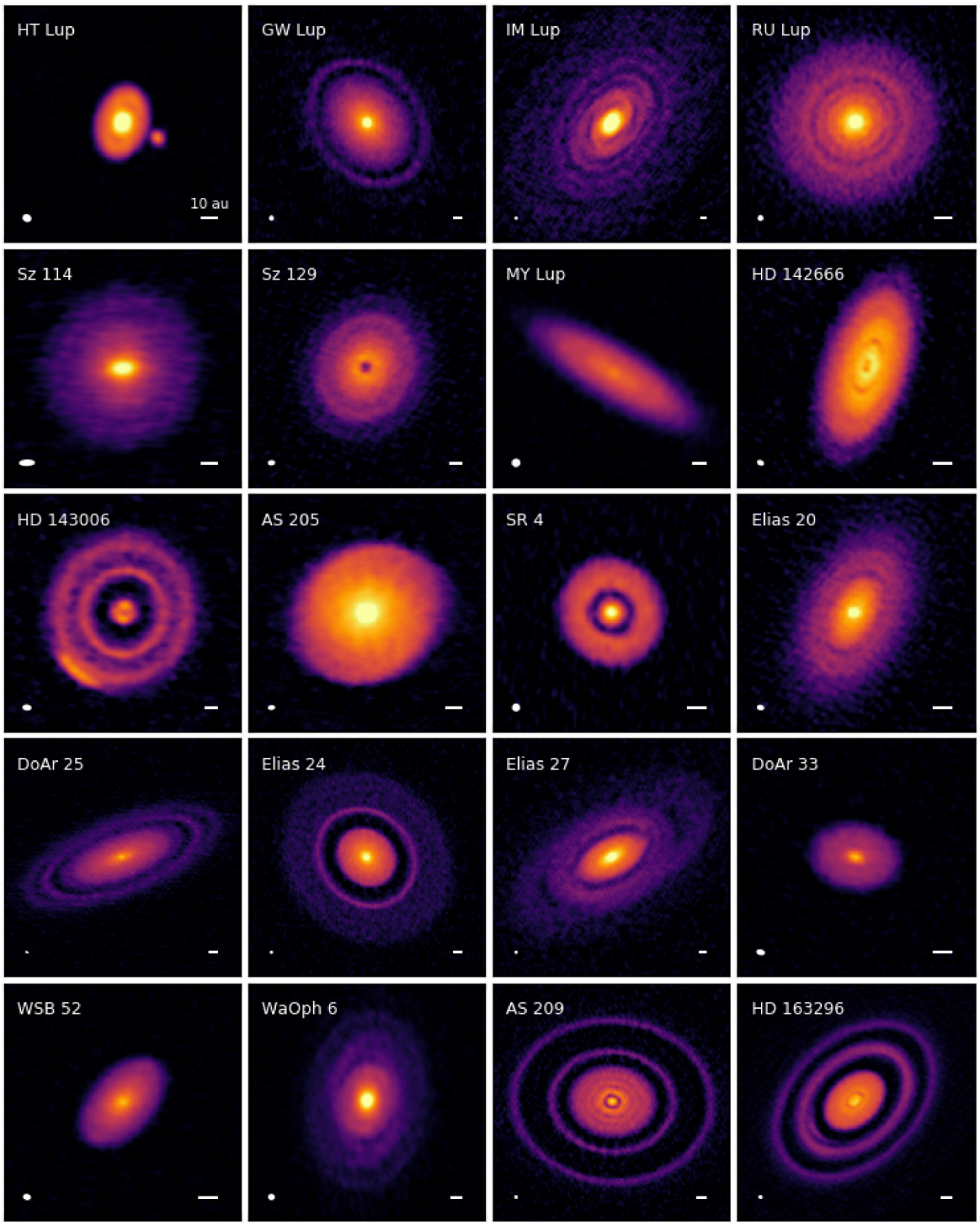

Figure 2.4: Gallery of 240 GHz (Band 6) continuum emission images for 20 disks in the DSHARP sample. Beam sizes and 10 au scalebars are shown in the lower left and right corners of each panel, respectively. Credit: ALMA (ESO/NAOJ/NRAO), Andrews et al. [2018].

crucial informations about the physical conditions since the line intensities and profiles depend, for instance, on the temperature, the gas density or the kinematic properties of the observed object. This is therefore a very powerful tool in astrophysics.

Molecular hydrogen is the most abundant molecule and could be an ideal probe to characterize the physical environments. Unfortunately, H_2 has no permanent electric dipole moment giving rise to rotational or vibrational lines due to its symmetry, so H_2 is particularly difficult to observe. We have to consider other molecules to trace the physical conditions. The second most abundant molecules, CO and CO isotopologues, have a dipolar moment. The wavelength of the well-known rotational transition of CO from level J = 1 to J = 0 is 2.6 mm, well inside the mm/sub-mm domain. CO is therefore easily observed and mapped with ground-based telescopes and is used as the main tracer of the physical conditions and, in particular, of H_2. The other commonly used molecules are HCO^+, H_2CO, CS, CN, HCN and HNC [Dutrey et al., 2014].Over the last decades, the new facilities (ALMA, NOEMA...) have allowed to observe at a better spatial and frequency resolution and detect additional molecules (DCN, N_2H^+, H_2O, HC_3N, CH_3OH...). Figure 2.5, for example, shows the detection of N_2H^+ 3 – 2, DCO^+ 4 – 3, and $C^{18}O$ 2 – 1 in the HD 163296 disk by Qi et al. [2015]. This demonstrates again that studying the physical conditions of disks naturally requires to do chemistry.

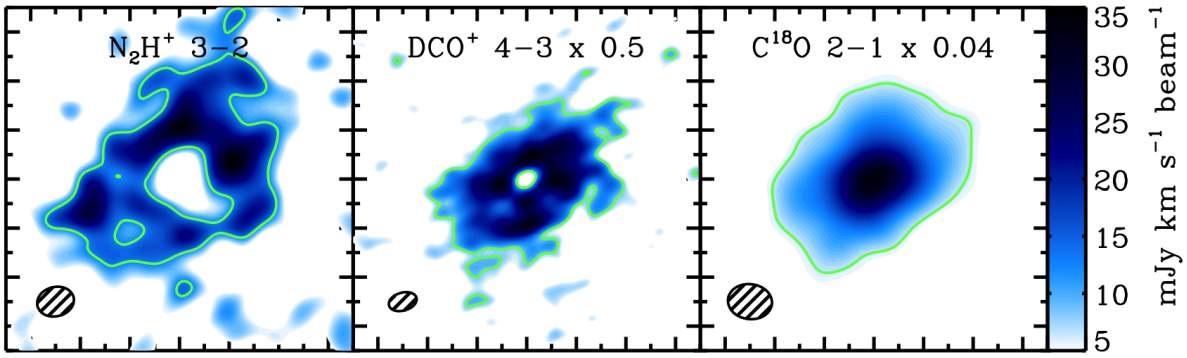

Figure 2.5: Detection of N_2H^+ 3 – 2, DCO^+ 4 – 3, and $C^{18}O$ 2 – 1 in the HD 163296 disk [Qi et al., 2015].

2.2 Physical properties and disk structure

In the following description, unless otherwise specified, we use subscript g for gas, subscript d for dust and subscript 0 for values given at reference radius. Volumes are expressed in cm^{-3} and the mass in g. n always describes a number density while ρ always describes a mass density. The structure described is that of an axisymmetric, non-self-gravitating, thin, accretion disk, evolving slowly between static states. Thus, the disk can be simply described using cylindrical coordinates decomposed into a radial distance r from the central star and an altitude z above the mid-plane. The main quantities discussed are the grain size a, the gas temperature $T_g(r, z)$, the dust temperature $T_d(a, r, z)$,

the gas number density $n_g(r, z)$, the dust number density $n_d(a, r, z)$, the gas molecular content and the ionization fraction.

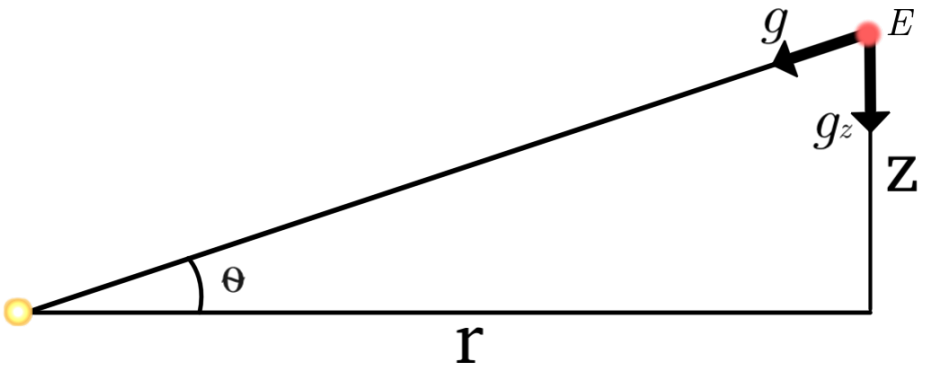

Figure 2.6: Fluid element E in a disk at a distance $d = \sqrt{r^2 + z^2}$ from the star.

2.2.1 Vertical structure

The vertical structure of a geometrically axisymmetric thick disk can be derived by considering hydrostatic vertical equilibrium. The most simple case is an optically thick disk irradiated by stellar flux with negligible mass compared to the mass of the star. This is the case for the majority of TTauri disks whose average mass is of the order of a few 1/100 of the central star.

If we assume, as a first approximation, that the gas is described by the equation of state, has the constant sound speed c_s, and that the disk is vertically isothermal, the gas pressure is given by:

$$P = \rho_g c_s^2 \tag{2.5}$$

where ρ_g is the mass density of the gas. The sound speed is related to the gas temperature via $c_s^2 = k_B T_g / \mu m_H$, where k_B is the Boltzmann's constant, m_H is the mass of an hydrogen atom and μ is the mean molecular weight. Thus, the gas pressure can be written in the form:

$$P = \frac{\rho_g k_B T_g}{\mu m_H} \tag{2.6}$$

The vertical pressure gradient is,

$$\frac{dP}{dz} = -\rho_g g sin(\theta) = \rho_g g_z \tag{2.7}$$

The fluid element E (see Fig. 2.6) is at a distance $d = \sqrt{r^2 + d^2}$ from the star. Assuming the disk contribution to the gravitational force is negligible, the vertical component of gravity g_z seen by the element in cylindrical coordinates is,

$$g_z = \frac{GM_*}{d^2} sin(\theta) = \frac{GM_*}{d^3} z. \tag{2.8}$$

where M_* is the mass of the central star and G is the gravitational constant. For a thin disk, $z << r$, so $g_z \simeq \Omega_K^2 z$, where $\Omega_K(r) = \sqrt{GM_*/r^3}$ is the Keplerian angular velocity. Substituting into Eq. 2.23 yields,

$$\frac{dP}{dz} = -\rho_g \Omega_K^2 \boldsymbol{z} = -\rho_g \sqrt{\frac{GM_*}{r^3}} z \tag{2.9}$$

Substituting Eq. 2.6 into Eq. 2.9 yields,

$$\frac{k_B}{\mu m_H} \frac{\partial(\rho_g T_g)}{\partial z} = -\rho_g \frac{GM_*}{r^3} z \tag{2.10}$$

$$\iff \frac{\partial(\rho_g T_g)}{\partial z} = -\frac{\rho_g \mu m_H}{k_B} \frac{GM_*}{r^3} z \tag{2.11}$$

$$\iff \frac{\partial \ln(\rho_g(r,z))}{\partial z} = -\left[\left(\frac{\mu m_H}{k_B T} \right) \left(\frac{GM_*}{r^3} \right) z + \frac{\partial \ln(T)}{\partial z} \right] \tag{2.12}$$

Equation 2.12 is the equation of the vertical hydrostatic equilibrium we want to solve analytically. In the isothermal case ($\partial \ln(T)/\partial z = 0$), the solution becomes trivial. Considering the gas scale height can be written as follows:

$$H_g(r) = \frac{c_S}{\Omega_K} = \sqrt{\frac{k_B T_{mid} r^3}{\mu m_H G M_*}} \tag{2.13}$$

where $T(z) = T(z = 0) = T_{mid}$, we can substitute Eq. 2.13 into the equation of the vertical hydrostatic equilibrium (Eq. 2.12) so that it becomes:

$$\frac{d \ln(\rho_g(r,z))}{dz} = -\frac{z}{H_g^2(r)} \tag{2.14}$$

Integrating Equation 2.14 over z, the solution is,

$$\rho_g(r,z) = \rho_g(r, z=0) \exp\left[-\frac{z^2}{2H_g(r)^2} \right] \tag{2.15}$$

where $\rho_g(r, z = 0) = \rho_{g,mid}(r)$ is the mid-plane density. Defining the surface density $\Sigma_g(r) = \int_z \rho dz$, we write:

$$\Sigma_g(r) = \rho_{g,mid}(r) \int_{-\infty}^{+\infty} \exp\left[-\frac{z^2}{2H_g(r)^2} \right] dz. \tag{2.16}$$

By integrating Eq. 2.16 and substituting into Eq. 2.15 we obtain:

$$\rho_g(r,z) = \frac{\Sigma_g(r)}{\sqrt{2\pi} H_g(r)} \exp\left[-\frac{z^2}{2H_g(r)^2} \right] \tag{2.17}$$

We have found the standard vertical mass density profile of the gas in an isothermal disk in hydrostatic equilibrium. It is clear that the profile has a gaussian shape.
As previously mentioned, actual disks are not exactly vertically isothermal even though the approximation is sufficient for most disk models. If the disk is accreting, the density profile of a non-isothermal disk will depart from a gaussian shape.

The shape of the disk depends on the ratio $H_g(r)/r = c_s/v_\phi$, where v_ϕ is the local azimutal velocity. If we parametrize the radial variation of c_s such that:

$$c_s \propto r^{-\beta}. \tag{2.18}$$

Then the aspect ratio depends upon,

$$\frac{H_g(r)}{r} \propto r^{-\beta+\frac{1}{2}} \tag{2.19}$$

If $\beta = 1/2$, the disk has a constant opening angle and has a *flat*[1] geometry. If $\beta > 1/2$, the disk is called *self-shadowed* and is irradiated by the star only at their inner edge. If $\beta < 1/2$, the disk thickness increases with r. Such geometry is called *flaring*, allowing the disk to intercept a significant fraction of the stellar flux. We will see that the majority of the disks have a flaring geometry.

2.2.2 Radial structure in disks

2.2.2.1 Disk rotation

Neglecting the gas pressure, each fluid element in the disk is in a perfectly Keplerian rotation around the star with a specific angular momentum $l = \Omega_K(r)r^2$ where $\Omega_K(r)$ is the Keplerian angular velocity:

$$\Omega_{g,K}(r) = \sqrt{\frac{GM_*}{r^3}} \iff v_{g,K}(r) = \sqrt{\frac{GM_*}{r}} \tag{2.20}$$

In circumstellar disks, however, the pressure decreases with the radial distance ($dP/dr < 0$). Thus, in addition to the gravity and centrifugal force, the radial force undergone by a fluid element is also balanced by a radial pressure gradient. As a consequence, the effective gravity "felt" by a parcel of gas is smaller than the gravity exerted by the star alone and therefore the orbital velocity of the gas is smaller than the Keplerian velocity.

Given a radial density profile, we can derive the orbital velocity of the gas $v_{g,\phi}$ in the mid-plane using the azimuthal component of the momentum equation,

$$\frac{\partial \boldsymbol{v}}{\partial t} + (\boldsymbol{v}.\nabla)\boldsymbol{v} = -\frac{1}{\rho_g}\nabla P - \nabla\Phi \tag{2.21}$$

which is written in the mid-plane as:

[1] As pointed out by (Dullemond 2013 les Houches), flat actually means $H_g \approx 0$ and we should instead prefer the term *conical*. However, as the term *flat* is more widely used in the literature, we will use the term *flat* in this thesis.

$$\frac{v_{g,\phi}^2}{r} = \frac{v_{g,K}^2}{r} + \frac{1}{\rho_{g,mid}}\frac{\mathrm{d}P}{\mathrm{d}r}. \tag{2.22}$$

where P is the pressure in the mid-plane of the disk. We see that the orbital velocity deviates from strict Keplerian rotation by a magnitude dependent on the pressure gradient. Considering Equation 2.5 and 2.13, we can estimate this magnitude as follows:

$$\begin{aligned}\frac{1}{\rho_{g,mid}}\frac{\mathrm{d}P}{\mathrm{d}r} &\sim -\frac{1}{\rho_{g,mid}}\frac{P}{r} \\ &\sim -\frac{1}{\rho_{g,mid}}\frac{\rho_{g,mid}c_s^2}{r} \\ &\sim -\frac{GM_*}{r^2}\left(\frac{H_g}{r}\right)^2\end{aligned} \tag{2.23}$$

Equation 2.22 can then be written as:

$$v_{g,\phi}^2 = v_{g,K}^2\left[1 - \mathcal{O}\left(\frac{H_g}{r}\right)^2\right]. \tag{2.24}$$

Equation 2.24 shows that the deviation to the Keplerian velocity $v_{g,K}$ is of the order of the the aspect ratio of the disk. For a thin (H_g/r), the contribution is negligible and to a good approximation the velocity is Keplerian. However, the consequences of this deviation on solid particles dynamics in the disk are critical for planet formation processes.

2.2.2.2 Disk radial distribution and evolution

Let us describe the matter radial distribution with the surface density $\Sigma_g(r)$. As just seen, the deviation from the Keplerian velocity is small and the angular momentum within the disk, to a good approximation is that of a Keplerian orbit $l = \Omega_K(r)r^2$, which is an increasing function of the radial distance. During the evolution of the disk, matter is lost via accretion by the star and the angular momentum cannot be conserved. The momentum lost close to the star must be redistributed throughout the disk. This process is called angular momentum transport.

Following Pringle [1981], we consider a parcel of gas and derive the equation of motion. The disk is assumed to be axisymmetric about its center of rotation so that we can use the coordinates (r, z). The disk has a surface density $\Sigma_g(r,t)$ and a radial velocity $v_r(r,t)$. Let us consider an annulus from r to $r + \Delta r$. The equation is then written,

$$\frac{\partial}{\partial t}(2\pi r \cdot \Delta r \cdot \Sigma_g) = v_r(r,t)\cdot 2\pi r\Sigma(r,t) - v_r(r+\Delta r,t)\cdot 2\pi(r+\Delta r)\cdot\Sigma_g(r+\Delta r, r). \tag{2.25}$$

Taking the limit for small values of Δr, we can perform an elementary derivation:

$$r\frac{\partial \Sigma_g}{\partial t} + \frac{\partial}{\partial r}(r\Delta v_r) = 0. \tag{2.26}$$

Considering the conservation of angular momentum we write,

$$r\frac{\partial}{\partial t}(\Sigma_g r^2\Omega) + \frac{\partial}{\partial r}(r\Sigma v_r \cdot r^2\Omega) = \frac{1}{2\pi}\frac{\partial G}{\partial r} \tag{2.27}$$

where $\Omega = \Omega(r)$ is the angular velocity of the disk and the right-hand side of the equation is the net effect of the viscous torques due to inner and outer annuli. From fluid dynamics [Pringle, 1981] the quantity G is written in terms of the kinematic viscosity ν as,

$$G = 2\pi r \cdot \nu\Sigma_g r\frac{\mathrm{d}\Omega}{\mathrm{d}r} \cdot r. \tag{2.28}$$

The right-hand side of Eq. 2.28 is the product of the annulus diameter, the viscous force per unit length and the level arm r. Then, substituting G in Eq. 2.27 by Eq. 2.28, eliminating v_r from these two equations and limiting to a Keplerian potential with $\Omega \propto r^{-3/2}$, we obtain,

$$\frac{\partial\Sigma_g}{\partial t} = \frac{3}{r}\frac{\partial}{\partial r}\left[r^{1/2}\frac{\partial}{\partial r}(\nu\Sigma_g r^{1/2})\right] \tag{2.29}$$

which represents the spatial- and time-dependent evolution equation of an accretion disk. Solving the equation to find the surface density distribution throughout the disk relies on the viscosity ν we consider.

Solutions: One of the most successful and practical solution is the self-similar one derived by Lynden-Bell and Pringle [1974]. They assumed that the viscosity was defined by a power-law distribution in radius, $\nu \propto r^\gamma$ and that at time $t = 0$, the disk has a surface density profile corresponding to a steady-state solution with an exponential cut-off at $r = r_0$. The initial surface density is,

$$\Sigma(t = 0) = \frac{C}{3\pi\nu_1 x^\gamma}\exp\left[-x^{(2-\gamma)}\right]. \tag{2.30}$$

where $x = r/r_0$, C a normalization factor and ν_0 the viscosity at r_0. The self-similar solution is then,

$$\Sigma(x, T) = \frac{C}{3\pi\nu_0 x^\gamma}T^{-(5/2-\gamma)/(2-\gamma)}\exp\left[-\frac{x^{(2-\gamma)}}{T}\right] \tag{2.31}$$

where,

$$T \equiv \frac{t}{t_s} + 1 \tag{2.32}$$

and,

$$t_s \equiv \frac{1}{3(2-\gamma)^2}\frac{r_0^2}{\nu_0}. \tag{2.33}$$

where t_s is the viscous time of the disk, which is of the order of a few 10^5 yr [Guilloteau et al., 2011]. The solution (Eq. 2.31 shows that the disk mass decreases as the disk size

increases to conserve angular momentum.

2.2.3 Thermal structure

Now that we have described the gas distribution in the disk, we want to determine the temperature structure the disk as a function of the distance r and altitude z. To answer this question, we must first determine what the cooling and heating processes at work in a disk are. In the case of a passive disk (not accreting), the temperature is fully determined by stellar radiation. However, if we consider an accreting disk, the temperature is also determined by viscous heating processes. In this section, we will first describe the temperature in a passive disk, then we will consider an active disk where both viscosity and stellar radiation contribute to the temperature.

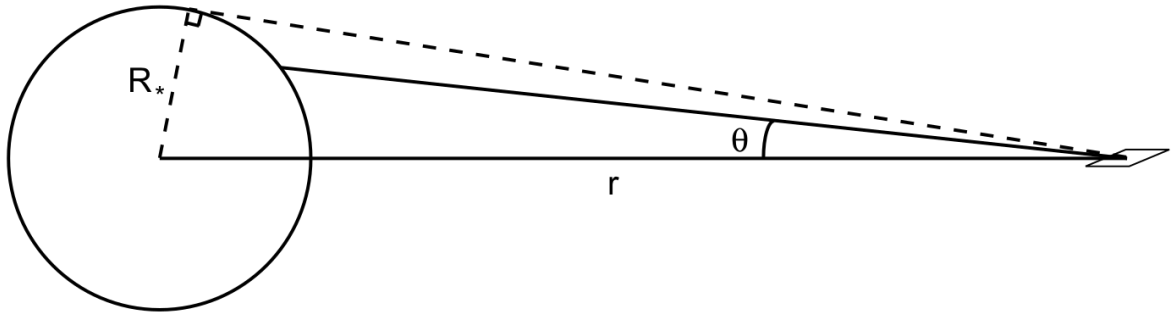

Figure 2.7: Unit surface area in the disk mid-plane at distance r from a star of radius R_*. The coordinates are [Extracted from Armitage, 2019]

Heating by stellar radiation In most disks, the main heating process is stellar irradiation (even accreting ones), in particular in the late stages of evolution. As we have seen, protoplanetary disks are optically thick objects and the stellar radiation will mostly be absorbed by the surface layers of the disk. However, the amount of absorption of radiation is totally dependent on the geometric shape of the disk. In the case of self-shadowed disks, only the inner edge is irradiated and the rest is not illuminated. In the case of flaring disks, there exist a shallow grazing angle allowing for the disk surface to be illuminated.

First, following Adams and Shu [1986], Kenyon and Hartmann [1987], Chiang and Goldreich [1997] and Armitage [2013], we consider a flat thin disk that absorbs all stellar light and re-emits it locally as a black-body. As see in Figure 2.7, we set up spherical polar coordinates and consider a stellar ray passing through the unit surface area at distance r from a star, forming an angle θ to the line joining the element to the center of the star. The star is modeled as a spherical black-body of effective temperature T_* and radius R_*. The flux passing through the surface area is,

$$F = \int I_* \sin\theta \cos\phi d\Omega \tag{2.34}$$

where I_* is the brightness of the star, ϕ is the azimuthal angle defining different rays with same angle θ and $d\Omega$ is the element of solid angle. If we only consider the flux coming from the upper surface of the star, the limits of the integral are,

$$\begin{aligned} -\pi/2 < \phi \leq \pi/2 \\ 0 < \theta < \sin^{-1}\left(\frac{R_*}{r}\right). \end{aligned} \tag{2.35}$$

Substituting $d\Omega = \sin\theta d\theta d\phi$ into Eq. 2.34 and solving the integral yields,

$$F = I_*\left[\sin^{-1}\left(\frac{R_*}{r}\right) - \left(\frac{R_*}{r}\right)\sqrt{1-\left(\frac{R_*}{r}\right)^2}\right]. \tag{2.36}$$

Moreover, considering that the brightness of the star is $I_* = (1/\pi)\sigma T_*^4$ and the flux emitted from the one-sided disk element is σT_{disk}^4, where σ is the Stefan-Boltzmann constant, then, as the emitted and absorbed flux are to be equal, the radial temperature profile becomes,

$$\left(\frac{T_{disk}}{T_*}\right) = \frac{1}{\pi}\left[\sin^{-1}\left(\frac{R_*}{r}\right) - \left(\frac{R_*}{r}\right)\sqrt{1-\left(\frac{R_*}{r}\right)^2}\right]. \tag{2.37}$$

Then, integrating over radii, the total disk flux is written as:

$$\begin{aligned} F_{disk} &= 2\int_{R_*}^{\infty} 2\pi r\sigma T_{disk}^4 dr \\ &= \frac{1}{4}F_* \end{aligned} \tag{2.38}$$

The results show that the luminosity of the disk represents one-quarter of that of the star so that a passive flat disk is predicted to be less luminous than the star.

Assuming we are sufficiently far from the star surface ($R_*/r \ll 1$) we can expand the right-hand-side of Equation 2.37 in a Taylor series so that the disk temperature can be written in a more friendly form:

$$T_{disk} \propto r^{-3/4}. \tag{2.39}$$

The sound speed is then $c_s \approx r^{-3/4}$ and if the disk is assumed vertically isothermal, the aspect ratio (see Eq. 2.19) becomes,

$$\frac{H_g}{r} \propto r^{1/8}. \tag{2.40}$$

This tells us that the disk must have a moderate flaring geometry even considering a *flat* disk model. If the disk flares, then the surface intercepts a larger amount of radiation and the disk has a higher temperature. Therefore, the temperature profile as defined by Eq. 2.39 shall be the steepest expected temperature profile for passive disks.

Let us now consider a more realistic disk with an assumed flaring angle. The analytical treatment is far more complex than the *flat* case, but we can simplify the resolution by considering the star to be a point-source with R_* always very small compared to the dimension of the disk. Let us call the grazing angle φ and assume that this angle is always very small ($\varphi \ll 1$). The stellar flux at distance r is $F_*(r) = L_*/4\pi r^2$ where L_* is the stellar luminosity. The heating irradiation is twice (we consider the two sides of the disk) the projection of the stellar flux onto the surface of the disk,

$$Q_+^{irr}(r) = 2 \times \sin\varphi F_*(r) \simeq \phi \frac{L_*}{4\pi r^2} \tag{2.41}$$

The disk must in turn re-emit in order not to become hotter and hotter. To a good approximation, the disk must irradiate the whole heating Q_+^{irr} away so that $Q_+^{irr} = Q_-^{irr}$ where Q_-^{irr} is the cooling rate. If we assume a Planck function with temperature T_{eff} then the cooling rate is,

$$Q_-^{irr} = 2\sigma T_{eff}^4. \tag{2.42}$$

Equating Eq. 2.41 and 2.42 we find,

$$T_{eff} = \left(\varphi \frac{L_*}{4\pi\sigma r^2}\right)^{1/4}. \tag{2.43}$$

By observing that $L_* = 4\pi R_*^2 \Sigma_g T_*^4$, Eq. 2.43 becomes:

$$T_{eff} = T_* \left(\frac{R_*}{r}\right)^{1/2} \varphi^{1/4} \tag{2.44}$$

inferring that the disk temperature is proportional to $r^{-1/2}$.

Combining irradiation and accretion In the case of an active disk, where both viscous heating Q_+^{accr} and irradiation Q_+^{irr} are at work, the energy balance must be written as:

$$Q_- = Q_+^{irr} + Q_+^{accr}. \tag{2.45}$$

Then, the effective temperature is [see Shakura and Sunyaev, 1973, for a detailed analysis of the viscous heating]:

$$T_{eff} = \left(\frac{3}{8\pi\sigma}\dot{M}\Omega_K^2 + \varphi\frac{L_*}{4\pi\sigma r^2}\right)^{1/4}. \tag{2.46}$$

where the first term of the right-hand side is the term of the viscous heating. Equation 2.46 shows that for small radii, T_{eff} is dominated by accretion while for large radii T_{eff} is dominated by stellar radiation.

2.3 Transport of angular momentum

During the accretion phase of a disk, angular momentum must be transferred outwards in order for the material to move inwards and be accreted onto the star. Characterizing the efficiency of this transport is paramount as it regulates the evolution of the disk. We note that there are also strong bipolar flows in class O and I YSO.

In this section, we will introduce how viscosity originates and discuss the basic principle of the transport of angular momentum and turbulence within disks.

2.3.1 Origins of viscosity

In Section 2.2.2.2, we used a term called ν without explicitly specifying its definition. Here, we briefly introduce the origin of viscosity, the typical values and its importance in the context of protoplanetary disks.

The first type of viscosity that astrophysicists thought of is the molecular viscosity, which originates from thermal motion of the gas. It turns out that molecular viscosity is in fact negligible in protoplanetary disks. Let us consider a gas in which the mean free path is $\lambda = 1/n\sigma$, where n is the number density of molecules and σ is the collisional cross-section. The viscosity is,

$$\nu \sim \lambda c_s. \tag{2.47}$$

For a typical distance $r = 10$ AU in a disk, the molecular viscosity will be $\nu = 2.5 \times 10^7$ cm^2/s. If we estimate the corresponding viscous timescale at this distance we find,

$$\alpha_\nu = \frac{r^2}{\nu} \approx 3 \times 10^{13} yr. \tag{2.48}$$

It is clear that the timescale is way too large to account for the observed disk evolution.

Shakura-Sunyaev viscosity Molecular viscosity appears to be too small to provide a source of turbulence that would drive the angular momentum transport. Shakura and Sunyaev [1973] proposed that turbulence within the disk can provide a viscosity that exceeds molecular viscosity. The idea is to parametrize the viscosity without specifically identifying the cause. They noted that the largest turbulent scales are of the same order as the vertical scale height H_g and that we can use the sound speed c_s as the characteristic velocity of the turbulent motions. The viscosity is thus written as follows:

$$\nu = \alpha c_s H_g \tag{2.49}$$

where α is a dimensionless parameter that measures the efficiency of the turbulence to generate angular momentum transport. It appears to be important to estimate the necessary value of α to account for the observed evolution of protoplanetary disks. Noting that $c_s \simeq H_g \Omega$, the viscous timescale can be written as,

$$\tau = \frac{r^2}{\nu} = \left(\frac{H_g}{r}\right)^{-2} \frac{1}{\alpha\Omega}. \tag{2.50}$$

Assuming a typical timescale of 1 Myr at 50 au for a very thin disk ($H_g/r \sim 0.05$) and star-mass $M_* = 0.5$ $M_\odot$ yields $\alpha = 0.02$. This is fairly of the order of the estimations derived from observations, which usually set up a value of about 10^{-2} (see Hartmann etal 1998).

We can find detailed discussions of this procedure in Frank et al. [2002] or Armitage [2019].

2.3.2 Turbulence

Characterizing turbulence in disks is important as it can account for the transport of angular momentum faster than molecular viscosity. When we want to characterize turbulent systems, the first thing we want to measure is the relative importance of inertial and viscous forces. The dimensionless Reynolds number of the flow allows for such important measurement. Considering a system of size L, a flow of velocity U and a viscosity ν, the Reynolds number is written as,

$$R_e = \frac{UL}{\nu} \tag{2.51}$$

Turbulence arises above typical values of Reynolds number. On the Earth, for instance, atmospheric flows generate turbulence above $R_e \approx 10^4$. Studies show that this is not the case for Keplerian disk flows which suggests that linear hydrodynamic instabilities alone cannot account for turbulence in disks. Based on the Rayleigh's criterion, in a differential rotating disk, the flow is stable if the following condition is respected:

$$\frac{\mathrm{d}l}{\mathrm{d}r} = \frac{\mathrm{d}}{\mathrm{d}r}(r^2\Omega) > 0. \tag{2.52}$$

In a purely Keplerian disk, $l \propto \sqrt{r}$. Thus, the flow in disks is always stable.

Many studies [Balbus et al., 1996, Balbus and Hawley, 1998, Lesur and Longaretti, 2005, Rebusco et al., 2009, Edlund and Ji, 2014] investigated non-linear hydrodynamics instabilies as alternative processes that lead to sufficiently strong turbulences. However, there is no satisfactory evidence that such instabilities exist in protoplanetary disks. It turns out that processes at the origin of turbulence are still poorly known to date.

Some authors have suggested that, instead of purely hydrodynamic origins, instabilies can be effectively generated by the coupling of a weak magnetic field to ionized gas.

2.3.3 Ionization fraction

Protoplanetary disks undergo intense radiations due to the central star or cosmic rays. These radiations have an impact on the degree of ionization of the gas and, consequently, on the evolution of the disk. Characterizing the ionization fraction is fundamental to understand how the coupling of gas to magnetic fields affects the turbulence and generates

instabilities in disks. Another important reason to quantify the ionization fraction is its implication to the chemical processes at play within disks.

The most simple way to quantify the ionization fraction is to pose the ratio of the number density of free electrons n_e to the number density of neutrals n_{tot},

$$x_e = \frac{n_e}{n_{tot}}. \tag{2.53}$$

We note that dust grains can also bear charges and hence play a role on processes implying ionized species. We will first consider the thermodynamic equilibrium process of thermal ionization, then the non-thermal ionization due to photons or energetic particles. We will see that, in most cases, disks are roughly neutral.

Thermal ionization Thermal ionization is generally not effective in disks as the necessary temperature to ionize alkali metals is above $T \sim 10^3$ K. Thermal ionization is hence only important in the innermost regions of the disk (< 1 AU). The ionization fraction of potassium as a function of the temperature is shown in Figure 2.8. We see that the ionization fraction at $T = 10^3$ K is of the order of $x \sim 10^{-12}$, which is very small.

Non-thermal ionization At larger radii, the ionization is non-thermal. It is unnecessary to consider thermodynamic equilibrium as the ionization is fully driven by high-energy particles or photons. The sources of ionization are, by order of their penetrating power, the UV photons, X-rays, cosmic rays, particles produced from radioactive decay within the disk [Stepinski, 1992] and electric discharges [Muranushi et al., 2012].

The contribution to the ionization fraction is mostly due the first three processes while the contribution of the other ones is negligible.

The UV flux is the main source of ionization. However, it is rapidly absorbed by dust grains and cannot efficiently penetrate deeply to the mid-plane. The cosmic rays can usually penetrate very deep inside the disk and reach the mid-plane. However, the density of this radiation is lower than the UV radiation. KeV X-rays (with a temperature k_bT of a few keV) originating from the coronae of T Tauri stars are also an important source photo-ionization and Compton scattering [Preibisch et al., 2005].

We conclude that the expected ionization fraction within is very low. Moreover, the ionization rates must be balanced against the rate of recombination between ions and electrons.

2.3.4 Magneto-rotational instability

In the presence of a weak vertical magnetic field, a Keplerian disk is destabilized. This is what we call the Magnetorotational Instability (MRI), described first by Balbus and Hawley [1991].

A Magnetohydrodynamic (MHD) flow remains stable if the angular velocity Ω is an increasing function of the radius r:

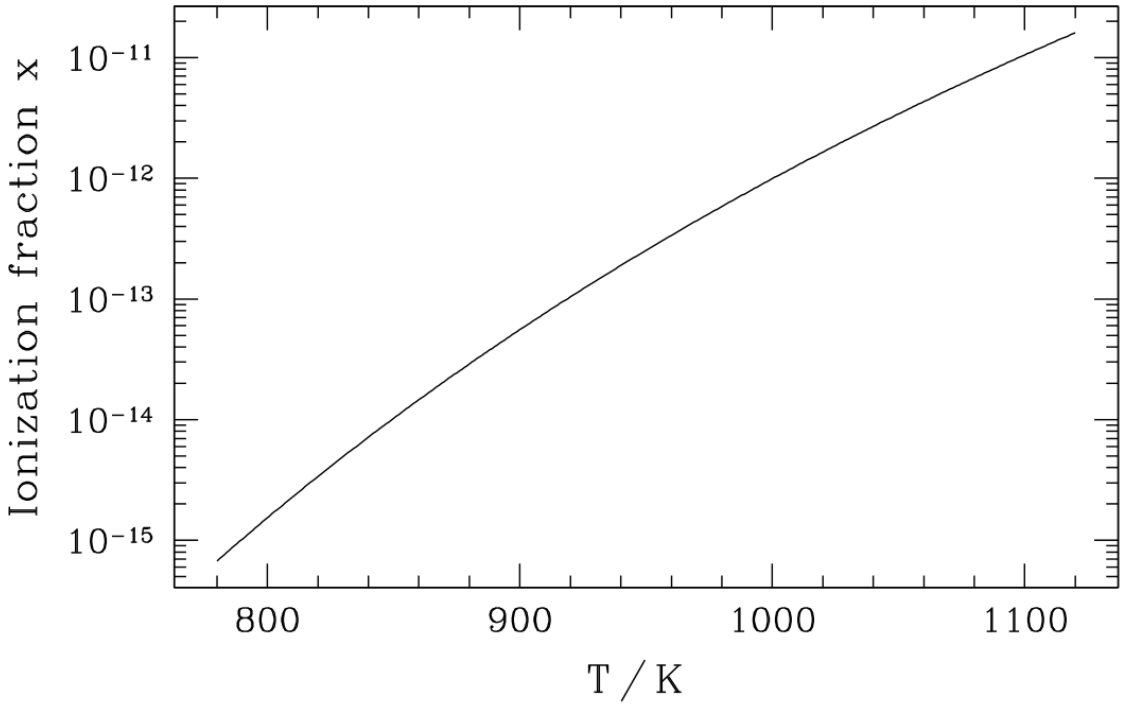

Figure 2.8: [Extracted from Armitage, 2019]

$$\frac{\mathrm{d}\Omega}{\mathrm{d}r} < 0. \tag{2.54}$$

This condition is always fulfilled in Keplerian rotation which places MRI at the center of modern accretion theories.

Let us consider a disk in Keplerian rotation bathed in a vertical weak magnetic field. If the field is slightly perturbed radially, the field lines act like springs that link fluid elements at different radii. Because of the Keplerian rotation, the orbital velocity of the inner (closer to the star) element is larger than the one of the outer element, creating a toroidal field line that generates a tension in the magnetic field linking the two fluid elements. This tension decreases the angular momentum of the inner element and increases the angular momentum of the outer one, resulting in an instability where the inner element drifts inward (and the outer element outward).

In order for the gas to be coupled to the magnetic field, it needs to be ionized to a certain degree. The critical ionization fraction needed to generate turbulence by the MRI is $n_e/n_{tot} \sim 10^{-12}$ [see Sano and Stone, 2002]. This critical value appear to be very small but it is sufficient to couple magnetic fields to the gas. However, There exist regions within where this critical value is not even obtained.

Dead zone It is assumed that protoplanetary disks have what we call a *dead zone* near the mid-plane.

As we have mentioned, the MRI can drive turbulence if the ionization fraction reaches

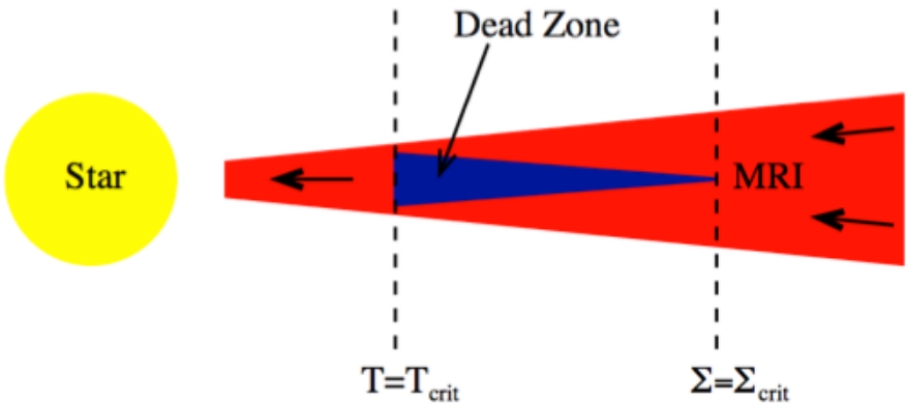

Figure 2.9: Illustration of the dead zone in a edge-on disks. Credits: Rebecca, G. Martin

a critical threshold. The gas is not effectively coupled to the magnetic field if the fraction is below this value.

In the innermost part of the disk, the temperature can reach a critical temperature T_{crit} that is large enough to allow for the gas to be thermally ionized and the MRI to occur. In the outermost regions of the disk, on the other hand, the column densities become low enough so that the flux can reach the mid-plane. Between these two critical radii, there exist a region near the mid-plane where the temperature and column density are such that the ionization fraction drops below the critical value $n_e/n_{tot} \sim 10^{-12}$ and no turbulence arises via MRI. This intermediate region is called a dead zone.

The dead zone has important consequences on the accretion flows. Indeed, material moving inward from larger radii will accumulate in the dead zone and create local inversion in the pressure radial profile. These inversions will lead to the accumulation of dust grains and locally enhance the dust-to-gas mass ratio

2.4 Disk dispersion

The timescale of the gas dispersal of a disk sets the timescale limit to form giant gas planets.

If the disk is purely driven by accretion then the evolution only involves the self-similar solution as described in Section. 2.2.2.2 for a viscous disk with a viscosity distribution $\nu \propto r^{\gamma}$. In that case, we observe that the decrease of the surface density by a viscous time t_s reaches the value:

$$\frac{\partial \Sigma(r,t)/\partial t}{\Sigma(r,t)} = \frac{1}{t+t_s}. \tag{2.55}$$

The disk dispersal is homogeneous and follows a slow evolution from a class II to a class III T Tauri star. However, most observations have indicated that this gradual evolution is very unlikely to be the only dissipation process at play in disks and suggest

that the dispersion is fast (about a few 10^5 yr). See, for instance, Simon and Prato [1995] or Wolk and Walter [1996]. We assume that processes other than viscous accretion must be at the origin of dispersion. The best-developed models accounting of fast dispersal are based on photoevaporation processes.

2.4.1 Photoevaporation

Photoevaporation is the process of mass loss via thermal winds. X rays and UV radiations emanating from the central star carry enough energy to counterbalance gravity and disperse disk gas. In particular, Extreme Ultraviolet (EUV) radiations ($E > 13.6$ eV) ionize the hydrogen atoms and dissociate the H_2 molecules in a surface layer of the disk, raising the temperature up to $T \simeq 10^4$ K. The sound speed of the photoionized gas is $c_s \simeq 10$ km.s^{-1}. If this sound speed exceeds the local orbital velocity, the gas can be dispersed away, otherwise the gas remains bound. Therefore, there is a critical radius r_g outside which the photoevaporation is effective, given by,

$$r_g = \frac{GM_*}{c_s^2}. \tag{2.56}$$

For a Solar mass star, r_g is at 9 AU. This threshold radius is directly related to the problem of Compton winds in Active Galactic Nuclei (AGN) studied by Begelman et al. [1983].

The mass loss due to photoevaporation is proportional to the stellar ionizing flux. For a flux ϕ, the integrated mass loss rate due to photoevaporation over the entire disk can be estimated as [Hollenbach et al., 1994],

$$\dot{M}_{wind} \approx 1.6.10^{-10} \left(\frac{\phi}{10^{41} s^{-1}}\right)^{1/2} \left(\frac{M_*}{M_\odot}\right)^{1/2} M_\odot \mathrm{yr}^{-1}. \tag{2.57}$$

The mass loss due to photoevaporation is negligible during the first few millions of years when the accretion rate is large. However, when the accretion rate decreases, the contribution of photoevaporation to gas dispersal becomes predominant. As most of the wind mass loss occurs close to r_g, with a radial profile of the mass loss given by $\dot{\Sigma}_g \propto r^{-5/2}$, photoevaporation creates an annulus of low density at $r \sim r_g$, preventing material flow from outside r_g to reach the inner regions, which over time leads to an empty inner annulus in the disk. Typical values of mass loss rate for CTTSs are $\dot{M}_{wind} \sim 10^{-9}$ to 10^{-8} $M_\odot \mathrm{yr}^{-1}$.

The combination of photoevaporation and viscous accretion are sufficient to account for rapid mass dispersal as constrained by observations [Alexander et al., 2014].

2.5 Solid particles in disks

Solid particles (known as dust, dust grains or grains) in typical protoplanetary disks account for only about 1 % of the total gas mass. Yet, dust grains are responsible for most of the stellar light extinction, they play a fundamental role in catalyzing chemical

reactions and they are at the origin of planetary formation processes. Grains are originally present in the interstellar medium in the form of sub-micro-metric solid particles well-mixed with the gas.

We discuss here the interaction of an orbiting solid particle with the gas and the implication on the motion and evolution of the particle within a typical early stage protoplanetary disks.

2.5.1 Gas-grain interaction

The evolution of a solid particle in a disk is different from that of the gas because the former is not affected by pressure gradients. For this reason, solid particles, to a good approximation, orbit at a Keplerian velocity. However, solid particles do interact with the gas through aerodynamic forces. The evolution is governed by the particle's stopping time τ_s, which is the characteristic time for a hypothetical solid particle initially at a relative velocity with the gas to reach the local gas velocity. The stopping time is a fundamental parameter to describe the aerodynamic coupling with the gas. Let us consider a particle of mass m that is moving with velocity Δv relative to the local gas. The stopping time of the particle is written as,

$$T_s = \frac{m\Delta v}{|F_{drag}|}, \tag{2.58}$$

where F_{drag} is the drag force due to the interaction between the particle and the gas with relative velocity Δv. It is often preferable to use a dimensionless stopping time $T_s(r, z)$ defined as the product of the stopping time τ_s with the Keplerian angular momentum $\Omega_K(r)$, which is a way to compare the stopping time to the dynamical time of the disk at radius r:

$$\tau_s = T_s\Omega_K = \frac{T_s}{T_K} \tag{2.59}$$

where $T_K = 1/\Omega_K$ is the characteristic Keplerian time. The dimensionless stopping time is usually called the *Stokes number*.

We now want to specify the order of magnitude of the drag force F_{drag}, whose value depends on the size of the particle relative to the mean free path of a gas molecule. Let us investigate two regimes of drag.

Epstein regime The gas-grain interaction is in the Epstein regime when the size of the particle a is smaller than the mean free path λ of a molecule in the gas ($a < 9\lambda/4$). If we consider the gas as an ensemble of collisionless particles with a mean speed obtained from properties of the Maxwell-Boltzmann distribution corresponding to their thermal motions:

$$v_{th} = \sqrt{\frac{8k_BT}{\pi\mu m_H}}, \tag{2.60}$$

the particle with relative speed $\Delta v << v_{th}$ with the gas will experience *Epstein drag* with a drag force,

$$\boldsymbol{F}_{drag} = -\frac{4\pi}{3}\rho_g a^2 v_{th}\Delta\boldsymbol{v} \tag{2.61}$$

where ρ_g is the mass density of the surrounding gas. Thus, this drag force will contribute to slow down the particle's velocity in relation to the gas. For a spherical particle of material density ρ_m and noticing that v_{th} is roughly equal to the sound speed c_s, substituting Eq. 2.61 into Eq. 2.58 yields,

$$T_s = \frac{\rho_m}{\rho_g}\frac{a}{v_{th}}. \tag{2.62}$$

The Epstein regime is relevant for small microscopic particles up to small macroscopic ones.

Stokes regime Conversely, in the Stokes regime, the size of the solid particle is larger than the mean free path of the molecules. Thus, the microscopic properties of the gas are not considered anymore. Instead, the gas is considered as an uniform fluid. The drag force is directly proportional to the local gas pressure and is written:

$$\boldsymbol{F}_{drag} = -\frac{C_{drag}}{2}\pi a^2 \rho_g v_g \Delta\boldsymbol{v} \tag{2.63}$$

where C_{drag} is a dimensionless factor accounting for the aerodynamics properties of the grain. See Whipple [1972] for a more detailed description of the Stokes regime.

2.5.2 Vertical settling

We now introduce the consequences of drag force on the vertical profile of dust grains in protoplanetary disks. Initially, dust grains have inherited the uniform distribution within the gas from the ISM. Let us consider a dust grain described by cylindrical coordinate (r, z). The gravitational force exerted by the star can be decomposed into a radial and a vertical component. As we have seen, a solid particle is in a Keplerian orbit so the radial component is directly balanced by the centrifugal force. The vertical component of the stellar gravitational force is,

$$F_{g,z} = -m\Omega_K^2 z. \tag{2.64}$$

where m is the mass of the grain and z its vertical coordinates. As the particle does not undergo the vertical pressure gradient, it is accelerated toward the mid-plane proportionaly to $F_{g,z}$ until its settling velocity reaches the terminal value v_{set} where the vertical gravitational force is balanced by drag forces. In the Epstein regime, the terminal velocity is,

$$v_{vet} = \frac{\rho_m}{\rho_g}\frac{a}{v_{th}}\Omega_K^2 z. \tag{2.65}$$

In a typical disk, for a 1 μm grain at 1 H_g, at 1 au from the star of mass ~ 0.5 $M_\odot$ and with $\rho_g = 6{\times}10^{-10}$ g cm^{-3} we find $v_{vet} \approx 0.06$ cm s^{-1}. The gas-grain coupling can be very fast for microscopic grains (≈ 1 s). The settling time,

$$t_{vet} = \frac{z}{|v_{vet}|} \sim \frac{\rho_g c_s}{\rho_m \Omega_K^2 a} \tag{2.66}$$

is about 1.5×10^5 yr, which is shorter than a typical disk lifetime.

If turbulence is negligible, the settling toward the mid-plane would be unlimited and would result in a ultra-dense layer of solids. In actual disks, turbulence is not negligible and counteracts the effect of settling by diffusing dust grains on both sides of the plane so that collisions between grains do not always lead to sticking but can also lead to destructive processes. If the amount of dust relative to the gas is sufficiently small, then the dust distribution undergoes diffusive evolution and we can write an advection-diffusion equation [Dubrulle et al., 1995, Fromang and Papaloizou, 2006],

$$\frac{\partial \rho_d}{\partial t} = D \frac{\partial}{\partial z}\left[\rho_g \frac{\partial}{\partial z}\left(\frac{\rho_d}{\rho_d}\right)\right] + \frac{\partial}{\partial z}(\Omega_K^2 T - s\rho_d z) \tag{2.67}$$

where ρ_d and ρ_g are the mass density of the dust and gas, respectively and D is a constant diffusion coefficient. Assuming that the stopping time τ_s is independent of z close to the mid-plane, we can find steady-state solutions to Eq. 2.67 in the following form:

$$\frac{\rho_d}{\rho_g} = \left(\frac{\rho_{d,0}}{\rho_{g,0}}\right) \exp\left[-\frac{z^2}{2H_d^2}\right] \tag{2.68}$$

where the dust scale height H_d is written as,

$$H_d = \sqrt{\frac{D}{\Omega_K^2 T_s}}. \tag{2.69}$$

If the constant diffusion coefficient D is approximately equal to the turbulent viscosity ν, the ratio of the dust scale height to the gas scale height becomes [See Boehler et al., 2013],

$$\frac{H_d}{H_g} \approx \sqrt{\frac{\alpha}{\tau_s}}. \tag{2.70}$$

where α is the viscosity coefficient as defined in Equation 2.49. We call this ratio the settling factor. It tells us that particles whose α value is sufficiently larger than their dimensionless stopping time are strongly settled toward the mid-plane. We note, however, that a reasonable value of α requires a rather large grain size which implies that sub-micron grains inherited from the ISM remain well coupled to the gas and that effective settling requires significant grain growth. Following Cuzzi et al. [1993], Youdin and Lithwick [2007] and Dong et al. [2015] we define another settling factor written as:

$$\frac{H_d}{H_g} = \frac{1}{\sqrt{1 + \tau_s \frac{S_c}{\alpha}}} \tag{2.71}$$

where S_c is the Schmidt number that we will define later. This settling factor definition is the one we used to compute our disk models as defined in Section. 4. Figure 2.10 shows the settling factor as defined in Dong et al. (2015) as a function of the dimensionless stopping time at 100 au of a typical TTauri disk model compared to the asymptotic behavior used by Boehler et al. [2013] and the values from the numerical simulations of Fromang and Nelson [2009]. It also allows to simply discriminate grains that are well-mixed to the gas (those that have a small stopping time) from those that significantly settle toward the mid-plane:

$$\begin{aligned} \tau_s \ll 10^{-3} &\implies \text{grains well coupled to the gas} \\ \tau_s \gg 10^{-3} &\implies \text{grains well decoupled to the gas} \end{aligned} \tag{2.72}$$

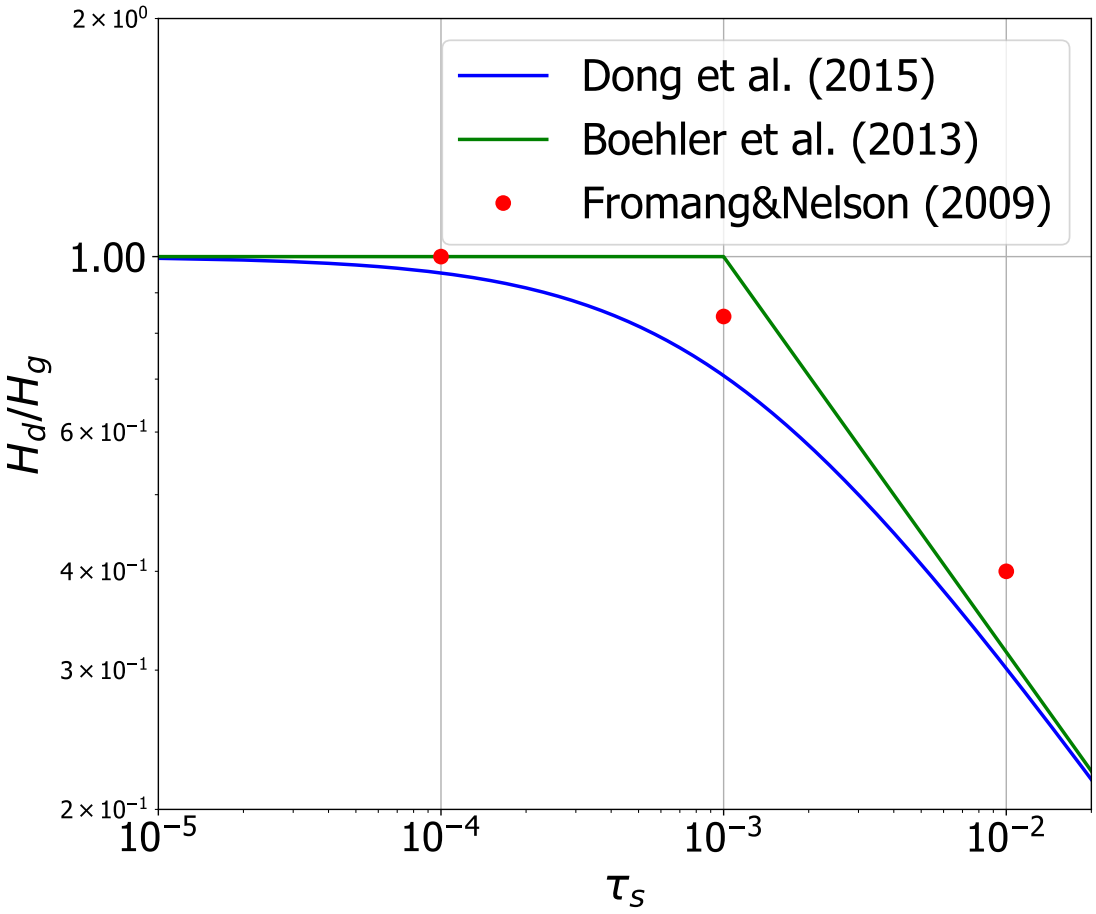

Figure 2.10: Settling factor as a function of the dimensionless stopping time at 100 au. In green the model given by Boehler et al. [2013], the red dots show the simulation values of Fromang and Nelson [2009] and the blue curve is the model we use Dong et al. [2015].

2.5.3 Radial drift

If we neglect gas friction, a dust particle would orbit at a Keplerian speed v_K so that the gravitational force exerted by the star on the particle is exactly equal to the centrifugal force due to the rotation. Now, if we consider a fluid element of the gas, the same forces at at work so that for a volume of gas at the same location as the grain particle the resulting velocity should be the same. However, as said above, both the gas and temperature have a smooth radial profile so the pressure decreases radially outward ($dP/dr < 0$). Thus, a fluid element of gas is also supported by an additional radial force due to pressure gradient in the opposite direction of the gravitational force. The effective gravitational force perceived by a gas element is slightly smaller than the actual gravitational force so that the centrifugal force needed to counterbalance gravity is smaller. Therefore, the gas orbits the star in a slightly sub-Keplerian speed,

$$v_{g,\phi} = (1 - \eta)v_K. \tag{2.73}$$

At a same radial distance, because of the difference in speed between the gas and solid, the latter *see* a headwind of speed ηv_K, which results in a drag force F_{drag} exerted on the solid. A solid particle will therefore loses energy depending on its stopping time and drift toward the inner region of the disk (see Fig. 2.11). Let us use the azimuthal and radial equations of motion to deduce the speed of the particle and let be v_r and v_ϕ the radial speed and the azimuthal speed of the particle, respectively. We write:

$$\frac{dv_r}{dt} = \frac{v_\phi^2}{r} - \Omega_K^2 r - \frac{1}{T_s}(v_r - v_{g,r}) \tag{2.74}$$

$$\iff \frac{d}{dt}(rv_\phi) = -\frac{r}{T_s}(v_\phi - v_{g,\phi}). \tag{2.75}$$

Let us assume that the particle's motion is almost Keplerian so that the azimuthal Eq. 2.75 can be simplified as follows:

$$\frac{d}{dt}(rv_\phi) \sim v_r \frac{d}{dr}(rv_K) = \frac{1}{2} v_r v_K. \tag{2.76}$$

This yields,

$$(v_\phi - v_{g,\phi}) \simeq -\frac{1}{2}\frac{T_s v_r v_K}{r}. \tag{2.77}$$

Thus, we can simplify Equation 2.74 by substituting for Ω_K using Eq. 2.73. Discarding the second order and higher, we obtain,

$$\frac{\mathrm{d}v_r}{\mathrm{d}t} = -\eta\frac{v_K^2}{r} + \frac{2v_K}{r}(v_\phi - v_{g,\phi}) - \frac{1}{T_s}(v_r - v_{g,r}). \tag{2.78}$$

Neglecting the particle's radial variation $\mathrm{d}v_r/\mathrm{d}t$, we substitute the term $(v_\phi - v_{g,\phi})$ from Eq. 2.77 into Eq. 2.78 and obtain,

$$v_r = \frac{(r/v_K)T_s^{-1}v_{g,r} - \eta v_K}{(v_K/r)T_s + (r/v_K)T_s^{-1}}. \tag{2.79}$$

Finally, expressing Eq. 2.79 in terms of the Stokes number τ_s yields,

$$v_r = \frac{\tau_s^{-1}v_{g,r} - \eta v_K}{\tau_s + \tau_s^{-1}}. \tag{2.80}$$

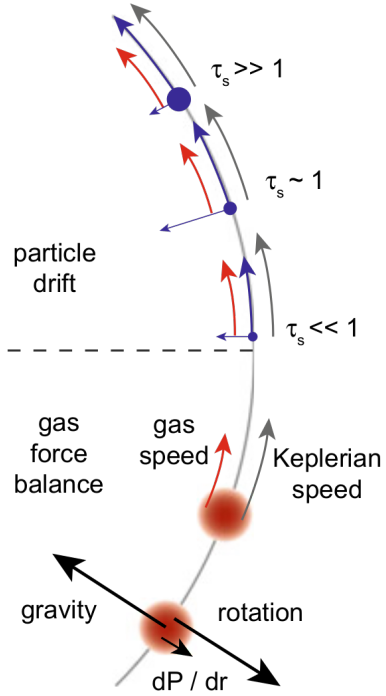

Figure 2.11: Illustration of the various possible radial motions of a solid particle in a disk as a function of the stopping times. The radial drift is maximum when $\tau_s \sim 1$ and minimum when $\tau_s >> 1$ or $\tau_s << 1$ [From Armitage, 2019].

The speed of the drift depends on the stopping time of the particle and therefore on its size. Figure 2.11 illustrates the radial motion as a function of the stopping time. Taking the appropriate limits we can deduce the speed of very small and very large particles. The radial drift is maximum for $\tau_s = 1$, which corresponds to a size of about a meter. For a one-meter size particle initially at 1 au from the star, the accretion timescale is only of about 100 years [Weidenschilling, 1977].

Turbulence plays an important role on the transport of solid particles. Indeed, turbulence will tend to diffuse dust grains both radially and vertically and equalize the concentration of the dust in the disk. We want to derive an equation for the evolution of dust concentration. To do so, we write the concentration of the dust relative to the gas as,

$$f = \frac{\Sigma_d}{\Sigma_g} \ll 1. \tag{2.81}$$

where Σ_d and Σ_g are the surface density of the dust and gas, respectively. The concentration f is generally of the order of 0.01 in disks. Assuming the total mass of the dust is conserved, we can write,

$$\frac{\partial \Sigma_d}{\partial t} + \nabla \cdot \boldsymbol{F}_d = 0. \tag{2.82}$$

where $\boldsymbol{F}_d$ is the flux of the dust. If we consider only small grains, the dynamics is dominated by advective and diffusive forces. In this case, it results from the continuity equation (Eq. 2.82) the following flux:

$$\boldsymbol{F}_d = \Sigma_d \boldsymbol{v} - D\Sigma_g \boldsymbol{\nabla}\left(\frac{\Sigma_d}{\Sigma_g}\right) \tag{2.83}$$

where $\boldsymbol{v}$ is the average speed of the gas and D is the turbulent diffusion coefficient. Moreover, if we also consider the conservation of the gas, we can write in polar cylindrical coordinates the following equation:

$$\frac{\partial f}{\partial t} = \frac{1}{r\Sigma_g}\frac{\partial}{\partial r}\left(Dr\Sigma_g \frac{\partial f}{\partial r}\right) - v_r \frac{\partial f}{\partial r}. \tag{2.84}$$

where the first term of the right-hand side of the equation is the diffusive component and the second term is the advective component due to the radial flow of the gas.
The relative importance between the processes can be defined by Schmidt number S_c as the ratio of the turbulent viscosity coefficient ν to the turbulent diffusion coefficient D:

$$S_c = \frac{\nu}{D} \tag{2.85}$$

To generalize Eq. 2.84 to larger grains that are not well-coupled to the gas, it is necessary to add an additional flux that accounts for the radial drift speed.

The inward velocity of the gas can be expressed in relation with the viscosity:

$$v_r = -\frac{3\nu}{2r}. \tag{2.86}$$

Chapter 3

Interstellar chemistry and gas-grain models

Contents

3.1 Introduction

In this chapter, we first introduce basic theoretical elements necessary to understand the physics and chemistry computed by the gas-grain code NAUTILUS that we used during this thesis and to understand the results presented in Chapter. 6. Secondly, we present NAUTILUS and its multi-grain version in Section. 3.4. Then, we explain how we used the code for disk modelling.

3.2 Gas-phase chemistry

Calculating the rate of a reaction is fundamental to characterize chemical evolution of astrophysical environments. In the gas-phase, the rates are temperature-dependent and this dependence is directly related to the molecular species at play in the reaction. In 1889, Svante Arrhenius experimentally related the rate constant k_{ij} of a reaction between a species i and a species j to the gas temperature T_g via the *Arrhenius equation*:

$$k_{ij} = \alpha_{ij} \exp\left(\frac{-E_{A,ij}}{k_b T_g}\right) \tag{3.1}$$

where k_b is the Boltzmann's constant, α_{ij} is the pre-exponential factor and $E_{A,ij}$ is the activation energy of the reaction. The activation energy is defined as the minimum energy that has to be provided to the system for the reaction to occur. Only interactions with a kinetic energy greater than the potential barrier are effective and allow to overcome the activation barrier. It is however rather common to use a modified version of the *Arrhenius equation* to cover a larger domain of temperature, in particular for very low temperatures. This modified equation is of the form:

$$k_{ij} = \alpha_{ij} \left(\frac{T_g}{T_0}\right)^{\beta} \exp\left(\frac{-E_{A,ij}}{k_b T_g}\right) \tag{3.2}$$

T_0 is a reference temperature and β is a value ranging between -1 and 1. When $\beta = 0$, the modified version becomes the classical *Arrhenius equation*.

A chemical reaction can be of two different types depending on the energy transfer during the process. If the system absorbs energy from its environment, the enthalpy variation is positive ($\Delta H > 0$), the reaction is said *endothermic*. On the other hand, if the system releases energy to the environment, the enthalpy variation is negative ($\Delta H < 0$). We note here that endothermic reactions are less likely to occur in the context of protoplanetary disks due to the low energy that the disk environment can provide (especially in the cold mid-plane). However, this kind of reactions can more easily occur with the presence of a third body i.e. called a catalyst. In the ISM and disk media, dust grains can act as catalyst and, as we will see, surface reactions will enhance the chemical richness.

3.2.1 Ionization and dissociation

For gas-phase reactions of dissociation and ionization, several mechanisms are at play. Either the gas-phase molecules directly interact with cosmic-rays, X-rays and UV photons, or the molecules interact with the UV photon induced by cosmic-rays. In NAUTILUS, the ionization or dissociation rates induced by cosmic-rays are computed with:

$$k_{diss}(i) = \alpha_i \zeta_{H_2} \frac{1}{(1-\omega)} \frac{n(H_2)}{n(H) + 2n(H_2)} \tag{3.3}$$

where ζ_{H_2} is the ionization rate induced by direct cosmic-rays and ω is the albedo of a grain.

The ionization or dissociation rates by UV photon from ISRF or induced by cosmic-rays are defined as:

$$k_{diss}(i) = \alpha_i \chi \exp(-\beta_i A_v) \tag{3.4}$$

where χ is the scaling factor characterizing the impinging intensity of the UV radiation, A_v is the visual extinction and the term $\exp(-\beta_i A_v)$ characterizes the attenuation by dust grains of the radiation field.

In Chapter. 5, we will show another method to define the photodissociation and photoionization rate as a function of the UV flux wavelength and why using this method matters for chemistry.

3.3 Surface Processes

3.3.1 Adsorption

To characterize the probability that an adsorbed species remains at the grain surface after a collision, we define a sticking coefficient $S(X)$. The sticking coefficient is determined by how well the collision event can dissipate the kinetic energy. It is a function of the surface temperature, surface coverage, structural details of the surface, of the kinetic energy and mass ratio between the species and the substrate. In low temperature regimes (of gas and surfaces), the sticking coefficient is usually close to 1 and its value decreases with higher gas and surface temperatures.

The accretion rate of a species X can therefore be defined as the collision rate times the sticking coefficient [Cuppen et al., 2017]:

$$f_{acc}(X) = S(X) v_X n_d(a_i) a_i^2 n_g(X) \tag{3.5}$$

where $n_d(a_i)$ is the grain number density of size a_i, $n_g(X)$ is the gas-phase number density of species X and v_X is the average gas-phase thermal velocity,

$$v_X = \sqrt{\frac{8 k_B T_g}{\pi m_X}} \tag{3.6}$$

with k_B the Boltzmann constant, m_X the mass of the species X.

The collision can lead to two different types of bonding depending on the potential interaction E_{pot} between the gas-phase species and the surface. The species can either be physically or chemically adsorbed.

Physical adsorption (physisorption) When a species is adsorbed to the surface without involving any chemical bonding and perturbation of the electronic structure, the species is said to be physically adsorbed (physisorbed). In this case, the interaction is governed by weak intermolecular forces only and is effective at a long-range distance. The most frequently used potential interaction describing physisorption is the Lennard-Jones expression, which is a combination of an attractive and a repulsive force:

$$E_{pot}(r) = D_s\left[-\left(\frac{\sigma}{r}\right)^{6} + \left(\frac{\sigma}{r}\right)^{-12}\right] \tag{3.7}$$

where r is the distance to the surface, D_s is the strength of the potential and σ is its range. The first term of the right-hand side of Eq. 3.7 is due to *Van Der Waals* forces and *London* dispersives forces. The electronic dipoles induced by the interaction leads to an attractive potential proportional to r^{-6}. The second term of the right-hand side of the equation, which was characterized empirically, represents repulsive forces. These forces originate from Pauli-repulsion when the distance r is sufficiently small that the overlap of charge distribution of the species and the surface is not negligible and balance the attractive forces. These forces increases by an r^{-12}. The typical binding energy of physisorption is of 10-400 meV.

Chemical adsorption (chemisorption) Chemisorption involves valence forces between the surface and the species and new chemical bonds are created during the interaction. The interaction describing chemisorption is the Morse potential:

$$E_{pot}(r) = D_s\left[1 - e^{-\alpha(r-r_e)}\right] \tag{3.8}$$

where α is the range of the potential and r_e is the equilibrium distance. The typical binding energy of chemisorption is of 1-10 eV. We note that chemisorption can only occur when the grain surface contains chemically active sites, the involved species is not saturated (i.e. H_2, O_2) and is able to overcome any activation barrier.

3.3.2 Desorption

Once accommodated on the surface, the species can either stay indefinitely or acquire sufficient energy to overcome the activation barrier necessary for desorption. Desorption designates the release of an adsorbed species back to the gas-phase. The energy acquired can originate from various processes resulting in two types of desorption: thermal and non-thermal. The main difference between these two types is the thermodynamic state. In the first case, the system remains thermally and chemically at equilibrium while in the second case the system undergoes discontinued flux of energy or matter from the

surrounding. Unlike the adsorption processes, the desorption is always activated with a minimum activation energy equal to the energy of adsorption.

3.3.2.1 Thermal desorption

The thermal desorption rate depends on the binding energy of the species to the surface $E_{bind}(X)$. It also depends on the vibrational frequency $v(X)$ as an adsorbed species which acquired the activation energy will desorb within the period of one vibration perpendicular to the surface [Tielens and Allamandola, 1987]. Hence, the desorption rate is,

$$k_{des,th}(X) = v(X) \exp\left(- \frac{E_{bind}(X)}{k_B T_d} \right) \tag{3.9}$$

where T_d is the surface temperature. The characteristic vibrational frequency of the adsorbed species on the surface is defined as,

$$v(X) = \sqrt{\frac{2E_{bind}(X)}{\pi^2 d^2 m_X}} \tag{3.10}$$

d is the characteristic width of the potential well taken as $d = 1$ Å.

3.3.2.2 Non-thermal desorption

When the adsorbed species is released in the gas-phase when the system is not at the thermodynamic equilibrium, the desorption is non-thermal. There are different types of non-thermal desorptions.

Desorption via cosmic-rays (sputtering) The adsorbed species can be ejected from the surface due to bombardement of the grains by energetic particles (ions, electrons, protons) [Leger et al., 1985]. Indeed, a cosmic-ray induces a temporary heating of the surface which causes the desorption of the adsorbed species to the gas-phase. The desorption rate due to the interaction with a cosmic-ray is determined by the amount of time the grain spends at the temperature due to the collision times the thermal desorption rate at this temperature [Hasegawa and Herbst, 1993]. Leger et al. [1985] shows that a cosmic-ray can heat the grain above 70 K. Therefore, following [Hasegawa and Herbst, 1993], the desorption rate due to cosmic-rays is defined as,

$$k_{des,cr}(X) = f(T_d = 70\text{K}) k_{des,th}(X, T_d = 70\text{K}). \tag{3.11}$$

Photodesorption rate Similarly to desorption via cosmic-rays, the absorption of a UV photon by a molecule bound to the surface can lead to its desorption or to the desorption of a nearby surface molecule [see Bertin et al., 2013, Fillion et al., 2014].

Active/chemical desorption Chemical desorption, also referred to as reactive desorption, is a desorption process due to the energy excess of an exothermic reaction that is

not sufficiently dissipated on the surface. The energy released by the reaction causes the ejection of the newly formed product in the gas-phase. As for thermal desorption, the chemical energy released must overcome the binding energy to desorb the product. Let us see in what way theory and experimental chemistry predict processes of chemical desorption, in particular in the context of astrophysics.

Thermal desorption and photodesorption cannot account alone for the observed abundances of gas-phase species, in particular in dark molecular clouds. This is why Garrod et al. [2006] suggested that chemical desorption could explain the observed abundance of certain molecules such as methanol in dark clouds. They proposed a model based on the Rice-Ramsperger-Kessel (RRK) theory which relates the released excess energy and the binding energy to a desorption probability.

Following this study, Garrod et al. [2007] proposed a prescription to treat this mechanism in a multi-layer regime, which is now used by most astrochemical models. Following this prescription, the fraction f of reactions leading to chemical desorption is driven by the competition between the desorption rate of the species and the dissipation of energy rate by the grain. It is written as follows:

$$CD = \frac{v(X)\Xi}{v_d + v(X)\Xi} = \frac{a\Xi}{1 + a\Xi} \tag{3.12}$$

where the efficiency parameter $a = v(X)/v_d$ is the ratio of the characteristic vibrational frequency of the newly formed species X to the rate at which the energy is dissipated by the grain surface. It is used to determine the efficiency of the process and has usually a value between 0.01 and 0.1. Ξ is the desorption probability as defined in the RRK theory and is given by,

$$\Xi = \left[1 - \frac{E_{bind}}{E_{exo}}\right]^{s-1} \tag{3.13}$$

with E_{exo} the exothermicity of the reaction and s the number of vibrational modes in the species/surface-bond system. The number s equals 2 for diatomic species. For all others $s = 3N - 5$, where N is the number of atoms in the molecule.

We note, however, that multiple experimental results [Minissale and Dulieu, 2014, Minissale et al., 2016] show that the efficiency of the chemical desorption process is very related to the type of surface and to the mantle's thickness. Minissale et al. [2016] proposed a new formalism to better determine the fraction of species chemically desorbed as a function of the substrates, such as graphite and amorphous silicate. They derived from a set of 10 experiments an analytical formula which estimates the chemical desorption efficiency as a function of the type of substrates. The efficiency of the desorption process depends on several assumptions and parameters. They assumed the equipartition of the energy of the newly formed species to reproduce what they experimentally observed, so that the total energy ΔH_R is distributed to all degrees of freedom $N_{free} = 3 \times N_{atoms}$. We note that only the kinetic energy perpendicular to the surface allows the species to desorb, providing that this energy is more important than the binding energy E_{bind}. As the initial translation motion is negligible, the species just have to bounce perpendicularly to

the surface and desorb. Assuming the collision is elastic, the kinetic energy perpendicular to the surface delivered to the species is a fraction $\varepsilon \Delta H_R/N$ of the total chemical energy, where ε is the fraction of kinetic energy kept by the product.

We can now write the probability that the chemical energy delivered to the product is higher than the binding energy as,

$$CD = \exp\left(- \frac{E_{bind}}{\varepsilon H_R/N_{free}} \right). \tag{3.14}$$

This analytical prescription is in good agreement with the experimental results.

This formalism, although available in the gas-grain code NAUTILUS, was not considered during this thesis and only the prescription of Garrod et al. [2007] was used.

3.3.3 Migration

When an atom is physisorbed on the surface, it is located in a potential minimum that prevents it from freely diffusing along the surface. However, surface diffusion of the species on the surface or into the bulk of the underlying solid can eventually occur via different mechanisms. The two main mechanisms are thermal migration and tunnelling.

3.3.3.1 Thermal migration

Thermal migration or thermal hopping occurs when the atom can thermally overcome the barrier separating its adsorption site from a neighboring site. The atom thus migrates through successive jumps between adjacent sites. The thermal migration rate is given by,

$$k_{\text{migr}}^{(\text{thermal})}(T) = \nu_0 e^{-\frac{E_{\text{diff}}}{k_B T_d}}. \tag{3.15}$$

where ν_0 is the characteristic frequency of the oscillations of the atom inside the well and $E_{\text{diff}} = k_B T_{\text{diff}}$ is the energy required to overcome the barrier to allow the atom to diffuse between physorption neighboring sites. Thermal diffusion is dependent on the temperature. The higher the temperature, the larger the thermal diffusion rates. If the temperature becomes too high, the atom can be thermally desorbed instead. We note that chemisorbed atoms cannot thermally diffuse.

3.3.3.2 Tunnelling

Sometimes, the surface temperature is not high enough to allow the atom to have sufficient energy and overcome the barrier, but the diffusion can still occur via quantum tunnelling. Similarly to Eq. 3.15, the migration rate via tunnelling through a rectangular barrier with height E_{diff} is given by,

$$k_{\text{migr}}^{(\text{tunnel})}(T) = \nu_0 \exp\left(\frac{2a}{\hbar}(2mE_{\text{diff}})^{1/2}\right) \tag{3.16}$$

where $a \simeq 1$ Å is the width of the barrier and m is the mass of the adsorbate. Tunnelling is the dominant process of diffusion when the temperature is low ($T \lessapprox 15$, depending on

the species involved), as it is the case in disks.

The total migration rate can thus be written as,

$$k_{\rm migr}(T) = k_{\rm migr}^{\rm (thermal)}(T) + k_{\rm migr}^{\rm (tunnel)}(T). \tag{3.17}$$

3.3.4 Surface chemistry

The interaction between adsorbed species and the surface is not limited to migration, chemical reactions at interfaces can also occur. Moreover, the presence of an interface acts as a catalyst which can greatly increases chemical reaction rates. This is particularly important in the context of astrophysics where dust grains play a major role in the formation and destruction of interstellar molecular hydrogen (we investigate molecular hydrogen in Section. 3.5). Figure 3.1 illustrates the main surface processes and reactions that species can undergo at the interface.

Langmuir-Hinshelwood mechanism The Langmuir-Hinshelwood (LH) mechanism describes surface reactions between two already adsorbed reactants if at least one of the reactant can diffuse on the surface. The LH mechanism is a thermal process as both reactants are thermalized to the surface temperature. This mechanism can be decomposed into this following three steps:

1. Adsorption of two reactants to the surface,
2. One or both reactants migrate,
3. When the reactants meet on an adsorption site, a chemical reaction is possible.

For an adsorbed species i and another j, the reaction rate is defined as Ruaud et al. [2016],

$$k_{ij} = \kappa_{ij}\left(\frac{1}{t_{hop}(i)} + \frac{1}{t_{hop}(j)}\right)\frac{1}{N_{site}n_d} \tag{3.18}$$

where κ_{ij} is the efficiency coefficient of the reaction on the same adsorption site, N_{site} is the total number of sites on a grain's surface and $n_{\rm d}$ is the dust number density. If the reaction is barrier-less, then the reaction occur with a probability of unity when the two reactants are in the same potential well and $\kappa_{ij} = 1$. If the reaction has a barrier, then κ_{ij} is defined as the result of the competition between the probability that one of the reactant overcomes the activation barrier and the probability that one of them leaves the adsorption site before the reaction to occur. κ_{ij} is then written as [Garrod and Pauly, 2011],

$$\kappa_{ij} = \frac{\nu_{ij}\kappa_{ij}^*}{\nu_{ij}\kappa_{ij}^* + k_{hop}(i) + k_{evap}(i) + k_{hop}(j) + k_{evap}(j)} \tag{3.19}$$

where $\kappa_{ij}^* = \exp(-E_{A,ij}/T_d)$ or $\kappa_{ij}^* = \exp[-2(a/\hbar)(2\mu E_{A,ij})^{1/2}]$ whether we consider the barrier crossing via thermal processes or tunnelling, respectively. ν_{ij} is the largest value

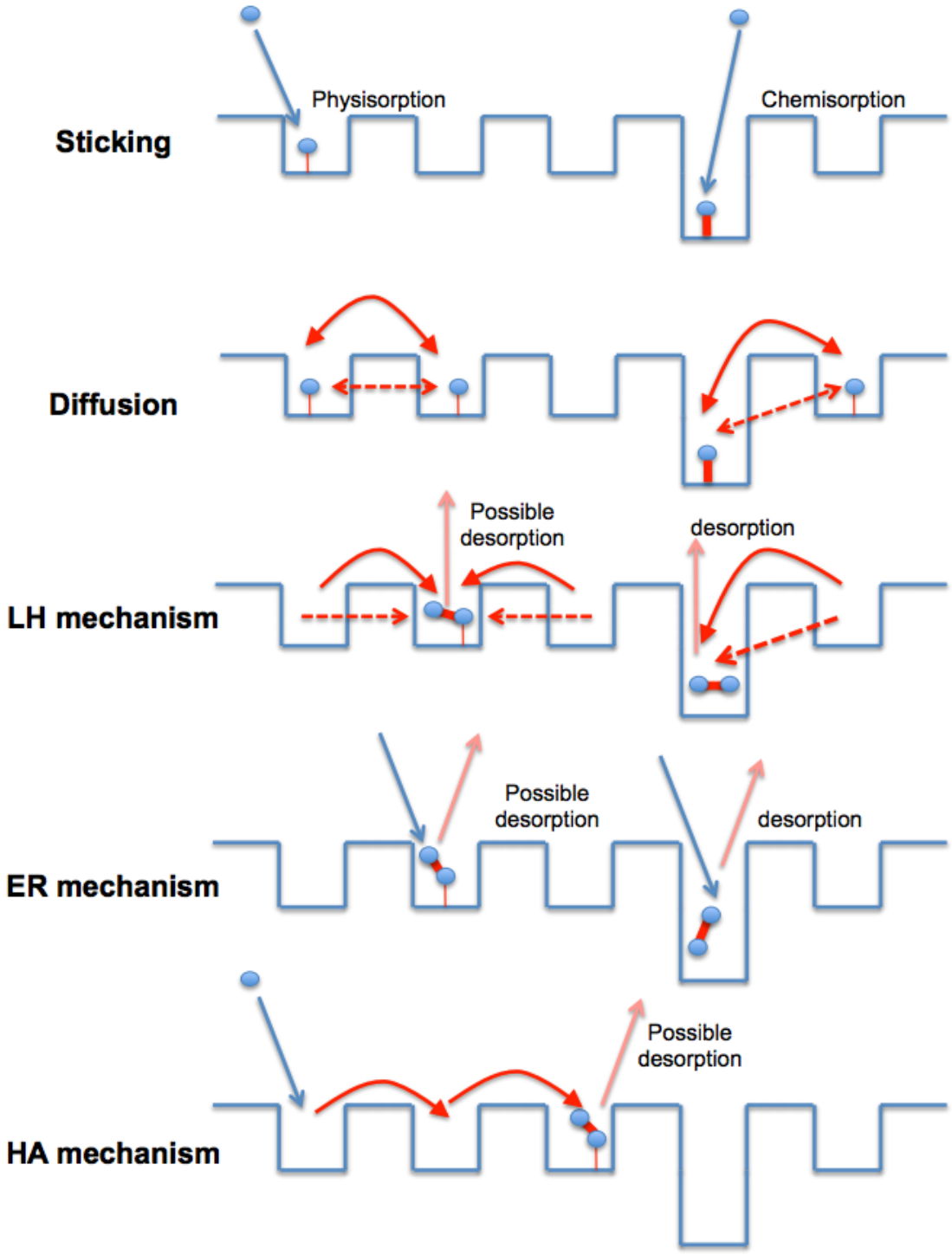

Figure 3.1: Illustration of the main surface processes. From Wakelam et al. [2017].

of the characteristic frequencies of the reactants i and j. In the latter, μ is the reduced mass of the system:

$$\mu = \frac{m(i)m(j)}{m(i) + m(j)}. \tag{3.20}$$

Eley-Rideal (ER) mechanism In this case, only one of the reactants is adsorbed and the other reactant is coming directly from the gas-phase. The mechanism can be decomposed into the following steps:

1. Adsorption of one reactant to the surface,
2. Collision of the other reactant with the adsorbed one,
3. Chemical reaction between the two reactants.

We note that this mechanism can only occur at the surface (not in the mantle) where the adsorbed species can directly interact with the gas-phase species. The reaction rate of this mechanism is written as,

$$k_{ij} = \frac{k_{acc}(i)}{n_{s,tot}}. \tag{3.21}$$

where $n_{\mathrm{s,tot}}$ is the total number of species at the surface.

Hot atom mechanism Sometimes, a species is not directly chemisorbed or physisorbed upon the first impact when the energy is not efficiently dissipated. Therefore, the newly adsorbed species is not in thermal equilibrium with the surface and it is able to diffuse on the surface and react with already nearby adsorbed species (i.e. a few Angstroms away from the impact site). This process is called *Hot Atom (HA) mechanism* or *Harris-Kasemo* [Harris and Kasemo, 1981] mechanism.

3.4 Gas-grain chemistry with the code NAUTILUS

As we have seen, the extreme physical environments usually found in space make laboratory experimentations hard to perform and *in-situ* experiments impossible. A quantitative study of astrochemistry requires the use of models. The following provides a description of time-dependent chemistry modelling where the gas-phase and solid-phase chemistry are coupled. In particular, we describe the gas-grain code NAUTILUS, extensively used to study the chemistry in various environments. NAUTILUS computes the chemical abundances as a function of time by solving a system of coupled differential equations and embeds all physical and chemical processes described in the previous section. The code is based on the development by Hasegawa et al. [1992] and on various successive improvements [Ruaud et al., 2016, Iqbal and Wakelam, 2018].

It is useful to introduce some basics of kinetics chemistry as well as the approach used by NAUTILUS to solve coupled systems. Then, we will present the multi-layer based model and the multi-grain version of the NAUTILUS code that we used for the thesis.

3.4.1 Chemical kinetics

Let us consider a gas-phase chemical reactions between two reactants X_1 and X_2 that leads to the formation of two products X_3 and X_4:

$$X_1 + X_2 \rightarrow X_3 + X_4. \tag{3.22}$$

The rate v of the reaction is,

$$v = -\frac{\mathrm{d}[X_1]}{\mathrm{d}t} = -\frac{\mathrm{d}[X_2]}{\mathrm{d}t} = \frac{\mathrm{d}[X_3]}{\mathrm{d}t} = \frac{\mathrm{d}[X_4]}{\mathrm{d}t} \tag{3.23}$$

where $[X_i]$ is the concentration of the species X_i. If the reactants form the products in a single reaction step, the reaction is said to be elementary. The rate of such reaction only depends on the reactant concentrations and can then be written as,

$$v = k_{12}[X_1][X_2] \tag{3.24}$$

where k_{12} is the rate constant of the reaction. If the rate constant is small (large), the reaction is likely to occur slowly (quickly). In the gas-phase, the value of the rate constant is usually defined by the *Arrhenius equation* (Eq. 3.1). The evolution of the concentration $[X_i]$ as a function of time is characterized by the balance between all processes which form and destroy the species. The evolution is then described by a first-order ordinary differential equation:

$$\frac{\mathrm{d}[X_i]}{\mathrm{d}t} = \text{Formation} - \text{Destruction}. \tag{3.25}$$

For a system consisting of N species X_i $(i = 1, ..., N)$, the problem is described by a non-linear system of N ordinary differential equations coupled to M chemical reactions. The system has the following form:

$$\begin{aligned} \frac{\mathrm{d}[X_1]}{\mathrm{d}t} &= f_1(X_1, ..., X_N) \\ \frac{\mathrm{d}[X_2]}{\mathrm{d}t} &= f_2(X_1, ..., X_N) \\ &... \\ \frac{\mathrm{d}[X_N]}{\mathrm{d}t} &= f_N(X_1, ..., X_N). \end{aligned} \tag{3.26}$$

Solving the system gives the concentration of each species as a function of time. However, the analytical solution of these N coupled differential equations is usually nearly impossible to find due to the non-linearity of the system and numerical methods are necessary.

Various numerical approaches have been developed to solve this kind of system. The most popular tool are numerical models based on the *rate-equation* method [D'Hendecourt et al., 1985, Hasegawa et al., 1992, Caselli et al., 1998], but we also note the existence of

the *master equation* and the macroscopic and microscopic Monte-Carlo methods. In the following, we only describe the *rate-equation* approach as it the one used by NAUTILUS and by most gas-grain astrochemical models. We leave it to the reader to investigate the other approaches; See for instance Biham et al. [2001] and Stantcheva et al. [2002] for a description of the *master equation* approach, Tielens and Hagen [1982], Vasyunin et al. [2009], Cuppen et al. [2009] for the Monte-Carlo methods.

3.4.2 The rate-equation approach

NAUTILUS is based on the rate-equation approach to describe and compute chemical kinetics. In this approach, the stiff ordinary differential equations introduced in subsection 3.4.1 are numerically solved using a multi-step integrator (e.g. Runge-Kutta or Adams integrators). The rate-equations perform well to describe a deterministic and continued evolution of a homogeneous many-body system. However, the approach performs rather poorly when statistical fluctuations arise such as on grain surfaces or when the number of species is small. Properly describing the evolution under such conditions requires more realistic stochastic techniques. The major advantage of the rate equations is their stability and their relative low CPU-consumption, even for very large chemical networks involving thousands of molecules. This explains why the rate equations remain intensively used for chemical kinetics simulations.

3.4.3 Three-phase model

We have seen that dust grains play a key role in the chemical evolution at low temperature and in the increase of molecular complexity. It is well established that grain cores build icy mantles by accreting gas-phase species that react at the surface thereafter. It is therefore crucial to build elaborate models of the formation and the evolution of icy species if we want to properly investigate the chemistry of astrophysical objects, in particular disks. The latest version of the NAUTILUS code is based on the three-phase model developed by Ruaud et al. [2016]. We present in the following the equations of the model as described in Ruaud et al. [2016]. Figure 3.2 provides an illustration of a grain described by a three-phase model with the associated processes. One can distinguish the grain core (grey), chemically inactive, the icy mantle (light blue) as well as the icy surface (dark blue) which can interact with the gas-phase species.

Description of the model The evolution as a function of time of the gas-phase, surface and mantle density of a species i, denoted as $n(i)$, $n_s(i)$ and $n_m(i)$ respectively, is determined by the following first-order differential equations:

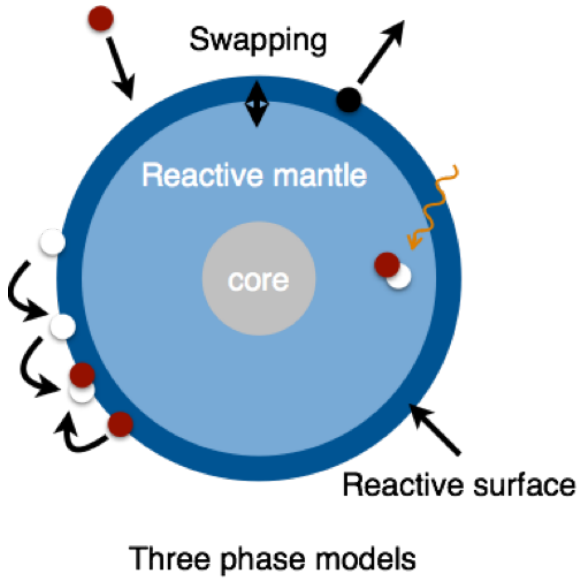

Figure 3.2: Illustration of the three phase model and surface reactions.

$$\left.\frac{\mathrm{d}n(i)}{\mathrm{d}t}\right|_{\mathrm{tot}} = \sum_{l}\sum_{j} k_{lj}n(l)n(j) + k_{diss}(j)n(j) + k_{des}(i)n_s(i) - k_{acc}(i)n(i) - k_{diss}(i)n(i) - n(i)\sum_{l} k_{ij}n(j), \tag{3.27}$$

$$\left.\frac{\mathrm{d}n_s(i)}{\mathrm{d}t}\right|_{\mathrm{tot}} = \sum_{l}\sum_{j} k^s_{lj}n_s(l)n_s(j) + k^s_{\mathrm{diss}}(j)n_s(j) + k_{\mathrm{acc}}(i)n(i) + k^m_{\mathrm{swap}}(i)n_m(i) + \left.\frac{\mathrm{d}n_m(i)}{\mathrm{d}t}\right|_{\mathrm{m\to s}} - n_s(i)\sum_{j} k^s_{ij}n_s(j) - k_{\mathrm{des}}(i)n_s(i) - k^s_{\mathrm{diss}}(i)n_s(i) - k^s_{\mathrm{swap}}(i)n_s(i) - \left.\frac{\mathrm{d}n_s(i)}{\mathrm{d}t}\right|_{\mathrm{s\to m}}, \tag{3.28}$$

$$\left.\frac{\mathrm{d}n_m(i)}{\mathrm{d}t}\right|_{\mathrm{tot}} = \sum_{l}\sum_{j} k^m_{lj}n_m(l)n_m(j) + k^m_{\mathrm{diss}}(j)n_m(j) + k^m_{\mathrm{swap}}(i)n_s(i) + \left.\frac{\mathrm{d}n_s(i)}{\mathrm{d}t}\right|_{\mathrm{s\to m}} - n_m(i)\sum_{j} k^m_{ij}n_m(j) - k^m_{\mathrm{diss}}(i)n_m(i) - k^m_{\mathrm{swap}}(i)n_m(i) - \left.\frac{\mathrm{d}n_m(i)}{\mathrm{d}t}\right|_{\mathrm{m\to s}}. \tag{3.29}$$

The model stipulates that a gas-phase species can be accreted to the surface while a species at the surface can either be desorbed or swapped into the mantle. A mantle

species, on the other hand, can only interact with species at the surface. k_{ij}, k^s_{ij} and k^m_{ij} [cm^{3}s^{-1}] are the reaction rates for the reaction of a species i with a species j in the gas-phase, at the surface and in the mantle, respectively. $k_{\rm acc}$ and $k_{\rm des}$ [s^{-1}] are the accretion and desorption rate at the surface, respectively. $k_{\rm diss}$ represents the dissociation rate by UV photons, cosmic-rays and UV photons induced by cosmic-rays. $k^s_{\rm swap}$ and $k^m_{\rm swap}$ [s^{-1}] are the surface-mantle and mantle-surface swapping rates, respectively. The transfer rates of a surface species i from the surface to the mantle or from the mantle to the surface are characterized by the terms $\mathrm{d}n_s(i)/\mathrm{d}t|_{s\to m}$ and $\mathrm{d}n_m(i)/\mathrm{d}t|_{m\to s}$, defined as follows:

$$\left.\frac{\mathrm{d}n_s(i)}{\mathrm{d}t}\right|_{\rm s\to m} = \alpha_{\rm gain}\frac{n_s(i)}{n_{\rm s,tot}}\frac{\mathrm{d}n_{\rm s,gain}}{\mathrm{d}t}, \tag{3.30}$$

and

$$\left.\frac{\mathrm{d}n_m(i)}{\mathrm{d}t}\right|_{\rm m\to s} = \alpha_{\rm loss}\frac{n_m(i)}{n_{\rm m,tot}}\frac{\mathrm{d}n_{\rm s,loss}}{\mathrm{d}t}. \tag{3.31}$$

$\mathrm{d}n_{\rm s,gain}/\mathrm{d}t$ and $\mathrm{d}n_{\rm s,loss}/\mathrm{d}t$ are the global rates of gain and loss at the surface, respectively, and are written as,

$$\frac{\mathrm{d}n_{\rm s,gain}}{\mathrm{d}t} = \sum_i\left[\sum_l\sum_j k^s_{lj}n_s(l)n_s(j) + k^s_{\rm diss}(j)n_s(j) + k_{\rm acc}(i)n(i)\right], \tag{3.32}$$

$$\frac{\mathrm{d}n_{\rm s,loss}}{\mathrm{d}t} = \sum_i\left[n_s(i)\sum_j k^s_{ij}n_s(j) + k_{\rm des}(i)n_s(i) + k^s_{\rm diss}(i)n_s(i)\right]. \tag{3.33}$$

We see that the sum of $\mathrm{d}n_{\rm s,gain}/\mathrm{d}t$ and $\mathrm{d}n_{\rm s,loss}/\mathrm{d}t$ represents the total rate of change at the grain surface,

$$\frac{\mathrm{d}n_{\rm s}}{\mathrm{d}t} = \frac{\mathrm{d}n_{\rm s,gain}}{\mathrm{d}t} + \frac{\mathrm{d}n_{\rm s,loss}}{\mathrm{d}t}. \tag{3.34}$$

We note that $\mathrm{d}n_{\rm s}/\mathrm{d}t > 0$ when the accretion from gas-phase species is dominant and $\mathrm{d}n_{\rm s}/\mathrm{d}t < 0$ when desorption is dominant.

The number of species i at the surface is given by $N_s(i) = n_s(i)/n_d$ where $n_s(i)$ is the surface number density of species i and n_d [cm^{-3}] is the grain number density. We define $\alpha_{\rm gain}$ and $\alpha_{\rm loss}$ as in Garrod and Pauly [2011],

$$\alpha_{\rm gain} = \frac{\sum_i N_s(i)}{\beta N_{\rm site}} \tag{3.35}$$

and

$$\alpha_{\rm loss} = \begin{cases} \frac{\sum_i N_m(i)}{\sum_i N_s(i)}, & \text{if} \quad \sum_i N_m(i) < \sum_i N_s(i) \\ \\ 1, & \text{otherwise} \end{cases} \tag{3.36}$$

where $N_{\rm site}$ is the total number of sites on the grain surface and where β sets the number

of active surface monolayers. Following Fayolle et al. [2011], we assume that $\beta = 2$ in order to take into account the non-uniformity of the surface.

The two terms $\mathrm{d}n_s(i)/\mathrm{d}t|_{s\to m}$ and $\mathrm{d}n_m(i)/\mathrm{d}t|_{m\to s}$ do not express actual swapping between the surface and the mantle. Indeed, they are related to the total net variation of surface density [Hasegawa and Herbst, 1993, Garrod and Pauly, 2011]. The swapping is actually determined by the terms k^s_{swap} and k^m_{swap}. These terms account for the fact that a species lying at the interface between the two phases can switch position with a species of the other phase.

The surface-mantle swapping is a pair-wise process, which means that the swapping rate of all species do not produce any collective net transfer between the mantle and the surface. The model described herein satisfies this requirement by computing the swapping rates from mantle to surface following Garrod [2013],

$$k^m_{\mathrm{swap}}(i) = \begin{cases} \frac{1}{t^m_{\mathrm{hop}}(i)}[s^{-1}] & \text{if } N_{\mathrm{lay,m}} < 1 \\ \\ \frac{1}{t^m_{\mathrm{hop}}(i) N_{\mathrm{lay,m}}}[s^{-1}] & \text{if } N_{\mathrm{lay,m}} > 1 \end{cases} \tag{3.37}$$

where $N_{\mathrm{lay,m}} = \sum_i N_m(i)/N_{\mathrm{site}}$ is the number of monolayers constituting the mantle and $t^m_{\mathrm{hop}}(i) = \nu^{-1}(i)\exp(E^m_{\mathrm{diff}}(i)/T_d)$ represents the time required for the considered species to migrate from one site to an adjacent one via thermal hopping. The surface to mantle rates are then calculated to match the mantle to surface rates,

$$k^s_{\mathrm{swap}}(i) = \frac{\sum_j k^m_{\mathrm{swap}}(j) n_m(j)}{n_{\mathrm{s,tot}}}[s^{-1}]. \tag{3.38}$$

3.4.4 NAUTILUS Multi Grain Code (NMGC)

As a simplification, most models usually consider a single grain size with a typical value of 0.1 μm representative of the observed interstellar grains. This assumption has the advantage of simplifying the implementation of the rate equations and speeding up the computation but this results in all grains having the same physical properties and thus the same chemical properties [Wakelam and Herbst, 2008, Wakelam et al., 2010].

Several authors have already studied the effect of multiple grain sizes but this has usually implied to make concessions on the consistency of the model so far. For instance, Acharyya et al. [2011] computed five different grain sizes in their models but the grain temperature was the same for all grains. The fact that the grains have a single temperature involves that surface chemistry is only dependent on the effective total surface area of the grains only, which can easily be mimicked by a single-grain model with an properly chosen number density of grains, questioning the benefit of multiple grain size models. Following this work, Pauly and Garrod [2016] and Ge et al. [2016] also developed models consisting of different grain sizes. However, they used a small number of grain sizes and did not consider the size-dependency on the effect of cosmic-ray induced desorption, which can be misleading as regards the chemical evolution. Indeed, big grains are nearly unaffected by cosmic-ray induced desorption while small ones can undergo strong des-

orption processes. Basically, one cannot build a model consisting of multiple sizes while neglecting most size-dependent parameters, especially when applied to chemistry.

In the original version of NAUTILUS, grains could only have a single size with a silicate composition [Hasegawa et al., 1992]. A more sophisticated version of NAUTILUS has been developed by Iqbal and Wakelam [2018], called the NMGC. This multi-grain version provides the user a full multi-grain network to obtain a more realistic description. The number of different grain sizes is to be suited to the need of the user with the knowledge that increasing the number of grains increases the computation time. The total grain surface available for accretion directly depends on the number density of grains and the total effective surface area depends on the choice of size sampling (number of bins) as well as the size distribution. In the NMGC, grains cannot collide and never interact or exchange mass or energy with each other. The only mass exchange is achieved via desorption and accretion of species. However, in the rate equation methods, only species located on grains of same size can interact with each other (as in single-grain models). To counteract this problem, Iqbal and Wakelam [2018] have duplicated the chemical networks on the surface of grains for different size bins by adding a specific number as prefix to each grain species. The NMGC has also been modified to enable computation of cosmic-ray induced desorption as well as cosmic-ray-peak-temperatures as a function of the grain radius. To date, two grain size distributions have been implemented in the NMGC. The first one is the MRN distribution from Mathis et al. [1977] and the second one the WD model from Weingartner and Draine [2001]. However, these models represent typical interstellar distributions. As presented in Chapter. 4, we used a slightly different grain size distribution in order to account for grain growth typically found in early protoplanetary disks. Figure. 3.3 is an illustration of the vertical dust grain distributions in the case of disks allowed by the single-grain version of NAUTILUS (left) in comparison with a distribution allowed by the NMGC (right).

One of the most important size-dependent parameter in regards to modelling chemical evolution is the grain temperature. A key element of the NMGC is that it can also use a full size-dependent temperature. The novelty brought by this present work is to use this functionality of the NMGC to build models consisting of several grain populations and corresponding number density, which we coupled, as we will see in the next chapter, to radiative transfer codes in order to have precise and consistent values of grain temperatures as a function of the grain size and, therefore, to perform more realistic chemical simulations. The model is described in Chapter. 4 and the coupling method in Chapter. 5

3.5 Stochastic formation rate of molecular hydrogen

3.5.1 Introduction

Molecular hydrogen H_2 is, by a few orders of magnitude, the most abundant molecule and probably account for most of the baryonic matter in the Universe [Dalgarno, 2000, Wakelam et al., 2017]. It is mostly found in its neutral form in dense regions where the self-shielding is large, which corresponds to $A_v \gtrapprox 0.01 - 0.1$ mag [Habart et al., 2005].

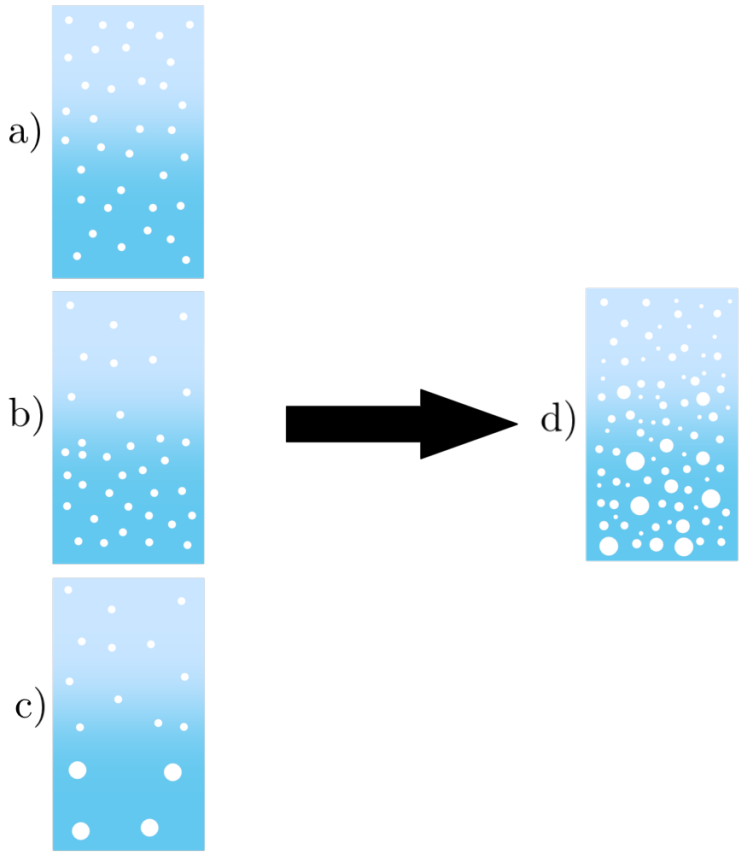

Figure 3.3: NAUTILUS using a single grain size (left-hand side) vs. the new NMGC (right-hand side). a) single grain size uniformly distributed, b) single grain size non-uniformly distributed, c) pseudo dust layering with a total conservation of mass, d) multiple grain sizes with independent distributions.

Molecular hydrogen plays a major role for our understanding of astrophysical environments. In Photon-Dominated Region (PDR)s regions, the emission of H_2 is a tracer of the physical conditions of the cloud surface [Hollenbach and Tielens, 1999]. It is also a major contributor to the cooling of the interstellar gas. In particular, H_2 regulates star formation process and the evolution of galaxies. Furthermore, H_2 controls and initiates the development of chemistry, which makes it a crucial element in understanding the chemical evolution.

3.5.2 Problematic of the H_2 formation rate in PDR regions

Nearly all molecular hydrogen molecules (H_2) form on grain surfaces. The NAUTILUS code initially implemented the H_2 formation rates using the Langmuir-Hinshelwood (LH) mechanism on grain surfaces under equilibrium temperature. The LH mechanism happens to be effective only over a relatively narrow temperature range (5-15 K) on flat surfaces [Katz et al., 1999, Vidali et al., 2004, 2005, Bron et al., 2014a]. This typical temperature range is commonly found throughout the Universe but small grains undergoing UV radiations can get warmer in unshielded regions. Such regions exist in protoplanetary disks, where the stellar UV field illuminates the small grains in the disk upper layer. The H_2 formation mechanism becomes inefficient. The lack of H_2 formation leaves a large fraction of atomic Hydrogen that can severely affect the chemical balance in the disk surface and deeper.

The problem we faced was to find a more realistic H_2 formation rates that accounts for a better computation of the gas-phase H_2 column densities in the upper layers of our disk models and to implement it in NAUTILUS. Several studies proposed more sophisticated mechanisms that theoretically produce comparable H_2 column densities to those derived by observations [e.g. Duley, 1996, Cazaux and Tielens, 2004, Cuppen and Herbst, 2005, Iqbal et al., 2012, 2014, Thi et al., 2020]. In this section we introduce the context, the problem and describe the prescription we chose and the method used to properly implement the new H_2 formation rates in the multi-grain version of NAUTILUS.

3.5.3 H_2 formation

Although there are multiple routes to the formation of H_2, formation rates in the gas-phase cannot produce enough quantities to account for the presence of H_2 given its destruction rates via UV photons, cosmic-rays, shocks and chemical reactions [Gould and Salpeter, 1963, Jura, 1974, Katz et al., 1999, Vidali et al., 2005]. It is recognized that dust grains act as catalysts in the formation of molecular hydrogen. Indeed, the formation of H_2 is a strongly exothermic reaction and the grain surface allows the nascent molecule to quickly release the 4.5 eV of excess energy due to the formation [Katz et al., 1999] in a time comparable to the vibration period of the vibrationally excited state of the newly formed molecule. The product molecule is released to the gas-phase immediately after the two hydrogen atoms get closer than $\sim$ twice the equilibrium internuclear distance of H_2 i.e. 0.7 Å.

The problem of the formation can simply be formulated as follows. A gas-phase hydrogen atom initially interacts with the grain surface with a probability ξ to be adsorbed. The adsorbed H atom spends an average time t_H, called residence time, before leaving the surface. If during the residence time t_h the H atom meets another H atom on the surface, they react and form an H_2 molecule with a certain probability. Therefore, the formation rate of H_2 on surfaces depends on the factors that influence the residence time and the diffusion of the H atoms.

The two main mechanisms leading to H_2 formation on the surface are the physisorption-based LH mechanism and the chemisorption-based Eley-Rideal (ER) mechanism[1]. Figure. 3.4 summarizes the two formation mechanisms.

3.5.3.1 Rate equation approach

The LH reaction occurs when two physisorbed atoms meet on the surface (subsection 3.3.4). The simplest method to solve this problem is based on laboratory data and is called the *rate equation approach*. In this approach, we calculate the following differential equation,

$$\frac{\mathrm{d}n}{\mathrm{d}t} = R_{\mathrm{ads}} - R_{\mathrm{des}} - R_{\mathrm{form}}^{(\mathrm{ER})} - R_{\mathrm{form}}^{(\mathrm{LH})} \tag{3.39}$$

where n is the number of physisorbed atoms on the surface and assumed to be a continuous variable dependent on the adsorption rate R_{ads}, the desorption rate R_{des}, the formation rate via the ER mechanism $R_{\mathrm{form}}^{(\mathrm{ER})}$ and the formation rate via the LH mechanism $R_{\mathrm{form}}^{(\mathrm{LH})}$ [see Bron et al., 2014b, for a detailed description of the rates].
Then, solving Eq. 3.39 with the surface temperature assumed to be constant yields an equilibrium population $n_{\mathrm{eq}}(T)$. The equilibrium population $n_{\mathrm{eq}}(T)$ and the H_2 formation rate $R_{\mathrm{H_2}}^{(\mathrm{eq})}(T)$ are therefore proportional to the grain surface. We can thus consider the formation efficiency η, which gives the fraction of H atoms colliding that are transformed into H_2:

$$\eta = \frac{2R_{\mathrm{H_2}}(T)}{k_{\mathrm{coll}}} \tag{3.40}$$

where k_{coll} is the collision rate. We see that this equation is independent of the grain size.

Despite its advantages (i.e. simplicity and fast computation), the rate equation approach, along with approximations gives rise to problems in some regimes. Indeed, by using the classical rate equation approach we assume that the number of species n at the surface is large enough to be treated as a continuous variable so that we can neglect stochastic fluctuations of population. It is not uncommon that the surface population on a grain is close to one and the LH mechanism is effective as soon as at least two atoms are present on the surface. The discrete nature of surface processes cannot be taken into account using this approach. Secondly, the approach usually assumes an equilibrium

[1] As pointed out by Bron et al. [2014a], Eley-Rideal reaction occurs when a gas atom falls onto an occupied site by an adsorbed atom. This process is valid both for a physisorbed and a chemisorbed atom. However, for simplicity, and because it is customary in the literature, we will associate the LH mechanism with physisorbed atoms and the ER mechanism with chemisorbed atoms only.

grain temperature. However, as we will see, temperature of grains, in particular that of the small ones, fluctuates substantially due to photon absorption events.

Furthermore, the LH mechanism is only effective in a typical narrow range of temperature [5 - 15 K] because of the very small binding energy that results from the weak van der Waals dispersion forces. This is problematic in the context of astrophysics because the equilibrium temperature is almost exclusively above $\sim$ 20 K in most unshielded regions. Yet, observations indicate that molecular hydrogen formation is efficient under a wide range of interstellar conditions, from the cold shielded dark clouds to PDRs regions with gas temperature of several 100 K.

It thus appeared necessary to developed other numerical techniques, in particular techniques that takes into account the random surface processes.

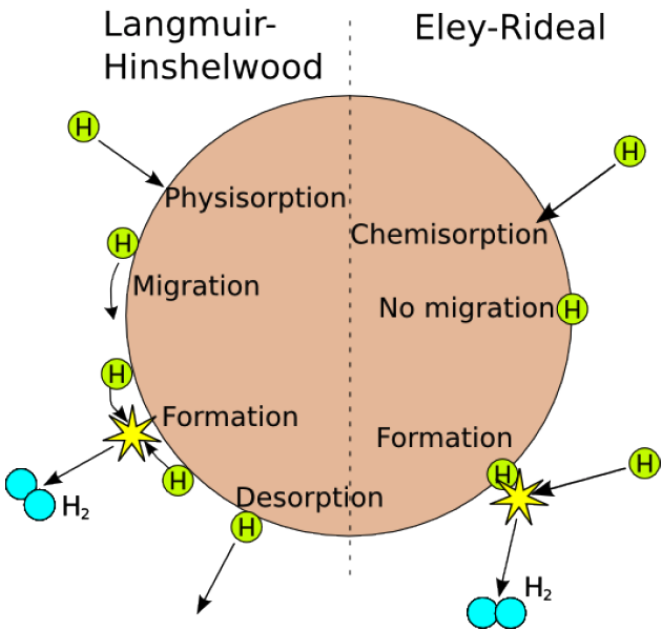

Figure 3.4: Illustration of the two main mechanisms that lead to formation of H_2. Left: physisorbed-based Langmuir-Hinshelwood (LH) mechanism. Right: chemisorbed-based Eley-Rideal (ER) mechanism [From Bron et al., 2014b].

3.5.3.2 Temperature fluctuations

Before describing the methods that account for the statistical effects, let us introduce some details about the temperature fluctuations of the small grains in order to put these effects in a meaningful context. We have seen that rate equation computes the H_2 formation processes on surfaces under radiative equilibrium between the absorption of short wavelength photons by dust grains and the re-emission of energy by thermal radiation in the infrared, which determines an equilibrium temperature T_e for grain surfaces. The definition of an equilibrium temperature is roughly valid for grains of size $>$ 500 nm whose energy stored is much higher than the energy deposited by a UV photon from the

ISRF [Greenberg, 1968, Duley, 1996]. For smaller grains (1 nm to 500 nm), however, whose heat capacity is small, the stored energy is comparable to the absorbed photon's energy which results in a significant increase of temperature in a transient spike [Desert et al., 1986, Draine and Li, 2001, Compiègne et al., 2011]. This effect can be very large for particles whose size is close to molecular size (e.g. PAH) where spikes can reach 10^3 K in some cases [Draine and Anderson, 1985]. It is admitted that these temperature spikes enhance reaction rates for adsorbed species on dust grains as well as desorption rates. For instance, the rapid heating of the grain will massively thermally desorb H_2 from the surface which, in turn will influence the gas-phase chemistry [Cuppen et al., 2006].

The temperature of grains undergoing important spikes cannot be calculated under the assumption of equilibrium heating and cooling. The strong dependence of the cooling rate R_c on the temperature T implies that a very small grain heated to a high temperature by absorption of a UV photon will cool quickly to a temperature near the equilibrium temperature T_e. The timescale of this cooling is approximately [Duley, 1996],

$$t_c \approx \frac{h\nu_{\rm abs}}{4\pi a^2 R_c} \tag{3.41}$$

where $h\nu_{\rm abs}$ is the energy of the incident UV photon. For $T > 100$ K, t_c is of the order of $\sim$ 1 sec, which is less than the typical time interval t_p between two absorptions of photons. Since $t_p \gg t_c$ and that most of the energy is removed during the time t_c, the grain surface will be able to cool to temperatures $T \ll T_e$ during the interval t_p and reach temperatures that allows for certain surface reactions to occur, in particular H_2 formation.

3.5.3.3 Statistical approach

The discrete nature of the surface population and temperature results in random fluctuations of these variables. To solve this problem using a statistical approach, models consider that the adsorbed atoms migrate randomly on the surface and one H_2 is formed each time two atoms meet. This mechanism has been studied extensively using a probability density function (PDF) driven by a master equation. This approach is thus commonly called the *master equation approach*. Unlike the rate equation approach, the master equation approach has the disadvantage of being particularly CPU-costly and it usually requires to make approximations to allows for a faster solution. Various approximations have been proposed such as the moment equation approach [Lipshtat and Biham, 2003, Le Petit et al., 2009].

For our study, we decide to adopt the prescription of Bron et al. [2014a] (called B14 hereafter) which consists in using an analytical approach based on the master equation which simultaneously accounts for the fluctuations of the dust temperature and the adsorbed H-atom population to compute the total H_2 formation rate. Although their method allows to quickly compute the ER mechanism without any approximation, the LH mechanism is computationally costly and requires to build fast and accurate approximation. Their H_2 formation rate parameter R_f (LH mechanism) for a carbonaceous dust population as a function of the radiation field intensity G_0 is shown in Figure 3.5. The different lines account for different proton number densities. The blue (10^4 cm^{-3}) and

purple (10^6 cm^{-3}) are the data from Fig. 6 of Bron et al. [2014a].

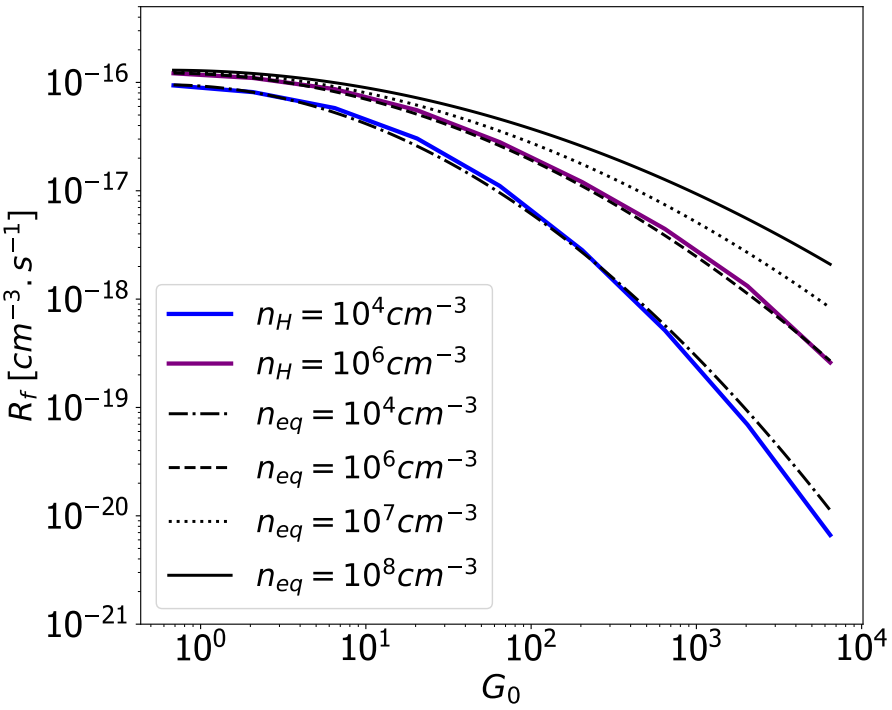

Figure 3.5: Integrated formation rate parameter R_f as a function of the radiation field intensity G_0 for different gas densities. The blue (10^4 cm^{-3}) and purple (10^6 cm^{-3}) are the data adapted from Fig. 6 of Bron et al. [2014a]. The black lines (10^4, 10^6, 10^7, 10^8 cm^{-3}) correspond to our analytical fits.

3.5.4 Implementation in Nautilus

The study of B14 lies in a domain of gas temperature and gas density (10^0 to 10^6 cm^{-3}) different from our present study but this difference can be corrected as both temperature and gas density only affect the results through the collision rate of atomic Hydrogen with the grains, which scales as $n_H\sqrt{T_g}$. Thus, we can estimate the rate for a given density $n_{\rm H}$ and a given temperature $T_{\rm g}$ by extracting or interpolating from B14's data the value corresponding to an equivalent gas density $n_{\rm eq}$,

$$n_{\rm eq} = n_H \sqrt{\frac{T_g}{100\,{\rm K}}} \frac{s(T_g)}{s(100\,{\rm K})} \tag{3.42}$$

where $s(T_g)$ is the sticking coefficient at temperature T_g as defined by Le Bourlot et al. [2012]:

$$s(T) = \left(1 + \frac{T^\beta}{T_2}\right)^{-1} \tag{3.43}$$

where $T_2 = 464$ K and $\beta = 1.5$, which approximately gives the same results as in Sternberg and Dalgarno [1995].

Figure 3.5 shows B14's rates (blue and purple lines in Fig. 3.5). We see that the formation rate is proportional to the gas density at low densities, then it progressively saturates for larger densities because the UV flux G becomes insufficient to dissociate H_2 and the fraction of atomic H decreases. At lower densities, this stochastic rate roughly decreases as $1/G$ because grains spend more time in the temperature range where the LH formation is efficient as the UV flux decreases.

We managed to interpolate B14's data using an analytical polylogarithmic function (see Appendix C for a detailed description). The analytical fit results are the black lines in Fig. 3.5. Each line corresponds to a proton number density (we show 10^4, 10^6, 10^7, 10^8 cm^{-3} as examples). The implementation is very simple: NAUTILUS reads the local gas density and local flux at the considered location within the model. Then, it computes the local H_2 formation rate using the polylogarithmic functions.

Chapter 4

Application of the NMGC to 2D disk model

Contents

4.1 Introduction

The first step before simulating the chemical evolution of disks using NAUTILUS was to build a 2D disk model with a full distribution of dust suited for the code. From the perspective to use a realistic description of dust grains, we want to consider dust settling and define a proper grain size distribution, which are both expected to affect the chemical evolution of the disk. For NAUTILUS, this implies to obtain the dust density number $n_{\rm d}(r, z, a)$ at each coordinates (i.e. $(r,\ z)$) of the disk for each grain species considered so that we can write the dust concentration as follows:

$$[\mathrm{X_d}] = \frac{n_d(r, z, a)}{n_H(r, z)}. \tag{4.1}$$

In this equation, a denotes the grain sizes and $n_{\rm H}(r, z)$ is the total hydrogen atom number density at radius r from the central star and altitude z above the mid-plane.

4.2 2D disk model

As established in Chapter. 2, g index always stands for gas and d always stands for dust. We use a reference radius for all equations taken at 100 au from the star. Thus, the index 0 always stands for 100 au. Unless specified, volumes are expressed in cm^3 and mass in g. n always describes a number density while ρ always describes a mass density. In general, the term gas refers to the number of hydrogen (atomic and molecular) which accounts for the total gas density. The disk is assumed to be in Keplerian rotation about the host star.

4.2.1 Gas description

Computation of vertical and radial temperature profiles The kinetic temperature T_k along the radius in the mid-plane is given by the power-law,

$$T_{\rm k}(r, z = 0) = T_{\rm mid,0}\left(\frac{r}{R_0}\right)^{-q} \tag{4.2}$$

where $T_{\rm mid,0}$ is the temperature at R_0 in the mid-plane. Then, following Dartois et al. [2003], we define a vertical temperature gradient using the formulation of Williams and Best [2014],

$$T_{\rm g}(r, z) = T_{\rm mid}(r) + (T_{\rm atm}(r) - T_{\rm mid}(r)) \sin\left(\frac{\pi z}{2 z_{\rm atm}}\right)^{2\sigma} \tag{4.3}$$

where σ is the siffness of the vertical temperature profile and $z_{\rm atm}$ is the atmosphere altitude (the upper boundary of the disk model).

Computation of the gas scale height Assuming static vertical equilibrium, the gas scale height at reference radius is given by,

$$H_{g,0} = \sqrt{\frac{k_B T_{mid,0} R_0^3}{\mu_m m_H G M_*}}. \tag{4.4}$$

where the radial profile of the gas scale height can be defined as,

$$H_g(r) = H_{\mathrm{g},0}\left(\frac{r}{R_0}\right)^h \tag{4.5}$$

where $H_{\mathrm{g},0}$ is the scale height of the gas at the reference radius R_0 and $h = \frac{3}{2} - \frac{q}{2}$.

Computation of the gas surface density The gas surface density $\Sigma_g(r)$ also follows a power-law radial profile,

$$\Sigma_g(r) = \Sigma_{g,0}\left(\frac{r}{R_0}\right)^{-p} \tag{4.6}$$

The gas disk mass can be given as a function of the surface density by

$$M_{gas} = \int_{R_{in}}^{R_{out}} 2\pi r \Sigma_g(r) dr = \int_{R_{in}}^{R_{out}} 2\pi r \Sigma_{g,0}\left(\frac{r}{R_0}\right)^{-p} dr \tag{4.7}$$

where R_{out} is the outer radius of the gas disk and R_{in} is the inner radius. Integrating Eq.4.7 allows to obtain $\Sigma_{g,0}$,

$$\Sigma_{g,0} = \frac{M_{gas} R_0^{-p}(2-p)}{2\pi(R_{out}^{2-p} - R_{in}^{2-p})}. \tag{4.8}$$

For instance, for $R_{out} = 300$ au, $M_{gas} = 0.008$ $\mathrm{M}_\odot$, $R_0 = 100$ au and $p = 1.5$, we get $\Sigma_{g,0}$ $= 0.335$ g.cm^{-2}.

Computation of the gas vertical profile The gas in the disk is considered to be in hydrostatic equilibrium at the mid-plane temperature. If the disk is vertically isothermal ($\partial \ln(T)/\partial z = 0$), the solution of the gas vertical density profile is gaussian distributed and is written as in Equation 2.17. However, since our model assumes a vertical gradient of the temperature, the vertical gas profile deviates from a gaussian distribution. The solution is not trivial and it is necessary to iteratively solve the equation of hydrostatic equilibrium (Equation 2.12). As our disk model is discretized, NAUTILUS computes the gas density for each z vertical point, called spatial points. Therefore, solving Eq. 2.12 at the spatial point z_j yields,

$$\ln(\rho_g(z_{\mathrm{j}})) = \ln(\rho_g(z_{\mathrm{j}-1})) - \left[\Omega^2 \frac{\mu m_H}{k_B T(z_j)} + \big(\ln(T(z_j)\big) - \ln(T(z_{\mathrm{z}-1}))\right]. \tag{4.9}$$

where Ω is the Keplerian angular velocity. We note that NAUTILUS computes the gas number density (in cm^{-3}) so that Eq. 4.9 is to be converted into the appropriate units.

4.2.2 Dust description

Dust quantity The material composition is distributed into two separate grain populations, one population of silicate grains (62.5 %) and the other of graphite grains (37.5 %), according to the MRN model [Mathis et al., 1977]. This leads to a material specific mass density equals to:

$$\rho_m = 2.5 g.cm^{-3}. \tag{4.10}$$

Mathis et al. [1977], Draine and Lee [1984], Laor and Draine [1993], and Weingartner and Draine [2001] also show that the number of species in the size interval $[a, a + da]$ is given by

$$dn(a) = Cn_H a^{-d} da \tag{4.11}$$

with C a normalization constant, $n_{\rm H}$ the number density of hydrogen nuclei and $dn(a)$ the number of grains in the size interval $[a, a + da]$. We first consider a continuous grain size distribution. We can use Eq.4.11 to obtain the dust mass per unit of volume:

$$m_{dust} = \int_{a_-}^{a_+} m(a) dn(a) = \int_{a_-}^{a_+} \frac{4\pi}{3} \rho_m C n_H a^{3-d} da \tag{4.12}$$

where $m(a)$ is the mass of grain species of size a per unit of volume and $\{a_-,a_+\}$ are the cutoff sizes of the bin. The integration of Eq.4.12 gives

$$m_{dust} = \frac{4\pi}{3} \rho_m C n_H \frac{1}{4-d} (a_+^{4-d} - a_-^{4-d}) \tag{4.13}$$

Then, the dust to gas ratio is

$$\zeta = \frac{m_{\rm dust}}{m_{\rm gas}} = \frac{m_{\rm dust}}{n_H \mu_a m_H} \tag{4.14}$$

where $m_{\rm gas}$ is the gas mass per unit of volume, m_H is the mass of hydrogen atom and μ_a is the mean molecular weight. Using Eq.4.13 and Eq.4.14 we solve for the normalization constant

$$C = \frac{3}{4\pi} \frac{\zeta \mu_a m_H}{\rho_m} (4-d) \frac{1}{(a_+^{4-d} - a_-^{4-d})} \tag{4.15}$$

Computation of the dust surface density We introduce the surface density of a grain population of size a following a radial power-law,

$$\sigma_d(r, a) = \sigma_{d,0}(a) \left(\frac{r}{R_0} \right)^{-p} \tag{4.16}$$

where $\sigma_{d,0}(a)$ is the surface density of the dust species of size a at the reference radius. Thus, we assume that the dust surface density follows the same law along the radius as the gas. The total dust surface density (accounting for all grain populations) is obtained

by integrating on all the grain sizes,

$$\Sigma_d(r) = \int_a \sigma_d(r,a)da. \tag{4.17}$$

As we will see, NAUTILUS computes a finite number of grain sizes so Eq. 4.17 is discretized and we define a grain population consisting of $N_{\rm d}$ grain sizes.

Computation of the vertical distribution We assume that the dust vertical profile is independent of the temperature so that it follows a Gaussian distribution regardless of the size,

$$\rho_d(r,z,a) = \rho_{d,mid}(r,a)\exp\left(\frac{-z^2}{2H_d(r,a)^2}\right). \tag{4.18}$$

where $\rho_{\rm d,mid}(r,a)$ is the density in the mid-plane at r for grains of size a.
The surface density at r for a grain size a $\sigma_d(r,a)$ can be expressed by integrating the dust mass density along the altitude:

$$\sigma_d(r,a) = \int_{-\infty}^{+\infty} \rho_d(r,z,a)dz \tag{4.19}$$

Therefore, Eq. 4.18 can be written as,

$$\rho_{d,mid}(r,a) = \frac{\sigma_d(r,a)}{\sqrt{2\pi}H_d(r,a)}\exp\left(\frac{-z^2}{2H_d(r,a)^2}\right). \tag{4.20}$$

Unlike the gas, the dust is settled along the altitude. Because dust grains do not react to pressure, the dust scale height $H_d(r,a)$ is different from the gas scale height $H_g(r)$ and depends on the grain size a since the dust scale height depends on the settling.

Computation of the settling factor We define the settling factor $s(r,a)$ following Equation. 4.21,

$$s(r,a) = \frac{H_d}{H_g} = \frac{1}{\sqrt{1+\tau_s\frac{S_c}{\alpha}}}. \tag{4.21}$$

The resulting settling factor is shown by the blue curve in Figure 2.10. We see that the ratio between H_d and H_g is directly dependent on the grain size a. Small grains are well coupled to the gas and their vertical profile roughly follows that of the gas while bigger grains are mainly subject to gravitational interactions and turbulence diffusion which define their vertical distribution [Dong et al., 2015]. Figure 4.1 illustrates the dust scale height of a set of 16 bins as defined in Table. 4.1. The bin values increase with the grain sizes. The scale height of the biggest grain size population decreases by several factors as compared to the grain population of the smallest size.

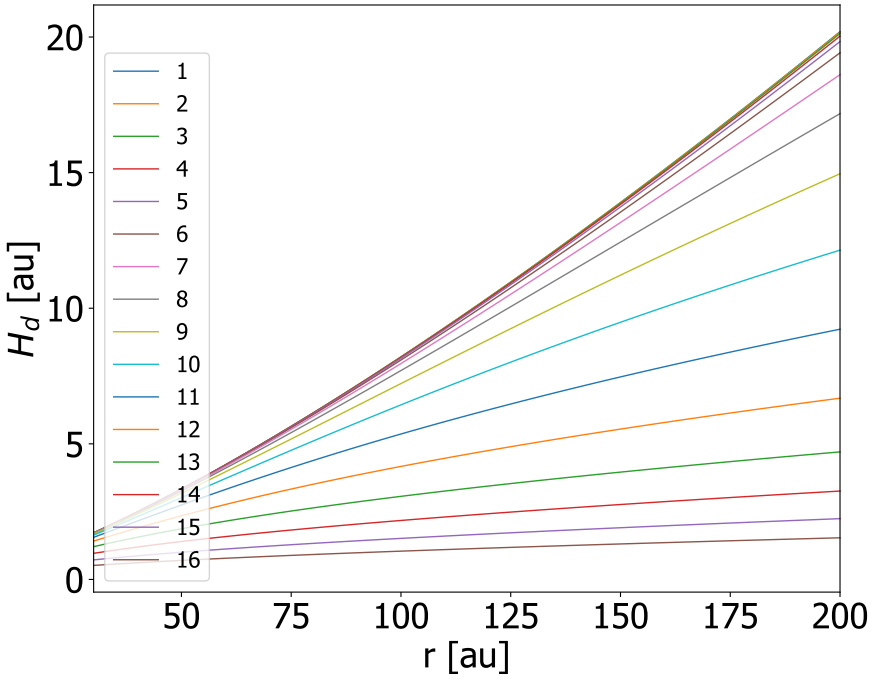

Figure 4.1: Scale heights of the 16 grain species as a function of the radius. The grain size ranges from 0.007 to 651 μm. The scale height of the smallest grains roughly follows the gas scale height. The larger grains tend to significantly settle toward the mid-plane.

Table 4.1: Overview of the 16 discretized grain sizes.

bin	averaged size (μm)	relative dust mass	relative area
1	0.007	0.10 %	30.5 %
2	0.015	0.15 %	20.8 %
3	0.032	0.22 %	14.2 %
4	0.069	0.33 %	9.73 %
5	0.15	0.48 %	6.67 %
6	0.32	0.70 %	4.59 %
7	0.68	1.03 %	3.19 %
8	1.46	1.50 %	2.25 %
9	3.13	2.20 %	1.64 %
10	6.69	3.22 %	1.25 %
11	14.4	4.72 %	1.03 %
12	31.0	6.91 %	0.90 %
13	66.0	10.1 %	0.84 %
14	142	14.8 %	0.80 %
15	304	21.7 %	0.78 %
16	651	31.8 %	0.76 %

Dust to gas ratio We assume that the vertically integrated dust to gas mass ratio ζ is constant and is independent of the settling factor. Therefore, we define a single ζ valid at all radii:

$$\zeta = \frac{\Sigma_d(r)}{\Sigma_g(r)} = \frac{\int \sigma_d(r,a)da}{\Sigma_g(r)} = \frac{1}{100}. \tag{4.22}$$

Computation of the grain size intervals To discretize the grain sizes, we divide the range into logarithmically distributed intervals. The cutoff of each interval k is defined by a maximum value $a_{max,k}$ and a minimum value $a_{min,k}$. We want to express the averaged grain size value of each interval. By using Eq.4.11 we can derive the averaged grain size of the kth interval $a_{av,k}$ as follows:

$$\frac{4\pi}{3} C n_H \int_{a_{min,k}}^{a_{max,k}} a^3 a^{-d} da = \frac{4\pi}{3} C n_H a_{av,k}^3 \int_{a_{min,k}}^{a_{max,k}} a^{-d} da \tag{4.23}$$

$$\iff \int_{a_{min,k}}^{a_{max,k}} a^{3-d} da = a_{av,k}^3 \int_{a_{min,k}}^{a_{max,k}} a^{-d} da \tag{4.24}$$

Then, by integrating we can isolate the averaged grain size:

$$\iff a_{av,k} = \left(\frac{1-d}{4-d} \cdot \frac{a_{max,k}^{4-d} - a_{min,k}^{4-d}}{a_{max,k}^{1-d} - a_{min,k}^{1-d}} \right)^{\frac{1}{3}} \tag{4.25}$$

To simplify notation we write $a_{\mathrm{av,k}} = a_k$. Following Heese et al. [2017] and using Eq. 4.25, we define a total $N_{\mathrm{d}} = 16$ different grain sizes that will be used in all the models. Table. 4.1 summarizes the different bins and their relative characteristics.

4.2.3 Extinction in a disk with multi-sized grains

Computing the extinction in the case of multiple grain populations requires to use specific approaches. Several methods can be used. One is to use radiative transfer codes to compute the dust extinction generated by the dust distribution and then couple the results to chemistry simulations. This is the method employed for this thesis, which is described in Chapter. 5.

Another approach would be to algebraically treat the extinction, in a case of multiple grain sizes, which does not require the use of radiative transfer simulations. Even though our present study considers the first approach, it is nevertheless necessary for the NMGC (and the future users) to be able to use a multi-grain extinction as a "standalone" mode. To do so, the algebraic calculation has also been embedded in the routine (coded for this thesis work to build the disk physical structure) for a standalone use of the NMGC. I believe this treatment is worth being introduced in this thesis.

The following is here to describe how our disk physical model treats the extinction in the case of a grain population of multiple sizes without the help of radiative transfer simulations. Before giving the definition of the extinction, we also remind the definition of the radiative transfer equation in the case of a non-emissive medium.

4.2.3.1 Solution of the radiative transfer equation

Calculation of the intensity in a cloud Let M be a point in the disk at which we want to know the local specific intensity I_ν. To obtain the intensity at M, we have to integrate the radiative transfer equation from the rear edge of the cloud to the point M. At the rear edge of the cloud, the optical depth τ_ν equals 0 and increases toward M. Assuming the angle between the observer and the ray is 0, the evolution equation of the specific intensity along the line of sight is,

$$\frac{\mathrm{d}I_\nu}{\mathrm{d}s} = -\kappa_\nu I_\nu + j_\nu \tag{4.26}$$

where s is the path along the line of sight, j_ν is the emissivity coefficient and κ_ν is the absorption coefficient. If $\kappa_\nu \neq 0$, we can write Eq. 4.26 to the equivalent (misleadingly) simple form by substituting s for the optical depth $\tau_\nu = \kappa_\nu \mathrm{d}s$:

$$\frac{\mathrm{d}I_\nu}{\mathrm{d}\tau_\nu} = -I_\nu + S_\nu \tag{4.27}$$

where $S_\nu = j_\nu/\kappa_\nu$ is called the *source function*.

Solution for a non-emissive medium In the case where the medium is non-emissive ($j_\nu = 0$), which is approximately the case for UV radiation in optically thin layers, the source function becomes equal to zero and the Eq. 4.27 is written as,

$$\frac{\mathrm{d}I_\nu}{I_\nu} = -\mathrm{d}\tau_\nu. \tag{4.28}$$

The integration is trivial and the formal solution in a purely absorbent medium is,

$$I_\nu = I_{0,\nu} e^{-\tau_\nu} \tag{4.29}$$

where $I_{0,\nu}$ is the specific intensity before it enters the cloud. Therefore, we see that the intensity at a point M in a cloud is equal to the incident intensity weighted by the absorbent medium.

4.2.3.2 General definition of the extinction

We can express the extinction in magnitude A_ν in terms of the reduction in intensity caused by the presence of dust in the line of sight,

$$A_\nu = -2.5 \log_{10} \left(\frac{I_\nu}{I_{0,\nu}} \right). \tag{4.30}$$

Substituting the flux from Eq. 4.29 yields,

$$A_\nu = 2.5 \log(e) \tau_\nu = 1.086 \cdot \tau_\nu. \tag{4.31}$$

where τ_ν is the frequency-dependent opacity (or optical depth).

Opacity The general definition of the opacity is,

$$\tau(\nu) = \int_s k(s, \nu) \mathrm{d}s \tag{4.32}$$

where $k(s, \nu)$ is an absorption coefficient and the integration is made along a path of light s. Both dust and gas contribute to the UV attenuation. Let us give a definition of the opacity for each of them.

4.2.3.3 Molecular opacity

For a line, the molecules contribute as follows:

$$\tau_m(\nu, s, z) = \sum_X \int_s n(X, r, z) \sigma_{abs}(X, \nu) ds \tag{4.33}$$

where X are the molecules that contribute to the attenuation (we note that $\{H_2, CO, N_2\}$ are the molecules that contribute the most), $n(X, r, z)$ is the number density [cm^{-3}] of species X at coordinates (r, z) and $\sigma_{abs}(X, \nu)$ is the absorption cross-section of species X at frequency ν. In the case of a disk model, the line s over which we integrate is either the altitude z above the considered point of coordinates (r, z) or the distance $l = \sqrt{r^2 + z^2}$ between the central star and the considered point.

4.2.3.4 Dust opacity

For a discretized grain size population, we write:

$$\tau_d(\nu, s, z) = \sum_i \int_s \kappa_e(a_k, \nu) n_d(a_k, r, z) ds \tag{4.34}$$

$\kappa_e(a_k, \nu)$ is the dust extinction coefficient and $n_d(a_k, r, z)$ is the number density [cm^{-3}] of the grains of size a_k at coordinates (r, z). When a radiation is intercepted by a dust grain, the radiation undergoes absorption and scattering processes. The sum of these two processes is called extinction. For this reason we consider the extinction coefficient rather than simply the absorption coefficient.

To define the extinction coefficient, we introduce the extinction efficiency:

$$Q_e(a_k, \nu) = \frac{\sigma_e(a_k, \nu)}{\sigma_g(a_k)} \tag{4.35}$$

where $\sigma_e(a_k, \nu)$ is the extinction cross-section for grains of size a_k and $\sigma_g(a_k) = \pi a_k^2$ is the geometrical cross-section. Since the extinction is a combined effect of absorption and scattering of light we write,

$$\sigma_e(a_k, \nu) = \sigma_{abs}(a_k, \nu) + \sigma_{sca}(a_k, \nu). \tag{4.36}$$

Consequently:

$$Q_e(a_k, \nu) = Q_{abs}(a_k, \nu) + Q_{sca}(a_k, \nu). \tag{4.37}$$

Then, considering Eq. 4.35, the extinction coefficient is defined as,

$$\kappa_e(a_k, \nu) = \sigma_e(a_k, \nu) = \sigma_g(a_k) Q_e(a_k, \nu). \tag{4.38}$$

If we define the geometrical cross-section as $\sigma_g(a_k) = \pi a_k^2$, Eq. 4.34 is finally:

$$\tau_d(\nu, r, z) = \sum_i \int_s n_d(a_k, r, z) a_k^2 \pi Q_e(a_k, \nu) ds \tag{4.39}$$

By integrating along the path s, Eq. 4.39 becomes,

$$\tau_d(\nu, r, z) = \pi \sum_i N_d(a_k) a_k^2 Q_e(a_k, \nu) \tag{4.40}$$

where $N_d(a_k)$ is the dust column density of grains of size a_k. Finally, the A_ν is written as,

$$A_\nu = 1.086\pi \cdot \sum_i N_d(a_k) a_k^2 Q_e(a_k, \nu) \tag{4.41}$$

This equation is used to calculate the A_ν in absence of radiative transfer simulations.

Extinction efficiency We now need to define the extinction efficiency $Q_e(a_k, \nu)$. To do so, we use a parametrisation of $Q_e(a_k, \nu)$ and define three different "regimes" depending on the grain size and wavelength:

$$\lambda \leq \pi a_k : Q_e(a_k, \nu) = 2 \tag{4.42}$$

$$\pi a_k < \lambda < 2\pi a_k : Q_e(a_k, \nu) = Q_c \left(\frac{\lambda}{\lambda_c} \right)^{\frac{\log_{10} Q_c}{log_{10} 2}} \tag{4.43}$$

$$\lambda \geq 2\pi a_k : Q_e(a_k, \nu) = Q_c \left(\frac{\lambda}{\lambda_c} \right)^{-2} \tag{4.44}$$

where Q_c is the extinction at the resonance where $\lambda = \lambda_c = 2\pi a_k$.

4.3 Implementation in NAUTILUS

4.3.1 Grid

NAUTILUS performs simulations in 1D. To create a 2D disk, we simulate the chemistry in 1D in the z direction at each considered radius and we interpolate between the radii. The total size of the box is chosen to be $z/H_g = 4$ so we convert the altitude z [au] into units of z/H_g. We divide the edge-on disk into a finite number of radius and altitudes

$$\begin{aligned} r &: (r_1, r_2, ..., r_i, ..., r_{\mathrm{N_r}}) \\ z &: (z_1, z_2, ..., z_j, ..., z_{\mathrm{N_p}}) \end{aligned} \tag{4.45}$$

with $N_\mathrm{r} = 13$ the number of implemented radii (from 30 au to 250 au) and N_p the number of spatial points implemented at each radius. We note that N_p is the same at all radii in order to maintain a 4 $\mathrm{H_g}$ box everywhere. Therefore, the structure is divided into cells of coordinates (r_i, z_j).

Each cell at (r_i, z_j) in the grid receives the abundances from all the grain species at the considered coordinates. The local dust to gas mass ratio ζ varies with z because of the dust settling but the vertically integrated ζ is constant.

Computation of the vertical grid As the total size of the box is 4 $\mathrm{H_g}$, z will be a table of spatial points vertically distributed and equally spaced. It is computed using the formula,

$$z(j) = \left(1 - \frac{2 \times j}{2 \times N_p - 1}\right) \times 4H_g \tag{4.46}$$

where $j = 0$, ..., $N_\mathrm{p} - 1$. The structure of the naked grid (without physical/chemical input) is represented in Figure. 4.2.

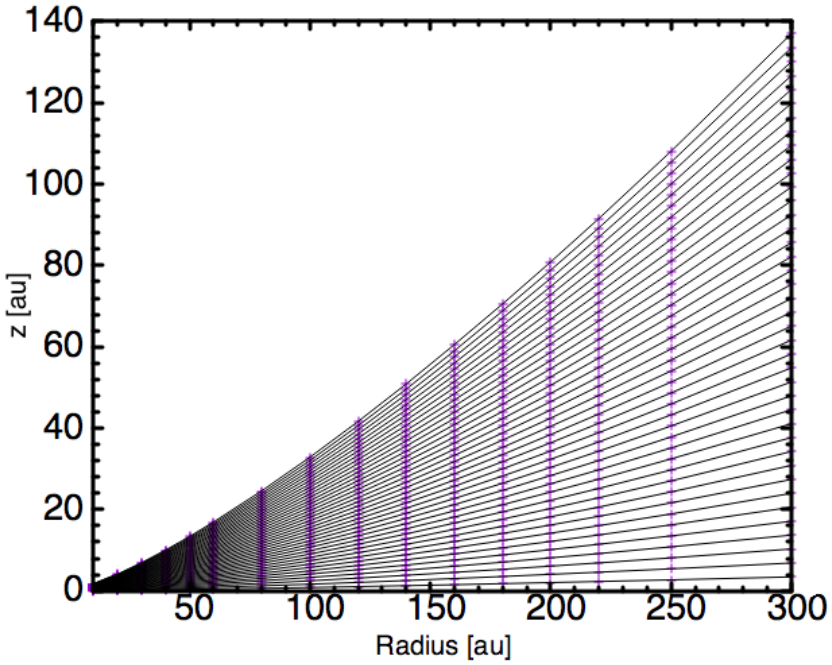

Figure 4.2: Naked grid of our disk model implemented by NAUTILUS. The purple crosses corresponds to the spatial points where NAUTILUS simulates the local chemical evolution.

4.3.2 Dust surface density in the case of multiple grain sizes

As described in subsection 4.2.2, we discretize the size intervals and write a_{k} the size of the kth grain population. The dust to gas ratio is expressed as

$$\Sigma_d(r) = \zeta \Sigma_g(r). \tag{4.47}$$

Moreover, since we assume that the dust surface densities follow the law as written in Eq. 4.16, we can write Equation. 4.47 at the reference radius. It becomes,

$$\Sigma_{d,0} = \zeta \Sigma_{g,0}. \tag{4.48}$$

Using a discretized version of Equation. 4.17, Eq. 4.48 is also

$$\sum_k \sigma_{d,0}(a_k) = \zeta \Sigma_{g,0}. \tag{4.49}$$

In other words, $\sigma_{d,0}(a_k)$ is a fraction x_{a_k} of the total dust surface density:

$$\sigma_{d,0}(a_k) = x_{a_k} \zeta \Sigma_{g,0}. \tag{4.50}$$

Using a discretized version of Equation. 4.13 we can express the fraction as

$$x_{a_k} = \frac{m_{a_k}}{\sum_k m_{a_k}} \tag{4.51}$$

Table 4.2: Overview of the disk model parameters.

Disk Parameters	
$\boldsymbol{T_{\star,\mathrm{eff}}}$ (star temperature)	3900 K
$\boldsymbol{L_\star}$ (star luminosity)	0.75 $L_\odot$
$\boldsymbol{M_\star}$ (star mass)	0.58 $M_\odot$
ISRF	DRAINE
$\boldsymbol{\Sigma_{g,0}}$ (gas (H + H_2) surface density at R_0)	0.335 g.cm^{-2}
$\boldsymbol{p}$ (surface density exponent)	1.5
$\boldsymbol{R_{\mathrm{in}}}$ (innermost radius)	1 au
$\boldsymbol{R_{\mathrm{out}}}$ (outermost radius)	250 au
$\boldsymbol{R_0}$ (reference radius)	100 au
$\boldsymbol{\zeta}$ (dust to gas mass ratio)	0.01
$\boldsymbol{T_{\mathrm{mid},0}}$ (observed T_{mid} at R_0)	10 K
$\boldsymbol{T_{\mathrm{atm},0}}$ (observed T_{atm} at R_0)	50 K
$\boldsymbol{\sigma}$ (stiffness of the vertical T profile)	2
$\boldsymbol{q}$ (radial T profile exponent)	0.4
$\boldsymbol{S_c}$ (Schmidt number)	1
$\boldsymbol{\alpha}$ (viscosity coefficient)	0.01
$\boldsymbol{d}$ (grain size distribution exponent)	3.5
$\boldsymbol{a_{\mathrm{min}}}$ (smallest grain radius)	5 nm
$\boldsymbol{a_{\mathrm{max}}}$ (biggest grain radius)	1 mm
number of bins	16
$\boldsymbol{\rho_{\mathrm{grain}}}$ (material density of dust)	2.5 g.cm^{-3}
$\mathbf{M_{disk}}$ (total disk mass)	$7.5.10^{-3}$ $M_\odot$

Therefore, using Eq. 4.50 and 4.51 allows to separately express the surface density $\sigma_{d,0}(a_k)$ of each grain population.

4.3.3 Results of the physical model

As mentioned in Chapter. 1, the NAUTILUS inputs of our disk model are the quantities derived by the observations of the Flying Saucer [see Dutrey et al., 2017], which are given in Table. 4.2. One of the most important parameter is the gas surface density at reference $\Sigma_{\mathrm{g},0}$ since all other densities are derived from it (see Eq. 4.50). We use a value of 0.335 g.cm^{-2}.

The physical results are shown in Figure 4.3. These represent the input physical structure of our disk model that NAUTILUS will use to perform the chemical simulations. We note that the UV fields G as well as the dust area-weighted temperature T_{a} (defined by Equation. 6.1 in Chapter. 6) derived from the temperature of the 16 grain species are computed beforehand the chemical simulations by a radiative transfer code which we will describe in Chapter. 5.

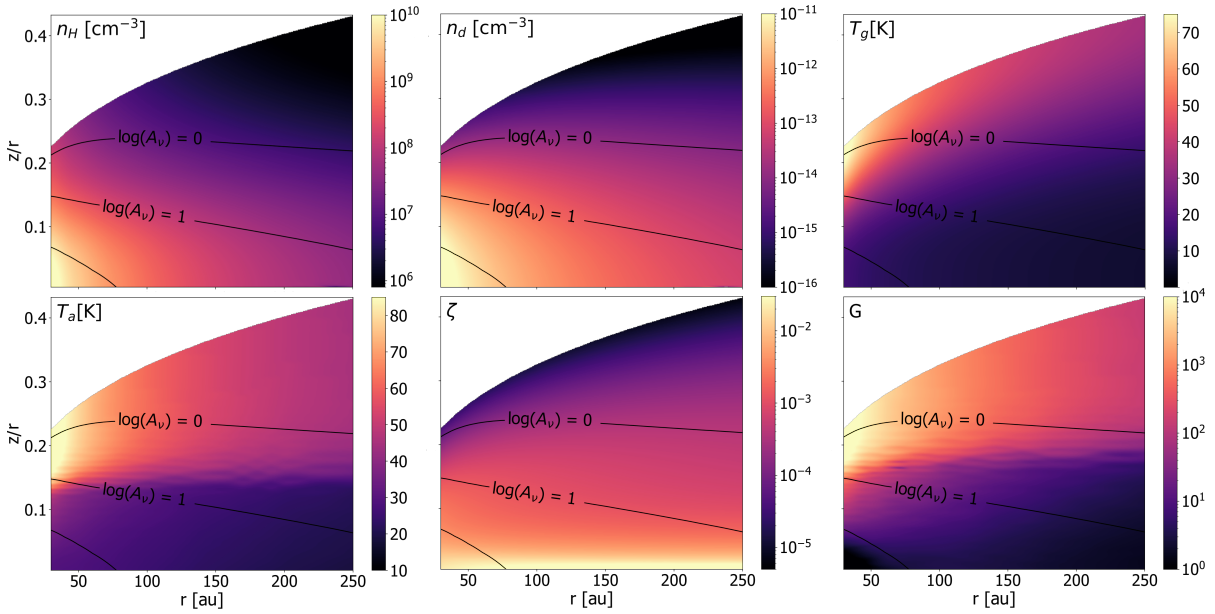

Figure 4.3: Physical structure of the disk model. $T_{\rm g}$ is the gas temperature, $n_{\rm H}$ is the gas number density, G is the local flux in the case of the HUV models (see Chapter. 6), ζ is the dust to gas mass ratio in the case of the multiple grain sizes, $n_{\rm d}$ and $T_{\rm a}$ (see Eq. 6.1) are the dust area-weighted density and temperature, respectively. The solid black lines represent the vertical extinction at $A_\nu = 0$, 1 and 2.

Chapter 5

Coupling radiative transfer to chemistry

Contents

5.1 Introduction: the importance of radiative transfer simulations

UV flux is found in nearly every astrophysical regions, not only in PDR regions but, as we will see, also in disks. The UV photons carry enough energy to photodissociate or photoionize the chemical species present in the disk. These photoprocesses govern the evolution of cooling species abundances and produce ions and radicals that enhance the chemical richness. The UV flux also regulates the grain temperature, which is also an extremely important parameter for chemistry since the grain surface are the major contributors to chemical complexity. Precisely characterizing the UV radiation sources, the UV penetration in the disk and, consequently, the grain temperature as well as the photorates, is therefore paramount to properly study the chemistry evolution. The finest way to do that is by using radiative transfer simulations. In the following, we first explain how the photoprocesses will be characterized in our simulations and then why coupling radiative transfer to chemistry matters.

Definition of the photorates The fundamental parameters that quantify the photoprocess events are the photodissociation and photoionization probability rates, or photorates. The evolution of abundance of a species X due to photoprocesses generated by UV photons in the gas phase is given by a first order differential equation of the form:

$$\frac{dn(X)}{dt} = K_p(Y)n(Y) - K_p(X)n(X) \tag{5.1}$$

where $n(X)$ [cm^{-3}] is the density of species X, $K_p(X)$ [s^{-1}] is the photoprocess rate of species X, $n(Y)$ and $K_p(Y)$ are the density and the photoprocess rate of another species Y, respectively.
Let us now define the photoprocess rate K_p. The relation between photon spectral density u_ν and photon-based intensity is

$$u_\nu = \frac{1}{c} I_{ph}(\nu) \tag{5.2}$$

where $I_{ph}(\nu) = I(\nu)/(h\nu)$ is the photon-based intensity [s^{-1}cm^{-3}nm^{-1}] summed over all angles. The total number of UV photons leading to a photoprocess event per cm^3 per second is then

$$N_p^{ph} = \int_\nu c k_p(\nu) u_\nu d\nu = \int_\nu k_p(\nu) I_{ph}(\nu) d\nu. \tag{5.3}$$

Where the integral is done along the whole line and where $k_p(\nu)$ is the photoprocess coefficient defined as,

$$k_p(\nu) = n_{ph}(\nu)\sigma_p(X,\nu) \tag{5.4}$$

where $n_{ph}(\nu)$ is the number of photons of energy $E = h\nu$ absorbed and $\sigma_p(X,\nu)$ is the photoprocess cross-section. Then, substituting Eq. 5.4 into Eq. 5.3 yields,

$$N_p^{ph} = \int_\nu n_{ph}(\nu)\sigma_p(X,\nu)I_{ph}(\nu)d\nu \tag{5.5}$$

Therefore, the probability $K_p(X)$ [s^{-1}] that a single photon leads to a photoprocess event to a chemical species X can be evaluated as in Heays et al. [2017]:

$$K_p(X) = \int_\nu \sigma_p(X,\nu)I_\nu(\nu)d\nu \equiv \int_\lambda \sigma_p(X,\lambda)I_\lambda(\lambda)d\lambda \tag{5.6}$$

In the case of a protoplanetary disk, for a species X bathed in the UV flux $I_\lambda(\lambda) = I_{\rm L}(\lambda, r, z)$ in a local cell L at cylindrical coordinates (r, z), we write the photorate as,

$$K_p(X,r,z) = \int_\lambda \sigma_p(X,\lambda)I_L(\lambda,r,z)d\lambda. \tag{5.7}$$

This is the equation that we have implemented in the NAUTILUS code.

Coupling radiative transfer simulations to chemistry The definition of photorates given by Equation. 5.7 shows that the evaluation of the photorates at each point in the disk requires to have a precise knowledge of the wavelength-dependent photodissociation/photoionization cross-sections $\sigma_p(X,\lambda)$ for each species X of interest and of the wavelength-dependent local UV flux $I_L(\lambda, r, z)$.

To compute the UV flux, we will use the 3D Monte-Carlo radiative transfer code POLARIS (introduced in Chapter. 6) to perform full radiative transfer simulations of our disk model considering the multiple grain populations (as described in Chapter. 4), so that we obtain a proper local flux in each cell of the disk. This will allow to precisely characterize the temperature of each grain population.

However, the penetration in the disk is attenuated by both the dust and the gas and radiative transfer simulations only consider the extinction by the dust grains and not by the gas, known as self and mutual shielding. The latter can have a significant effect in some parts of the disk and in some wavelength ranges. Moreover, as the chemistry evolves with time, the gas shielding can also change so that the local flux value can evolve with time as well. It is therefore necessary to find a way to add the contribution of the gas to the UV extinction.

This chapter will consist in describing 1) the molecular cross-sections and 2) the solution employed to couple both the dust and gas extinction in order to compute precise time- and wavelength-dependent photorates. Figure 5.1 is a schematic view of the coupling between the radiative transfer and chemistry codes. POLARIS uses the disk physical structure to compute both the size-dependent dust temperature in the disk $T_{\rm d}(a_{\rm k}, r, z)$ and the UV local flux attenuated by the dust opacity $I_{\rm d}(\lambda, r, z)$. These results are presented in Chapter. 6. Then, NAUTILUS uses these outputs to compute the local flux attenuated both by the dust and the gas $I_{\rm L}(\lambda, r, z)$, the photorates $K_{\rm p}(X, r, z)$and then the time-dependent chemical concentrations $X_{\rm mol}(r, z, t)$.

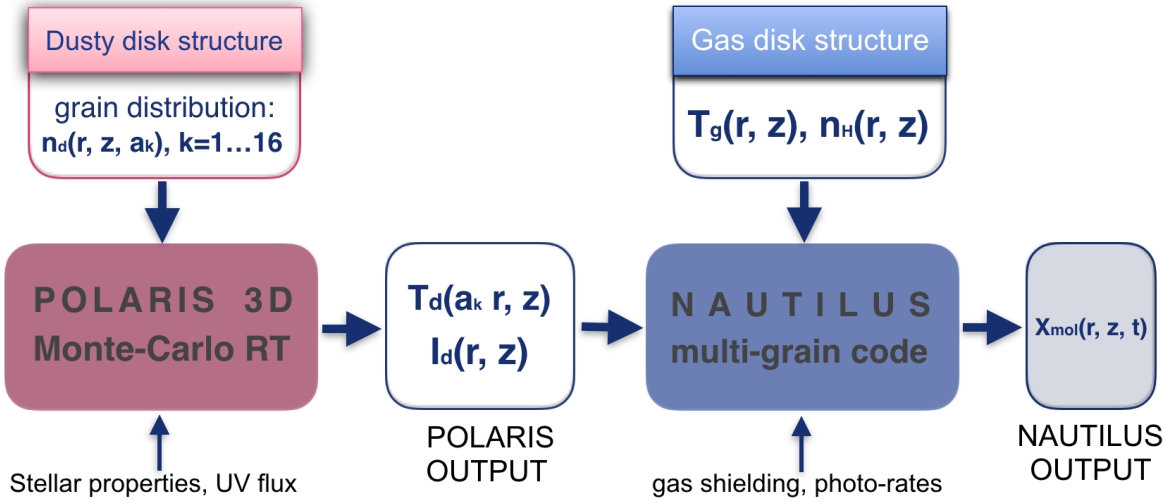

Figure 5.1: Illustration of the pipeline between the radiative transfer code POLARIS and the chemistry code NAUTILUS. POLARIS computes the dust temperature $T_{\rm d}(a_{\rm k}, r, z)$ and the local UV flux $I_{\rm d}(\lambda, r, z)$ using a dust disk structure. NAUTILUS takes as input the POLARIS output coupled with a gas disk structure in order to compute the molecular concentrations as a function of time $X_{\rm mol}(r, z, t)$.

5.2 Wavelength-dependent cross-sections

The wavelength-dependent and space-independent photoprocess cross-section $\sigma_p(\lambda)$ of astronomical relevant molecules are collected from theoretical and experimental studies performed in laboratories. These cross-sections are crucial to describe gas-phase photoprocess events, both to interpret observations and compute abundance evolutions via gas-grain codes.

5.2.1 Properties

When a molecule AB absorbs a UV photon, its excited state can lead to several photoprocess channels, each of which occurring with a certain probability. This includes non-destructive emission $\mathrm{AB}^* \rightarrow \mathrm{AB} + \mathrm{h}\nu$, ionization $\mathrm{AB}^* \rightarrow \mathrm{AB}^+ + \mathrm{e}^-$ or dissociation $\mathrm{AB}^* \rightarrow \mathrm{A} + \mathrm{B}$. The photoionization and photodissociation cross-sections are the product of the photoabsorption cross-section and an ionization or dissociation decay probability. The ratio of the rate constant for a particular process to occur to the rate constant for the total possible processes is called *branching ratio*.

The wavelength-dependence of a cross-section is directly related to the electronic structure of the chemical species. The characterization of the cross-sections according to the wavelength of the absorbed photon is performed either experimentally or via theoretical calculations.

5.2.2 Databases

Public databases have been created to compile photoabsorption, ionization and dissociation cross-sections. We note, among others, the MPI Mainz UV/VIS Spectral Atlas[1], which provides a full set of laboratory photoabsorption cross-sections. Other databases specifically collect astrochemical relevant molecular cross-sections such as the MOLAT[2] and SESAM[3] databases of vacuum-ultraviolet spectroscopy from the Observatory of Paris. For this thesis work, we used the cross-sections of 102 relevant atoms and molecules extracted from the Leiden University database[4] [Heays et al., 2017].

5.2.3 Molecular shielding

While UV photon absorption by dust grains accounts for most of the attenuation at all wavelengths, some molecular species can effectively absorb UV photons at specific wavelengths depending on their respective cross-sections. This absorption process may lead to extinction of the flux at these specific wavelengths, decreasing their own photodissociation rates as well as the ones of other species. This process is called shielding or self-shielding. The reader is referred to van Dishoeck and Black [1988] for a detailed study. We note that H_2, CO and N_2 are the molecules that contributes the most to shielding and self-shielding, even at relatively low column densities relative to H [see Heays et al., 2017] so that the shielding can compete with the dust attenuation in certain areas such as PDRs. Therefore, in all our models, the molecular opacities were computed by only considering these three species. The contribution of the others is negligible and computationally expensive. More details will be given in the next section. Figure 5.2 exhibits the photoabsorption cross-section (left) and the photodissociation cross-section (right) of these three species as a function of the wavelength in the UV domain.

5.3 Approximation of the radiation fields

5.3.1 Sources of radiation fields

We want to define the value $K_d(X)$ of each species involved in the NAUTILUS chemical network at specific time-steps and at every coordinates (r, z) of the disk. The first tricky step is the modelling of the radiation field. As we study disks with a flaring geometry, we assume that the disk surface is exposed to the star radiation. We thus consider two main sources of radiation: the ISRF, that will be computed vertically, and the Stellar Radiation field (SRF). The local photorates will be a result of both the stellar field and the interstellar radiation field. The star is treated as a source point with a radius far smaller than the dimension of the disk.

[1] http://satellite.mpic.de/spectral_atlas
[2] https://molat.obspm.fr/
[3] http://sesam.obspm.fr/
[4] https://home.strw.leidenuniv.nl/~ewine/photo/index.php?file=cross_sections.php

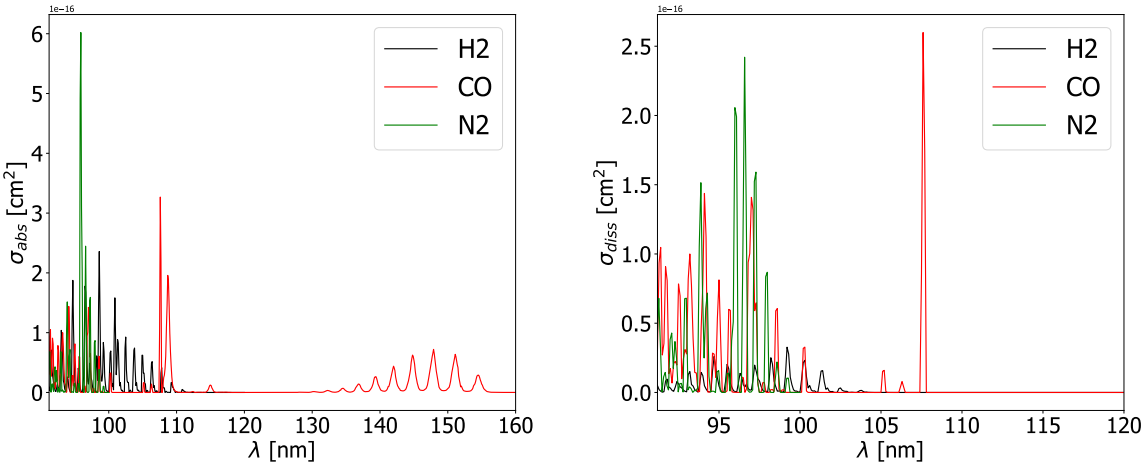

Figure 5.2: cross-sections of H_2, CO and N_2. Left panel: photoabsorption cross-sections. Right panel: photodissociation cross-sections.

5.3.2 Penetration in the disk

We need to describe the penetration into the disk and the attenuation of the radiation field by the dust and gas. This is critical for chemical simulations since characterizing the field in every parts of the disk is necessary to compute the photorates. As mentioned in the previous section, the field is a contribution of stellar and interstellar radiations so that we can write:

$$I_{tot} = I_{ISRF} + I_{*}. \tag{5.8}$$

where I_{ISRF} is the incident unattenuated specific intensity from the ISRF, $I_*(r, z)$ is the spatially diluted incident unattenuated specific intensity from the stellar source.

Figure 5.3 shows the radiation fields received by a point M at coordinates $(r,\ z)$ in a disk structure as defined in our models (see Section 4). The point M is irradiated by the two radiation fields (the ISRF and the SRF). Let us consider Eq. 4.29 to solve Eq. 5.8. By solving independently I_{ISRF} and I_* and by neglecting scattering (we can neglect scattering to evaluate the impact of shielding), we can write in a simple form Eq. 5.8 as,

$$I_L(\nu, r, z) \approx I_{ISRF} e^{-\tau_\nu^V} + I_*(r, z) e^{-\tau_\nu^R} \tag{5.9}$$

where τ_ν^V is the vertical optical depth generated by the disk matter above the local point M at $(r,\ z)$ and τ_ν^R is the optical depth generated by the disk medium lying between the star and the point M. Since the optical depths are a contribution of both dust and gas, we write:

$$\begin{aligned} \tau_\nu^V &= \tau_m^V + \tau_d^V \\ \tau_\nu^R &= \tau_m^R + \tau_d^R \end{aligned} \tag{5.10}$$

where the index m denotes the molecular contribution and d the dust contribution to the attenuation. Equation 5.9 then becomes,

$$I_L(\nu, r, z) \approx I_{ISRF} e^{-(\tau_m^V + \tau_d^V)} + I_*(r, z) e^{-(\tau_m^R + \tau_d^R)} \tag{5.11}$$

This equation gives the value of the total local flux originating from the central source and the ISRF attenuated by the dust and the gas. However, the radiative transfer code can only treat the flux attenuated by the dust, which is of the form:

$$I_d(\nu, r, z) \approx I_{ISRF} e^{-\tau_d^V} + I_*(r, z) e^{-\tau_d^R}. \tag{5.12}$$

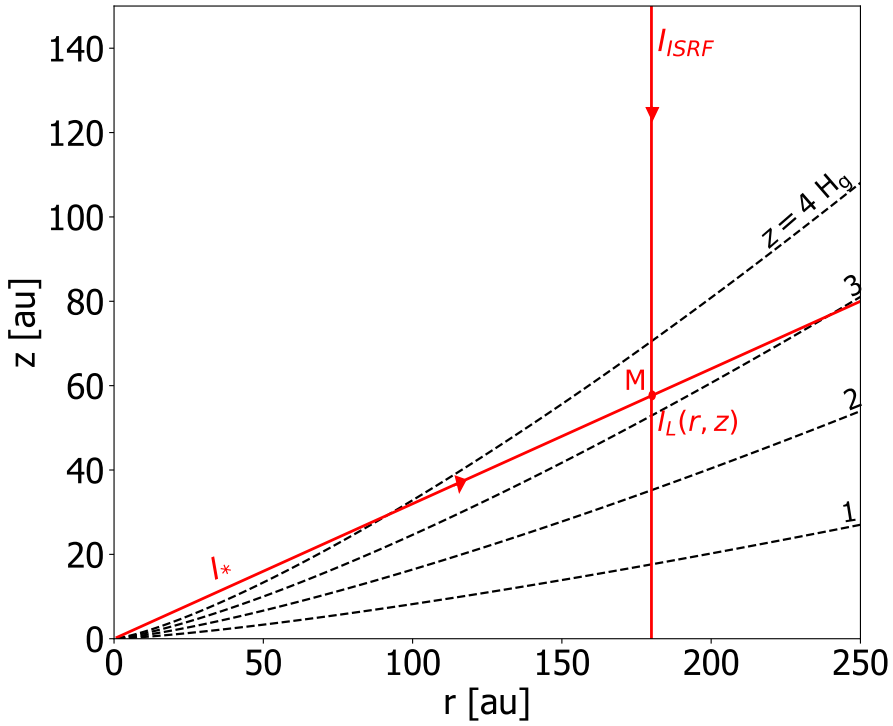

Figure 5.3: Flux received by a point M located at coordinates (r, z).

5.3.3 Approximation of the local flux

POLARIS can solve Eq. 5.12 but for a comprehensive study we need to actually solve the whole Eq. 5.11. While computing the vertical molecular opacity τ_m^V is trivial, characterizing the molecular opacity τ_m^R is much more difficult. Indeed, it requires to know the time-dependent molecular extinction between the star and the considered point whereas the chemical model computes the chemistry in a limited number of discretized radii and a limited number of discretized altitudes. We will simplify this problem by introducing an approximated form of Eq. 5.11.

We introduce the ratio RV defined as,

$$RV = \frac{\tau_m^R}{\tau_m^V}. \tag{5.13}$$

We note that the ratio RV is therefore spatially-, frequency- and time-dependent. By factorizing $e^{-\tau_m^V}$ in Equation 5.11, we can write,

$$I_L(\nu, r, z) \approx e^{-\tau_m^V} \left(I_{ISRF} e^{-\tau_d^V} + I_*(r, z) e^{-\tau_d^R} e^{-\tau_m^V (RV-1)} \right). \tag{5.14}$$

The only problematic component in Eq. 5.14 is the term $A = e^{-\tau_m^V (RV-1)}$. By examining the relative values of τ_m^R and τ_m^V, we can reduce the ratio RV to three limiting cases.

case 1: $\boldsymbol{\tau_m^R \approx \tau_m^V}$ in a few surface layers, $RV \approx 1$, we can write $A \approx 1$ and Eq. 5.14 becomes,

$$I_L(\nu, r, z) \approx e^{-\tau_m^V} \left(I_{ISRF} e^{-\tau_d^V} + I_*(r, z) e^{-\tau_d^R} \right). \tag{5.15}$$

By substituting Eq. 5.12 into Eq. 5.15, it yields,

$$I_L(\nu, r, z) \approx e^{-\tau_m^V} I_d(\nu, r, z). \tag{5.16}$$

case 2: $\boldsymbol{\tau_m^R \gg \tau_m^V}$ Except for a few disk layers (close to the disk surface), RV is always much greater than one as the molecular extinction between the star and the local point is very often much larger than the vertical molecular extinction. In that case, we also can approximate Eq. 5.15 as Eq. 5.16.

case 3: $\boldsymbol{\tau_m^R \ll \tau_m^V}$ Since in most regions of the disk we have $RV \gg 1$, we assume that the case where $RV \ll 1$ almost never occurs (this assumption is intuitive by looking at Fig. 5.3), especially if the disk has a very pronounced flaring geometry. The situation where $RV \ll 1$ is restricted to very narrow surface layers where the molecular opacity is small. Again, Eq. 5.15 can be approximated as Eq. 5.16.

case 4: $\boldsymbol{\tau_m \ll 1}$ We can consider a specific case when both molecular opacities are negligible (for instance when the wavelengths are large). In that case, molecules no longer contribute to the attenuation and the local flux is simply the flux computed by POLARIS as defined in Eq. 5.12 and the approximation Eq. 5.16 still holds true.

Consequently, Eq. 5.15 can reasonably be approximated as Eq. 5.16 in all regions of the disk. This will greatly simplifies the computation of the flux since computing the molecular photorates only requires to know the time-dependent vertical molecular opacity τ_m^V. The resulting flux will be presented in the following chapter.

Chapter 6

The case of low-mass star disk

Contents

6.1 Introduction

It is important to remind that the disk models are not intended to be as realistic as possible but rather aim to explore the influence of the grain size and temperature distributions as described in the previous sections on the chemistry of typical low-mass star disks. The first step was to perform radiative transfer simulations prior to simulate the chemistry to obtain a full dust temperature and local flux. We present the results of these simulations in Section. 6.2. Then, a set of various models were built in order to independently test and compare the influence of several key parameters (grain distribution, grain temperature and H_2 formation rates). Section. 6.3 is dedicated to present a detailed comparison of the different models. Finally, the chemistry results are presented in Sections. 6.4, 6.5, 6.6 and 6.7.

6.2 Radiative transfer results

6.2.1 The 3D Monte-Carlo radiative transfer code POLARIS

In our disk models, the UV flux as well as the grain temperature distribution of each grain size interval throughout the disk are computed using the three-dimensional Monte-Carlo (MC) continuum and line radiative transfer code POLARIS. The code can perform dust heating and complex polarized radiative transfer simulations by handling a full set of parameters (density, temperature, velocity, and magnetic field distributions) [see Reissl et al., 2016, to have a detailed analysis of the POLARIS code].

We assume spherical grains consisting of a homogeneous mixture of 62.5 % of silicate grains and 37.5 % of carbonaceous grains. The scattering and absorption coefficients, based on Mie scattering [Mie, 1908], are computed using the MIEX code [Wolf and Voshchinnikov, 2004] and using optical properties from Draine and Lee [1984] and Laor and Draine [1993].

6.2.2 Radiation source

6.2.2.1 Characterization

The main heating source of the dust grains originates from the interaction with the radiation field penetrating in the disk. Properly characterizing this field is therefore important to compute the dust temperature. The original goal of this work was to build disk models inspired from the Flying Saucer's characteristics. However, as an edge-on disk, it is observationally difficult to characterize the SED of its central T Tauri star. We will exploit the spectra of well-known TTauri stars to reconstruct the assumed spectrum of the Flying Saucer. In particular, we will use the spectrum of TW Hydrae and DM Tau [France et al., 2014] as the intensity of the Flying Saucer's central star is assumed to lie between these two known T Tauri stars. The radiation source is a composition of the central stellar field and the ISRF. Figure. 6.1 shows the different SED used as input for the radiative transfer simulations. The radiation field is computed using 100 logarithmically

distributed wavelengths between 50 nm and 2 mm. The spatial grid involves 300 radii logarithmically spaced by a factor of 1.05 between 1 and 300 au, and 181 angles with the same factor between 0 and π. We present herein the two radiation sources.

Interstellar radiation field The interstellar radiation field is straight-forward to characterize. We consider the SED from Draine1978 between 91.2 nm and 200 nm with the extension of van Dishoeck and Black [1982] for longer wavelengths. The SED is shown by the blue solid line in Fig. 6.1. The illumination is isotropic.

Central field The central stellar source is defined as a typical low-mass pre-main sequence star with a mass of $M_* = 0.58$ M$_\odot$, a luminosity $L_* = 0.75$ M$_\odot$. We assume that the star radiates as a black-body with an effective temperature $T_{*,eff} = 3900$ K. Besides the stellar radiation field, TTauri stars also exhibit a important UV excess originating from the inner disk boundary and accretion shocks on the stellar surface. This UV excess is very wavelength-dependent, with spectral lines like Lyman α having substantial intensities. This excess is not relevant for the dust thermal balance and could be ignored to a good approximation. However, the UV spectrum can strongly affect the chemistry and photo-processes are highly wavelength-dependent. Properly considering this UV excess is therefore necessary. For this reason, the radiative transfer code takes as central radiation input the sum of the stellar black body spectrum (red solid line in Fig. 6.1) and the UV excess typically found in the TTauri stars. The green solid line in Figure. 6.1 shows the sum of the black-body at 3900 K with the UV spectrum shape of TW Hydrae at 1 au [France et al., 2014]. POLARIS thus uses this stellar spectrum (green line), in addition to the ISRF (blue line), to compute the dust temperature and the local flux in each cell of the disk model.

6.2.2.2 Stellar flux before and after molecular shielding

As we have seen in the previous section and in Chapter. 5, POLARIS provides as output the resulting radiation field in all the disk. But this field as computed by POLARIS is only attenuated by the dust grains. In a real disk, the radiation flux also encounters molecular or atomic gas that affect its propagation through the disk, in particular in the UV range (Fig. 5.2).

In chemistry simulations, the effect of molecular and atomic shielding is often estimated using empirical attenuation factors as a function of line-of-sight visual extinction [e.g. Lee et al., 1996]. In this work, we used a slightly more elaborated method which requires to compute the local flux using Equation. 5.16 introduced in Chapter. 5. The term $I_d(\nu, r, z)$ in the right-hand side of the equation is the flux as computed by POLARIS. But computing the real local flux $I_L(\nu, r, z)$ also requires to know the vertical opacity τ_m^V generated by the molecules from outside the disk to the local cell.

Figure 6.2 shows a comparison between the flux (sum of stellar and interstellar radiation fields) attenuated only by the dust (dotted lines) and the flux attenuated by both the dust and the gas (solid lines) for various altitudes ($z = 0$ H$_g$, 2 H$_g$, 4 H$_g$) at 100 au from the star as a function of the wavelength in nm. The flux attenuated by the gas are

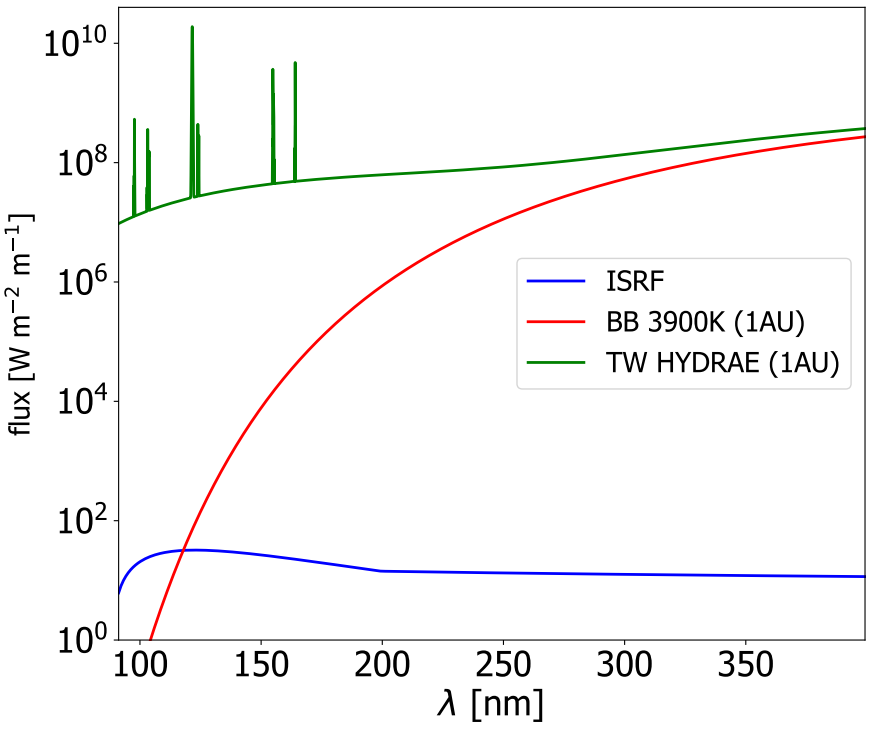

Figure 6.1: SED of the sources used for the radiative transfer simulations in W.m^{-2}.m^{-1}. The solid blue line the the ISRF spectrum from Draine1978 and vanDishoeck+Black1982. The red line is a black-body shape of a central star of effective temperature $T_{*,eff}$ = 3900 K at 1 au. The green line is the spectrum of the TTauri star TW Hydrae at 1 au. We see the excess of UV radiation due to events occurring near the stellar surface.

those of a disk after an integration time of 10^6 years using the chemical code NAUTILUS. At 4 H_g (in the upper atmosphere), the flux is almost not attenuated (the contribution of the gas is negligible). At 2 and 0 H_g, the attenuation by the gas becomes substantial. The attenuation by spectral lines, in particular those of H_2, is clearly visible. We see that the attenuation by the gas occurs only in a narrow range of the UV spectrum ($\lessapprox$ 160 nm), which is consistent with the molecular cross-sections as shown in Figure. 5.2.

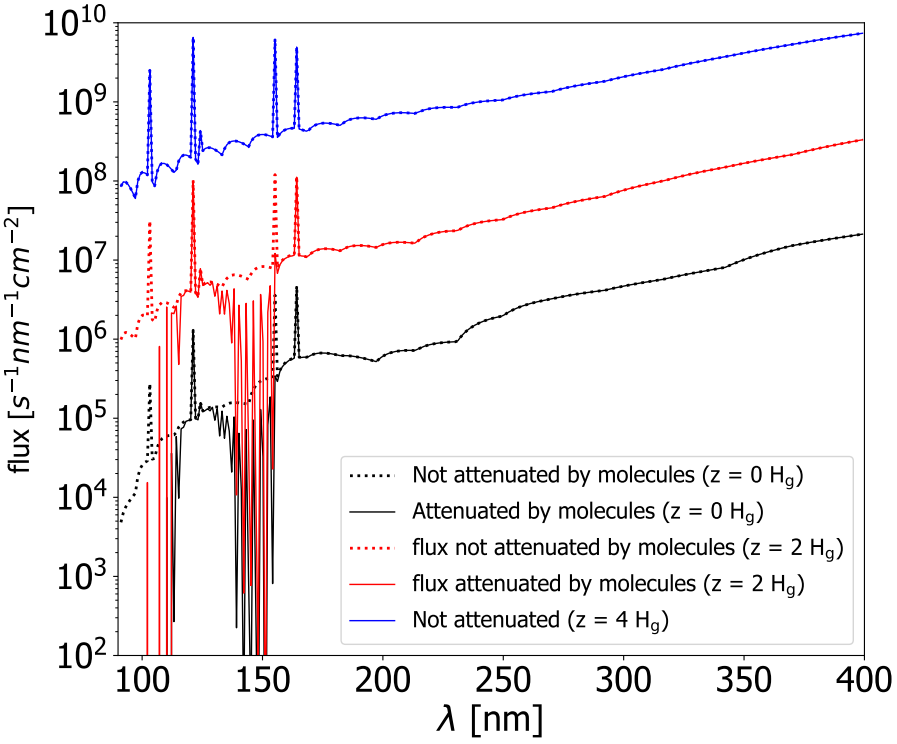

Figure 6.2: Stellar and interstellar fields as a function of the wavelength for various altitudes (z = 0 H_g, 2 H_g, 4 H_g). Dotted lines show the flux attenuated only by the dust. Solid lines show the flux attenuated by both the dust and gas. The flux attenuated by the gas are those of a disk after an integration time of 10^6 years using the chemical code NAUTILUS.

6.2.3 Dust temperature

We applied the radiative transfer simulations to our multi-grain disk model described in Chapter. 4 to compute the dust temperature as a function of a size distribution as in Heese et al. [2017]. In all models, we use the 16 grain size intervals as shown in Table. 4.1. Figure 6.3 shows the vertical temperature profile of all the grain sizes at 100 au from the star. Larger grains are colder than smaller ones. The solid black line is the gas temperature profile $T_g(z)$ as defined by Equation. 4.3. The dashed black line is the averaged value of the dust temperature. With the aim of comparing the multi-grain models with single-grain grain models with equivalent dust temperature, it is convenient

to introduce an area-weighted dust temperature T_a defined as,

$$T_a(r,z) = \frac{\sum_k a_k^2 T_d(a_k,r,z) N(a_k)}{\sum_k a_k^2 N(a_k)}. \tag{6.1}$$

the temperature profile of T_a is shown by the red solid line. All our single-grain models uses T_a as the dust temperature. The dust temperature in the upper layers of the disk strongly depends on the size. At the 100 au (Fig. 6.3), the temperature ranges from 21 K for the coldest grains to 65 K for the hottest ones. On the other hand, the temperature range is much smaller in the mid-plane (7 K to 29 K). The vertical dust temperature suggests that the disk is divided in two separate layers. The temperature profiles remain grossly constant along the altitude above and below $z \approx 2$ H_g. But we see a substantial drop in grain temperature located around $z = 2$ H_g for all grain sizes. This change in temperature is directly linked to the penetration of the UV flux, highlighted by the big solid blue line in Fig. 6.3. Basically, this demonstrates that the disk is divided into an optically thin layer ($z > 2$ H_g) and an optically thick layer ($z < 2$ H_g). See also Figure 4.3 (bottom-right panel), which clearly shows that this two-layer profile is valid throughout the whole disk.

Figure 6.4b shows the dust temperature (red points) in the disk surface (4 H_g) at 100 au for the 16 sizes. Although the grain size generally increases with the grain temperature, the smallest grains are not the hottest ones. Indeed, the temperature increases with size for sizes in the range 0.007 μm to 0.1 μm, then decreases for sizes in range 0.32 μm to 15 μm, and increases again slightly for larger grains.

We can explain this behavior by looking at the blue points on the figure. 6.4b. They show the ratios between the absorption cross-section for wavelengths at which the star radiates (≈ 1 μm) and the absorption cross-section for wavelengths at which the dust re-emits (≈ 20 μm) as a function of the grain size. The ratio of the absorbed to emitted radiation clearly increases up to grain of sizes ≈ 0.1 μm, leading to higher grain temperature, then decreases for larger grains up to 15 μm. The behavior is slightly reversed for grain sizes > 15 μm.

6.3 Model description for chemistry

We want to compare the effect of various parameters on the chemistry evolution in disks. In order to achieve this comparison, we decline our disk model described in the previous chapters in ten different models. These models are presented in Table. 6.1. All models have the same initial physical parameters as seen in Table. 4.2 but each one of them has specificities related to the following four parameters: 1) the dust temperature, 2) the dust size distribution, 3) the radiation field and 4) the B14's H_2 formation process.

The set is divided into two groups: a group using a single grain size distribution, called the single-grain models and another group using the dust distribution as determined in subsection 4.2.2, called the multi-grain models. The reason to operate this way is to allow for a direct comparison of our multi-grain models to more *classical* ones using a single grain size.

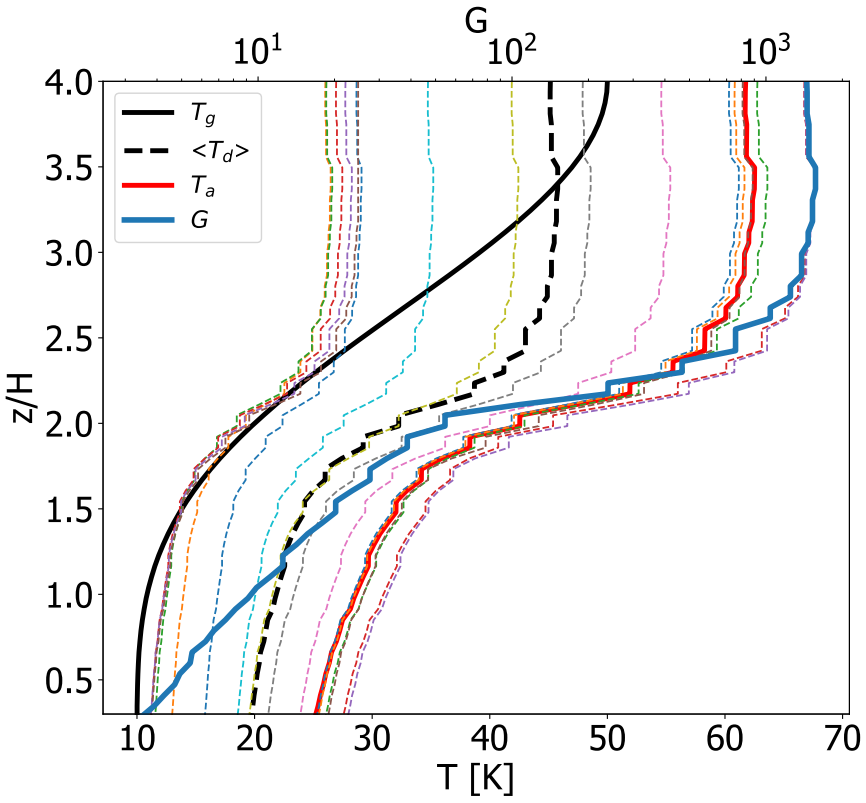

Figure 6.3: Vertical dust temperature profile of the 16 grain size populations (dashed colored lines) located at 100 au from the central star. The solid black line is the vertical gas temperature $T_g(z)$. The dashed black line is the averaged vertical dust temperature. The red solid line the area-weighted dust temperature as defined by Equation. 6.1. The solid blue line highlights the vertical UV flux at 100 au.

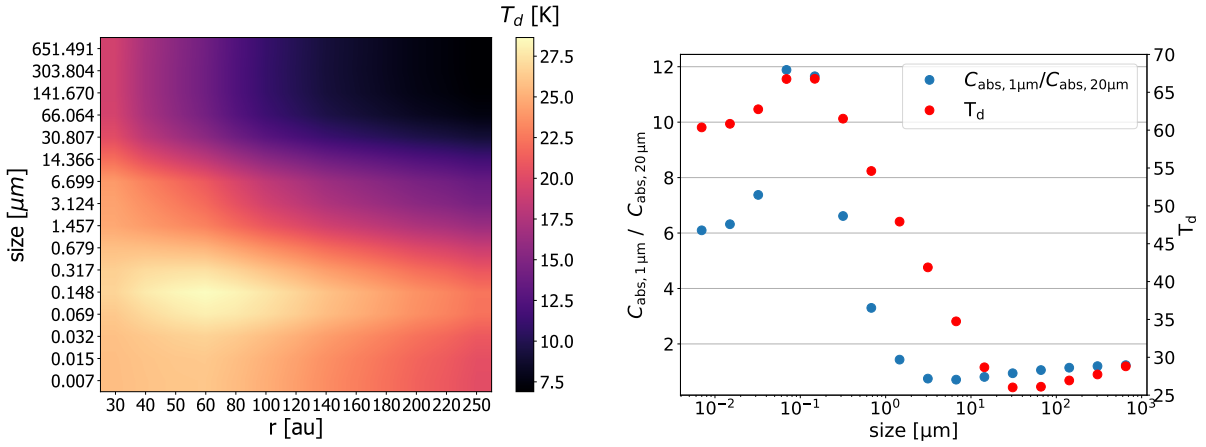

(a) (b)

Figure 6.4: Left: Grain temperature in the disk mid-plane at all computed radii and for all 16 sizes. As expected, bigger grains are colder than smaller ones. We note, however, that the hottest grains are those of size ≈ 0.1 μm. Right: Blue points: ratio of the absorption cross-sections for wavelengths characteristic for stellar radiation ($C_{abs,1\mu m}$) and dust emission ($C_{abs,20\mu m}$). Red points: dust temperature at $r = 100$ au and $z = 4$ H_g. The largest value of ratio is found for grains of size ≈ 0.1 μm, explaining why these grains usually exhibit the largest temperature.

The UV excess originating from the CTTSs, given the strong wavelength-dependence of photo-processes, inevitably affects the chemistry evolution in the disk. As we have suggested in subsection 6.2.2, we adopt two regimes of radiation by using the spectrum of two well-known CTTSs, a relatively high-UV emitting T Tauri star, TW Hydrae and a relatively low emitting one, DM Tau. This is meant to give an indication of the effect of different UV intensities on the chemistry. Models using the spectrum of TW Hydrae are called HUV (high UV) while models using the Spectrum of DM Tau are called LUV. Both FUV spectra are provided in the CTTS FUV spectra database[1] [France et al., 2014].

It becomes necessary at this stage to make some important comments on the implementation of B14's prescription in NAUTILUS (subsection 3.5.4). First, B14's results are calculated with a PDR code using a scaled-up ISRF field. In the situation of our disk model, we will have to estimate the rates after penetration of the flux inside the disk i.e. after extinction by dust and gas. Therefore, the G_0 value is not only decreased but the shape of the spectra is also changed (its hardness decreases...), which will affect the results. It was not contemplated to run the same code as B14 to calculate appropriate rates during the thesis. There is also no simple way to account for the effect of the extinction using these results. To limit the error and to maintain a reasonable approximation on the rates we restrict the implementation of B14's rate in the upper layers of the disk (> 2.5 H_g) only, which is appropriate since this corresponds to the altitudes where the effects of temperature and population fluctuation become substantial. Secondly, B14's calculations assumed a simple power-law size distribution from 1 to 300 nm composed of only carbonaceous grains (amorphous carbon). Changing the dust population would

[1] https://cos.colorado.edu/~kevinf/ctts_fuvfield.html

also require running the code. Again, running the code was not envisaged. However, in NAUTILUS, since we restrict the computation of these rates at high altitudes and that big grains ($\gtrapprox 0.7$ μm) are almost absent because of the settling factor, the grain population is grossly similar to a simple power-law in about the same size distribution as B14. Again, we remind the reader that the main goal of performing simulations of these models is not to be as realistic as possible. In the following, we describe in more details the various models we used, then we present the chemistry results of the simulations with NAUTILUS.

6.3.1 Single-grain models

These models use a single grain population of size 0.1 μm throughout the whole disk. Even though the dust scale height is defined by Equation 4.21, grains of this size virtually exhibit no settling so that these models are equivalent to non-settled dust models (Wakelam+etal2016). Consequently, we can assume that the vertical density profile of the dust follows that of the gas with a dust to gas mass ratio of $\sim 1/100$ everywhere. In the following, the term x in the model names denotes either H for high or L for low.

Model 1: xUV-LH-T_g: In this model, the dust temperature profile follows that of the gas temperature T_g given by the solid black line in Figure 6.3, meaning that the dust temperature T_d is equal to T_g in the whole disk. Top right panel of Figure 4.3 is therefore the dust temperature 2D distribution of this model. Depending on whether the stellar UV field is high (HUV) of low (LUV), Model 1 is either called HUV-LH-T_g or LUV-LH-T_g.

Model 2: xUV-LH-T_a: This single-grain model is similar to Model 1 except for the dust temperature. Model 2 uses the area-weighted dust temperature T_a given by Equation 6.1 (solide red line in Fig. 6.3). Bottom left panel of Figure 4.3 represents the dust temperature 2D distribution of this model. As T_a is sgnificantly higher than T_g, we expect molecular depletion to occur at lower altitudes than in Model 1.

Model 3: xUV-B14-T_a: This model is similar to Model 2 but in addition we add the B14 treatment of the H_2 formation rate. The expected result in this model is thus a higher production of H_2 in the PDRs layers than in Model 1 and 2.

6.3.2 Multi-grain models

As opposed to single-grain models, all the multi-grain models use the full dust distribution, consisting of the 16 grain sizes [0.007 μm, 651 μm]. Each grain population has a specific surface temperature and settling factor. See subsection 4.2.2 for a full description. Each population is chemically active and takes into account the surface processes described in Chapter. 3.

Table 6.1: We compute a total of ten models. Six single-grain models, consisting of a single grain size (0.1 μm) and four multi-grain models consisting of a full grain size and temperature distribution. HUV stands for high UV field and LUV for low UV field. We write LH for the classical treatment of the Langmuir-Hinshelwood mechanism and B14 when the formalism of Bron et al. [2014a] is used. T_g means that the dust temperature equals to that of the gas, T_a is the weighted-area dust temperature as defined by Equation. 6.1. T_i is the temperature of i^{th} grain population. M stands for multigrain model. For instance, the model M-HUV-B14 is a multi-grain model computed using B14's method with a high UV field.

	bins	**sizes (μm)**	**T_d**	**HUV**	**LUV**	**H_2 formation**
HUV-LH-T_g	1	0.1	T_g	✓		LH
HUV-LH-T_a	1	0.1	T_a	✓		LH
HUV-B14-T_a	1	0.1	T_a	✓		B14
LUV-LH-T_g	1	0.1	T_g		✓	LH
LUV-LH-T_a	1	0.1	T_a		✓	LH
LUV-B14-T_a	1	0.1	T_a		✓	B14
M-HUV-LH	16	$[5.10^{-3} - 10^3]$	$T_{k\ \{k=1...16\}}$	✓		LH
M-HUV-B14	16	$[5.10^{-3} - 10^3]$	$T_{k\ \{k=1...16\}}$	✓		B14
M-LUV-LH	16	$[5.10^{-3} - 10^3]$	$T_{k\ \{k=1...16\}}$		✓	LH
M-LUV-B14	16	$[5.10^{-3} - 10^3]$	$T_{k\ \{k=1...16\}}$		✓	B14

Model 4: M-xUV-LH: This multi-grain model uses the full dust size and temperature distributions but does not consider the B14 prescription.

Model 5: M-xUV-B14: The B14 prescription is used in this model, as opposed to Model 4. This model, with grain growth, dust settling, a grain temperature and size distribution and the H_2 formation rate derived from B14 is our most sophisticated model.

6.3.3 Chemistry simulation setup

The chemical abundances in the disks are calculated using the time-dependent equation embedded in NAUTILUS Section. 3.4. All our models 1) use the atomic initial abundances as presented in Table. 6.2 to initiate chemical simulations 2) all the chemical output are extracted after an integration time of 5.10^6 years 3) incorporate the same chemical network and chemical processes described in Chapter. 3.

Important chemistry results are presented in Sections. 6.4, 6.5, 6.6 and 6.7. Most results will be presented at the reference radius i.e. 100 au. The chemical abundances are all given relatively to the number of hydrogen atoms (H + 2× H_2).

6.3.4 Validation of photorates calculation in the models

To validate the calculation of photorates using the formalism of cross-section (described in Chap. 5), we can estimate the probability of photo-dissociation of unshielded H_2 under

Table 6.2: Adopted elemental initial abundances relative to H.

Element	abundance (relative to H)	mass (amu)
H_2	0.5	2.00
He	9.0(-2)	4.00
C	1.7(-4)	12.00
N	6.2(-5)	14.00
O	2.4(-4)	16.00
Si	8.0(-9)	28.00
S	8.0(-8)	32.00
Fe	3.0(-9)	56.00
Na	2.0(-9)	23.00
Mg	7.0(-9)	24.00
Cl	1.0(-9)	35.00
P	2.0(-10)	31.00
F	6.7(-9)	19.00

the interstellar radiation field and compare it with a reference value. Using the flux given by POLARIS we find $K_{\mathrm{d0}}(H_2) = 7.1 \times 10^{-11}$ [s^{-1}]. We choose to compare it with the reference value given by Sternberg et al. [2014] equals to 5.8×10^{-11} [s^{-1}]. We note that the value given by the cross-section formalism is slightly larger than the value from Sternberg et al. [2014] but both values are sufficiently similar to validate the photorates.

6.4 General dependence of chemistry on disk parameters

We first discuss the global results of all models, in particular the global effects of the dust temperatures, flux intensity and B14's prescription.

6.4.1 Effect of the two flux regimes: HUV and LUV

Our disk models received two intensities of radiation fields (HUV and LUV). Table 6.3 and 6.4 show the vertically integrated column densities [cm^{-2}] of hydrogen, molecular hydrogen and a set of simple observed molecules in disks (i.e. CO, CS, and CN). Comparing the two tables reveals that, for a given species and a given model, 1) the column densities all have the same order of magnitude whether the flux is high (HUV) of low (LUV) 2) but the values are not exactly equal (e.g. n(CO) = 3.24×10^{17} in HUV-LH-T_g and n(CO) = 4.11×10^{17} in LUV-LH-T_g). These small differences are directly related to the UV flux intensity that affects differently the PDR regions of the disk whether the flux is high or low. This can be seen by comparing Figures. A.1 with B.1 and A.2 with B.2, where the most noticeable discrepancies between the profiles of a given species lies within the range [3 H_g, 4 H_g], which grossly represents the PDRs layers of the disk. This is mostly explained by the change in the location of the H/H_2 transition. For instance, the H/H_2 transition occurs at a higher altitude ($z \approx 3.5$) in the case of M-LUV-LH than in the

case of M-HUV-LH ($z \approx 3$). Therefore, this change in transition impacts the chemistry. Typically, we find more CO in all LUV models than in HUV because the shielding of H_2 is more efficient in LUV models, enabling more CO to be formed. We note that the column density of CS is one order of magnitude larger in M-LUV-B14 than in M-HUV-B14.

We see that the effect of the different UV intensity is globally limited to the upper layers of the disk. Indeed, once the UV flux is sufficiently attenuated deeper in the disk to allow effective routes to H_2 formation in both HUV and LUV regimes, the chemistry in both cases becomes the same. Because of this limited impact of the flux, we assume that most of the analysis of HUV models can be considered valid for the LUV ones. To simplify the study, we will mainly focus the discussion on the HUV models and will refer to the LUV models if required.

Table 6.3: Column densities [cm^{-2}] of main molecules at 100 au for the HUV models. Last three columns summarize the main properties of the model with respect to the H_2 formation and grains (% of grains, in sites, with a temperature above 20 K between 0 and 1.5 H and 1.5 and 2.5 H).

	H	**H_2**	**CO**	**CS**	**CN**	H_2 formation	0 to 1.5 H	1.5 to 2.5 H
HUV-LH-T_g	$1.48.10^{21}$	$8.19.10^{22}$	$3.24.10^{17}$	$4.40.10^{12}$	$3.79.10^{13}$	"cold" grains	0%	25%
HUV-LH-T_a	$9.80.10^{21}$	$7.78.10^{22}$	$1.01.10^{18}$	$3.38.10^{12}$	$3.08.10^{12}$	more H	100%	100%
HUV-B14-T_a	$3.20.10^{20}$	$8.25.10^{22}$	$1.46.10^{18}$	$1.35.10^{11}$	$1.34.10^{13}$	less H	100%	100%
M-HUV-LH	$8.26.10^{21}$	$7.86.10^{22}$	$7.46.10^{16}$	$6.69.10^{13}$	$4.62.10^{13}$	more H	96%	99%
M-HUV-B14	$1.32.10^{20}$	$8.26.10^{22}$	$9.02.10^{17}$	$1.92.10^{14}$	$3.49.10^{14}$	less H	96%	99%

Table 6.4: Column densities [cm^{-2}] of main molecules at 100 au for the LUV models.

	H	**H_2**	**CO**	**CS**	**CN**
LUV-LH-Tg	$9.70.10^{20}$	$8.22.10^{22}$	$4.11.10^{17}$	$2.34.10^{12}$	$1.01.10^{13}$
LUV-HL-Ta	$7.89.10^{21}$	$7.87.10^{22}$	$1.21.10^{18}$	$3.75.10^{12}$	$1.87.10^{12}$
LUV-B14-Ta	$9.68.10^{19}$	$8.26.10^{22}$	$1.47.10^{18}$	$2.96.10^{11}$	$2.25.10^{13}$
M-LUV-LH	$6.70.10^{21}$	$7.93.10^{22}$	$1.79.10^{17}$	$3.55.10^{13}$	$5.87.10^{13}$
M-LUV-B14	$1.34.10^{19}$	$8.27.10^{22}$	$1.15.10^{18}$	$1.32.10^{13}$	$4.67.10^{13}$

6.4.2 Dust temperature dependence on the mid-plane chemistry

Unlike the PDR layers, the mid-plane chemistry is not dependent on the two regimes of UV flux. Indeed, as mentioned in the previous section, the UV flux is sufficiently attenuated in the HUV and LUV models for the chemistry to be similar in both cases. Moreover, B14's prescription is not triggered near the mid-plane since the dust temperature is low enough to efficiently form H_2 via the usual LH mechanism in all models. As a consequence, the only parameters (among the four) that should affect the chemistry is the

dust temperature and size distribution. This is demonstrated by the simulation results which show that only the dust temperature and size distribution change the chemistry from a model to another.

In the case of the single-grain models (see Figs. A.1 and B.1), all models using the same grain temperature ($T_d = T_g$ or T_a), regardless of the flux regime, have the same vertical profile at altitudes $z < 1.5$ H_g. Similarly, since all multi-grain models use the exact same grain temperature and size distribution, they all exhibit the same vertical molecular density profile at altitudes $z < 1.5$ H_g (for a given species) regardless of the incident flux and the use of B14's prescription. Figure 6.5 shows the example of carbon monoxide CO in HUV multi-grain models. The solid red line denotes the altitude ($z \approx 1.5$ H_g) below which the vertical density profile is identical in all models. The main consequence is that the difference in column density between the various models is the results of what is occurring above this threshold altitude.

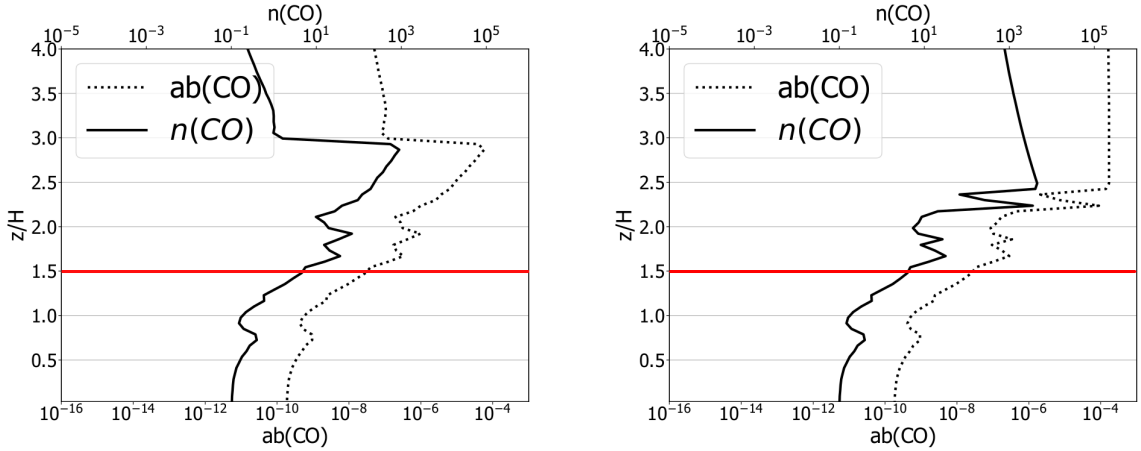

(a) M-HUV-LH (b) M-HUV-B14

Figure 6.5: Vertical profiles of CO at 100 au from the star of the HUV multi-grain models. The solid line is the number density [cm^{-3}] and the dashed line is the abundance relative to the total number of H atoms. We see that under the altitude $z \approx 1.5$ represented by the solid red line, the profile of both models is the same. This is true for most other molecules (see Figs. A.1 and A.2).

6.4.3 Effect of dust temperature and B14's formalism on the upper layers

Effect of dust temperature Single-grain models are divided into "hot"-grain models ($T_d = T_a$, see HUV-LH-T_a and HUV-B14-T_a) and one "cold"-grain model ($T_d = T_g$, see HUV-LH-T_g). As expected, the shift in the H/H_2 transition occurs closer to the disk surface in HUV-LH-T_g than in the hot-grain models. The formation rate of H_2 is inversely related with the dust surface temperature so HUV-LH-T_g produces more H_2 in the upper layers and the remaining amount of H is thus decreased. Indeed, the gas temperature remains relatively low at every altitude so using $T_d = T_g$ implies a partially

efficient formation of H_2 even close to the disk surface. This is clearly demonstrated by Figure 6.6 which shows the vertical profile of hydrogen at 100 au for the single-grain models. We see that in HUV-LH-T_a the quantity of H remains important at low altitudes because the dust temperature remains too high to efficiently produce H_2 as compared with HUV-LH-T_g. The multi-grain models (see Fig. A.2), on the other hand, all use the same dust temperature distribution so there is no possible relevant comparison within these models. But it appears clear that the H/H_2 transition in M-HUV-LH (M-LUV-LH) is very similar to the transition in HUV-LH-T_a (LUV-LH-T_a) (see middle and right panel of Fig. 6.6). This similarity is mainly due to the dust settling prescribed in the multi-grain models. Indeed, in these models, the "cold" grain populations are more settled toward the mid-plane (because of their larger stopping time) and are mostly absent at high altitudes, meaning that only the small 'hot' grains (producing low amount of H_2) regulate the chemistry in the upper layers.

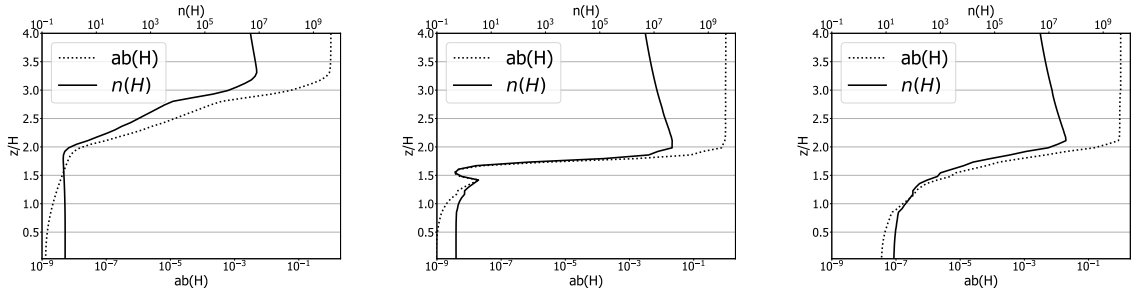

(a) HUV-LH-T_g (b) HUV-LH-T_a (c) M-HUV-LH

Figure 6.6: Vertical profiles of hydrogen at 100 au from the star of two HUV single-grain models (left and middle panels) and of the multi-grain model M-HUV-LH (right panel). The solid line is the number density $[cm^{-3}]$ and the dashed line is the abundance relative to the total number of H atoms.

Effect of B14's prescription The models adopting the formalism of B14 produce, as expected, more gas-phase H_2 in the upper layers ($z > 2.5$ H_g) than the other models. Figure 6.7 shows the vertical profile of H_2 for the HUV multi-grain models. In M-HUV-B14, we see that considering H_2 formation rates that takes into account the fluctuations of surface temperature and population produces a large amount of H_2, so that the abundance of H_2 is near 0.5 at all altitudes, even in the PDR regions.

6.5 Global HUV model comparison of common observed molecules: the case of CO, CS and CN

Tables. 6.3 and 6.4 reveal that there is no simple trend to extract from column densities. In this section, we try to explore and to understand the influence of each model on the formation of simple commonly observed molecules in disks. We consider the case of CO, CS and CN and use Tables. 6.3 and 6.4 and Figures. A.1 and A.2 for the analysis.

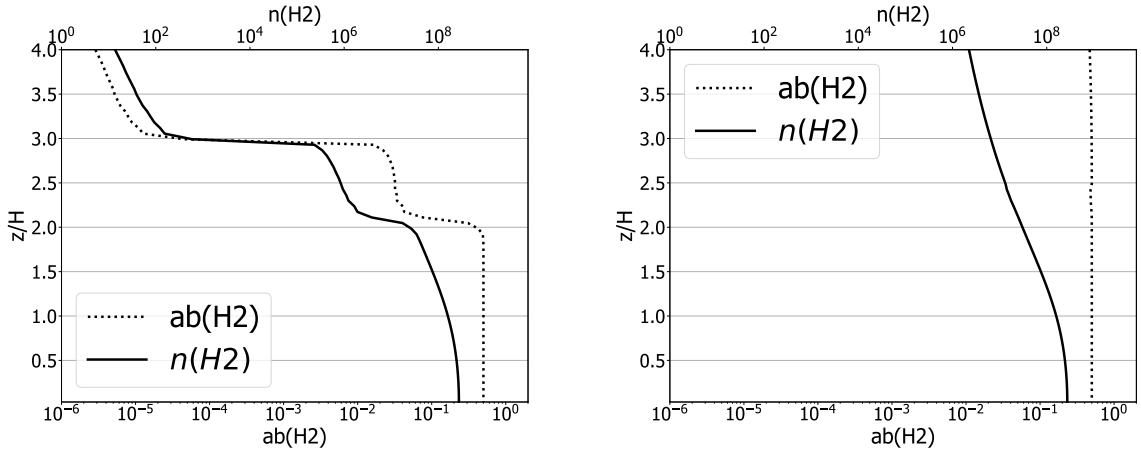

(a) M-HUV-LH (b) M-HUV-B14

Figure 6.7: Vertical profiles of H_2 at 100 au from the star of the HUV multi-grain models. The solid line is the number density $[cm^{-3}]$ and the dashed line is the abundance relative to the total number of H atoms.

6.5.1 Gas-phase CO

Before investigating the gas-phase CO, it is to be noted that 1) CO is formed in the gas-phase 2) is sensitive to photodissociation and 3) has a small binding energy $E_{\rm bind}(CO)$ = 1300 K [Minissale et al., 2016]. It is therefore not surprising that LUV-B14-T_a is the model that produces the largest gas-phase CO column density as it combines a low UV flux, a large column density of H_2 produced using the B14's formalism and that shields CO from the UV flux and a high dust temperature everywhere which decreases the efficiency of CO absorption on grains. Conversely, M-HUV-LH is the model that produces the smallest CO column density. This model combines the HUV flux, more penetration of the UV due to the dust settling and a low formation rate of H_2. More globally, 1) LUV models produce more CO than their HUV counterparts because CO is less photodissociated in the upper layers 2) models using B14 produce more gas-phase CO than their LH analogous because CO is more efficiently shielded by the large amount of H_2 in the upper layers of the B14 models 3) more significantly, the adsorption rates of CO are more efficient in the "cold" single-grain model HUV-LH-T_g than in all the other models since the dust temperature in HUV-LH-T_g (LUV-LH-T_g) is globally lower than in the others. Thus HUV-LH-T_g and LUV-LH-T_g have a small column density of CO.

Single-grain VS multi-grain models: The flux penetration in multi-grain models is slightly larger than in the single-grain models so CO is globally more photodissociated in the upper layers of the multi-grain models than in the single ones. The depletion of CO at $z \leq 1$ H_g is less important in multi-grain models than in single-grain ones. The reason is due to the dust temperature that is low enough in single-grain models for CO to freeze-out while there is always a fraction of abundant small gains whose temperature remains high enough to decrease the absorption efficiency of CO in multi-grain models.

6.5.2 Gas-phase CN

In all our models, the major reactions that produce gas-phase CN in the upper layers at 100 au are the following gas-phase bimolecular reactions: $N + C_2 \rightarrow C + CN$ (69%) and $N + CH \rightarrow H + CN$ (22%). Then, we also see that CH is mostly destroyed by the reaction $H + CH \rightarrow C + H_2$, meaning that less H implies less available CH to form CN. Or, said otherwise, more H_2 implies more CN. Therefore, we have to investigate parameters that affect the formation of H_2 i.e. dust temperature and B14's formalism. In single-grain models, the trend is clear in the upper layers. Figure A.1 shows that CN in HUV-LH-T_g becomes more abundant at high altitudes (3 - 4 Hg) than in HUV-LH-T_a because HUV-LH-T_g produces H_2 more efficiently. The effect is even more pronounced by comparing HUV-LH-T_g with HUV-B14-T_a. We note that this effect is less obvious in the multi-grain models (A.2).

Globally, Table. 6.3 shows that, increasing the dust temperature decreases the column density of CN by one order of magnitude (see HUV-LH-T_g vs. HUV-LH-T_a) while forcing the formation of H_2 re-boosts the formation of H_2 and therefore of CN (see HUV-LH-T_a vs. HUV-B14-T_a and M-HUV-LH vs. M-HUV-B14).

6.5.3 Gas-phase CS

The major reactions that lead to the formation of gas-phase CS in the upper layers of all models is a sequence of a bimolecular reaction and a dissociative recombination reaction: $H_2 + CS^+ \rightarrow H + HCS^+$ and $HCS^+ + e^- \rightarrow H + CS$. This sequence is dependent on the presence of H_2 so, as for CN, more H_2 implies more CS. Moreover, the binding energy of CS being relatively low ($E_{\rm bind}(CS) = 1900$ K), CS will freeze out onto grain surface at relatively high altitudes so that the gas-phase abundance of CS will results in the competition between gas-phase production and the sticking rates.

Single-grain models In HUV-LH-T_g (LUV-LH-T_g), the grain temperature is low enough to start producing a large amount of H_2 at high altitudes, resulting in a broad peak (between ~ 2 to $3\,H_g$). Then, below $z = 2$ H_g, CS starts to freeze out, explaining the dramatic drop of CS density (Fig. A.1 (a)). In HUV-LH-T_a, on the other hand, the dust temperature remains too high to effectively produce H_2 above ~ 2 H_g. Then, because of the steep temperature slope around $z = 2$ H_g (see red line in Fig. 6.3), the CS density dramatically increases before rapidly decreasing as dust temperature becomes low enough for CS to freeze out. This results in the very narrow CS abundance peak at $z \sim 1.8\,H_g$ in seen in Figure A.1 (b). In HUV-B14-T_a, the H_2 formation in the upper layers is very efficient because of the use of B14's formalism so that CS abundance is two orders of magnitude larger than in HUV-LH-T_g and HUV-LH-T_a in the disk surface (Fig. A.1 (c)). However, since HUV-B14-T_a does not exhibit any peak around $z = 2$ H_g, the total CS column density is smaller than in the other single-grain models.

Multi-grain models The chemical scheme is roughly the same as for the single-grain models. However, we note important differences in CS vertical profile at $z < 2$ H_g,

which is clearly highlighted by Table. 6.3 where the CS column density of the multi-grain models is systematically larger than that of the single-grain ones. This larger CS column density is due to the dust temperature distribution in the multi-grain models, where a significant fraction of the grain surface areas remains too hot for CS to freeze out (all grain populations on the right side of the red line in Fig. 6.3), even at low altitudes, resulting in a larger quantity of gas-phase CS than in the single-grain models.

6.6 mid-plane chemistry

6.6.1 Reservoirs

We explore here the total atomic reservoirs of C, N and O both in the gas-phase and on the grain surfaces in the mid-plane of the disk. All species that have been investigated represent at least 0.5 % of the total quantity of carbon, nitrogen or oxygen. The results are shown in Figure 6.8. We can decrease the space parameter of the study by using the following simplifications. 1) As the relative importance between reservoirs is roughly constant along the distance to the star, we study the reservoirs at the reference radius only. 2) As previously discussed, the chemistry below $z = 1.5\,\mathrm{H}$ is unchanged from a model to another under the same dust temperature. Therefore, it is sufficient to discuss HUV-LH-T_g, HUV-LH-T_a and M-HUV-LH only.

Carbon-bearing species Figure 6.8 (top) shows that frozen CO_2 is the main carrier of carbon, both in HUV-LH-T_a and M-HUV-LH with 58.1% and 51.3% of elemental carbon, respectively, while the quantity of CO_2 is negligible relative to the other species in HUV-LH-T_g. The reason is the dust temperature that is too high in these two models to allow for a large quantity of hydrogen to successively hydrogenate the frozen atomic oxygen to form water. Instead, the atomic oxygen easily diffuses on the surface and the relatively high temperature allows to overcome the activation barrier to rapidly form CO_2 by reacting with the frozen CO. In HUV-LH-T_g, on the other hand, Figure 6.8 (top) show that the main carrier of carbon is CH_4 with 49.1%. Initially, just like in HUV-LH-T_a and M-HUV-LH, CO easily freezes onto the grain surface. However, in HUV-LH-T_g, the hydrogenation of CO is more efficient and CO is channeled to CH_3OH through several hydrogenation sequences. Then, the photo-dissociation of CH_3OH leads to the formation of CH_4. The other main carrier of carbon is the complex organic species CH_3OH, which holds about 10% of total carbon.

Oxygen-bearing species Frozen CO_2 is the main carrier of oxygen in HUV-LH-T_a and M-HUV-LH with 82.0% and 72.5%, respectively (Fig. 6.8, bottom), for the exact same reasons given above for the carbon-bearing species. In HUV-LH-T_g, on the other hand, H_2O is by far the largest carrier of oxygen with 76.4%. Again, in HUV-LH-T_g, the other main carrier of oxygen is the complex organic species CH_3OH, which also holds about 10% of total oxygen.

Nitrogen-bearing species Nitrogen is mostly in the form of N_2 in M-HUV-LH (67.8%) and in HUV-LH-T_g (32.4%) (Fig. 6.8, middle) . Moreover, inside each model, the gas-phase abundance of N_2 is noticeably larger than the one of the other species. The reason for that is a combined effect of the faster conversion of atomic nitrogen into N_2 in the gas-phase compared to the depletion of N and the high grain temperature that prevents N_2 from depleting onto the surfaces. Indeed, The binding energy of N_2 ($E_b(N_2) = 1100\,K$ on amorphous water ice surface) is smaller than most of the other molecules and slightly smaller than that of CO [Minissale et al., 2016, Wakelam et al., 2017] so that N_2 is retained more efficiently in the gas. We note that, given the low dust temperature, the gas-phase abundance of N_2 in HUV-LH-T_g is the smallest of all models. In HUV-LH-T_a, N_2 is still the main carrier of nitrogen but remains in the gas-phase because of the large dust temperatures. On the grains, NH_3 is the main carrier of nitrogen with 42.7% of the elemental nitrogen. Therefore N_2 is expected to be the carrier of nitrogen in the disk mid-plane but remains mostly in the gas-phase in hot grain models. The other main carriers of nitrogen are HCN (29.2% in HUV-LH-T_g, 12.3% in HUV-LH-T_a) and CH_2NH_2 (22.9% in HUV-LH-T_a, 8.3% in HUV-LH-T_g).

Main conclusions In the mid-plane, disks composed of cold grains have their carbon and oxygen reservoirs locked in CH_4 and H_2O, respectively, while disks composed of hot grains have both their carbon and oxygen reservoirs locked in CO_2. This demonstrates here the major role of the grain temperature on the surface chemistry. As for the nitrogen, it appears more difficult to draw a conclusion on the reservoirs regarding the dust temperature.

6.6.2 Surface chemistry

We further investigate the surface chemistry in the mid-plane of the same three models. In particular, for the multi-grain models, we explore the grain size- and temperature-dependence on the surface abundance of five molecules of particular interest i.e. CO, CO_2, CH_4, H_2S and NH_3. The study is performed at three well-spaced radii: 30, 100 and 200 au. Figure 6.9 presents the surface abundance per total atomic hydrogen for various molecules at the final stage of time evolution i.e. 5.10^6 yrs as a function of the grain radius a and their temperature in the mid-plane of the disk. The crosses, the square markers, and the round markers stand for the multi-grain model at 30 au, 100 au and 200 au respectively. The triangle pointing upward represents the surface abundance in the single-grain model HUV-LH-T_g and the triangle pointing downward represents the abundance in the model HUV-LH-T_a, both at 100 au.

6.6.2.1 Carbon- and oxygen-bearing molecules: CO, CO_2 and CH_4

As seen in subsection 6.5.1, CO is essentially formed in the gas-phase prior to being adsorbed onto grain surfaces. The binding energy of CO is relatively small. Therefore, given the dust temperature range ($\sim$ 7 to 26 K) in the mid-plane, the abundance of sCO will greatly depend on the dust temperature. 6.9 (top-left) shows the abundance of sCO

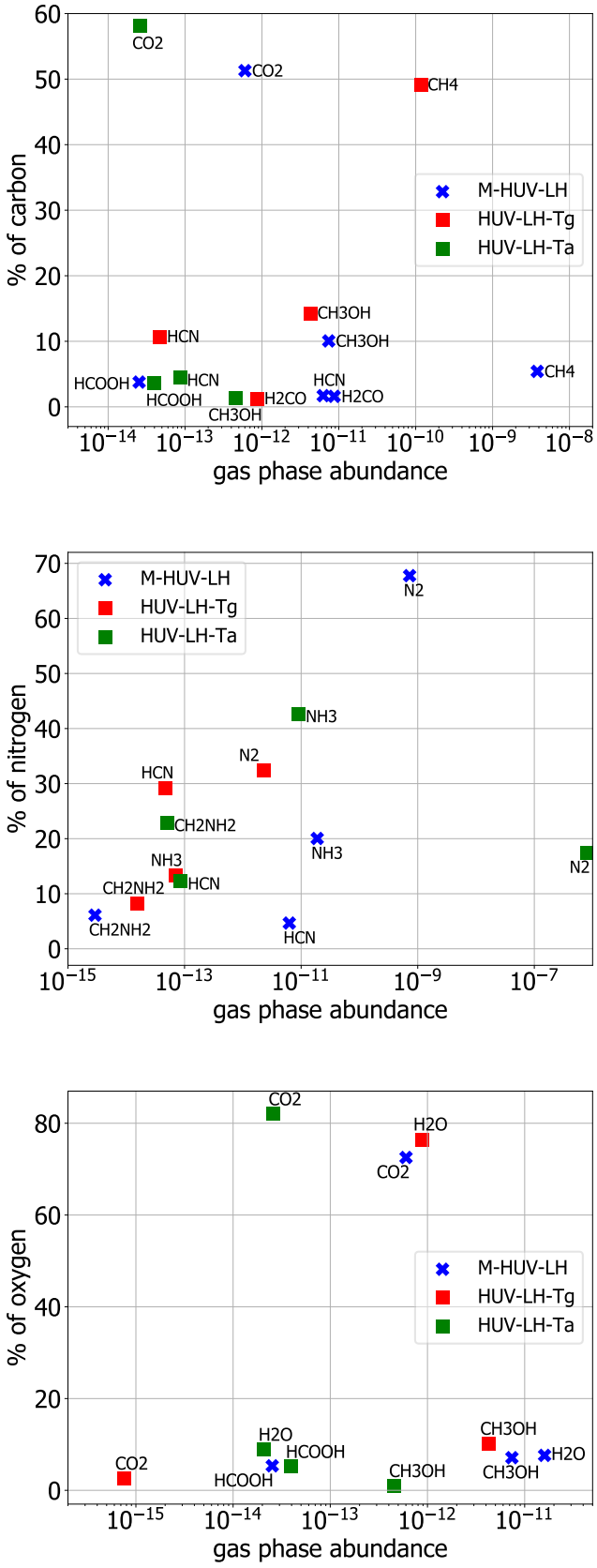

Figure 6.8: Species that contains at least 0.5% of elemental carbon (top), nitrogen (middle) and oxygen (bottom) in the mid-plane at 100 au: percentage of the carbon/nitrogen/oxygen locked in the species as a function of the gas-phase species abundance.

as a function of the grain size. We see an obvious separation around the grain size 1 μm at all radii. The thermal desorption rate is low on the large colder grains (size $>$ 1 μm) so that CO remains locked on the mantle. Conversely, sCO can overcome the desorption barrier and efficiently desorb on small hot grains (size $<$ 1 μm), resulting in small abundances of sCO on theses grains. Moreover, once on the surface, CO will chemically react to form other molecules, in particular CO_2.

Unlike CO, the binding energy of CO_2 is quite high [$E_b(CO_2) = 2600$ K Wakelam et al., 2017] so that the abundance of sCO_2 depends poorly on the dust temperature in this range, which is clearly shown in Fig. 6.9 (top-right). Instead, it appears to be inversely proportional to the grain size and exhibits a notable drop on grains of size $>$ 10 μm at 200 au. This behavior can be explained by the following two effective formation routes to sCO_2:

$$\mathrm{sO + sCO \rightarrow sCO_2\ (E_A = 1000K)} \tag{6.2}$$

$$\mathrm{sOH + sCO \rightarrow sCO_2 + sH.} \tag{6.3}$$

These two routes are oxygenation reactions whose rate increases with temperature (in the considered range). The surface temperature allows for oxygen to diffuse and react with sCO or sH and form sOH. For Reaction. 6.2 to occur, the surface temperature must be high enough to overcome the activation barrier. If the dust temperature is below a threshold value, the reaction is not activated, explaining the drop in abundance on large grains at 200 au (and further). Therefore, the outer disk should form slightly fewer CO_2 ices than the inner disk ($\sim$ 30 au). Overall, disks with colder grains will produce less CO_2 and more CH_4 (see Sec. 6.6.1).

CH_4 ice is mostly formed via the hydrogenation of sCH_3. The efficiency of hydrogenation reactions decreases with dust temperature, explaining why sCH_4 abundances is strongy anti-correlated with dust temperature in 6.9 (bottom-left). Icy CH_3, on the other hand, is formed via the following two sequences:

$$\mathrm{sCO + h\nu \rightarrow sC + sO} \tag{6.4}$$

$$\mathrm{sH_2 + sC \rightarrow sCH_2} \tag{6.5}$$

$$\mathrm{sH_2 + sCH_2 \rightarrow sCH_3 + sH} \tag{6.6}$$

$$\mathrm{sCH_3 + sH \rightarrow sCH_4} \tag{6.7}$$

and

$$\mathrm{sCH_3OH + h\nu \rightarrow sOH + sCH_3.} \tag{6.8}$$

Since both sequences require the presence of sCO (Methanol CH_3OH is formed on the surface via successive hydrogenations of sCO), CH_4 ice is more likely to be found on larger grains and in the outer disk.

6.6.2.2 Sulfur-bearing molecules: the case of H_2S

The hydrogen sulfide molecule H_2S has been detected in multiple sources such as dense cloud cores or cometary comae. Recently, Phuong et al. [2018] reported the first detection of H_2S in the cold and dense ring about the TTauri star GG Tau A. The low H_2S column densities observed in GG Tau A and in dense molecular clouds are assumed to be the result of a strong sulfur depletion [Hudson and Gerakines, 2018, Phuong et al., 2018].

In our models, after the full integration time, we find that $\sim$ 99% of H_2S is in the form of ice and that icy H_2S is mostly formed by successive hydrogenation of adsorbed S or S-bearing complex molecules:

$$\mathrm{sS} \xrightarrow{\mathrm{sH}} \mathrm{sHS} \xrightarrow{\mathrm{sH}} \mathrm{sH_2S} \tag{6.9}$$

$$\mathrm{sCH_3SH} \xrightarrow{\mathrm{sH}} \mathrm{sCH_3} + \mathrm{H_2S}. \tag{6.10}$$

We note that the channels to sCH_3SH involve successive hydrogenations of sCS. Reaction 6.9 occurs on grains of all sizes while Reaction 6.10 is only found to be effective on the cold grains.

As hydrogenation sequences are less effective on warm grain surfaces, Figure 6.9 (middle-right) shows a strong anti-correlation between sH_2S abundance and grain temperature observed at all radii (The smallest sH_2S abundances are located on the hottest grains while the largest abundances are found on the largest grains). Grains at 100 and 200 au exhibit roughly the same sH_2S abundances while grains of size < 1 μm at 10 au exhibit larger abundances than in 100 and 200 au because of higher collision rates in the inner regions. The abundance of sH_2S is approximately the same on grains of size > 10 μm at all radii ($\sim 6\ 10^{-9}$).

6.6.2.3 Nitrogen-bearing molecules: the case of NH_3

In the three investigated models, the main nitrogen-bearing ice species in the mid-plane is NH_3, followed by HCN, N_2 and CN at all radii. The main formation pathway to sNH_3 is 1) the accretion of gas-phase atomic nitrogen N onto grain surfaces followed by the successive hydrogenation of N [see Aikawa et al., 2015, Eistrup et al., 2018, Ruaud and Gorti, 2019] 2) the accretion of gas-phase NH_3. Hydrogenation reactions are more efficient on cold grain surfaces. The accretion rate of NH_3, given its high binding energy ($E_b(NH_3) = 5500$ K), does not depend on the dust temperature and is therefore more effective on the grain populations that possess a large number density as this implies a high collision rate.

The cold-grain model HUV-LH-T_g thus forms more sNH_3 than HUV-LH-T_a because the former has colder grains (see the triangles in Fig. 6.9, middle-left). For the multi-grain models, the abundance of sNH_3 is approximately inversely proportional to the grain size in the range 0.007 μm to $\sim$ 1 μm at 30, 100 and 200 au from the star (see the crosses, squares, and circles in Fig. 6.9, middle-left) because the accretion rate of NH_3 is proportional to the grain surface area (the smaller grains have a larger surface area

than the bigger ones). Beyond the size = 1 μm, the surface abundance remains roughly constant at all sizes and at all radii as the grain temperature is low enough to allow for efficient hydrogenation, although it is less noticeable at 30 au because grains are hotter closer to the star.

As the disk evolves, a large quantity of nitrogen-bearing species on grain mantles are transformed into complex molecules and new formation routes to NH_3 become effective. We note, for instance, the important destructive hydrogenation of sNH_2CO,

$$sNH_2CO \xrightarrow{sH} sNH_3 + sCO. \tag{6.11}$$

6.7 In-depth investigations

6.7.1 Water

6.7.1.1 Introduction

Determining how, where and when water is formed in protoplanetary disks is critical if one wants to understand the origin of water delivery to planetary surfaces. Water has commonly been observed around T Tauri stars, in particular spectral lines in the gas-phase of the inner regions using near- and mid-infrared [Carr and Najita, 2008, Pontoppidan et al., 2010] or far-infrared observations [Riviere-Marichalar et al., 2012]. However, icy water in the outer disks is far more difficult to detect due to low excitation lines. It is assumed [Dominik et al., 2005, Lecar et al., 2006, Podio et al., 2013, Du and Bergin, 2014] that water cannot exist in the form of ice on grain surfaces inside the snow-line (T_d $\sim$ 150 K). In typical disks around T Tauri stars, the radial snow-line location is located between a few to ten au from the star. As the innermost computed radius in our models (30 au) is far beyond the radial snow-line, there will be no discussion on the radial water snow-line location in the following.

6.7.1.2 Gas-phase

Three main parameters control water gas-phase abundance 1) photo-desorption via FUV photons and cosmic rays 2) dust temperature and 3) chemical reactions in the gas-phase, in particular via the following sequence

$$H_2 + OH^+ \rightarrow H + H_2O^+ \tag{6.12}$$
$$H_2O^+ + H_2 \rightarrow H + H_3O^+ \tag{6.13}$$
$$H_3O^+ + e^- \rightarrow H + H_2O. \tag{6.14}$$

The sequence shows that H_2 and OH^+ are main precursors to H_2O. Whether H_2 or OH^+ is the limiting factor is determined by this other sequence:

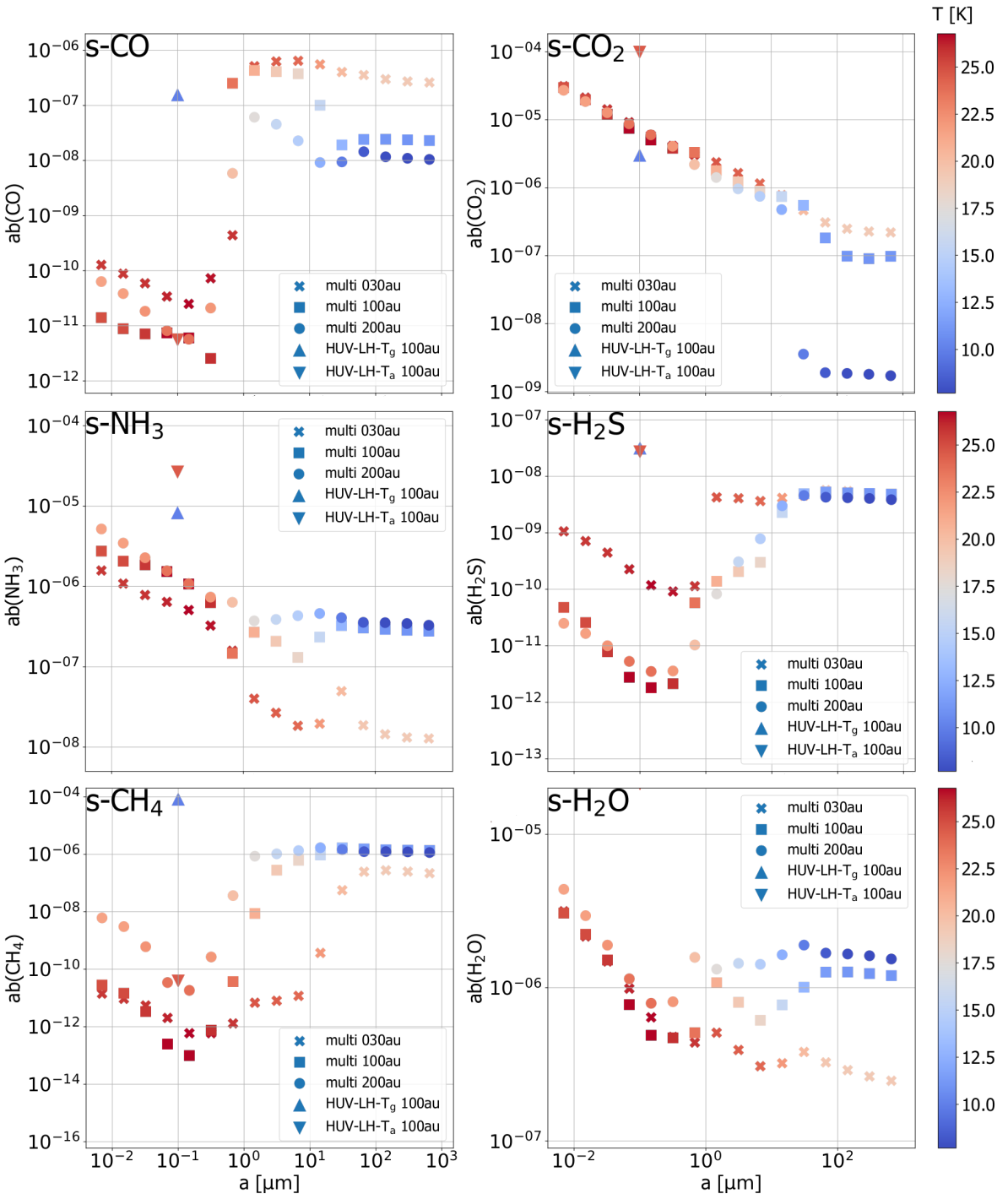

Figure 6.9: Grain surface abundance per total atomic hydrogen for various molecules at the final stage of integration i.e. 5.10^6 yrs as a function of the grain radius a in relation to the grain temperatures. Cross markers stand for the multi-grain model at 30 au, the square markers stand for the multi-grain model at 100 au and the round markers stand for 200 au. The triangles pointing upward represent the surface abundance in the single-grain model HUV-LH-T$_g$ (grains of size 0.1 μm) and the triangle pointing downward represents the abundance in the single-grain model HUV-LH-T$_a$, both at 100 au.

$$H_2 + CR \rightarrow H_2^+ + e^- \tag{6.15}$$
$$H_2^+ + H_2 \rightarrow H_3^+ + H \tag{6.16}$$
$$H_3^+ + O \rightarrow OH^+ + H_2. \tag{6.17}$$

These two sequences show that H_2O formation depends on H_2 and OH^+ but the latter also depends on H_2. Therefore, this is the H_2 abundance that sets the gas-phase formation of water and accounts for the difference between the models (not cosmic-rays or OH^+). But the gas-phase formation of H_2O represents only a small fraction of all H_2O molecules formed as most H_2O are formed on grain surfaces. The abundance of gas-phase water is thus mainly governed by both the formation rate of icy water and by the photo-desorption rate (thermal-desorption is ineffective in most parts of the disk because the binding energy of water is high). The formation rate depends on the grain temperature while the photo-desorption rate depends on the FUV flux and cosmic-rays. The analysis of the results herein (Figs. 6.10 and 6.11) shows that the dust temperature plays the major role in the production of gas-phase water.

Single-grain models The vertical snow-line forms a clear boundary between high and low gas-phase H_2 abundance at $z/r \sim 0.15$ (Figure 6.10) and we see that HUV-B14-T_a produces the most distinct boundary of all three models. The snow-line corresponds roughly to the abrupt drop in the UV flux as shown in Figure 4.3 (bottom-right panel). The cold-grain model HUV-LH-T_g produces substantially more water in the upper layers than the other single-grain models analogous. The reason is the low dust temperature that increases the hydrogenation rates on the grain surfaces (same process as in section 6.6.1). The photo-desorption rates are approximately equal in the three models (same flux) but since HUV-LH-T_g produces a larger water abundance on grain surfaces the final gas-phase abundance is much larger. It results in a column density of water about a factor 10 larger in HUV-LH-T_g than in the other two models. On the other hand, the B14's prescription increases only marginally the column density of gas-phase water.

Multi-grain models The vertical snow-line is far less apparent (Figure 6.11, top row, middle and right column). Both models have approximately the same distribution of abundance because they use the same dust temperature distribution. We notice, however, that B14's prescription in M-HUV-B14 produces marginally higher water abundance in the upper layer of the disk than in M-HUV-LH, due to the gas-phase formation of water via the two sequences presented above.

6.7.1.3 Water on icy grain mantles

Single-grain models The vertical snow-line is clearly defined in single-grain models although we note the presence of a notable high-abundance band (Fig. 6.10, bottom-left) following approximately $z = 3$ H_g in HUV-LH-T_g. This is due to the following activated hydrogenation surface reaction:

$$\mathrm{sH} + \mathrm{sHOOH} \rightarrow \mathrm{sH_2O} + \mathrm{sOH}\ (\mathrm{E_A} = 1400\mathrm{K}). \tag{6.18}$$

Indeed, the band indicates the altitude at which the reaction is activated. Below the band, the reaction is not activated and water ice is effectively photo-desorbed (see the hole in Figs. 6.10, bottom-left) while above the band the photo-desorption rate is stronger than the formation rate via Reaction 6.18. In the band location, the surface formation rate slightly prevails over the photo-desorption rate, resulting in this sudden increase of abundance. In HUV-LH-T_a, as the dust temperature is higher, Reaction 6.18 is activated at lower altitudes, resulting in a larger high abundance band around $z = 2$ H_g and the abundance hole is displaced to the outer disk below $z = 2$ H_g (Fig. 6.10, bottom-middle). HUV-B14-T_a, on the other hand, does not exhibit such a peak in abundance because B14's prescription uses a large fraction of available surface hydrogen sH to produce H_2. This is the reason why this model exhibits the most distinct vertical snow-line.

Multi-grain models Reaction 6.18 is also effective in multi-grain models. Yet, the multiple dust temperatures implies that this reaction is activated in a much broader range of altitudes. Then, the formation of sH_2O via hydrogenation can be effective at higher altitudes on cold medium- and large-sized grains so that the snow-line is located at a higher altitude in both models ($z \sim 3$ H_g)

Near the mid-plane In all models, water is found in the form of ice around the mid-plane, where the desorption by UV flux and cosmic-rays is limited and where hydrogenation is effective. For single-grain models, the width of the region where water is on the icy mantles is larger in HUV-LH-T_g than in the two others because, again, the dust temperature is smaller. As for the multi-grain models, Figure 6.9 (bottom-right) provides a good insight on which grain population the formation of icy H_2O is effective. We see that the abundance is inversely proportional to the grain size at 30 au due to the large binding energy of water. At 100 and 200 au, the abundance on big grains (> 0.1 μm) remains large because the low grain temperature at these radii allows for more effective hydrogenations.

6.7.2 Complex organic molecules (COMs)

6.7.2.1 Introduction

Simple organic molecules have been regularly detected over the last decades such as H_2CO [Dutrey et al., 1997, Aikawa et al., 2003, Öberg et al., 2011], HC_3N [Chapillon et al., 2012], CH_3CN [Öberg et al., 2015] and CH_3OH [Walsh et al., 2016]. In the following, we study the production pathways to already observed Complex Organic Molecules (COM)s, in particular the well-known methyl cyanide CH_3CN and methanol CH_3OH in the gas-phase as well as on the grain mantles of our disk models.

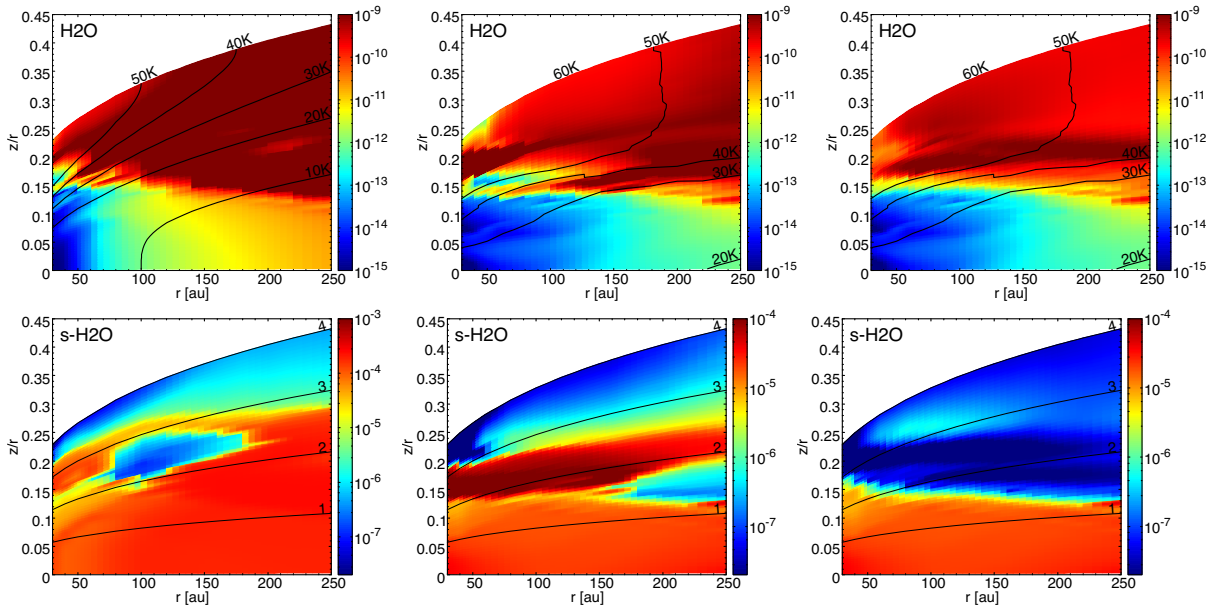

(a) HUV-LH-T_g (b) HUV-LH-T_a (c) HUV-B14-T_a

Figure 6.10: Water abundance in the gas-phase (top) and on the grain surfaces (bottom) of the single-grain models. Left column shows the abundances in HUV-LH-T_g, middle in HUV-LH-T_a and right one in HUV-B14-T_a. In the top row, the solid black lines show the dust temperature iso-contours, in the bottom row they denote iso-contours of scale heights.

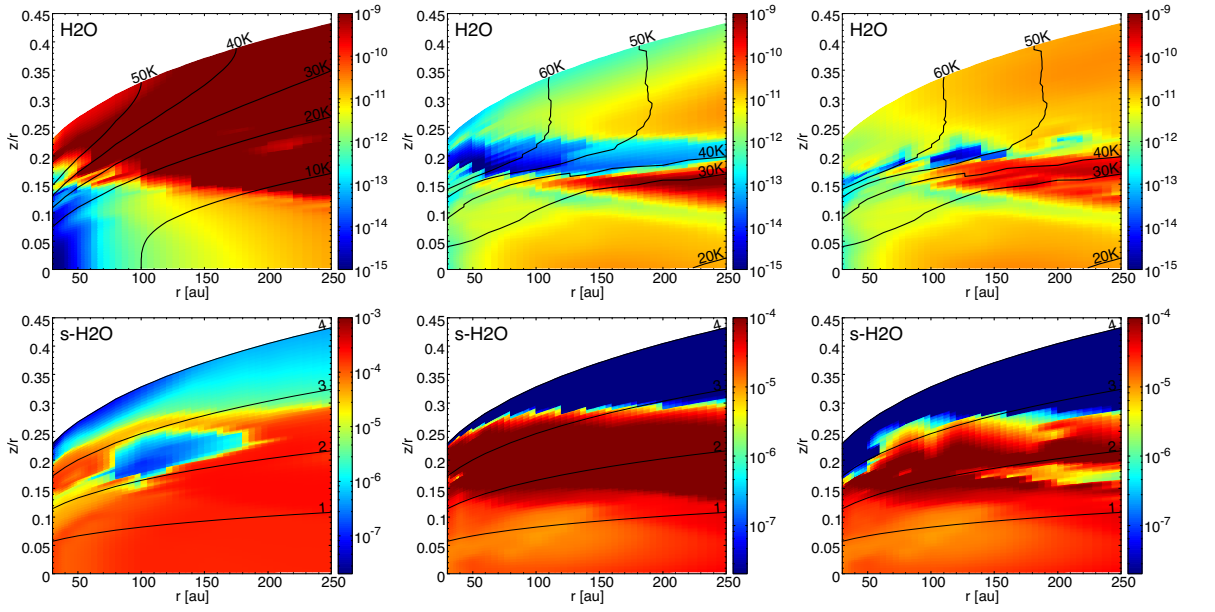

(a) HUV-LH-T_g (b) M-HUV-LH (c) M-HUV-B14

Figure 6.11: Water abundance in the gas-phase (top) and on the grain surfaces (bottom). Left column shows the abundances in HUV-LH-T_g and middle and right column in the multi-grain models. In the top row, the solid black lines show the dust temperature iso-contours, in the bottom row they denote iso-contours of scale heights.

6.7.2.2 Methyl cyanide (CH_3CN)

C-N bonded species are fundamental precursors for the synthesis of Glycine, an amino acid [Goldman et al., 2010]. CH_3CN has been observed for the first time in a disk by Öberg et al. [2015], around the Herbig Ae star MWC 480 (Herbig objects are pre-main sequence stars whose disk exhibits warmer temperatures and stronger UV flux than T Tauri disks). We explore herein the CH_3CN formation efficiency of the models.

CH_3CN to HCN abundance ratio To compare our results with observations, we discuss the vertically integrated abundance of CH_3CN relative to HCN i.e. the ratio CH_3CN/HCN [Mumma and Charnley, 2011, Öberg et al., 2015]. The single-grain model HUV-LH-T_g produces a ratio CH_3CN/HCN of $\sim 14\%$ between 100 and 140 au. As for the other single-grain models HUV-LH-T_a and HUV-B14-T_a, they form not more than 1% in the same range of radii. On the other hand, the outer regions (200-250 au) of these two models produce a ratio of up to 9%. It thus appears that disks with colder grains produce a larger ratio than disks with warmer grains. In all multi-grain models, there is a rather constant ratio along the radius, which never exceeds 1% and never goes below 0.1%. We note that M-HUV-B14 produces slightly more CH_3CN than M-HUV-LH. Overall, the model HUV-LH-T_g (with the coldest grains overall) is the one that globally produces the largest CH_3CN/HCN ratio.

Gas-phase formation of CH_3CN in the multi-grain models We discuss the formation routes to gas-phase CH_3CN, in particular in the upper regions of our multi-grain disks. The main known pathways to the formation of CH_3CN are 1) the reactions of HCN with CH_3^+ and 2) the photo-desorption of sCH_3CN. We note that the thermal desorption rates are very small since the binding energy of CH_3CN [$E_b(CH_3CN) = 4680$ K Wakelam et al., 2017] is large enough to prevent the thermal desorption to occur. Results show that only photo-desorption is effective in M-HUV-LH while the reaction HCN + $CH_3^+ \rightarrow CH_3CN$ is very effective in M-HUV-B14. This is explained by the fact that the production of CH_3^+ requires the presence of H_2:

$$C^+ \xrightarrow{H_2} CH_2^+ \xrightarrow{H_2} H + CH_3^+ \tag{6.19}$$

and M-HUV-B14 forms more H_2 in the upper layers. Figure 6.12 shows the vertical abundance of CH_3CN of M-HUV-LH (blue line) and M-HUV-B14 (ref line) at 100 au. The difference in abundance between the upper layers of the two models is clearly visible as the difference is nearly $\sim$ ten order of magnitude at $z > 3$ H_g. On the other hand, as one would expect, the difference decreases from $z = 2.5$ H_g as one goes deeper in the disk until both models finally produce the same amount of CH_3CN below $z = 2$ H_g.

Surface chemistry in the mid-plane Figure 6.14 (bottom) shows the abundance of CH_3CN ices in the mid-plane relative to the grain size as a function of the radius after 5×10^6 years. It appears that most sCH_3CN preferably remains on smaller grains (<

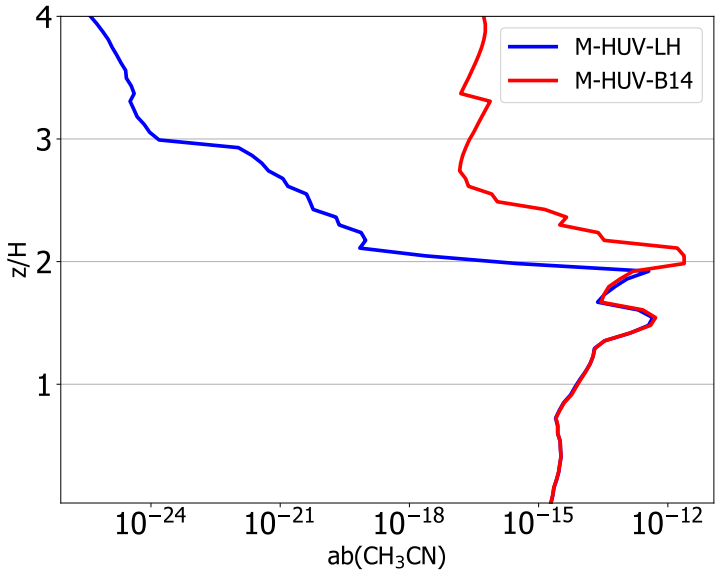

Figure 6.12: Altitude above the mid-plane as a function of the abundance relative to H of CH_3CN at 100 au. Blue line shows the abundance produced by model M-HUV-LH, red line shows the abundance produced by model M-HUV-B14. We see that the abundance decreases at $z > 2$ H_g in M-HUV-LH while M-HUV-B14 keeps a rather high abundance at high altitudes. This is due to the available quantity of gas-phase H_2 in M-HUV-B14, which enhances the production of CH_3^+.

0.317 μm). This can be explained by looking at the the two main reactions forming sCH_3CN, which are 1) the adsorption of gas-phase CH_3CN and 2) the following bimolecular reaction:

$$sCH_3 + sCN \rightarrow sCH_3CN. \tag{6.20}$$

First, the binding energy of CH_3CN is large so the ratio of the adsorption rate to the desorption rate is simply larger on grains coming from a population with a large number density. Secondly, the binding energy of the precursor CN is also quite large so it is preferably found on small grains for the same reasons. CH_3, despite a low binding energy, will briefly stick and quickly react with sCN. Then, to a lesser extent, CH_3CN can also be formed on larger cold grain surfaces, but the photo-desorption rates are large enough for CH_3CN to be desorbed and to progressively seed small grains with time.

6.7.2.3 Methanol (CH_3OH) and formaldehyde (H_2CO)

CH_3OH to H_2CO abundance ratio we discuss the vertically integrated abundance of CH_3OH relative to H_2CO (CH_3OH/H_2CO). In M-HUV-B14, after 10^6 years of integration, the averaged ratio between 80 and 120 au is equal to 1.3. This appears to be consistent with the observed ratio in TW Hydrae [Walsh et al., 2016, Carney et al., 2019]. In M-HUV-LH, on the other hand, the averaged ratio is equal to 2.4 (about twice that of M-HUV-B14). The difference can be explained by considering the main pathway to the formation of gas-phase H_2CO:

$$H_2 + CH_3^+ \rightarrow CH_5+ \tag{6.21}$$
$$CH_5^+ + e^- \rightarrow H + H + CH_3/H_2 + CH_3 \tag{6.22}$$
$$O + CH_3 \rightarrow H + H_2CO. \tag{6.23}$$

Indeed, the sequence shows that H_2 is a key element in the formation process of H_2CO. As H_2 is more abundant in M-HUV-B14, H_2CO is thus more abundant in this model than in M-HUV-LH.

Gas-phase CH_3OH in the multi-grain models The organic molecule CH_3OH is mainly formed via successive hydrogenation of adsorbed CO on the grain surfaces. Figure 6.13 shows the vertical abundance of CH_3OH of M-HUV-LH (blue line) and M-HUV-B14 (ref line) at 100 au. The vertical profile of gas-phase CH_3OH is divided into two layers in both models. In the upper layer ($z > 2$ H_g), we see that M-HUV-B14 forms more CH_3OH than M-HUV-LH. This is due to the more efficient shielding generated by the large amount of H_2 formed via B14's prescription, which allows for more CO to be formed. In the bottom layer ($z < 2$ H_g), as expected, both models produce the same vertical profile. The two layers are separated by an abrupt drop in abundance at ~ 2 H_g. This corresponds to the dust temperature transition (Fig. 6.3). The lower layer (< 2 H) contains most of CH_3OH

column density, which is consistent with the fact that CO is more depleted in this region and thus more abundant on the grain surfaces.

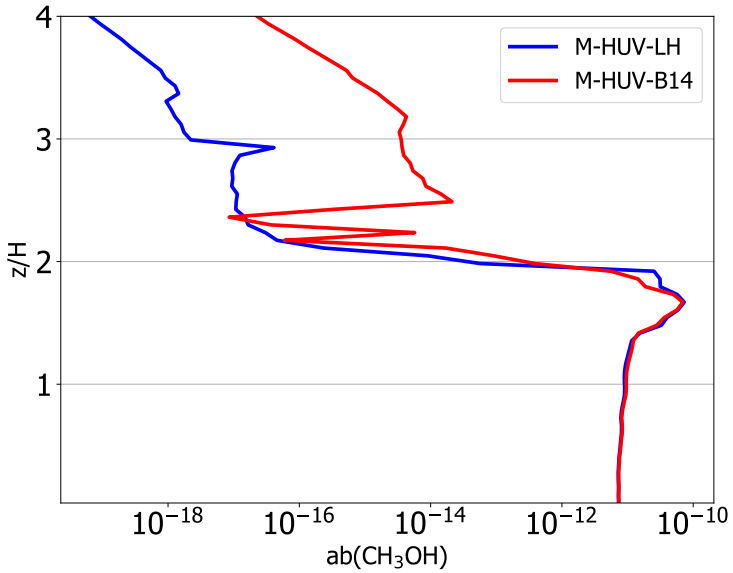

Figure 6.13: Altitude above the mid-plane as a function of the abundance relative to H of CH_3OH at 100 au. Blue line shows the abundance produced by model M-HUV-LH, red line shows the abundance produced by model M-HUV-B14. We see that the abundance decreases at $z > 2$ H_g in both models, although M-HUV-B14 maintains a larger abundance than M-HUV-LH above 2 H_g.

Grain size dependence on surface chemistry Let us explore the grain size-dependence on the formation of icy CH_3OH. Figure 6.14 gives a set of maps of ice abundance in the mid-plane with grain sizes as a function of the computed radii. Top left panel is the grain temperature which allows to analyse the surface abundance in view of the surface temperature. We remind that these results are the same for all multi-grain models. On icy mantles, both sH_2CO and sCH_3OH are formed via the same hydrogenation sequence:

$$sCO \xrightarrow{H} sHCO \xrightarrow{H} sH_2CO \xrightarrow{H} sCH_3O \xrightarrow{H} sCH_3OH. \tag{6.24}$$

However, we note that H_2CO is also mainly formed in the gas-phase. As seen in Figure 6.14 (top right), CO tends to be efficiently adsorbed onto cold surfaces. The map of H_2CO (bottom left) grossly follows the same distribution although the trend is globally less pronounced. CH_3OH, on the other hand, exhibits a totally different distribution and tend to concentrate on small grain surfaces (bottom right). The main reason comes from the fact that the binding energy increases as the molecules become more complex [e.g., $E_b(CO)$ ∼1200 K, $E_b(H_2CO)$ ∼3200 K, $E_b(CH_3OH)$ ∼5500 K Minissale et al., 2016, Noble et al., 2012, Collings et al., 2004] and that the hydrogenation of H_2CO (which leads

to CH_3OH) has an activation barrier and cannot efficiently occur on cold grain surfaces.

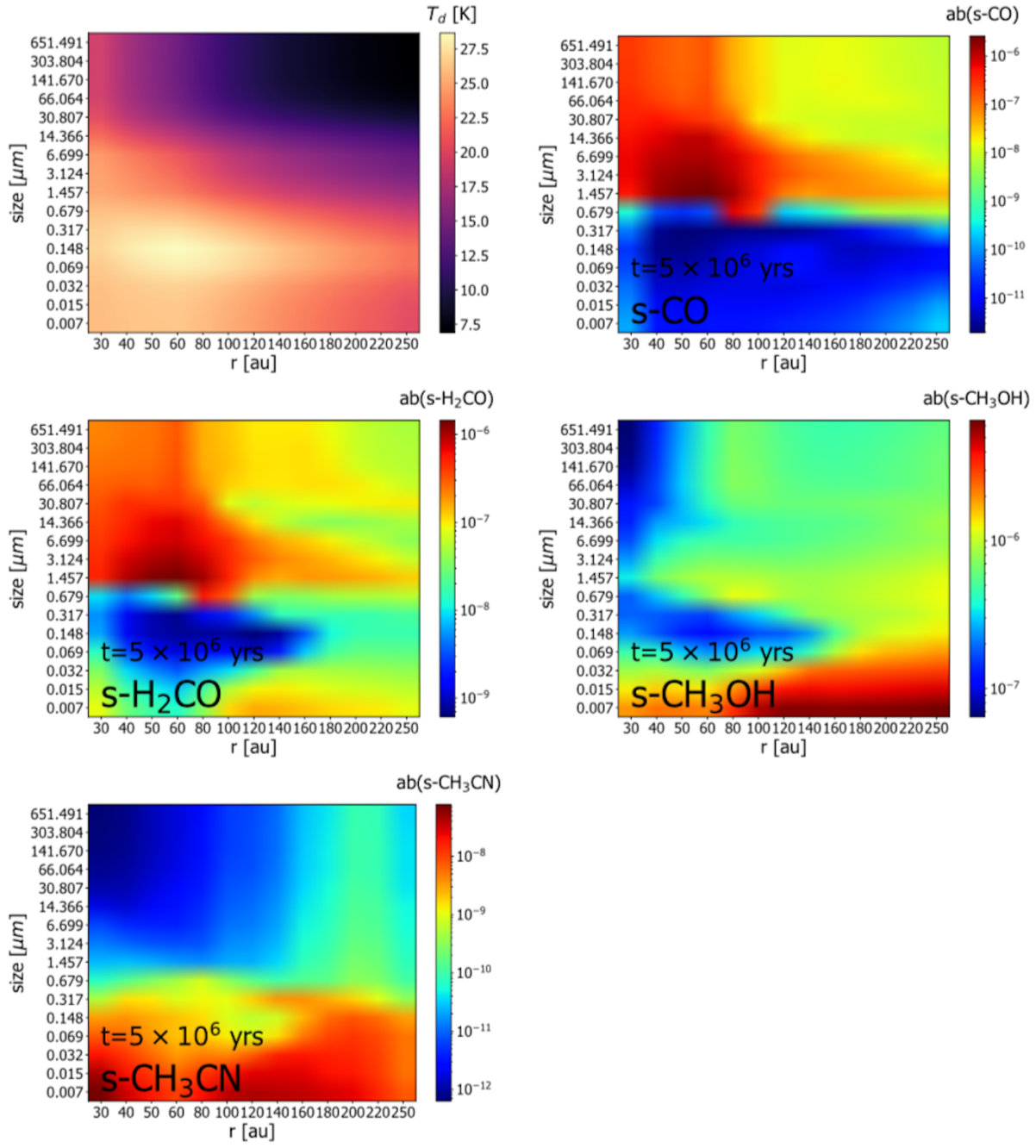

Figure 6.14: multi-grain models: Maps of ice abundance in the mid-plane, with grain sizes as a function of the radius. Top left panel is the grain temperature in the disk mid-plane at all computed radii and for all 16 sizes. As expected, bigger grains are colder than smaller ones. We note, however, that the hottest grains are those of size ≈ 0.1 μm.We see that the hottest region is located at around 60 au from the star on grains of size 0.148 μm.

Chapter 7

Conclusion

Contents

7.1 In hindsight

When I began my PhD thesis in 2017, a postdoctoral researcher in the group, Wasim Iqbal, was finalizing the development of the multi-grain version of NAUTILUS. In the meantime, a PhD student working in the Institute for Theoretical Physics and Astrophysics at Kiel, Julia Kobus, started working on protoplanetary disks using the 3D radiative transfer Monte-Carlo code POLARIS in the group of Sebastian Wolf. These two distinct events, when brought together, allowed to mark the originality of this project. The work presented in this thesis is then an association of efforts coming from many people, which enabled me to play, and sometimes mess around, with different tools with the goal to find out a little more about protoplanetary disks.

The study of protoplanetary disks (and, in fact, the study of most astrophysical objects) is distinguished by the fact that it requires skills from many different topics of physics and chemistry (hydrodynamics, quantum mechanics, radiative transfer, thermodynamics, radioastronomy, optics, kinetic chemistry, organic chemistry, and so on). This multidisciplinary is what makes studying the topic both interesting and challenging. It also reminds us that astrophysics is necessarily a social discipline, since it cannot be performed by isolated individuals. I was happy to modestly contribute, during this thesis, in the collective effort that seeks to understand the origin of planetary systems.

I present in the next section a short summary of the thesis. The various subsections are roughly introduced in the chronological order of the thesis work. Then, I introduce a few possible directions that can be pursued from the present work.

7.2 The thesis in a nutshell

7.2.1 Disk modelling using multiple grain sizes

We built new chemical models of protoplanetary disks that consistently account for the effect of grain sizes on the dust temperature, the UV penetration and, consequently, on the chemistry. We tested the novel method in the case of a typical disk around a T Tauri star using parameters derived from the Flying Saucer observations with 16 grain sizes (Chapter. 4).

7.2.2 The Nautilus Multi Grain Code (NMGC)

A large fraction of my work was dedicated to using the NMGC in this context of protoplanetary disks, which was not done before. The task was quite challenging due to different aspects. The first aspect was computation. Indeed, while the single-grain version of NAUTILUS requires about 13 hours in cpu-time to fully compute one disk model, the NMGC using 16 bins requires nearly 520 hours in cpu-time on a regular laptop machine (2.3 GHz Intel Core i7). It appeared necessary to use more sophisticated computation methods such as the use of supercomputers and parallelization. The second aspect was the development and the implementation in NAUTILUS of a more refined

way of computing the self and mutual shielding of molecules, which consisted in using the frequency-dependent photo-process molecular cross-sections extracted from the Leiden database (Chapter. 5). The update of the KIDA database, that sets the reaction rates in the code, was also part of the work performed for NAUTILUS[1] and will continue to be part of my job in the future. The third aspect was the need to implement in the code the B14 H_2 formation rates in the PDR-like regions of the disk (Chapter. 3). Retrieving the H_2 formation rates was rather tricky as it implied to make the proper approximations. Moreover, interpolating required to use analytical polylogarithmic functions (see Appendix C) to fit the formation rates.

7.2.3 H_2 formation rates in the PDR regions

By comparing the first multi-grain simulation results with single-grain models, we identified the H_2 formation rates via the Langmuir-Hinshelwood mechanism as inefficient for a grain size distribution and the amount of H_2 as critical for the chemistry of the upper layers. We therefore decided to implement in the chemistry code the parametric method of B14, who prescribes a stochastic formation rates taking into account the fluctuation of temperature and surface population for the distribution of small grains ($\sim$ 5 nm to 300 nm). Using this prescription appeared to be more appropriate to produce enough H_2 in the upper layers.

7.2.4 Radiative transfer simulation results

Julia Kobus and I worked closely and meticulously together in order to make sure both sides would produce perfectly consistent results from our respective multi-grain disk models. The radiative transfer simulations provided a local UV intensity $I_d(r, z)$ properly attenuated by the multiple grain populations within the disk and, accordingly, a full size-independent dust temperature $T_d(a_k, r, z)$. The key results are as follows:

- The extinction of the UV flux by the grain size distribution resulted in a three-layer disk, an optically thin upper layer ($z > 2$ H_g), an optically thick layer ($z < 2$ H_g), and a transition layer corresponding to the molecular layer of the disk.See Figure 6.3.
- The grain vertical temperature profiles were impacted accordingly: the upper layer exhibits constant high grain temperatures while the lower layer exhibits constant small grain temperatures. Between the two, the dust temperatures exhibit large variation from higher to lower temperatures (Chapter. 6).
- Fewer grain bins would have account for the same chemical results (see Figure 6.4) so that the number of sizes could have been divided by two, reducing the computation time by 50.

[1]This work was not introduced in the thesis. Indeed, although it required a few coding skills and a few hours of work, I believed that this was part of a necessary side work needed to achieve the thesis, and that its presentation was mostly irrelevant for the reader's comprehension.

7.2.5 Main chemistry results of our Flying Saucer disk models

Our results show that the chemistry of protoplanetary disks cannot be properly reproduced by using a single grain size, multiple grain sizes appear necessary to represent the chemistry of protoplanetary. The key chemistry results of the thesis, in no particular order of importance, can be summarized as follows:

- For an optically thick disk, the intensity of the stellar UV flux (in the case of T Tauri stars) has very little effects on the disk mid-plane chemistry. The chemical material delivery to planetary embryos should not be different from a T Tauri disk to another. This may not be the case in optically thin disk (in particular around Herbig stars).
- A consequence of the previous point is that the chemistry in the mid-plane is mostly regulated by the dust temperature. This explains why two different models using the same grain temperature exhibit the same chemistry ($z < 1.5$ H_g) while a model using another dust temperature will exhibit a different chemistry.
- The formation of H_2 in the upper layers of disks that possess a low dust temperature ($T \lessapprox 50$ K) is more effective than in disks with a higher dust temperature. The H/H_2 transition is dependent on the dust temperature. The colder the grains the closer to the surface the transition occurs.
- A low UV flux penetration and/or a large shielding by H_2 combined with relatively hot grains will produce a large gas-phase CO column density. This has to be compared with ALMA observations.
- The oxygen and carbon reservoirs of colder dust disks will be mainly locked in sCH_4 and sH_2O, respectively, while both these reservoirs will be locked in sCO_2 in hotter dust disks.
- Analogously to the previous point, the small grains in the inner disk form more icy CO_2 than larger grains in the outer disk. Conversely, CH_4 is more likely to be found on larger grains in the outer disk.
- The location of the water vertical snowline depends on the balance between the UV penetration and the dust temperature. Indeed, water is formed on sufficiently cold grains and are then photo-desorbed by the UV flux. But, if the UV penetration is too high, the grains become too warm to witness water formation so the water gas-phase abundance is low. If the UV penetration is moderate, water is effectively formed and photo-desorbed. Then, if the UV penetration is too low, water is effectively formed but is not photo-desorbed anymore, this is where the snowline appears.
- In our models, H_2 also appears to be important to form complex molecules, such as H_2CO or CH_3OH, in the disk upper layers.
- In the mid-plane, both sCH_3OH and sCH_3CN are preferably locked on the small abundant grains rather than the larger grains. More generally, icy molecules with

high binding energy will be more likely to be found on the smaller grains than on the larger ones.

7.3 Future perspectives

7.3.1 Comparison with the Flying Saucer

The most direct and obvious observational perspective is the comparison with the Flying Saucer. Dutrey et al. [2017] observed the vertical and radial distribution of CO and CS in the Flying Saucer. Figure 7.1 shows the median tomographically reconstructed distribution (TRD) of CO and CS (color) with H_2 density and scale height contours (black). The CO emission is observed at 1-3 scale heights while the CS emission peaks is confined at around 1 scale height.

To compare these results with the models we want to highlight the difference in location of CO and CS. Figure 7.2 illustrates 2D maps of CO (red) and CS (green) where 90 % of the mass is located. The peak of abundance at all radii is represented by the dotted lines. Figure 7.2a shows the case of a single-grain model (HUV-B14-T_a) and Figure 7.2b shows the case of a multi-grain model (M-HUV-B14). The figure indicates that CS appears to be above CO in single-grain models while CO is above CS in multi-grain models. The configuration in the multi-grain models looks more consistent with the observations. This, of course, represents a preliminary work but looks promising and demands further investigation.

7.3.2 The case of optically thin disks

The disk parameters imply a vertically integrated dust to gas mass ratio of 1/100, which is directly inherited from the observed ratio in the ISM. This basically produces an optically thick disk, where, as we have seen in Chap. 6, the UV flux penetration in the mid-plane is greatly attenuated whether the flux is high (HUV) or low (LUV). In such disks, the chemistry in the mid-plane is almost not impacted by the T Tauri UV flux. A direct follow-up of this work will be to perform the same simulations in the case of an optically thin disk, consisting, for instance, in a dust to gas mass ratio of 1/1000 and where changing the stellar radiation field would affect the mid-plane dust temperature, the chemistry routes and, consequently, the composition of planetary embryos.

I show a comparison between the vertical profile of CO at 100 au of the optically thick models presented in this thesis (Fig.7.3a) and of a new optically thin model (Fig.7.3b). We notice that the abundance of CO is increased by more than one order of magnitude in the mid-plane in the case of the optically thin model. This is something expected as the collision rate is reduced by a factor of ten. CO is therefore ten times more likely to remain in the gas-phase. However, as the difference is more than a factor of ten, we may also suspect that the photo-desorption rate is larger since there is a larger UV flux penetration in the optically thin disk. This work still requires more analysis and will be further investigated in the future.

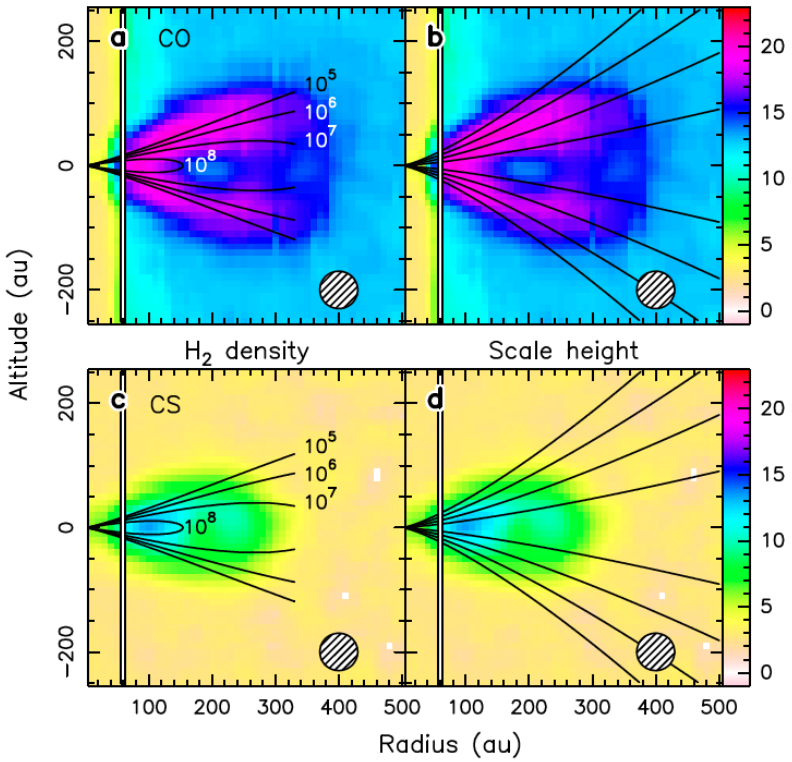

Figure 7.1: CO and CS median tomographically reconstructed distribution (TRD) against a standard disk model corresponding to the Table.2 in Dutrey et al. [2017]. (a) CO TRD (color) with H_2 density in black contours. (b) CO TRD with the scale height from 1 to 4 scale in black contours. (c) and (d) as (a) and (b) but for CS.

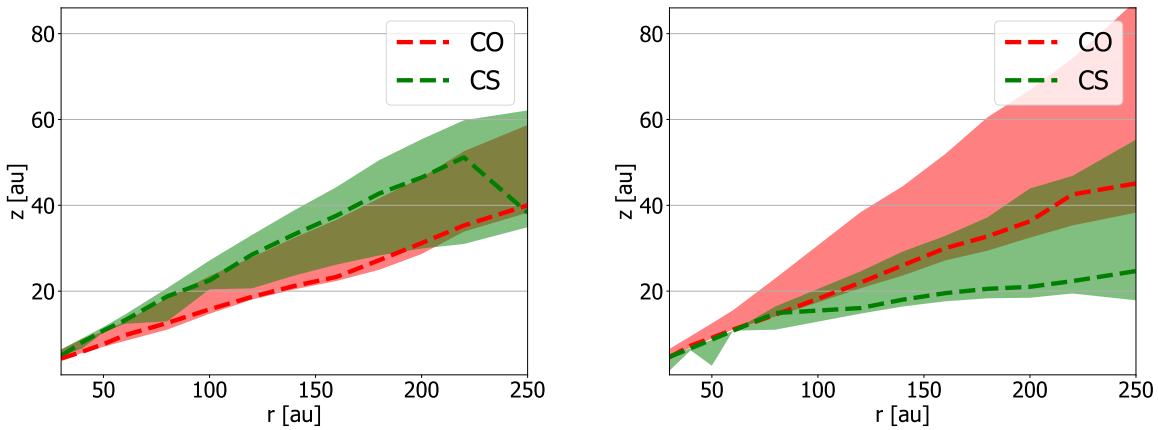

(a) HUV-B14-T_a (b) M-HUV-B14

Figure 7.2: 2D maps of CO (red) and CS (green) where 90 % of the mass is located. The peak of abundance at all radii is represented by the dotted lines. (a): the case of the single-grain model HUV-B14-T_a. (b): the case of the multi-grain model M-HUV-B14.

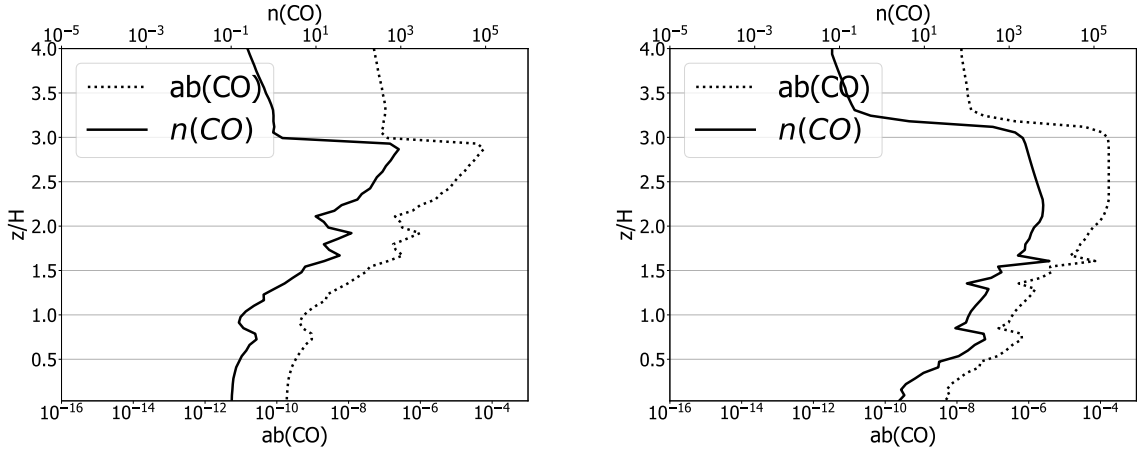

(a) Optically thick M-HUV-LH.

(b) Optically thin M-HUV-LH

Figure 7.3: Vertical profile of CO number density (solid line) and CO abundance (dotted line). (a): classical optically thick model (dust-to-gas-mass ratio = 1/100). (b): optically thin model (dust-to-gas-mass ratio = 1/1000).

Bibliography

Kinsuk Acharyya, George E. Hassel, and Eric Herbst. The Effects of Grain Size and Grain Growth on the Chemical Evolution of Cold Dense Clouds. ApJ, 732(2):73, May 2011. doi: 10.1088/0004-637X/732/2/73. (Cited on page 87.)

F. C. Adams and F. H. Shu. Infrared Spectra of Rotating Protostars. ApJ, 308:836, September 1986. doi: 10.1086/164555. (Cited on page 56.)

Fred C. Adams, Charles J. Lada, and Frank H. Shu. Spectral Evolution of Young Stellar Objects. ApJ, 312:788, January 1987. doi: 10.1086/164924. (Cited on page 42.)

Yuri Aikawa, Munetake Momose, Wing-Fai Thi, Gerd-Jan van Zadelhoff, Chunhua Qi, Geoffrey A. Blake, and Ewine F. van Dishoeck. Interferometric Observations of Formaldehyde in the Protoplanetary Disk around LkCa 15. PASJ, 55:11–15, February 2003. doi: 10.1093/pasj/55.1.11. (Cited on page 143.)

Yuri Aikawa, Kenji Furuya, Hideko Nomura, and Chunhua Qi. Analytical Formulae of Molecular Ion Abundances and the N_2H^+ Ring in Protoplanetary Disks. ApJ, 807(2): 120, July 2015. doi: 10.1088/0004-637X/807/2/120. (Cited on page 139.)

R. Alexander, I. Pascucci, S. Andrews, P. Armitage, and L. Cieza. The Dispersal of Protoplanetary Disks. In Henrik Beuther, Ralf S. Klessen, Cornelis P. Dullemond, and Thomas Henning, editors, *Protostars and Planets VI*, page 475, January 2014. doi: 10.2458/azu_uapress_9780816531240-ch021. (Cited on page 64.)

M. A. Allodi, R. A. Baragiola, G. A. Baratta, M. A. Barucci, G. A. Blake, P. Boduch, J. R. Brucato, C. Contreras, S. H. Cuylle, D. Fulvio, M. S. Gudipati, S. Ioppolo, Z. Kaňuchová, A. Lignell, H. Linnartz, M. E. Palumbo, U. Raut, H. Rothard, F. Salama, E. V. Savchenko, E. Sciamma-O'Brien, and G. Strazzulla. Complementary and Emerging Techniques for Astrophysical Ices Processed in the Laboratory. Space Sci. Rev., 180 (1-4):101–175, December 2013. doi: 10.1007/s11214-013-0020-8. (Cited on page 34.)

Ph. André. The Initial Conditions for Protostellar Collapse: Observational Constraints. In Jerome Bouvier and Jean-Paul Zahn, editors, *EAS Publications Series*, volume 3 of *EAS Publications Series*, pages 1–38, January 2002. doi: 10.1051/eas:2002043. (Cited on pages 13 and 43.)

Sean M. Andrews, Jane Huang, Laura M. Pérez, Andrea Isella, Cornelis P. Dullemond, Nicolás T. Kurtovic, Viviana V. Guzmán, John M. Carpenter, David J. Wilner, Shangjia Zhang, Zhaohuan Zhu, Tilman Birnstiel, Xue-Ning Bai, Myriam Benisty, A. Meredith Hughes, Karin I. Öberg, and Luca Ricci. The Disk Substructures at High Angular Resolution Project (DSHARP). I. Motivation, Sample, Calibration, and Overview. ApJ, 869(2):L41, December 2018. doi: 10.3847/2041-8213/aaf741. (Cited on pages 13, 48 and 49.)

Philip J. Armitage. *Astrophysics of Planet Formation*. 2013. (Cited on page 56.)

Philip J. Armitage. Physical Processes in Protoplanetary Disks. *Saas-Fee Advanced Course*, 45:1, January 2019. doi: 10.1007/978-3-662-58687-7_1. (Cited on pages 13, 14, 56, 60, 62 and 70.)

Steven A. Balbus and John F. Hawley. A Powerful Local Shear Instability in Weakly Magnetized Disks. I. Linear Analysis. ApJ, 376:214, July 1991. doi: 10.1086/170270. (Cited on page 61.)

Steven A. Balbus and John F. Hawley. Instability, turbulence, and enhanced transport in accretion disks. *Reviews of Modern Physics*, 70(1):1–53, January 1998. doi: 10.1103/RevModPhys.70.1. (Cited on page 60.)

Steven A. Balbus, John F. Hawley, and James M. Stone. Nonlinear Stability, Hydrodynamical Turbulence, and Transport in Disks. ApJ, 467:76, August 1996. doi: 10.1086/177585. (Cited on page 60.)

M. C. Begelman, C. F. McKee, and G. A. Shields. Compton heated winds and coronae above accretion disks. I. Dynamics. ApJ, 271:70–88, August 1983. doi: 10.1086/161178. (Cited on page 64.)

A. Belloche, P. André, D. Despois, and S. Blinder. Molecular line study of the very young protostar IRAM 04191 in Taurus: infall, rotation, and outflow. A&A, 393:927–947, October 2002. doi: 10.1051/0004-6361:20021054. (Cited on page 30.)

Mathieu Bertin, Edith C. Fayolle, Claire Romanzin, Hugo A. M. Poderoso, Xavier Michaut, Laurent Philippe, Pascal Jeseck, Karin I. Öberg, Harold Linnartz, and Jean-Hugues Fillion. Indirect Ultraviolet Photodesorption from CO:N_2 Binary Ices — an Efficient Grain-gas Process. ApJ, 779(2):120, December 2013. doi: 10.1088/0004-637X/779/2/120. (Cited on page 77.)

Ofer Biham, Itay Furman, Valerio Pirronello, and Gianfranco Vidali. Master Equation for Hydrogen Recombination on Grain Surfaces. ApJ, 553(2):595–603, June 2001. doi: 10.1086/320975. (Cited on page 84.)

Peter Bodenheimer. Angular Momentum Evolution of Young Stars and Disks. ARA&A, 33:199–238, January 1995. doi: 10.1146/annurev.aa.33.090195.001215. (Cited on page 30.)

Y. Boehler, A. Dutrey, S. Guilloteau, and V. Piétu. Probing dust settling in protoplanetary discs with ALMA. MNRAS, 431(2):1573–1586, May 2013. doi: 10.1093/mnras/stt278. (Cited on pages 14, 67 and 68.)

Emeric Bron, Jacques Le Bourlot, and Franck Le Petit. Surface chemistry in the interstellar medium. II. H_2 formation on dust with random temperature fluctuations. A&A, 569:A100, September 2014a. doi: 10.1051/0004-6361/201322101. (Cited on pages 14, 19, 90, 91, 93, 94 and 128.)

Emeric Bron, Jacques Le Bourlot, and Franck Le Petit. Surface chemistry in the interstellar medium. II. H_2 formation on dust with random temperature fluctuations. A&A, 569:A100, September 2014b. doi: 10.1051/0004-6361/201322101. (Cited on pages 14, 91 and 92.)

M. T. Carney, M. R. Hogerheijde, V. V. Guzmán, C. Walsh, K. I. Öberg, E. C. Fayolle, L. I. Cleeves, J. M. Carpenter, and C. Qi. Upper limits on CH_3OH in the HD 163296 protoplanetary disk. Evidence for a low gas-phase CH_3OH-to-H_2CO ratio. A&A, 623: A124, March 2019. doi: 10.1051/0004-6361/201834353. (Cited on page 147.)

John S. Carr and Joan R. Najita. Organic Molecules and Water in the Planet Formation Region of Young Circumstellar Disks. *Science*, 319(5869):1504, March 2008. doi: 10.1126/science.1153807. (Cited on page 140.)

D. Carrera, A. Johansen, and M. B. Davies. How to form asteroids from mm-sized grains. In I. Boisse, O. Demangeon, F. Bouchy, and L. Arnold, editors, *Twenty Years of Giant Exoplanets*, pages 105–108, October 2015. (Cited on page 33.)

P. Caselli, T. I. Hasegawa, and Eric Herbst. A Proposed Modification of the Rate Equations for Reactions on Grain Surfaces. ApJ, 495(1):309–316, March 1998. doi: 10.1086/305253. (Cited on page 83.)

Paola Caselli, Priscilla J. Benson, Philip C. Myers, and Mario Tafalla. Dense Cores in Dark Clouds. XIV. N_2H^+ (1-0) Maps of Dense Cloud Cores. ApJ, 572(1):238–263, June 2002. doi: 10.1086/340195. (Cited on page 30.)

S. Cazaux and A. G. G. M. Tielens. H_2 Formation on Grain Surfaces. ApJ, 604(1): 222–237, March 2004. doi: 10.1086/381775. (Cited on page 90.)

Edwige Chapillon, Anne Dutrey, Stéphane Guilloteau, Vincent Piétu, Valentine Wakelam, Franck Hersant, Fréderic Gueth, Thomas Henning, Ralf Launhardt, Katharina Schreyer, and Dmitry Semenov. Chemistry in Disks. VII. First Detection of HC_3N in Protoplanetary Disks. ApJ, 756(1):58, September 2012. doi: 10.1088/0004-637X/756/1/58. (Cited on page 143.)

E. I. Chiang and P. Goldreich. Spectral Energy Distributions of T Tauri Stars with Passive Circumstellar Disks. ApJ, 490(1):368–376, November 1997. doi: 10.1086/304869. (Cited on page 56.)

Mark P. Collings, Mark A. Anderson, Rui Chen, John W. Dever, Serena Viti, David A. Williams, and Martin R. S. McCoustra. A laboratory survey of the thermal desorption of astrophysically relevant molecules. MNRAS, 354(4):1133–1140, November 2004. doi: 10.1111/j.1365-2966.2004.08272.x. (Cited on page 148.)

M. Compiègne, L. Verstraete, A. Jones, J. P. Bernard, F. Boulanger, N. Flagey, J. Le Bourlot, D. Paradis, and N. Ysard. The global dust SED: tracing the nature and evolution of dust with DustEM. A&A, 525:A103, January 2011. doi: 10.1051/0004-6361/201015292. (Cited on page 93.)

H. M. Cuppen and Eric Herbst. Monte Carlo simulations of H_2 formation on grains of varying surface roughness. MNRAS, 361(2):565–576, August 2005. doi: 10.1111/j.1365-2966.2005.09189.x. (Cited on page 90.)

H. M. Cuppen, O. Morata, and Eric Herbst. Monte Carlo simulations of H_2 formation on stochastically heated grains. MNRAS, 367(4):1757–1765, April 2006. doi: 10.1111/j.1365-2966.2006.10079.x. (Cited on page 93.)

H. M. Cuppen, E. F. van Dishoeck, E. Herbst, and A. G. G. M. Tielens. Microscopic simulation of methanol and formaldehyde ice formation in cold dense cores. A&A, 508 (1):275–287, December 2009. doi: 10.1051/0004-6361/200913119. (Cited on page 84.)

H. M. Cuppen, C. Walsh, T. Lamberts, D. Semenov, R. T. Garrod, E. M. Penteado, and S. Ioppolo. Grain Surface Models and Data for Astrochemistry. Space Sci. Rev., 212 (1-2):1–58, October 2017. doi: 10.1007/s11214-016-0319-3. (Cited on page 75.)

Jeffrey N. Cuzzi, Anthony R. Dobrovolskis, and Joelle M. Champney. Particle-Gas Dynamics in the Midplane of a Protoplanetary Nebula. Icarus, 106(1):102–134, November 1993. doi: 10.1006/icar.1993.1161. (Cited on page 67.)

A. Dalgarno. Astrophysical Importance of H_2. In F. Combes and G. Pineau Des Forets, editors, *Molecular Hydrogen in Space*, page 3, January 2000. (Cited on page 88.)

A. Dalgarno. A serendipitous journey. ARA&A, 46:1–20, September 2008. doi: 10.1146/annurev.astro.46.060407.145216. (Cited on page 33.)

E. Dartois, A. Dutrey, and S. Guilloteau. Structure of the DM Tau Outer Disk: Probing the vertical kinetic temperature gradient. A&A, 399:773–787, February 2003. doi: 10.1051/0004-6361:20021638. (Cited on page 98.)

M. De Becker. Astrochemistry: the issue of molecular complexity in astrophysical environments. *Bulletin de la Societe Royale des Sciences de Liege*, 82:33–94, May 2013. (Cited on page 33.)

F. X. Desert, F. Boulanger, and S. N. Shore. Grain temperature fluctuations - A key to infrared spectra. A&A, 160(2):295–300, May 1986. (Cited on page 93.)

L. B. D'Hendecourt, L. J. Allamandola, and J. M. Greenberg. Time dependent chemistry in dense molecular clouds. I. Grain surface reactions, gas/grain interactions and infrared spectroscopy. A&A, 152:130–150, November 1985. (Cited on page 83.)

C. Dominik, C. Ceccarelli, D. Hollenbach, and M. Kaufman. Gas-Phase Water in the Surface Layer of Protoplanetary Disks. ApJ, 635(1):L85–L88, December 2005. doi: 10.1086/498942. (Cited on page 140.)

Ruobing Dong, Zhaohuan Zhu, Roman R. Rafikov, and James M. Stone. Observational Signatures of Planets in Protoplanetary Disks: Spiral Arms Observed in Scattered Light Imaging Can be Induced by Planets. ApJ, 809(1):L5, August 2015. doi: 10.1088/2041-8205/809/1/L5. (Cited on pages 14, 67, 68 and 101.)

B. T. Draine and N. Anderson. Temperature fluctuations and infrared emission from interstellar grains. ApJ, 292:494–499, May 1985. doi: 10.1086/163181. (Cited on page 93.)

B. T. Draine and H. M. Lee. Optical Properties of Interstellar Graphite and Silicate Grains. ApJ, 285:89, Oct 1984. doi: 10.1086/162480. (Cited on pages 100 and 120.)

B. T. Draine and Aigen Li. Infrared Emission from Interstellar Dust. I. Stochastic Heating of Small Grains. ApJ, 551(2):807–824, April 2001. doi: 10.1086/320227. (Cited on page 93.)

Bruce T. Draine. *Physics of the Interstellar and Intergalactic Medium*. 2011. (Cited on pages 25, 26, 27 and 29.)

Fujun Du and Edwin A. Bergin. Water Vapor Distribution in Protoplanetary Disks. ApJ, 792(1):2, September 2014. doi: 10.1088/0004-637X/792/1/2. (Cited on page 140.)

B. Dubrulle, G. Morfill, and M. Sterzik. The dust subdisk in the protoplanetary nebula. Icarus, 114(2):237–246, April 1995. doi: 10.1006/icar.1995.1058. (Cited on page 67.)

W. W. Duley. *Temperature fluctuations and very cold dust*, volume 209 of *Astrophysics and Space Science Library*, page 29. 1996. doi: 10.1007/978-94-009-0335-7_3. (Cited on pages 90 and 93.)

C. P. Dullemond. Formation of (exo-)planets. *Astronomische Nachrichten*, 334(6):589, June 2013. doi: 10.1002/asna.201311899. (Cited on page 33.)

C. P. Dullemond, D. Hollenbach, I. Kamp, and P. D'Alessio. Models of the Structure and Evolution of Protoplanetary Disks. In Bo Reipurth, David Jewitt, and Klaus Keil, editors, *Protostars and Planets V*, page 555, January 2007. (Cited on pages 13 and 32.)

M. M. Dunham, A. M. Stutz, L. E. Allen, II Evans, N. J., W. J. Fischer, S. T. Megeath, P. C. Myers, S. S. R. Offner, C. A. Poteet, J. J. Tobin, and E. I. Vorobyov. The Evolution of Protostars: Insights from Ten Years of Infrared Surveys with Spitzer and Herschel. In Henrik Beuther, Ralf S. Klessen, Cornelis P. Dullemond, and Thomas Henning, editors, *Protostars and Planets VI*, page 195, January 2014. doi: 10.2458/azu_uapress_9780816531240-ch009. (Cited on page 30.)

A. Dutrey, S. Guilloteau, and M. Guelin. Chemistry of protosolar-like nebulae: The molecular content of the DM Tau and GG Tau disks. A&A, 317:L55–L58, January 1997. (Cited on page 143.)

A. Dutrey, D. Semenov, E. Chapillon, U. Gorti, S. Guilloteau, F. Hersant, M. Hogerheijde, M. Hughes, G. Meeus, H. Nomura, V. Piétu, C. Qi, and V. Wakelam. Physical and Chemical Structure of Planet-Forming Disks Probed by Millimeter Observations and Modeling. In Henrik Beuther, Ralf S. Klessen, Cornelis P. Dullemond, and Thomas Henning, editors, *Protostars and Planets VI*, page 317, January 2014. doi: 10.2458/azu_uapress_9780816531240-ch014. (Cited on pages 13, 46 and 50.)

A. Dutrey, S. Guilloteau, V. Piétu, E. Chapillon, V. Wakelam, E. Di Folco, T. Stoecklin, O. Denis-Alpizar, U. Gorti, R. Teague, T. Henning, D. Semenov, and N. Grosso. The Flying Saucer: Tomography of the thermal and density gas structure of an edge-on protoplanetary disk. A&A, 607:A130, Nov 2017. doi: 10.1051/0004-6361/201730645. (Cited on pages 17, 38, 109, 155 and 156.)

E. M. Edlund and H. Ji. Nonlinear stability of laboratory quasi-Keplerian flows. Phys. Rev. E, 89(2):021004, February 2014. doi: 10.1103/PhysRevE.89.021004. (Cited on page 60.)

Christian Eistrup, Catherine Walsh, and Ewine F. van Dishoeck. Chemical evolution in planet-forming regions. Impact on volatile abundances and C/O ratios of planet-building material. In Maria Cunningham, Tom Millar, and Yuri Aikawa, editors, *IAU Symposium*, volume 332 of *IAU Symposium*, pages 69–72, September 2018. doi: 10.1017/S1743921317009802. (Cited on page 139.)

E. C. Fayolle, K. I. Öberg, H. M. Cuppen, R. Visser, and H. Linnartz. Laboratory H_2O:CO_2 ice desorption data: entrapment dependencies and its parameterization with an extended three-phase model. A&A, 529:A74, May 2011. doi: 10.1051/0004-6361/201016121. (Cited on page 87.)

Jean-Hugues Fillion, Edith C. Fayolle, Xavier Michaut, Misha Doronin, Laurent Philippe, Joseph Rakovski, Claire Romanzin, Noel Champion, Karin I. Öberg, Harold Linnartz, and Mathieu Bertin. Wavelength resolved UV photodesorption and photochemistry of CO2 ice. *Faraday Discussions*, 168:533–552, January 2014. doi: 10.1039/C3FD00129F. (Cited on page 77.)

Kevin France, Eric Schindhelm, Edwin A. Bergin, Evelyne Roueff, and Hervé Abgrall. High-resolution Ultraviolet Radiation Fields of Classical T Tauri Stars. ApJ, 784(2):127, April 2014. doi: 10.1088/0004-637X/784/2/127. (Cited on pages 120, 121 and 126.)

Juhan Frank, Andrew King, and Derek J. Raine. *Accretion Power in Astrophysics: Third Edition*. 2002. (Cited on page 60.)

S. Fromang and R. P. Nelson. Global MHD simulations of stratified and turbulent protoplanetary discs. II. Dust settling. A&A, 496(3):597–608, March 2009. doi: 10.1051/0004-6361/200811220. (Cited on pages 14 and 68.)

S. Fromang and J. Papaloizou. Dust settling in local simulations of turbulent protoplanetary disks. A&A, 452(3):751–762, June 2006. doi: 10.1051/0004-6361:20054612. (Cited on page 67.)

Gaia Collaboration, A. G. A. Brown, A. Vallenari, T. Prusti, J. H. J. de Bruijne, F. Mignard, R. Drimmel, C. Babusiaux, C. A. L. Bailer-Jones, U. Bastian, M. Biermann, D. W. Evans, L. Eyer, F. Jansen, C. Jordi, D. Katz, S. A. Klioner, U. Lammers, L. Lindegren, X. Luri, W. O'Mullane, C. Panem, D. Pourbaix, S. Randich, P. Sartoretti, H. I. Siddiqui, C. Soubiran, V. Valette, F. van Leeuwen, N. A. Walton,

C. Aerts, F. Arenou, M. Cropper, E. Høg, M. G. Lattanzi, E. K. Grebel, A. D. Holland, C. Huc, X. Passot, M. Perryman, L. Bramante, C. Cacciari, J. Castañeda, L. Chaoul, N. Cheek, F. De Angeli, C. Fabricius, R. Guerra, J. Hernández, A. Jean-Antoine-Piccolo, E. Masana, R. Messineo, N. Mowlavi, K. Nienartowicz, D. Ordóñez-Blanco, P. Panuzzo, J. Portell, P. J. Richards, M. Riello, G. M. Seabroke, P. Tanga, F. Thévenin, J. Torra, S. G. Els, G. Gracia-Abril, G. Comoretto, M. Garcia-Reinaldos, T. Lock, E. Mercier, M. Altmann, R. Andrae, T. L. Astraatmadja, I. Bellas-Velidis, K. Benson, J. Berthier, R. Blomme, G. Busso, B. Carry, A. Cellino, G. Clementini, S. Cowell, O. Creevey, J. Cuypers, M. Davidson, J. De Ridder, A. de Torres, L. Delchambre, A. Dell'Oro, C. Ducourant, Y. Frémat, M. García-Torres, E. Gosset, J. L. Halbwachs, N. C. Hambly, D. L. Harrison, M. Hauser, D. Hestroffer, S. T. Hodgkin, H. E. Huckle, A. Hutton, G. Jasniewicz, S. Jordan, M. Kontizas, A. J. Korn, A. C. Lanzafame, M. Manteiga, A. Moitinho, K. Muinonen, J. Osinde, E. Pancino, T. Pauwels, J. M. Petit, A. Recio-Blanco, A. C. Robin, L. M. Sarro, C. Siopis, M. Smith, K. W. Smith, A. Sozzetti, W. Thuillot, W. van Reeven, Y. Viala, U. Abbas, A. Abreu Aramburu, S. Accart, J. J. Aguado, P. M. Allan, W. Allasia, G. Altavilla, M. A. Álvarez, J. Alves, R. I. Anderson, A. H. Andrei, E. Anglada Varela, E. Antiche, T. Antoja, S. Antón, B. Arcay, N. Bach, S. G. Baker, L. Balaguer-Núñez, C. Barache, C. Barata, A. Barbier, F. Barblan, D. Barrado y Navascués, M. Barros, M. A. Barstow, U. Becciani, M. Bellazzini, A. Bello García, V. Belokurov, P. Bendjoya, A. Berihuete, L. Bianchi, O. Bienaymé, F. Billebaud, N. Blagorodnova, S. Blanco-Cuaresma, T. Boch, A. Bombrun, R. Borrachero, S. Bouquillon, G. Bourda, H. Bouy, A. Bragaglia, M. A. Breddels, N. Brouillet, T. Brüsemeister, B. Bucciarelli, P. Burgess, R. Burgon, A. Burlacu, D. Busonero, R. Buzzi, E. Caffau, J. Cambras, H. Campbell, R. Cancelliere, T. Cantat-Gaudin, T. Carlucci, J. M. Carrasco, M. Castellani, P. Charlot, J. Charnas, A. Chiavassa, M. Clotet, G. Cocozza, R. S. Collins, G. Costigan, F. Crifo, N. J. G. Cross, M. Crosta, C. Crowley, C. Dafonte, Y. Damerdji, A. Dapergolas, P. David, M. David, P. De Cat, F. de Felice, P. de Laverny, F. De Luise, R. De March, D. de Martino, R. de Souza, J. Debosscher, E. del Pozo, M. Delbo, A. Delgado, H. E. Delgado, P. Di Matteo, S. Diakite, E. Distefano, C. Dolding, S. Dos Anjos, P. Drazinos, J. Duran, Y. Dzigan, B. Edvardsson, H. Enke, N. W. Evans, G. Eynard Bontemps, C. Fabre, M. Fabrizio, S. Faigler, A. J. Falcão, M. Farràs Casas, L. Federici, G. Fedorets, J. Fernández-Hernández, P. Fernique, A. Fienga, F. Figueras, F. Filippi, K. Findeisen, A. Fonti, M. Fouesneau, E. Fraile, M. Fraser, J. Fuchs, M. Gai, S. Galleti, L. Galluccio, D. Garabato, F. García-Sedano, A. Garofalo, N. Garralda, P. Gavras, J. Gerssen, R. Geyer, G. Gilmore, S. Girona, G. Giuffrida, M. Gomes, A. González-Marcos, J. González-Núñez, J. J. González-Vidal, M. Granvik, A. Guerrier, P. Guillout, J. Guiraud, A. Gúrpide, R. Gutiérrez-Sánchez, L. P. Guy, R. Haigron, D. Hatzidimitriou, M. Haywood, U. Heiter, A. Helmi, D. Hobbs, W. Hofmann, B. Holl, G. Holland , J. A. S. Hunt, A. Hypki, V. Icardi, M. Irwin, G. Jevardat de Fombelle, P. Jofré, P. G. Jonker, A. Jorissen, F. Julbe, A. Karampelas, A. Kochoska, R. Kohley, K. Kolenberg, E. Kontizas, S. E. Koposov, G. Kordopatis, P. Koubsky, A. Krone-Martins, M. Kudryashova, I. Kull, R. K. Bachchan, F. Lacoste-Seris, A. F. Lanza, J. B. Lavigne, C. Le Poncin-Lafitte, Y. Le-

breton, T. Lebzelter, S. Leccia, N. Leclerc, I. Lecoeur-Taibi, V. Lemaitre, H. Lenhardt, F. Leroux, S. Liao, E. Licata, H. E. P. Lindstrøm, T. A. Lister, E. Livanou, A. Lobel, W. Löffler, M. López, D. Lorenz, I. MacDonald, T. Magalhães Fernandes, S. Managau, R. G. Mann, G. Mantelet, O. Marchal, J. M. Marchant, M. Marconi, S. Marinoni, P. M. Marrese, G. Marschalkó, D. J. Marshall, J. M. Martín-Fleitas, M. Martino, N. Mary, G. Matijevič, T. Mazeh, P. J. McMillan, S. Messina, D. Michalik, N. R. Millar, B. M. H. Mirand a, D. Molina, R. Molinaro, M. Molinaro, L. Molnár, M. Moniez, P. Montegriffo, R. Mor, A. Mora, R. Morbidelli, T. Morel, S. Morgenthaler, D. Morris, A. F. Mulone, T. Muraveva, I. Musella, J. Narbonne, G. Nelemans, L. Nicastro, L. Noval, C. Ordénovic, J. Ordieres-Meré, P. Osborne, C. Pagani, I. Pagano, F. Pailler, H. Palacin, L. Palaversa, P. Parsons, M. Pecoraro, R. Pedrosa, H. Pentikäinen, B. Pichon, A. M. Piersimoni, F. X. Pineau, E. Plachy, G. Plum, E. Poujoulet, A. Prša, L. Pulone, S. Ragaini, S. Rago, N. Rambaux, M. Ramos-Lerate, P. Ranalli, G. Rauw, A. Read, S. Regibo, C. Reylé, R. A. Ribeiro, L. Rimoldini, V. Ripepi, A. Riva, G. Rixon, M. Roelens, M. Romero-Gómez, N. Rowell, F. Royer, L. Ruiz-Dern, G. Sadowski, T. Sagristà Sellés, J. Sahlmann, J. Salgado, E. Salguero, M. Sarasso, H. Savietto, M. Schultheis, E. Sciacca, M. Segol, J. C. Segovia, D. Segransan, I. C. Shih, R. Smareglia, R. L. Smart, E. Solano, F. Solitro, R. Sordo, S. Soria Nieto, J. Souchay, A. Spagna, F. Spoto, U. Stampa, I. A. Steele, H. Steidelmüller, C. A. Stephenson, H. Stoev, F. F. Suess, M. Süveges, J. Surdej, L. Szabados, E. Szegedi-Elek, D. Tapiador, F. Taris, G. Tauran, M. B. Taylor, R. Teixeira, D. Terrett, B. Tingley, S. C. Trager, C. Turon, A. Ulla, E. Utrilla, G. Valentini, A. van Elteren, E. Van Hemelryck, M. van Leeuwen, M. Varadi, A. Vecchiato, J. Veljanoski, T. Via, D. Vicente, S. Vogt, H. Voss, V. Votruba, S. Voutsinas, G. Walmsley, M. Weiler, K. Weingrill, T. Wevers, Ł. Wyrzykowski, A. Yoldas, M. Žerjal, S. Zucker, C. Zurbach, T. Zwitter, A. Alecu, M. Allen, C. Allende Prieto, A. Amorim, G. Anglada-Escudé, V. Arsenijevic, S. Azaz, P. Balm, M. Beck, H. H. Bernstein, L. Bigot, A. Bijaoui, C. Blasco, M. Bonfigli, G. Bono, S. Boudreault, A. Bressan, S. Brown, P. M. Brunet, P. Bunclark, R. Buonanno, A. G. Butkevich, C. Carret, C. Carrion, L. Chemin, F. Chéreau, L. Corcione, E. Darmigny, K. S. de Boer, P. de Teodoro, P. T. de Zeeuw, C. Delle Luche, C. D. Domingues, P. Dubath, F. Fodor, B. Frézouls, A. Fries, D. Fustes, D. Fyfe, E. Gallardo, J. Gallegos, D. Gardiol, M. Gebran, A. Gomboc, A. Gómez, E. Grux, A. Gueguen, A. Heyrovsky, J. Hoar, G. Iannicola, Y. Isasi Parache, A. M. Janotto, E. Joliet, A. Jonckheere, R. Keil, D. W. Kim, P. Klagyivik, J. Klar, J. Knude, O. Kochukhov, I. Kolka, J. Kos, A. Kutka, V. Lainey, D. LeBouquin, C. Liu, D. Loreggia, V. V. Makarov, M. G. Marseille, C. Martayan, O. Martinez-Rubi, B. Massart, F. Meynadier, S. Mignot, U. Munari, A. T. Nguyen, T. Nordlander, P. Ocvirk, K. S. O'Flaherty, A. Olias Sanz, P. Ortiz, J. Osorio, D. Oszkiewicz, A. Ouzounis, M. Palmer, P. Park, E. Pasquato, C. Peltzer, J. Peralta, F. Péturaud, T. Pieniluoma, E. Pigozzi, J. Poels, G. Prat, T. Prod'homme, F. Raison, J. M. Rebordao, D. Risquez, B. Rocca-Volmerange, S. Rosen, M. I. Ruiz-Fuertes, F. Russo, S. Sembay, I. Serraller Vizcaino, A. Short, A. Siebert, H. Silva, D. Sinachopoulos, E. Slezak, M. Soffel, D. Sosnowska, V. Straižys, M. ter Linden, D. Terrell, S. Theil, C. Tiede, L. Troisi, P. Tsalmantza, D. Tur, M. Vaccari, F. Vachier, P. Valles, W. Van Hamme,

L. Veltz, J. Virtanen, J. M. Wallut, R. Wichmann, M. I. Wilkinson, H. Ziaeepour, and S. Zschocke. Gaia Data Release 1. Summary of the astrometric, photometric, and survey properties. A&A, 595:A2, November 2016. doi: 10.1051/0004-6361/201629512. (Cited on page 47.)

R. Garrod and T. Pauly. Modeling the formation of interstellar CO_2, CO and water ice. In José Cernicharo and Rafael Bachiller, editors, *The Molecular Universe*, volume 280 of *IAU Symposium*, page 173, May 2011. (Cited on pages 80, 86 and 87.)

R. T. Garrod, V. Wakelam, and E. Herbst. Non-thermal desorption from interstellar dust grains via exothermic surface reactions. A&A, 467(3):1103–1115, June 2007. doi: 10.1051/0004-6361:20066704. (Cited on pages 78 and 79.)

Robin Garrod, In Hee Park, Paola Caselli, and Eric Herbst. Are gas-phase models of interstellar chemistry tenable? The case of methanol. *Faraday Discussions*, 133:51, January 2006. doi: 10.1039/b516202e. (Cited on page 78.)

Robin T. Garrod. A Three-phase Chemical Model of Hot Cores: The Formation of Glycine. ApJ, 765(1):60, March 2013. doi: 10.1088/0004-637X/765/1/60. (Cited on page 87.)

M. Gaudel, A. J. Maury, A. Belloche, S. Maret, Ph. André, P. Hennebelle, M. Galametz, L. Testi, S. Cabrit, P. Palmeirim, B. Ladjelate, C. Codella, and L. Podio. Angular momentum profiles of Class 0 protostellar envelopes. A&A, 637:A92, May 2020. doi: 10.1051/0004-6361/201936364. (Cited on page 30.)

J. X. Ge, J. H. He, and Aigen Li. Interstellar chemical differentiation across grain sizes. MNRAS, 460(1):L50–L54, July 2016. doi: 10.1093/mnrasl/slw058. (Cited on page 87.)

Nir Goldman, Evan J. Reed, Laurence E. Fried, I. F. William Kuo, and Amitesh Maiti. Synthesis of glycine-containing complexes in impacts of comets on early Earth. *Nature Chemistry*, 2(11):949–954, November 2010. doi: 10.1038/nchem.827. (Cited on page 145.)

Peter Goldreich and William R. Ward. The Formation of Planetesimals. ApJ, 183: 1051–1062, August 1973. doi: 10.1086/152291. (Cited on page 33.)

I. E. Gordon, L. S. Rothman, C. Hill, R. V. Kochanov, Y. Tan, P. F. Bernath, M. Birk, V. Boudon, A. Campargue, K. V. Chance, B. J. Drouin, J. M. Flaud, R. R. Gamache, J. T. Hodges, D. Jacquemart, V. I. Perevalov, A. Perrin, K. P. Shine, M. A. H. Smith, J. Tennyson, G. C. Toon, H. Tran, V. G. Tyuterev, A. Barbe, A. G. Császár, V. M. Devi, T. Furtenbacher, J. J. Harrison, J. M. Hartmann, A. Jolly, T. J. Johnson, T. Karman, I. Kleiner, A. A. Kyuberis, J. Loos, O. M. Lyulin, S. T. Massie, S. N. Mikhailenko, N. Moazzen-Ahmadi, H. S. P. Müller, O. V. Naumenko, A. V. Nikitin, O. L. Polyansky, M. Rey, M. Rotger, S. W. Sharpe, K. Sung, E. Starikova, S. A. Tashkun, J. Vand er Auwera, G. Wagner, J. Wilzewski, P. Wcisło, S. Yu, and E. J. Zak. The HITRAN2016 molecular spectroscopic database. J. Quant. Spec. Radiat. Transf., 203:3–69, December 2017. doi: 10.1016/j.jqsrt.2017.06.038. (Cited on page 34.)

Robert J. Gould and Edwin E. Salpeter. The Interstellar Abundance of the Hydrogen Molecule. I. Basic Processes. ApJ, 138:393, August 1963. doi: 10.1086/147654. (Cited on page 90.)

Pierre Gratier, Emeric Bron, Maryvonne Gerin, Jérôme Pety, Viviana V. Guzman, Jan Orkisz, Sébastien Bardeau, Javier R. Goicoechea, Franck Le Petit, Harvey Liszt, Karin Öberg, Nicolas Peretto, Evelyne Roueff, Albrech Sievers, and Pascal Tremblin. Dissecting the molecular structure of the Orion B cloud: insight from principal component analysis. A&A, 599:A100, March 2017. doi: 10.1051/0004-6361/201629847. (Cited on page 35.)

J. Mayo Greenberg. *Interstellar Grains*, page 221. 1968. (Cited on page 93.)

S. Guilloteau, A. Dutrey, V. Piétu, and Y. Boehler. A dual-frequency sub-arcsecond study of proto-planetary disks at mm wavelengths: first evidence for radial variations of the dust properties. A&A, 529:A105, May 2011. doi: 10.1051/0004-6361/201015209. (Cited on page 55.)

Emilie Habart, Malcolm Walmsley, Laurent Verstraete, Stephanie Cazaux, Roberto Maiolino, Pierre Cox, Francois Boulanger, and Guillaume Pineau des Forêts. Molecular Hydrogen. Space Sci. Rev., 119(1-4):71–91, August 2005. doi: 10.1007/s11214-005-8062-1. (Cited on page 88.)

J. Harris and B. Kasemo. On precursor mechanisms for surface reactions. *Surf. Sci.*, 105, December 1981. doi: 10.1016/0167-2584(81)90068-2. (Cited on page 82.)

Tatsuhiko I. Hasegawa and Eric Herbst. New gas-grain chemical models of quiscent dense interstellar clouds :the effects of H2 tunnelling reactions and cosmic ray induced desorption. MNRAS, 261:83–102, March 1993. doi: 10.1093/mnras/261.1.83. (Cited on pages 77 and 87.)

Tatsuhiko I. Hasegawa, Eric Herbst, and Chun M. Leung. Models of Gas-Grain Chemistry in Dense Interstellar Clouds with Complex Organic Molecules. ApJS, 82:167, September 1992. doi: 10.1086/191713. (Cited on pages 82, 83 and 88.)

A. N. Heays, A. D. Bosman, and E. F. van Dishoeck. Photodissociation and photoionisation of atoms and molecules of astrophysical interest. A&A, 602:A105, June 2017. doi: 10.1051/0004-6361/201628742. (Cited on pages 34, 113 and 115.)

S. Heese, S. Wolf, A. Dutrey, and S. Guilloteau. Spread of the dust temperature distribution in circumstellar disks. A&A, 604:A5, July 2017. doi: 10.1051/0004-6361/201730501. (Cited on pages 13, 36, 37, 103 and 123.)

J. Holdship, N. Jeffrey, A. Makrymallis, S. Viti, and J. Yates. Bayesian Inference of the Rates of Surface Reactions in Icy Mantles. ApJ, 866(2):116, October 2018. doi: 10.3847/1538-4357/aae1fa. (Cited on page 35.)

D. J. Hollenbach and A. G. G. M. Tielens. Photodissociation regions in the interstellar medium of galaxies. *Reviews of Modern Physics*, 71(1):173–230, January 1999. doi: 10.1103/RevModPhys.71.173. (Cited on page 90.)

David Hollenbach, Doug Johnstone, Susana Lizano, and Frank Shu. Photoevaporation of Disks around Massive Stars and Application to Ultracompact H II Regions. ApJ, 428: 654, June 1994. doi: 10.1086/174276. (Cited on page 64.)

Jane Huang, Sean M. Andrews, Cornelis P. Dullemond, Andrea Isella, Laura M. Pérez, Viviana V. Guzmán, Karin I. Öberg, Zhaohuan Zhu, Shangjia Zhang, Xue-Ning Bai, Myriam Benisty, Tilman Birnstiel, John M. Carpenter, A. Meredith Hughes, Luca Ricci, Erik Weaver, and David J. Wilner. The Disk Substructures at High Angular Resolution Project (DSHARP). II. Characteristics of Annular Substructures. ApJ, 869 (2):L42, December 2018. doi: 10.3847/2041-8213/aaf740. (Cited on page 48.)

Reggie L. Hudson and Perry A. Gerakines. Infrared Spectra and Interstellar Sulfur: New Laboratory Results for H_2S and Four Malodorous Thiol Ices. ApJ, 867(2):138, November 2018. doi: 10.3847/1538-4357/aae52a. (Cited on page 139.)

Wasim Iqbal and Valentine Wakelam. Nautilus multi-grain model: Importance of cosmic-ray-induced desorption in determining the chemical abundances in the ISM. A&A, 615: A20, Jul 2018. doi: 10.1051/0004-6361/201732486. (Cited on pages 37, 82 and 88.)

Wasim Iqbal, Kinsuk Acharyya, and Eric Herbst. Kinetic Monte Carlo Studies of H_2 Formation on Grain Surfaces over a Wide Temperature Range. ApJ, 751(1):58, May 2012. doi: 10.1088/0004-637X/751/1/58. (Cited on page 90.)

Wasim Iqbal, Kinsuk Acharyya, and Eric Herbst. H_2 Formation in Diffuse Clouds: A New Kinetic Monte Carlo Study. ApJ, 784(2):139, April 2014. doi: 10.1088/0004-637X/784/2/139. (Cited on page 90.)

Anders Johansen, Jeffrey S. Oishi, Mordecai-Mark Mac Low, Hubert Klahr, Thomas Henning, and Andrew Youdin. Rapid planetesimal formation in turbulent circumstellar disks. Nature, 448(7157):1022–1025, August 2007. doi: 10.1038/nature06086. (Cited on page 33.)

M. Jura. Formation and destruction rates of interstellar H_2. ApJ, 191:375–379, July 1974. doi: 10.1086/152975. (Cited on page 90.)

N. Katz, I. Furman, O. Biham, V. Pirronello, and G. Vidali. Molecular Hydrogen Formation on Astrophysically Relevant Surfaces. ApJ, 522(1):305–312, September 1999. doi: 10.1086/307642. (Cited on page 90.)

S. J. Kenyon and L. Hartmann. Spectral Energy Distributions of T Tauri Stars: Disk Flaring and Limits on Accretion. ApJ, 323:714, December 1987. doi: 10.1086/165866. (Cited on page 56.)

Kaitlin Kratter and Giuseppe Lodato. Gravitational Instabilities in Circumstellar Disks. ARA&A, 54:271–311, September 2016. doi: 10.1146/annurev-astro-081915-023307. (Cited on page 30.)

Ari Laor and Bruce T. Draine. Spectroscopic Constraints on the Properties of Dust in Active Galactic Nuclei. ApJ, 402:441, Jan 1993. doi: 10.1086/172149. (Cited on pages 100 and 120.)

R. B. Larson. Cloud fragmentation and stellar masses. MNRAS, 214:379–398, June 1985. doi: 10.1093/mnras/214.3.379. (Cited on page 29.)

J. Le Bourlot, F. Le Petit, C. Pinto, E. Roueff, and F. Roy. Surface chemistry in the interstellar medium. I. H_2 formation by Langmuir-Hinshelwood and Eley-Rideal mechanisms. A&A, 541:A76, May 2012. doi: 10.1051/0004-6361/201118126. (Cited on page 94.)

F. Le Petit, B. Barzel, O. Biham, E. Roueff, and J. Le Bourlot. Incorporation of stochastic chemistry on dust grains in the Meudon PDR code using moment equations. I. Application to the formation of H{2} and HD. A&A, 505(3):1153–1165, October 2009. doi: 10.1051/0004-6361/200912269. (Cited on page 93.)

M. Lecar, M. Podolak, D. Sasselov, and E. Chiang. On the Location of the Snow Line in a Protoplanetary Disk. ApJ, 640(2):1115–1118, April 2006. doi: 10.1086/500287. (Cited on page 140.)

H. H. Lee, E. Herbst, G. Pineau des Forets, E. Roueff, and J. Le Bourlot. Photodissociation of H_2_ and CO and time dependent chemistry in inhomogeneous interstellar clouds. A&A, 311:690–707, July 1996. (Cited on page 121.)

A. Leger, M. Jura, and A. Omont. Desorption from interstellar grains. A&A, 144(1): 147–160, March 1985. (Cited on page 77.)

G. Lesur and P. Y. Longaretti. On the relevance of subcritical hydrodynamic turbulence to accretion disk transport. A&A, 444(1):25–44, December 2005. doi: 10.1051/0004-6361: 20053683. (Cited on page 60.)

A. Lipshtat and O. Biham. Moment equations for chemical reactions on interstellar dust grains. A&A, 400:585–593, March 2003. doi: 10.1051/0004-6361:20021902. (Cited on page 93.)

D. Lynden-Bell and J. E. Pringle. The evolution of viscous discs and the origin of the nebular variables. MNRAS, 168:603–637, September 1974. doi: 10.1093/mnras/168.3. 603. (Cited on page 55.)

Eric E. Mamajek. Initial Conditions of Planet Formation: Lifetimes of Primordial Disks. In Tomonori Usuda, Motohide Tamura, and Miki Ishii, editors, *American Institute of Physics Conference Series*, volume 1158 of *American Institute of Physics Conference Series*, pages 3–10, August 2009. doi: 10.1063/1.3215910. (Cited on pages 30 and 32.)

J. S. Mathis, W. Rumpl, and K. H. Nordsieck. The size distribution of interstellar grains. ApJ, 217:425–433, Oct 1977. doi: 10.1086/155591. (Cited on pages 88 and 100.)

D. McElroy, C. Walsh, A. J. Markwick, M. A. Cordiner, K. Smith, and T. J. Millar. The UMIST database for astrochemistry 2012. A&A, 550:A36, February 2013. doi: 10.1051/0004-6361/201220465. (Cited on page 35.)

Brett A. McGuire. 2018 Census of Interstellar, Circumstellar, Extragalactic, Protoplanetary Disk, and Exoplanetary Molecules. ApJS, 239(2):17, December 2018. doi: 10.3847/1538-4365/aae5d2. (Cited on pages 19, 27, 33, 35, 44 and 45.)

Gustav Mie. Beiträge zur Optik trüber Medien, speziell kolloidaler Metallösungen. *Annalen der Physik*, 330(3):377–445, Jan 1908. doi: 10.1002/andp.19083300302. (Cited on page 120.)

M. Minissale and F. Dulieu. Influence of surface coverage on the chemical desorption process. J. Chem. Phys., 141(1):014304, July 2014. doi: 10.1063/1.4885847. (Cited on page 78.)

M. Minissale, F. Dulieu, S. Cazaux, and S. Hocuk. Dust as interstellar catalyst. I. Quantifying the chemical desorption process. A&A, 585:A24, January 2016. doi: 10.1051/0004-6361/201525981. (Cited on pages 78, 133, 136 and 148.)

Michael J. Mumma and Steven B. Charnley. The Chemical Composition of Comets—Emerging Taxonomies and Natal Heritage. ARA&A, 49(1):471–524, September 2011. doi: 10.1146/annurev-astro-081309-130811. (Cited on page 145.)

Takayuki Muranushi, Satoshi Okuzumi, and Shu-ichiro Inutsuka. Interdependence of Electric Discharge and Magnetorotational Instability in Protoplanetary Disks. ApJ, 760(1):56, November 2012. doi: 10.1088/0004-637X/760/1/56. (Cited on page 61.)

Joan R. Najita and Edwin A. Bergin. Protoplanetary Disk Sizes and Angular Momentum Transport. ApJ, 864(2):168, September 2018. doi: 10.3847/1538-4357/aad80c. (Cited on page 30.)

A. Natta. Course 6: Star Formation. In F. Casoli, J. Lequeux, and F. David, editors, *Infrared Space Astronomy, Today and Tomorrow*, volume 70, page 193, January 2000. (Cited on page 30.)

J. A. Noble, P. Theule, F. Mispelaer, F. Duvernay, G. Danger, E. Congiu, F. Dulieu, and T. Chiavassa. The desorption of H_2CO from interstellar grains analogues. A&A, 543: A5, July 2012. doi: 10.1051/0004-6361/201219437. (Cited on page 148.)

Karin I. Öberg, Chunhua Qi, Jeffrey K. J. Fogel, Edwin A. Bergin, Sean M. Andrews, Catherine Espaillat, David J. Wilner, Ilaria Pascucci, and Joel H. Kastner. Disk Imaging Survey of Chemistry with SMA. II. Southern Sky Protoplanetary Disk Data and Full Sample Statistics. ApJ, 734(2):98, June 2011. doi: 10.1088/0004-637X/734/2/98. (Cited on page 143.)

Karin I. Öberg, Viviana V. Guzmán, Kenji Furuya, Chunhua Qi, Yuri Aikawa, Sean M. Andrews, Ryan Loomis, and David J. Wilner. The comet-like composition of a protoplanetary disk as revealed by complex cyanides. Nature, 520(7546):198–201, April 2015. doi: 10.1038/nature14276. (Cited on pages 45, 143 and 145.)

Tyler Pauly and Robin T. Garrod. The Effects of Grain Size and Temperature Distributions on the Formation of Interstellar Ice Mantles. ApJ, 817(2):146, February 2016. doi: 10.3847/0004-637X/817/2/146. (Cited on page 87.)

N. T. Phuong, E. Chapillon, L. Majumdar, A. Dutrey, S. Guilloteau, V. Piétu, V. Wakelam, P. N. Diep, Y. W. Tang, T. Beck, and J. Bary. First detection of H_2S in a protoplanetary disk. The dense GG Tauri A ring. A&A, 616:L5, August 2018. doi: 10.1051/0004-6361/201833766. (Cited on page 139.)

H. M. Pickett, R. L. Poynter, E. A. Cohen, M. L. Delitsky, J. C. Pearson, and H. S. P. Müller. Submillimeter, millimeter and microwave spectral line catalog. J. Quant. Spec. Radiat. Transf., 60(5):883–890, November 1998. doi: 10.1016/S0022-4073(98)00091-0. (Cited on page 34.)

L. Podio, I. Kamp, C. Codella, S. Cabrit, B. Nisini, C. Dougados, G. Sandell, J. P. Williams, L. Testi, W. F. Thi, P. Woitke, R. Meijerink, M. Spaans, G. Aresu, F. Ménard, and C. Pinte. Water Vapor in the Protoplanetary Disk of DG Tau. ApJ, 766(1):L5, March 2013. doi: 10.1088/2041-8205/766/1/L5. (Cited on page 140.)

Klaus M. Pontoppidan, Colette Salyk, Geoffrey A. Blake, Rowin Meijerink, John S. Carr, and Joan Najita. A Spitzer Survey of Mid-infrared Molecular Emission from Protoplanetary Disks. I. Detection Rates. ApJ, 720(1):887–903, September 2010. doi: 10.1088/0004-637X/720/1/887. (Cited on page 140.)

Thomas Preibisch, Yong-Cheol Kim, Fabio Favata, Eric D. Feigelson, Ettore Flaccomio, Konstantin Getman, Giusi Micela, Salvatore Sciortino, Keivan Stassun, Beate Stelzer, and Hans Zinnecker. The Origin of T Tauri X-Ray Emission: New Insights from the Chandra Orion Ultradeep Project. ApJS, 160(2):401–422, October 2005. doi: 10.1086/432891. (Cited on page 61.)

J. E. Pringle. Accretion discs in astrophysics. ARA&A, 19:137–162, January 1981. doi: 10.1146/annurev.aa.19.090181.001033. (Cited on pages 54 and 55.)

Chunhua Qi, Karin I. Öberg, Sean M. Andrews, David J. Wilner, Edwin A. Bergin, A. Meredith Hughes, Michiel Hogherheijde, and Paola D'Alessio. Chemical Imaging of the CO Snow Line in the HD 163296 Disk. ApJ, 813(2):128, November 2015. doi: 10.1088/0004-637X/813/2/128. (Cited on pages 13 and 50.)

P. Rebusco, O. M. Umurhan, W. Kluźniak, and O. Regev. Global transient dynamics of three-dimensional hydrodynamical disturbances in a thin viscous accretion disk. *Physics of Fluids*, 21(7):076601–076601, July 2009. doi: 10.1063/1.3167411. (Cited on page 60.)

S. Reissl, S. Wolf, and R. Brauer. Radiative transfer with POLARIS. I. Analysis of magnetic fields through synthetic dust continuum polarization measurements. A&A, 593:A87, Sep 2016. doi: 10.1051/0004-6361/201424930. (Cited on page 120.)

P. Riviere-Marichalar, F. Ménard, W. F. Thi, I. Kamp, B. Montesinos, G. Meeus, P. Woitke, C. Howard, G. Sandell, L. Podio, W. R. F. Dent, I. Mendigutía, C. Pinte, G. J. White, and D. Barrado. Detection of warm water vapour in Taurus protoplanetary discs by Herschel. A&A, 538:L3, February 2012. doi: 10.1051/0004-6361/201118448. (Cited on page 140.)

Maxime Ruaud and Uma Gorti. A Three-phase Approach to Grain Surface Chemistry in Protoplanetary Disks: Gas, Ice Surfaces, and Ice Mantles of Dust Grains. ApJ, 885(2): 146, November 2019. doi: 10.3847/1538-4357/ab4996. (Cited on pages 35 and 139.)

Maxime Ruaud, Valentine Wakelam, and Franck Hersant. Gas and grain chemical composition in cold cores as predicted by the Nautilus three-phase model. MNRAS, 459 (4):3756–3767, July 2016. doi: 10.1093/mnras/stw887. (Cited on pages 80, 82 and 84.)

Takayoshi Sano and James M. Stone. The Effect of the Hall Term on the Nonlinear Evolution of the Magnetorotational Instability. I. Local Axisymmetric Simulations. ApJ, 570(1):314–328, May 2002. doi: 10.1086/339504. (Cited on page 62.)

N. I. Shakura and R. A. Sunyaev. Reprint of 1973A&A....24..337S. Black holes in binary systems. Observational appearance. A&A, 500:33–51, June 1973. (Cited on pages 58 and 59.)

M. Simon and L. Prato. Disk Dissipation in Single and Binary Young Star Systems in Taurus. ApJ, 450:824, September 1995. doi: 10.1086/176187. (Cited on page 64.)

T. Stantcheva, V. I. Shematovich, and E. Herbst. On the master equation approach to diffusive grain-surface chemistry: The H, O, CO system. A&A, 391:1069–1080, September 2002. doi: 10.1051/0004-6361:20020838. (Cited on page 84.)

Tomasz F. Stepinski. Generation of dynamo magnetic fields in the primordial solar nebula. Icarus, 97(1):130–141, May 1992. doi: 10.1016/0019-1035(92)90062-C. (Cited on page 61.)

A. Sternberg and A. Dalgarno. Chemistry in Dense Photon-dominated Regions. ApJS, 99:565, August 1995. doi: 10.1086/192198. (Cited on page 95.)

Amiel Sternberg, Franck Le Petit, Evelyne Roueff, and Jacques Le Bourlot. H I-to-H_2 Transitions and H I Column Densities in Galaxy Star-forming Regions. ApJ, 790(1): 10, July 2014. doi: 10.1088/0004-637X/790/1/10. (Cited on page 129.)

Jonathan Tennyson, Sergei N. Yurchenko, Ahmed F. Al-Refaie, Emma J. Barton, Katy L. Chubb, Phillip A. Coles, S. Diamantopoulou, Maire N. Gorman, Christian Hill, Aden Z. Lam, Lorenzo Lodi, Laura K. McKemmish, Yueqi Na, Alec Owens, Oleg L. Polyansky, Tom Rivlin, Clara Sousa-Silva, Daniel S. Underwood, Andrey Yachmenev, and

Emil Zak. The ExoMol database: Molecular line lists for exoplanet and other hot atmospheres. *Journal of Molecular Spectroscopy*, 327:73–94, September 2016. doi: 10.1016/j.jms.2016.05.002. (Cited on page 34.)

W. F. Thi, S. Hocuk, I. Kamp, P. Woitke, Ch. Rab, S. Cazaux, and P. Caselli. Warm dust surface chemistry. H_2 and HD formation. A&A, 634:A42, February 2020. doi: 10.1051/0004-6361/201731746. (Cited on page 90.)

A. G. G. M. Tielens and L. J. Allamandola. *Composition, Structure, and Chemistry of Interstellar Dust*, volume 134, page 397. 1987. doi: 10.1007/978-94-009-3861-8_16. (Cited on page 77.)

A. G. G. M. Tielens and W. Hagen. Model calculations of the molecular composition of interstellar grain mantles. A&A, 114(2):245–260, October 1982. (Cited on page 84.)

E. F. van Dishoeck and J. H. Black. The excitation of interstellar C2. ApJ, 258:533–547, July 1982. doi: 10.1086/160104. (Cited on page 121.)

Ewine F. van Dishoeck. Astrochemistry: overview and challenges. In Maria Cunningham, Tom Millar, and Yuri Aikawa, editors, *IAU Symposium*, volume 332 of *IAU Symposium*, pages 3–22, September 2018. doi: 10.1017/S1743921317011528. (Cited on page 33.)

Ewine F. van Dishoeck and John H. Black. The Photodissociation and Chemistry of Interstellar CO. ApJ, 334:771, November 1988. doi: 10.1086/166877. (Cited on page 115.)

A. I. Vasyunin, D. A. Semenov, D. S. Wiebe, and Th. Henning. A Unified Monte Carlo Treatment of Gas-Grain Chemistry for Large Reaction Networks. I. Testing Validity of Rate Equations in Molecular Clouds. ApJ, 691(2):1459–1469, February 2009. doi: 10.1088/0004-637X/691/2/1459. (Cited on page 84.)

G. Vidali, J. E. Roser, G. Manicò, and V. Pirronello. Experimental study of the formation of molecular hydrogen and carbon dioxide on dust grain analogues. *Advances in Space Research*, 33(1):6–13, January 2004. doi: 10.1016/j.asr.2003.08.003. (Cited on page 90.)

Gianfranco Vidali, Joe Roser, Giulio Manicó, Valerio Pirronello, Hagai B. Perets, and Ofer Biham. Formation of molecular hydrogen on analogues of interstellar dust grains: experiments and modelling. In *Journal of Physics Conference Series*, volume 6 of *Journal of Physics Conference Series*, pages 36–58, January 2005. doi: 10.1088/1742-6596/6/1/003. (Cited on page 90.)

V. Wakelam, E. Herbst, J. Le Bourlot, F. Hersant, F. Selsis, and S. Guilloteau. Sensitivity analyses of dense cloud chemical models. A&A, 517:A21, July 2010. doi: 10.1051/0004-6361/200913856. (Cited on page 87.)

V. Wakelam, J. C. Loison, E. Herbst, B. Pavone, A. Bergeat, K. Béroff, M. Chabot, A. Faure, D. Galli, W. D. Geppert, D. Gerlich, P. Gratier, N. Harada, K. M. Hickson, P. Honvault, S. J. Klippenstein, S. D. Le Picard, G. Nyman, M. Ruaud, S. Schlemmer,

I. R. Sims, D. Talbi, J. Tennyson, and R. Wester. The 2014 KIDA Network for Interstellar Chemistry. ApJS, 217(2):20, April 2015. doi: 10.1088/0067-0049/217/2/20. (Cited on pages 34 and 35.)

Valentine Wakelam and Eric Herbst. Polycyclic Aromatic Hydrocarbons in Dense Cloud Chemistry. ApJ, 680(1):371–383, June 2008. doi: 10.1086/587734. (Cited on page 87.)

Valentine Wakelam, Emeric Bron, Stephanie Cazaux, Francois Dulieu, Cécile Gry, Pierre Guillard, Emilie Habart, Liv Hornekær, Sabine Morisset, Gunnar Nyman, Valerio Pirronello, Stephen D. Price, Valeska Valdivia, Gianfranco Vidali, and Naoki Watanabe. H_2 formation on interstellar dust grains: The viewpoints of theory, experiments, models and observations. *Molecular Astrophysics*, 9:1–36, December 2017. doi: 10.1016/j.molap.2017.11.001. (Cited on pages 14, 81, 88, 136, 138 and 145.)

Catherine Walsh, Ryan A. Loomis, Karin I. Öberg, Mihkel Kama, Merel L. R. van 't Hoff, Tom J. Millar, Yuri Aikawa, Eric Herbst, Susanna L. Widicus Weaver, and Hideko Nomura. First Detection of Gas-phase Methanol in a Protoplanetary Disk. ApJ, 823(1): L10, May 2016. doi: 10.3847/2041-8205/823/1/L10. (Cited on pages 45, 143 and 147.)

S. J. Weidenschilling. Aerodynamics of solid bodies in the solar nebula. MNRAS, 180: 57–70, July 1977. doi: 10.1093/mnras/180.1.57. (Cited on page 70.)

S. J. Weidenschilling. Dust to planetesimals: Settling and coagulation in the solar nebula. Icarus, 44(1):172–189, October 1980. doi: 10.1016/0019-1035(80)90064-0. (Cited on page 33.)

Joseph C. Weingartner and B. T. Draine. Dust Grain-Size Distributions and Extinction in the Milky Way, Large Magellanic Cloud, and Small Magellanic Cloud. ApJ, 548(1): 296–309, February 2001. doi: 10.1086/318651. (Cited on pages 88 and 100.)

S. Weinreb, A. H. Barrett, M. L. Meeks, and J. C. Henry. Radio Observations of OH in the Interstellar Medium. Nature, 200(4909):829–831, November 1963. doi: 10.1038/200829a0. (Cited on page 26.)

F. L. Whipple. On certain aerodynamic processes for asteroids and comets. In Aina Elvius, editor, *From Plasma to Planet*, page 211, January 1972. (Cited on page 66.)

J. P. Williams, L. Blitz, and C. F. McKee. The Structure and Evolution of Molecular Clouds: from Clumps to Cores to the IMF. In V. Mannings, A. P. Boss, and S. S. Russell, editors, *Protostars and Planets IV*, page 97, May 2000. (Cited on page 30.)

Jonathan P. Williams and William M. J. Best. A Parametric Modeling Approach to Measuring the Gas Masses of Circumstellar Disks. ApJ, 788(1):59, Jun 2014. doi: 10.1088/0004-637X/788/1/59. (Cited on page 98.)

Thomas L. Wilson, Kristen Rohlfs, and Susanne Hüttemeister. *Tools of Radio Astronomy*. 2013. doi: 10.1007/978-3-642-39950-3. (Cited on pages 13 and 47.)

S. Wolf and N. V. Voshchinnikov. Mie scattering by ensembles of particles with very large size parameters. *Computer Physics Communications*, 162(2):113–123, Sep 2004. doi: 10.1016/j.cpc.2004.06.070. (Cited on page 120.)

Scott J. Wolk and Frederick M. Walter. A Search for Protoplanetary Disks Around Naked T Tauri Stars. AJ, 111:2066, May 1996. doi: 10.1086/117942. (Cited on page 64.)

Satoshi Yamamoto. *Introduction to Astrochemistry: Chemical Evolution from Interstellar Clouds to Star and Planet Formation*. 2017. doi: 10.1007/978-4-431-54171-4. (Cited on pages 13, 26 and 28.)

Andrew N. Youdin and Jeremy Goodman. Streaming Instabilities in Protoplanetary Disks. ApJ, 620(1):459–469, February 2005. doi: 10.1086/426895. (Cited on page 33.)

Andrew N. Youdin and Yoram Lithwick. Particle stirring in turbulent gas disks: Including orbital oscillations. Icarus, 192(2):588–604, December 2007. doi: 10.1016/j.icarus.2007.07.012. (Cited on page 67.)

Appendices

Appendix A

High UV (HUV) flux

A.1 Vertical profiles of abundance and density at 100 au

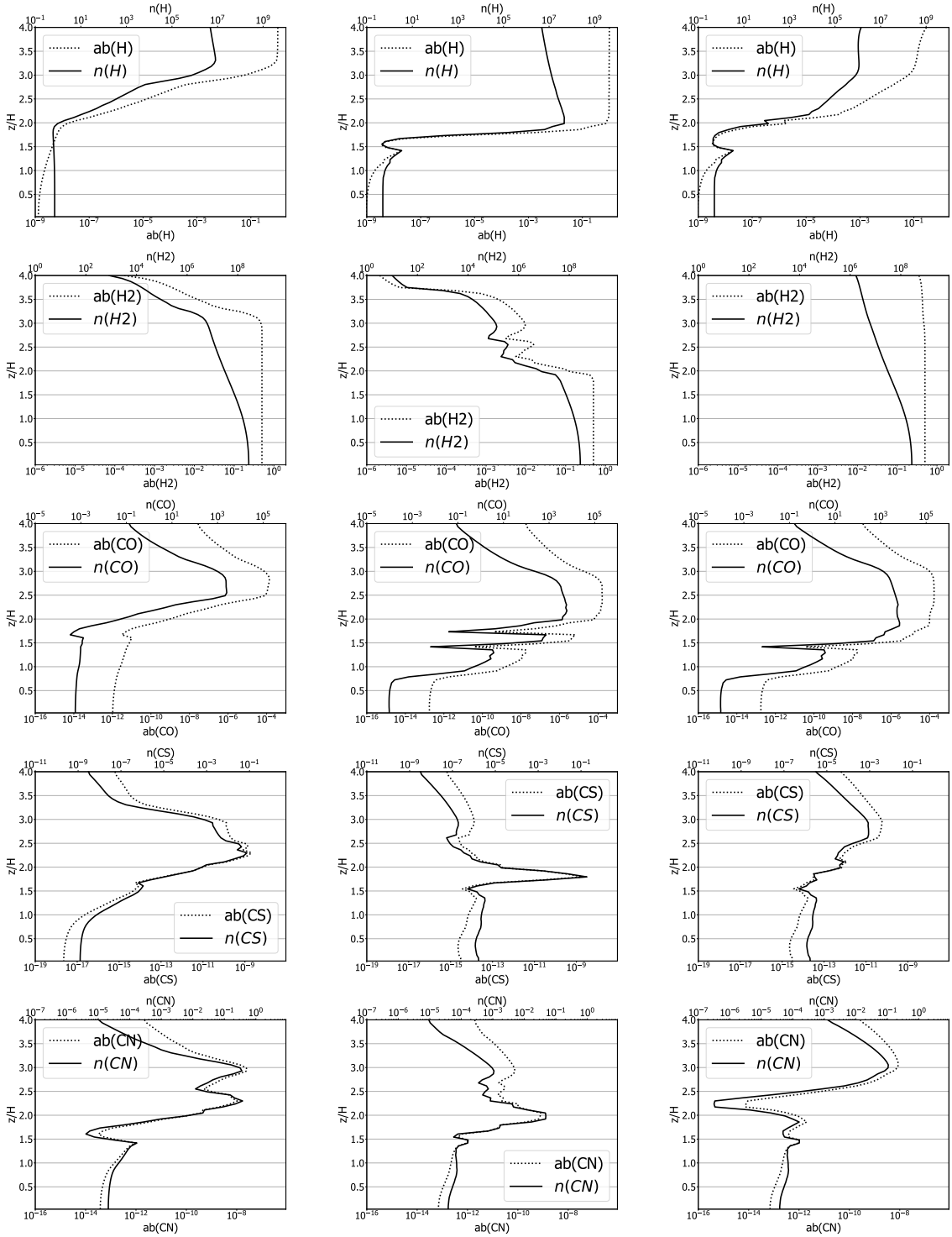

(a) HUV-LH-T_g (b) HUV-LH-T_a (c) HUV-B14-T_a

Figure A.1: Vertical profiles of H, H_2, CO, CS and CN at 100 au from the star of the HUV single-grain models. The dotted line is the abundance relative to H and the solid line is the density $[cm^{-3}]$.

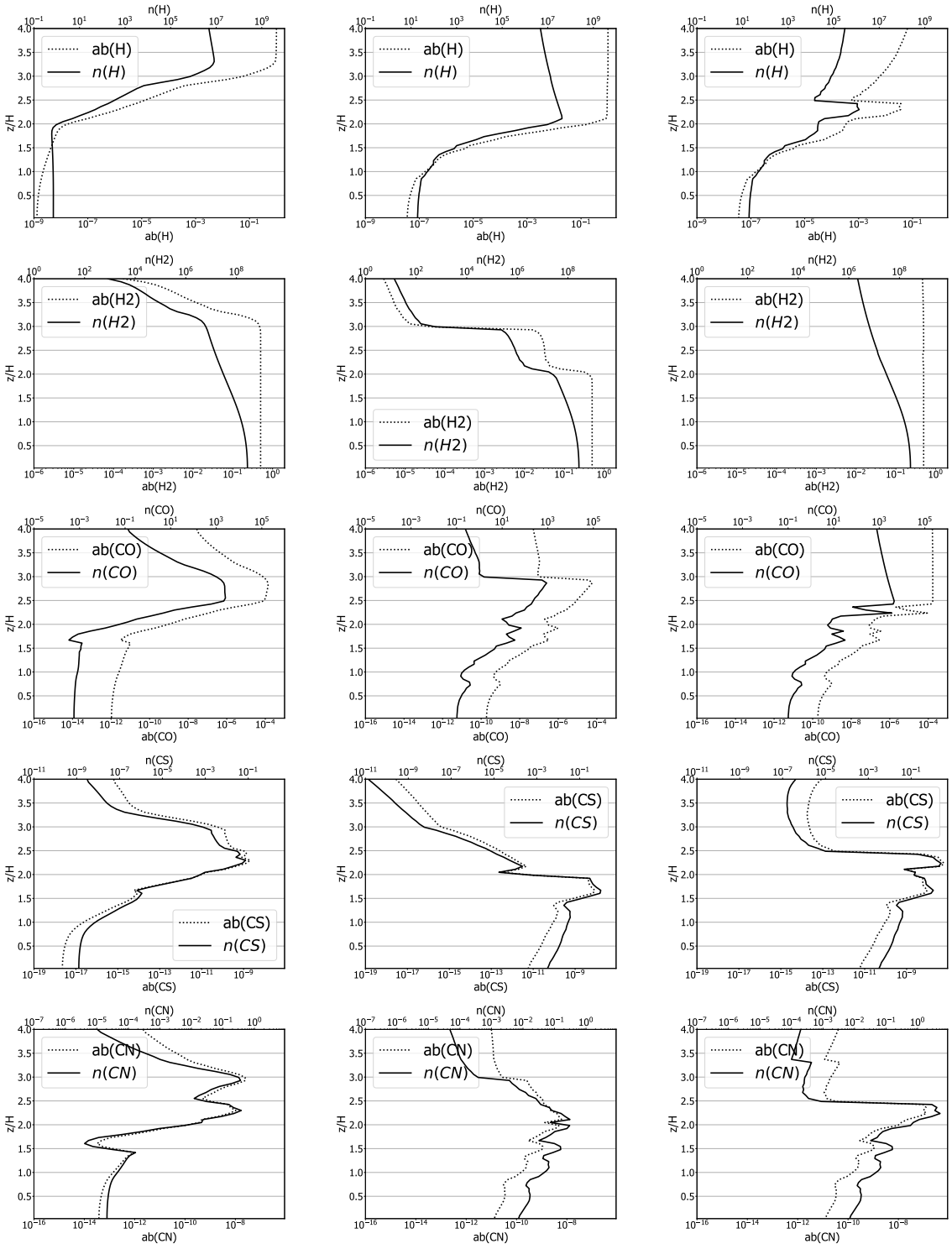

(a) HUV-LH-T_g (b) M-HUV-LH (c) M-HUV-B14

Figure A.2: Vertical profiles of H, H_2, CO, CS and CN at 100 au from the star of the HUV single-grain model HUV-LH-T_g on the left column, and multi-grain models on middle and right columns. The dotted line is the abundance relative to H and the solid line is the density $[cm^{-3}]$.

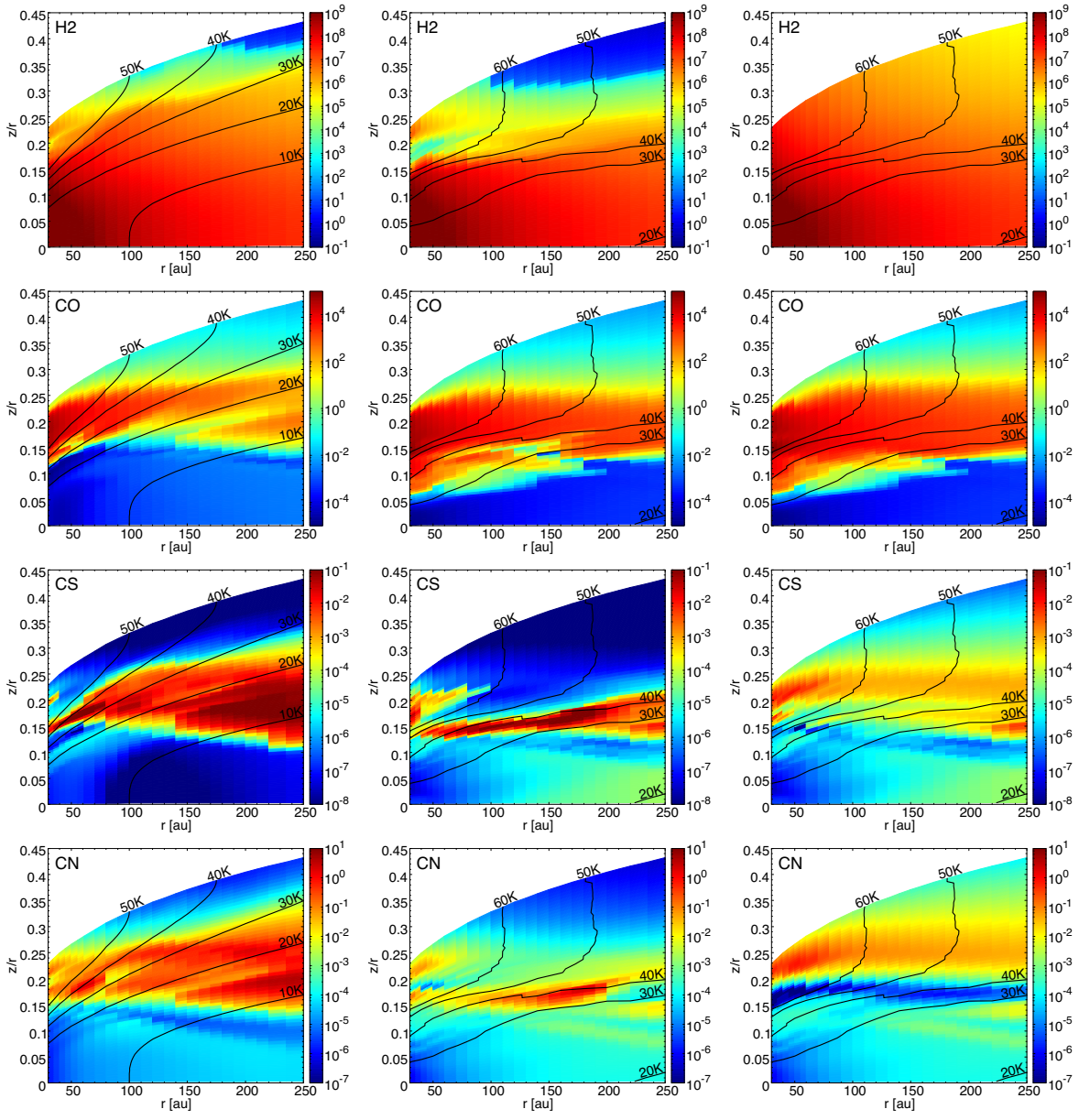

(a) HUV-LH-T_g (b) HUV-LH-T_a (c) HUV-B14-T_a

Figure A.3: Density [cm^{-3}] of H_2, CO, CS and CN in the gas-phase of the single-grain models in HUV regime. Left column is the HUV-LH-T_g models, middle one is HUV-LH-T_a and right one is HUV-B14-T_a.

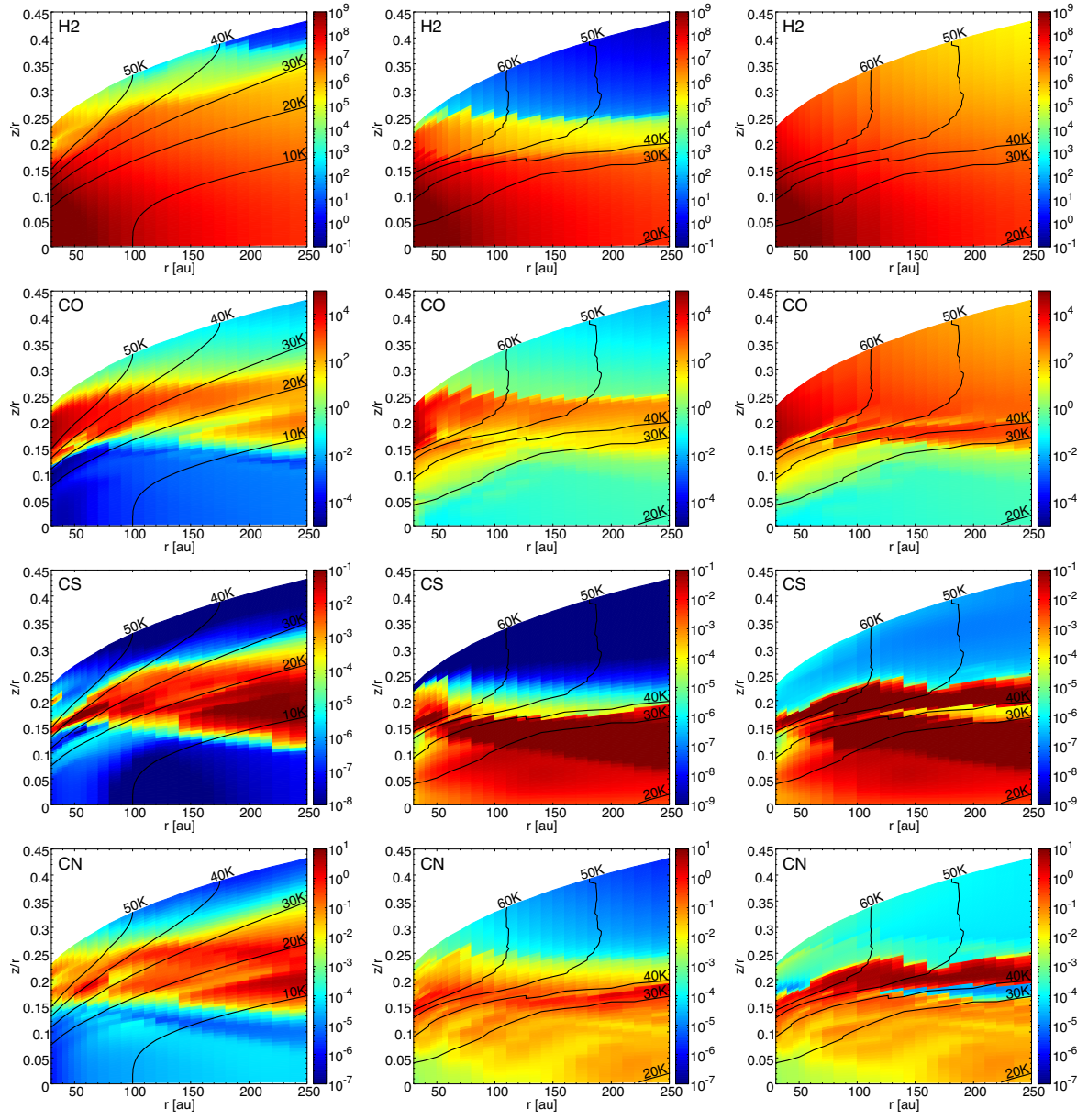

(a) HUV-LH-T_g (b) M-HUV-LH (c) M-HUV-B14

Figure A.4: Density [cm^{-3}] of H_2, CO, CS and CN in the gas-phase of HUV-LH-T_g (left column) and of the multi-grain models in HUV regime.

Appendix B

Low UV (LUV) flux

B.1 Vertical profiles of abundance and density at 100 au

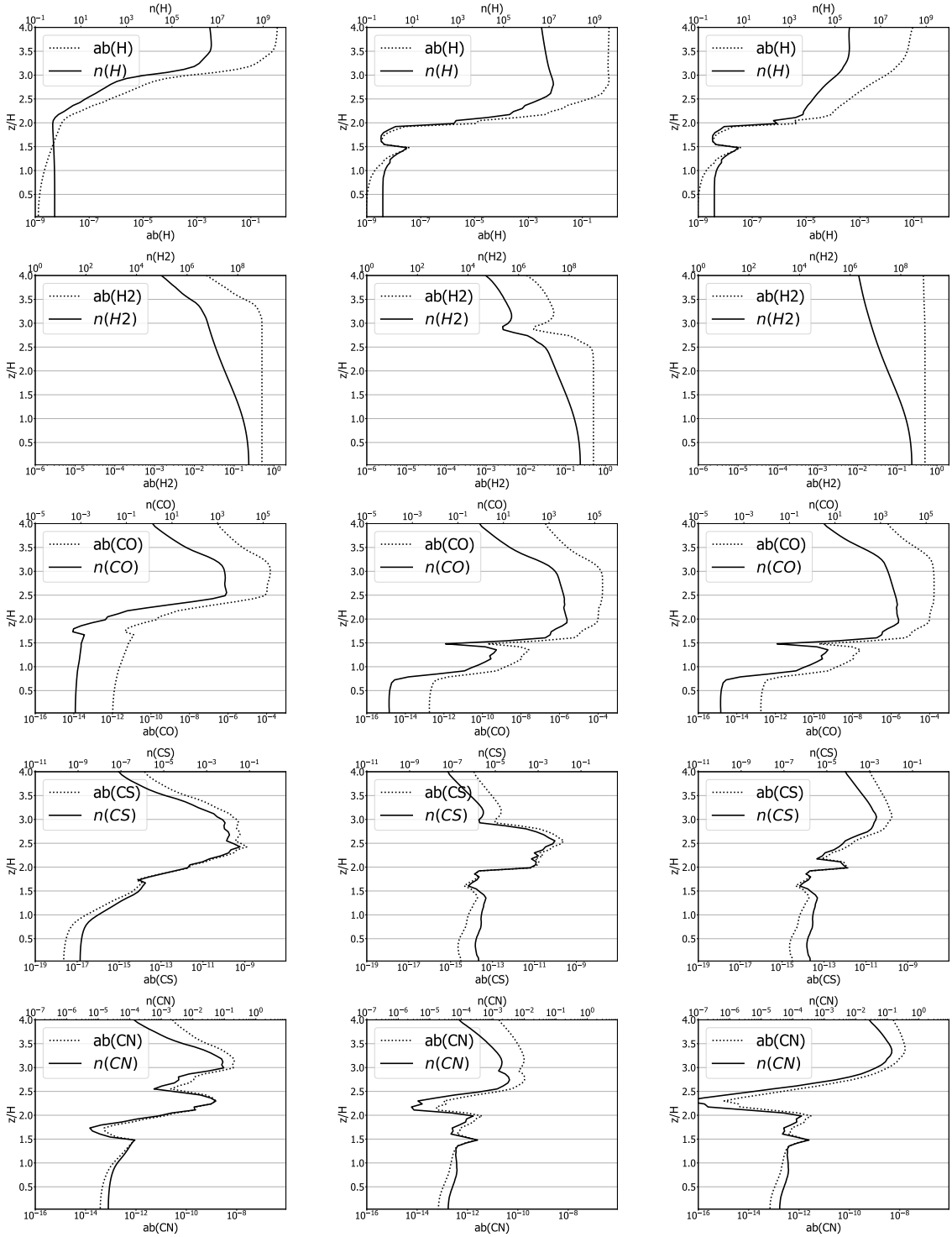

(a) LUV-LH-T_g (b) LUV-LH-T_a (c) LUV-B14-T_a

Figure B.1: Vertical profiles of H, H_2, CO, CS and CN at 100 au from the star of the LUV single-grain models. The dotted line is the abundance relative to H and the solid line is the density $[cm^{-3}]$.

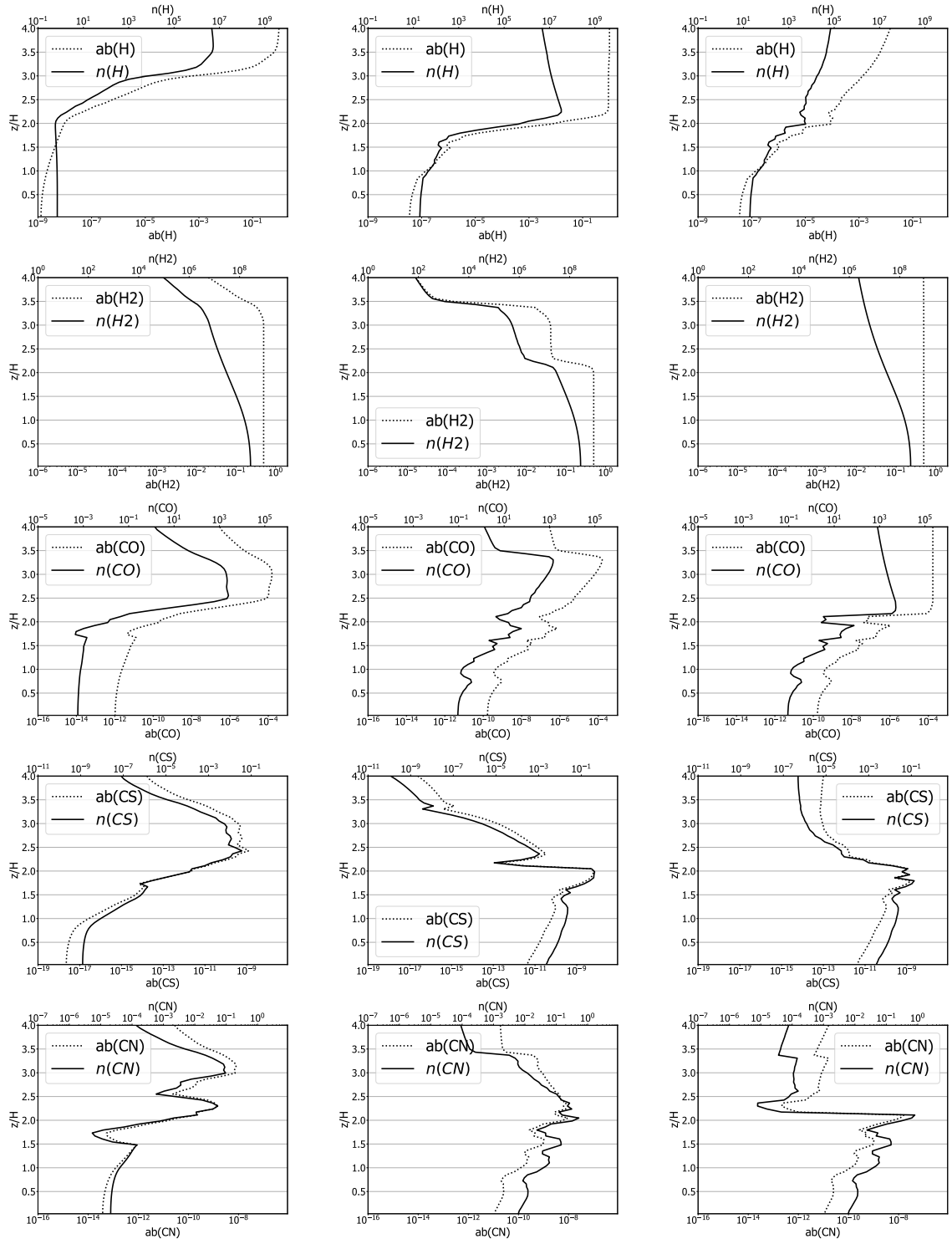

(a) LUV-LH-T_g (b) M-LUV-LH (c) M-LUV-B14

Figure B.2: Vertical profiles of H, H_2, CO, CS and CN at 100 au from the star of the LUV single-grain model HUV-LH-T_g on the left column, and multi-grain models on middle and right columns. The dotted line is the abundance relative to H and the solid line is the density $[cm^{-3}]$.

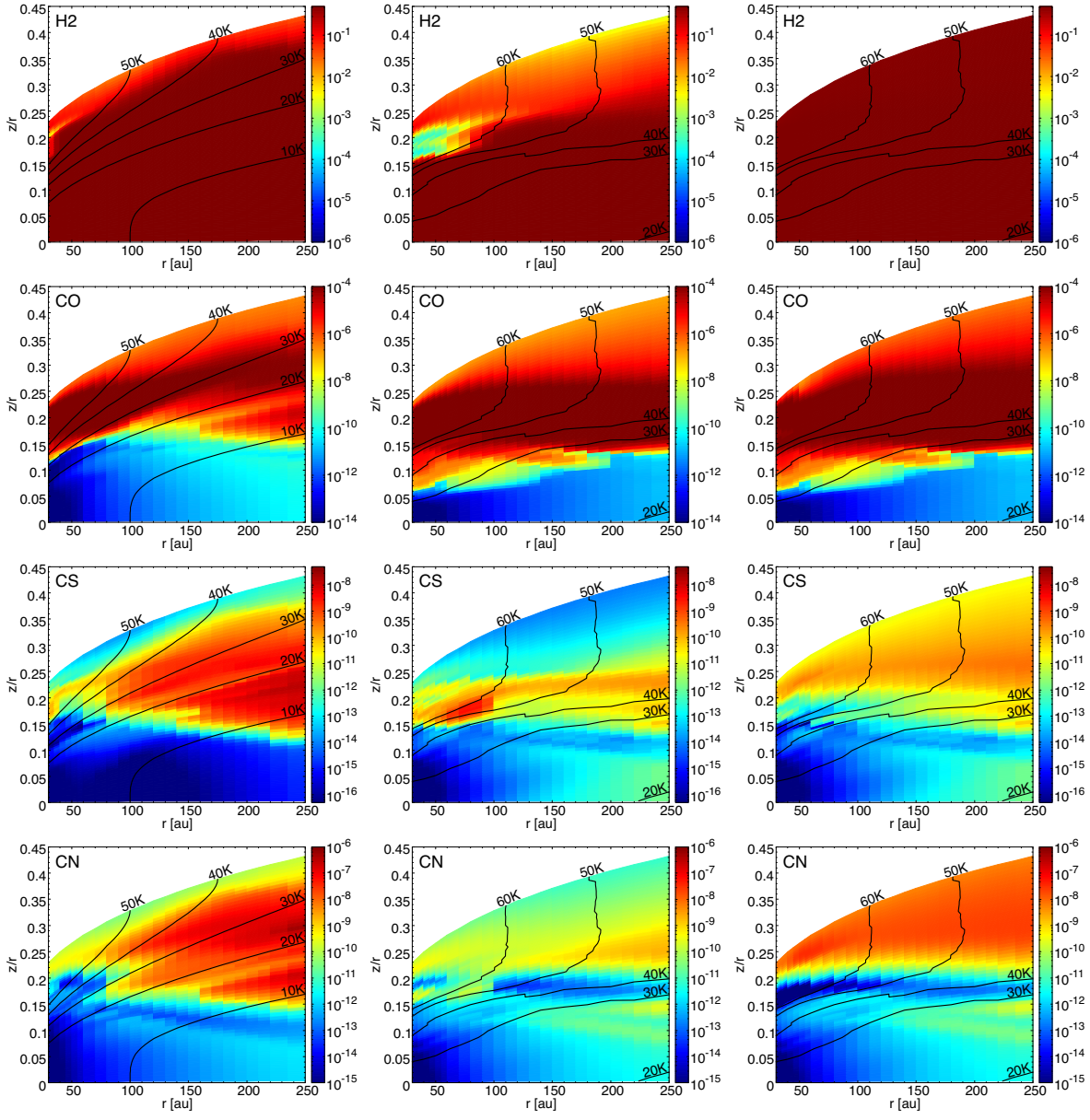

(a) LUV-LH-T_g (b) LUV-LH-T_a (c) LUV-B14-T_a

Figure B.3: Density [cm^{-3}] of H_2, CO, CS and CN in the gas-phase of the single-grain models in LUV regime. Left column is the HUV-LH-T_g models, middle one is HUV-LH-T_a and right one is HUV-B14-T_a.

Appendix C

Fitting B14's H_2 formation rate curves

C.1 Reproduction of the detailed calculation in a notebook

details

April 6, 2020

```
In [2]: import numpy as np
        import pandas as pd

        import matplotlib as mpl
        import matplotlib.pyplot as plt
        import matplotlib.patches as mpatches
        from matplotlib import rcParams
        rcParams['font.family'] = 'sans-serif'
        rcParams['font.sans-serif'] = ['Tahoma']
        pd.set_option('display.float_format', '{:.5e}'.format)
```

0.1 1) IMPORT EMERIC'S DATA

0.1.1 columns:

- G0: radiation in unit of reference.

- Rf1, Rf2, Rf3, Rf4: formation rates for 4 different values of density (10^0, 10^2, 10^4, 10^6) with full computation

- Rnof1, Rnof2, Rnof3, Rnof4: formation rates with equilibrium rate equation. (won't be used here)

```
In [3]: #------ PROCESS DATA ------
        # name of columns
        name = ['G0', 'Rf1', 'Rf2', 'Rf3', 'Rf4', 'Rnof1', 'Rnof2', 'Rnof3', 'Rnof4']
        #extract data
        fig6 = pd.read_table('fig6.dat', sep=" ", comment='#', header=None)
        #name the column
        fig6.columns = name
        #take a look
        print(fig6)
```

```
           G0          Rf1          Rf2          Rf3          Rf4        Rnof1  \
0 6.85809e-01 1.66385e-19 1.38545e-17 9.38084e-17 1.21371e-16 1.00917e-26
1 2.07912e+00 1.06726e-19 9.32349e-18 8.13432e-17 1.09842e-16 2.51379e-27
2 6.49126e+00 4.44985e-20 4.12677e-18 5.79388e-17 8.66831e-17 2.47124e-28
3 2.04243e+01 1.20147e-20 1.16280e-18 3.03514e-17 5.53411e-17 6.93762e-30
4 6.45458e+01 2.40317e-21 2.37371e-19 1.10893e-17 2.81101e-17 1.16572e-31
5 2.03877e+02 4.04461e-22 4.02695e-20 2.82860e-18 1.20172e-17 2.75242e-33
6 6.45091e+02 5.92033e-23 5.91143e-21 5.14627e-19 4.44063e-18 1.27487e-34
7 2.03840e+03 7.29342e-24 7.28971e-22 6.93872e-20 1.32061e-18 1.20733e-35
8 6.45054e+03 6.76252e-25 6.76138e-23 6.64927e-21 2.60143e-19 2.14067e-36

        Rnof2       Rnof3       Rnof4
```

```
0 1.00917e-24 1.00916e-22 1.00789e-20
1 2.51381e-25 2.51379e-23 2.51199e-21
2 2.47125e-26 2.47125e-24 2.47103e-22
3 6.93776e-28 6.93777e-26 6.93775e-24
4 1.16569e-29 1.16571e-27 1.16572e-25
5 2.75242e-31 2.75240e-29 2.75240e-27
6 1.27487e-32 1.27487e-30 1.27485e-28
7 1.20733e-33 1.20733e-31 1.20728e-29
8 2.14066e-34 2.14067e-32 2.14066e-30
```

0.1.2 We have 8 points in the data which gives the following figure (figure 6 in B14):

```
In [4]: #PLOT FIGURE 6
        fig_6 = plt.figure(figsize=(9.6, 7.2))
        ax = fig_6.add_subplot(111)
        rf1 = ax.loglog(fig6['G0'], fig6['Rf1'], lw=2, ls='-', c="red", label="$n_H = 10^0cm^{-3}$")
        rf2 = ax.loglog(fig6['G0'], fig6['Rf2'], lw=2, ls='-', c="green",label="$n_H = 10^2cm^{-3}$")
        rf3 = ax.loglog(fig6['G0'], fig6['Rf3'], lw=2, ls='-', c="blue",label="$n_H = 10^4cm^{-3}$")
        rf4 = ax.loglog(fig6['G0'], fig6['Rf4'], lw=2, ls='-', c="purple",label="$n_H = 10^6cm^{-3}$")
        lns = rf1 + rf2 + rf3 + rf4
        labs = [l.get_label() for l in lns]
        ax.legend(lns, labs, loc=0, fontsize=18)

        ax.set_xlabel('$G_0$', fontsize = 17)
        ax.set_ylabel('$R_f$ [$cm^{-3}.s^{-1}$]', fontsize = 17)
        plt.title('figure 1 - Emerics data', fontsize=18)
        ax.set_xlim(7e-1,9e3)
        ax.set_ylim(2e-26, 3e-16)
        ax.tick_params(labelsize=15)
        plt.show()
```

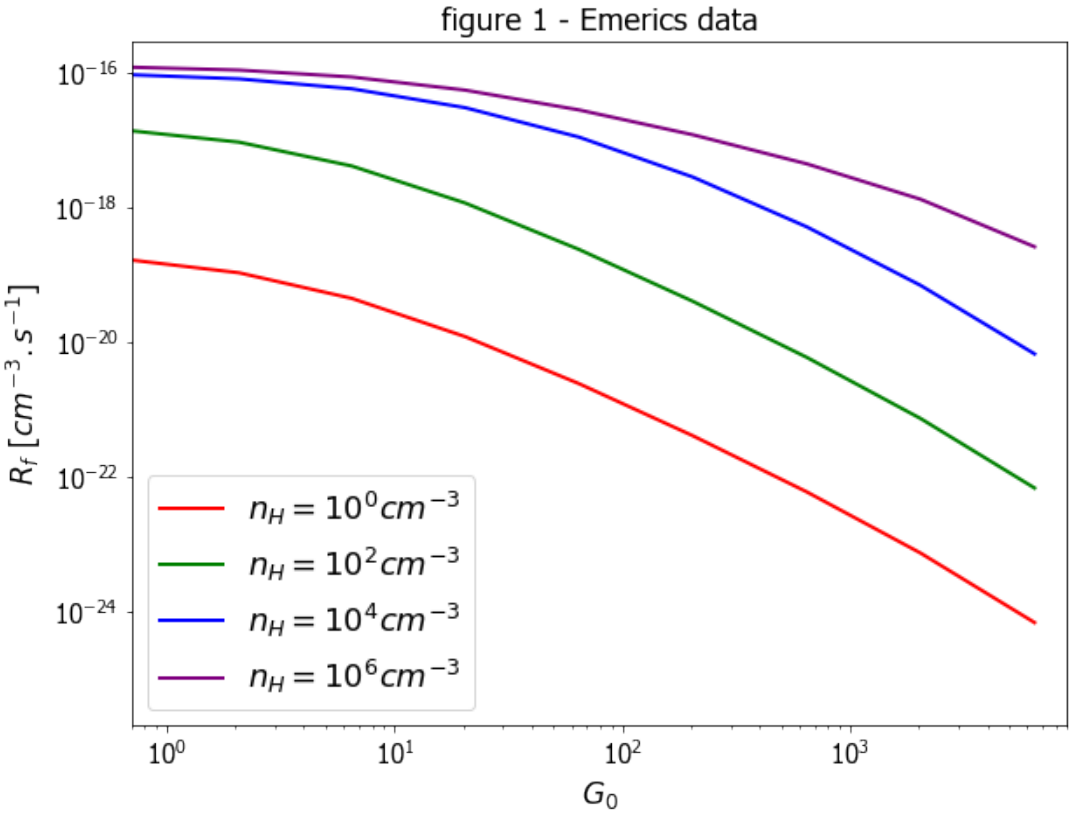

0.1.3 --> n_H, as defined in B14, is the total number of protons in cm^{-3}. The figure shows the formation rate as a function of the radiation, for different values of n_H, at 100 K.

0.2 2) HOW TO ESTIMATE THE RATES FOR A GIVEN GAS DENSITY AND GAS TEMPERATURE

0.2.1 --> Emeric's method: Find the equivalent number density n_{eq} by scaling-up in temperature and density. For a given gas density n_0 and a given gas temperature T_0, we should take in Emeric's data (interpolate) the value corresponding to:

0.3 $$n_{eq} = n_0 \sqrt{\frac{T_0}{100K}} \frac{s(T_0)}{s(100K)}$$ **(1)**

0.3.1 where $s(T_0)$ is the sticking coefficient:

0.4 $$s(T_0) = \frac{1}{1+\left(\frac{T_0}{T_2}\right)^{\beta}}$$ **(2)**

0.4.1 where $T_2 = 464K$ and $\beta = 1.5$ (B14, Sternberg & Dalgarno (1995).)

0.4.2 Therefore, we use equation (1) to get the equivalent density using the density of protons and gas temperature at given coordinates (r, z) in NAUTILUS.

0.4.3 Examples of equivalent density by choosing temperature and density:

```
In [5]: def n_eq(n_0, T_0, S_T0, S_100):  #EQUATION (1)
            return n_0*np.sqrt(T_0/100)*(S_T0/S_100)
```

```
S_100 = 1/(1 + (100/464)**1.5) #EQUATION (2)

#250AU from the star at z = 4H: smallest density in high radiation
T_small = 3.46572E+01  #choose a gas temperature
n_small = 3.67566E+05  #choose a gas density (number of protons)
S_Tsmall = 1/(1 + (T_small/464)**1.5)  #EQUATION (2)

#30AU from the star at z = 4H: big density but also high radiation.
T_high = 7.98777E+01  #choose a gas temperature
n_high = 1.26986E+08  #choose a gas density (number of protons)
S_Thigh = 1/(1 + (T_high/464)**1.5)  #EQUATION (2)

n_eq_small = n_eq(n_small, T_small, S_Tsmall, S_100)
n_eq_high = n_eq(n_high, T_high, S_Thigh, S_100)

print('smallest value of density in our model (250AU, 4H): %.3e cm^-3' %n_eq_small)
print('high density in high radiation field (30AU, 4H): %.3e cm^-3' %n_eq_high)
```

```
smallest value of density in our model (250AU, 4H): 2.333e+05 cm^-3
high density in high radiation field (30AU, 4H): 1.165e+08 cm^-3
```

0.5 3) FITTING EMERIC'S CURVES

0.5.1 A) FIRST STEP:

0.5.2 Get the value of the maximum rate formation for any n_H. Let's plot the values of the max formation rate $R_{f,max}$ using Emeric's data. In other words, the value of the rate at smallest radiation as a function of the density:

In [6]:
```
#----raw data
rf1 = fig6['Rf1'].loc[0] #first value in the column for a density of 10^0.
rf2 = fig6['Rf2'].loc[0]
rf3 = fig6['Rf3'].loc[0]
rf4 = fig6['Rf4'].loc[0]
x_raw = [1.00e0, 1.00e2, 1.00e4, 1.00e6] #densities
y_raw = [rf1, rf2, rf3, rf4]

#----plot
fig_neq = plt.figure(figsize=(9.6, 7.2))
ax = fig_neq.add_subplot(111)
ax.set_xlabel('$n_H$ [$cm^{-3}$]', fontsize = 17)
ax.set_ylabel('$R_{f,max}$ [$cm^{-3}.s^{-1}$]', fontsize = 17)
ax.loglog(x_raw, y_raw, lw=2, ls='-.', marker='o', c="red", label="Original data")
ax.set_xlim(5e-1,1e10)
ax.legend(loc=0, fontsize=18)
ax.tick_params(labelsize=15)
```

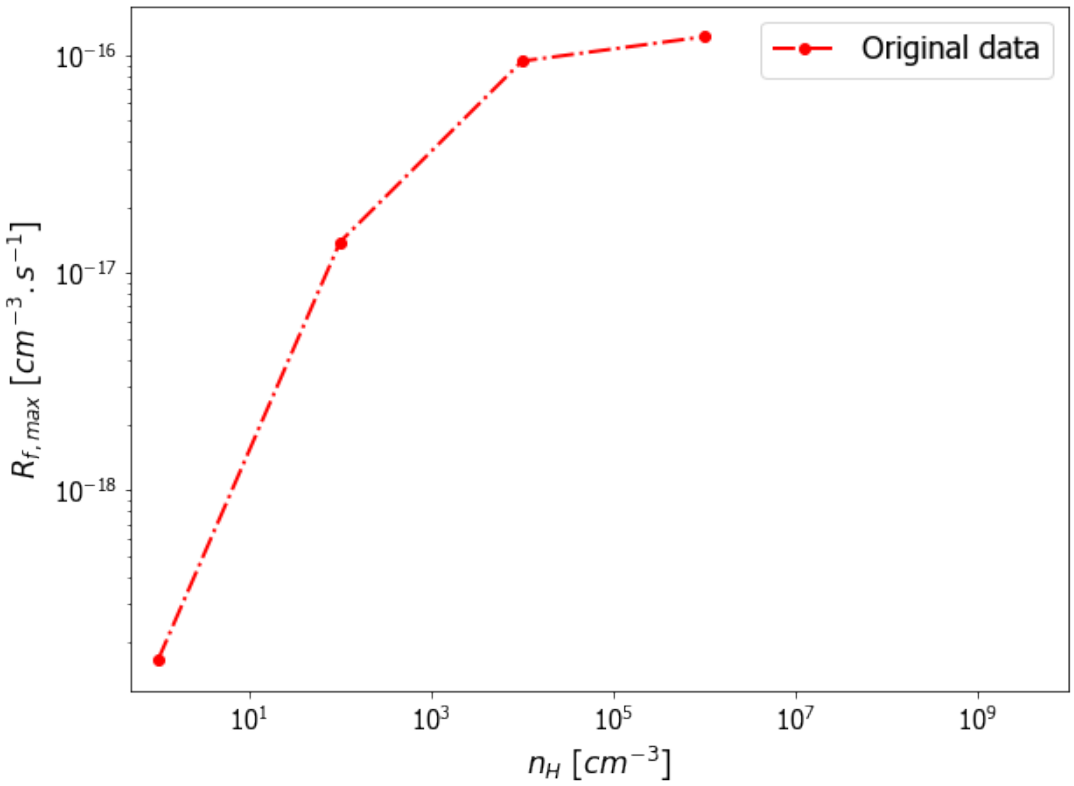

0.5.3 we use the following equation to fit this curve:

0.6 $R_{f,max}(n_H) = a(0) + \sum_{i=1}^{8} a(i) log(n_H)^i$ (3)

0.6.1 computed using the fitting algorithm of polyfit from Numpy library. The coefficients are:

$a(8) = -4.22721562.10^{-7}$
$a(7) = 1.36421392.10^{-5}$
$a(6) = -9.77585488.10^{-5}$
$a(5) = -1.38199458.10^{-3}$
$a(4) = 2.71155186.10^{-2}$
$a(3) = -1.62166137.10^{-1}$
$a(2) = 2.70415877.10^{-1}$
$a(1) = 8.65799199.10^{-1}$
$a(0) = -1.87663716.10^{1}$

0.6.2 which gives:

```
In [8]: #----plot
        def rf_max(x): #---> fit used in NAUTILUS
         return - 4.22721562e-07*np.log10(x)**8 + 1.36421392e-05*np.log10(x)**7 \
                - 9.77585488e-05*np.log10(x)**6 - 1.38199458e-03*np.log10(x)**5 \
                + 2.71155186e-02*np.log10(x)**4 - 1.62166137e-01*np.log10(x)**3 \
                + 2.70415877e-01*np.log10(x)**2 + 8.65799199e-01*np.log10(x)    \
                - 1.87663716e+01
```

```
density_log = np.logspace(0, 11, 100) #density in log scale

fig_neq = plt.figure(figsize=(9.6, 7.2))
ax = fig_neq.add_subplot(111)
ax.set_xlabel('$n_H$ [$cm^{-3}$]', fontsize = 17)
ax.set_ylabel('$R_{f,max}$ [$cm^{-3}.s^{-1}$]', fontsize = 17)
ax.loglog(x_raw, y_raw, lw=2, ls='-.', marker='o', c="red", label="Original data")
ax.loglog(density_log, 10**rf_max(density_log), label="fitted data")
ax.legend(loc=0, fontsize=18)
ax.set_xlim(5e-1,1e10)
ax.tick_params(labelsize=15)
```

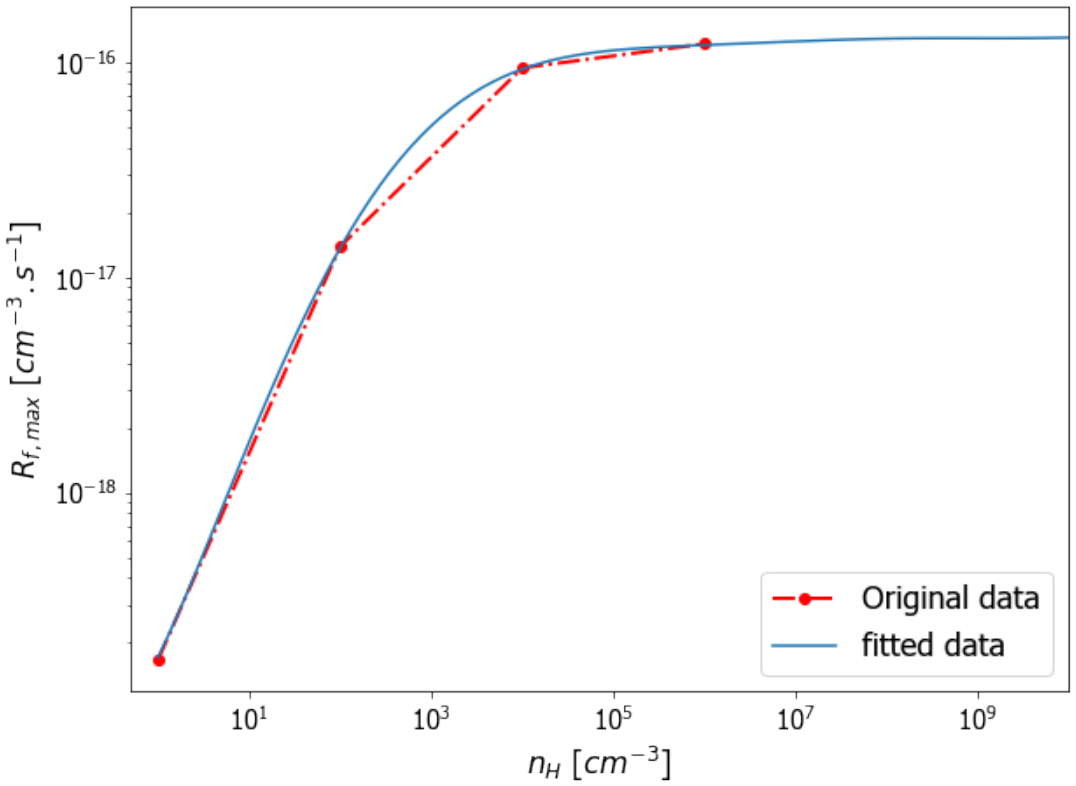

0.6.3 Thus, we have the interpolated value of the rates at smallest radiation for any given density in the following range: [$10^0\ cm^{-3}$, $10^{11}\ cm^{-3}$]

0.6.4 B) SECOND STEP:

0.6.5 Now comes the tricky part of how to interpolate the value for high radiation. We observe an asymptotic behavior at high radiation, but we also see a saturation in high densities. In any case, the fit must be dependent on the density. We use the following equation:

0.7 $$Q(G, n_H) = R_{f,max}(n_H) + \sum_{k=1}^{3} \left(\frac{b(k)}{n_H^{\beta}(k)} \right) log(G)^k \quad \textbf{(4)}$$

0.8 $$R_f(G, n_H) = 10^{Q(G, n_H)} \quad \textbf{(5)}$$

0.8.1 $R_{f,max}(n_H)$ is the value of the formation rate at minimum G as defined by equation (3), G is the radiation field in reference units, n_H is the number density of protons, b(k) and $\beta(k)$ are coefficients.

0.8.2 the values of the coefficients are:

$b(3) = 0.02165607$
$b(2) = -0.5315985$
$b(1) = -0.24083058$
$\beta(3) = 0.5$
$\beta(2) = -0.085$
$\beta(1) = -0.09$

In [28]:
```
#--density---
n_eq = 1e6 #choose equivalent density you want in cm^{-3}.
#------------

#--create radiation array in log scale from ---
G0_raw = fig6['G0']
G0 = np.logspace(np.log10(min(G0_raw)), np.log10(max(G0_raw)), 100)
#-----------------------------------

#---fit curve
def Q(x, a3, a2, a1, rfmax, neq):
 return (a3/neq**0.5)*np.log10(x)**3 + (a2/neq**0.085)*np.log10(x)**2 +\
        (a1/neq**0.09)*np.log10(x) + rfmax



fit_0 = 10**Q(G0, 0.02165607,  -0.5315985,   -0.24083058, rf_max(1e0), 1e0)
fit_4 = 10**Q(G0, 0.02165607,  -0.5315985,   -0.24083058, rf_max(1e4), 1e4)
fit_6 = 10**Q(G0, 0.02165607,  -0.5315985,   -0.24083058, rf_max(n_eq), n_eq)
fit_8 = 10**Q(G0, 0.02165607,  -0.5315985,   -0.24083058, rf_max(1e8), 1e8)
fit_10 = 10**Q(G0, 0.02165607,  -0.5315985,   -0.24083058, rf_max(1e10), 1e10)
#-----------

#---PLOT
fig = plt.figure(figsize=(9.6, 7.2))
ax = fig.add_subplot(111)
ax.set_xlabel('$G$', fontsize = 17)
ax.set_ylabel('$R_f$ [$cm^{-3}.s^{-1}$]', fontsize = 17)
ax.loglog(fig6['G0'], fig6['Rf1'], lw=2, ls='-', c="red", label="$n_H = 10^0cm^{-3}$")
```

```
ax.loglog(fig6['G0'], fig6['Rf2'], lw=2, ls='-', c="green",label="$n_H = 10^2cm^{-3}$")
ax.loglog(fig6['G0'], fig6['Rf3'], lw=2, ls='-', c="blue",label="$n_H = 10^4cm^{-3}$")
ax.loglog(fig6['G0'], fig6['Rf4'], lw=2, ls='-', c="purple",label="$n_H = 10^6cm^{-3}$")

ax.loglog(G0, fit_0,  ms=1, ls=':', color="black", label="$n_{eq} = 10^0 cm^{-3}$")
ax.loglog(G0, fit_4,  ms=1, ls='-.', color="black", label="$n_{eq} = 10^2 cm^{-3}$")
ax.loglog(G0, fit_6,  ms=1, ls='--', color="black", label="$n_{eq} = %.1e cm^{-3}$" %n_eq)
ax.loglog(G0, fit_8,  ms=1, ls='-', color="black", label="$n_{eq} = 10^8 cm^{-3}$")
ax.loglog(G0, fit_10,  ms=1, ls='-', color="black", label="$n_{eq} = 10^{10} cm^{-3}$")
#plot fit for low value below:
#ax.loglog(G0, fit_low,  ms=1, color="black", label="$n_{eq} = 10^2 cm^{-3}$")

plt.legend(loc=0,fontsize=14)
ax.tick_params(labelsize=20)
#-----
```

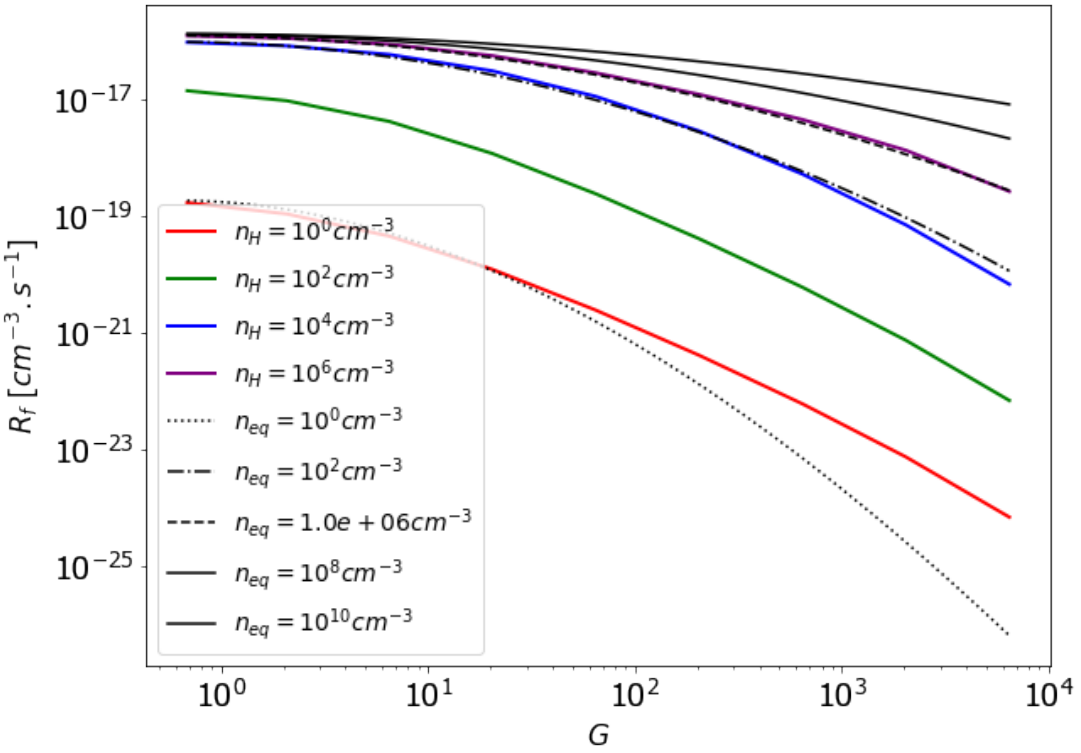

0.8.3 We see that the fit gives pretty bad results for low densities and that the extrapolation above 10^6 cm^{-3} is probably flawed. However, this probably doesn't compromise much the results of our simulations. Indeed, firstly, the space parameters of our models lie exclusively above the blue curve. Secondly, most of our high densities are located in very low radiation fields where the error of the fit should be minimal. Finally, we notice that in regions of high radiation fields our equivalent densities grossly follow the purple line around where the fit gives best results.

In [ ]:

In [ ]:

Appendix D

publications

D.1 Reproduction of an article submitted in 2020 in Astronomy & Astrophysics (in revision)

Astronomy & Astrophysics manuscript no. impact_of_temperature-aa
December 18, 2020

Impact of Size-dependent Grain Temperature on Gas-Grain Chemistry in Protoplanetary Disks: the case of low-mass star disks

S. Gavino[1], A. Dutrey[1], V.Wakelam[1], S. Guilloteau[1], J.Kobus[2], S.Wolf[2], W. Iqbal[3], E. Di Folco[1], E. Chapillon[1,4], and V. Piétu[4]

[1] Laboratoire d'Astrophysique de Bordeaux, Université de Bordeaux, CNRS, B18N, Allée Geoffroy Saint-Hilaire, F-33615 Pessac
[2] University of Kiel, Institute of Theoretical Physics and Astrophysics, Leibnizstrasse 15, 24118 Kiel, Germany
[3] South-Western Institute for Astronomy Research (SWIFAR), Yunnan University (YNU), Kunming 650500, People's Republic of China
[4] IRAM, 300 rue de la piscine, F-38406 Saint Martin d'Hères Cedex, France

Received September 15, 1996; accepted March 16, 1997

ABSTRACT

Context. Grain surface chemistry is key to the composition of protoplanetary disks around young stars.
Aims. The temperature of grains depends on their size. We evaluate the impact of this temperature dependence on the disk chemistry.
Methods. We model a moderately massive disk with 16 different grain sizes. We use the 3D Monte-Carlo POLARIS code to calculate the dust grain temperatures and the local UV flux. We model the chemistry using the 3-phase astro-chemical code NAUTILUS. Photo processes are handled using frequency-dependent cross-sections, and a new method to account for self and mutual shielding. The multi-grain model outputs are compared to those of single-grain size models (0.1 μm), with two different assumptions for their equivalent temperature.
Results. We find that the Langmuir-Hinshelwood (LH) mechanism alone is not efficient to form H_2 at 3-4 scale-heights (H), and adopt a parametric fit to a stochastic method to model H_2 formation instead. We find the molecular layer composition (1-3 H) to depend on the amount of remaining H atoms. Differences in molecular surface densities between single and multi-grain models are mostly due to what happens above 1.5 H. At 100 au, models with colder grains produce H_2O and CH_4 ices in the mid-plane, and warmer ones more CO_2 ices, both allowing efficient depletion of C and O as soon as CO sticks on grain surfaces. COMs production is enhanced by the presence of warmer grains in the multi-grain models.
Conclusions. Chemical models with a single grain size are sensitive to the adopted grain temperature, and cannot account for all expected effects. A spatial spread of the snowlines is expected to result from the ranges in grain temperature. The amplitude of the effects will depend on the dust disk mass.

Key words. Stars: circumstellar matter – Protoplanetary disks – Astrochemistry – Radio-lines: stars – Radiative transfer

1. Introduction

As planets form in protoplanetary disks, studying the physical and chemical evolution of their gas and dust content along the whole disk lifetime is important in order to investigate how planetary formation proceeds. In the early stages of disks (the so-called proto-stellar phase) small dust grains are essentially dynamically well coupled to the gas. When grain growth occurs (up to at least cm-sized particles) larger particles, which dynamically decouple from the gas-phase, settle towards the disk mid-plane. This vertically changes the gas-to-dust ratio in the disk. Moreover, grain growth also allows UV to penetrate deeper in the disk, changing its chemistry.

As a consequence of the complex interplay of physical and chemical processes, it is now demonstrated that the disk structure can be separated vertically in three distinct regions: from top to bottom, the irradiated tenuous disk atmosphere (above $3-4\,H$ or scale heights) where the gas can be hot and is ionized or in atomic form, the warm denser molecular layer ($1-3\,H$) where most molecules reside and below $1\,H$, the mid-plane. Beyond the CO snow-line, which is typically located at a radius about 20 au in a TTauri disk, the mid-plane is very dense and cold ($\leq$ 20 K). This area is essentially shielded from the stellar radiation, with both low ionization and turbulence levels. In this cold region, most molecules are stuck onto dust grains which exhibit icy mantles that can still be processed by cosmic rays.

Thanks to ALMA, several high angular resolution and sensitive observations of disks orbiting either low or intermediate mass young stars (TTauri and Herbig Ae stars) have quantitatively confirmed this general scheme. CO observations of HD 163296 have clearly shown the CO gas-phase depletion in the dark, cold disk mid-plane (de Gregorio-Monsalvo et al. 2013), revealing also that the CO gas is located in the intermediate warm molecular layer. More recently, the ALMA observations of the edge-on TTauri disk called the Flying Saucer (Dutrey et al. 2017) directly show the molecular layer at intermediate scales ($1-2H$) with CS, the denser gas tracer being located at about $1H$, below the CO emission ($1-3H$) which better traces the whole envelope of the molecular layer.

In the last 10 years, several astrochemical models have emerged that attempt to incorporate the observed complexity of disk physics in order to provide more accurate molecular abundance and surface density predictions. While the very first models included only the gas-phase chemistry, gas-grain coupling

Send offprint requests to: Sacha Gavino
e-mail: sacha.gavino@u-bordeaux.fr

was added to take into account firstly adsorption and desorption for a few molecules (e.g. Woitke et al. 2009) and then reactions on the grain surface (e.g. Semenov & Wiebe 2011; Walsh et al. 2014). Another step was finally achieved with models which include 3 material phases: the gas-phase and 2 phases for the gas-grain chemistry with grains modelled by an icy surface layer and an active mantle (Ruaud & Gorti 2019; Wakelam et al. 2019). Thermo-chemical models which calculate the density and thermal structures in a self-consistent manner have been also developed (e.g. Hollenbach & Gorti 2009). Recently, Ruaud & Gorti (2019) have also coupled such a thermo-chemical model (Gorti et al. 2011) to a 3-phase chemical model.

An important improvement in chemical models was to introduce more realistic dust disk structures by taking into account grain growth and dust settling. Grain growth reduces the dust cross-section and therefore increases the UV penetration while dust settling locally changes the gas-to-dust ratio. Grain growth was first introduced in disk chemistry by Aikawa & Nomura (2006). Dust settling is often mimicked by adding larger grains in the mid-plane (e.g. Wakelam et al. 2019).

Several authors have already studied the effect of multiple grain sizes onto chemistry. As an example, Acharyya et al. (2011) used five different grain sizes in their models but the grain temperature was the same for all grains. Following this work, Pauly & Garrod (2016) tested the impact of a simple temperature distribution, with $T(a) \propto a^{-(1/6)}$, a being the grain size, while Ge et al. (2016) explored a small range of temperatures (14.9–17.9) for the Cold Neutral Medium. More recently, Iqbal & Wakelam (2018) also developed a model handling different grain sizes.

On another hand, Akimkin et al. (2013) developed a disk model where they couple the dust grain time evolution (grain growth and settling) to chemistry. Another improvement was achieved with the development of grids of thermo-chemical models allowing multi-wavelengths fitting of dust and molecular lines such as DIANA (Woitke et al. 2019). However, these elaborate approaches use a single grain temperature which is either fixed or derived from a dust radiative transfer simulation while the temperature of a grain depends on its size (e.g. Wolf 2003), larger grains being colder. Chapillon et al. (2008) found in the disk of CQ Tau, whose temperature is well above the CO snow-line temperature, an important CO depletion. They suggested that CO may remain trapped onto larger grains that are cold enough to prevent thermal CO desorption. Heese et al. (2017) have investigated the dust temperature variations with grain size and position (radius and altitude above the mid-plane) in a typical TTauri disk using the 3D dust radiative transfer code Mol3D (Ober et al. 2015). The dust temperature variations in the molecular layer appear to be significant enough to affect the disk chemistry. This dependency questions the applicability of elaborate, self-consistent, thermo-chemical models that rely on a single grain size and temperature.

We explore here the impact of the variations of the grain temperature with their size onto the chemistry of a representative TTauri disk. Our goal is not to build a complete chemical model that incorporates the best of all previous studies, neither to make grid models that could provide relevant comparisons with the observations. Instead, we only intend to check the limits of an assumption that is used in most previous models, and explore the main consequences of dust grain temperature dependence with size.

For this purpose, we have coupled the 3D Monte-Carlo continuum radiative transfer code POLARIS (Reissl et al. 2016) to the NAUTILUS Multi Grain Code (Hersant et al. 2009; Ruaud et al. 2016) using the 3-phase version which also takes into account a grain size distribution (Iqbal & Wakelam 2018). We present the two codes and how we parametrize the gas and dust disk in Section 2. Section 3 deals with the disk model description and global results. We discuss in more detail the results in Section 4 and we state our conclusions in Section 5.

2. Model description

To estimate the impact of the grain temperature onto the chemistry, we couple the radiative 3D Monte-Carlo code POLARIS with the astro-chemistry code NAUTILUS. This requires to independently assume a gas and dust disk structure, a gas temperature, a dust distribution and settling. Moreover, the coupling between the two codes requests for NAUTILUS a new method to calculate the dust extinction, the self and mutual shielding using the UV flux calculated by POLARIS in each disk cell. Figure 1 is a scheme summarizing how we proceed.

2.1. Disk Model

Our disk structure is derived from a simple disk model where truncated power laws describe most of the quantities: surface density, mid-plane temperature, velocity field, with sharp inner and outer radii. A detailed model description is given in Appendix A

We adopt a power-law grain size distribution $dn(a) = Ca^{-d}da$ with $dn(a)$, the number of grain of size a and C a normalisation constant that can be derived from the dust mass (see Appendix A.2). The resulting distribution is discretized into 16 logarithmically distributed intervals, with grain sizes ranging from $a_{min} = 5$ nm to $a_{max} = 1$ mm. The fraction of mass and area per bin are given in Table A.1.

Our goal being to evaluate the impact of dust grain temperatures, we assume a common gas temperature structure for all our simulations (including single and multi-grain models), in order to avoid chemical effects that could be due to gas only. We selected values derived from the observations of the Flying Saucer TTauri disk (see Dutrey et al. 2017), whose edge-on orientation allow a direct measure of the 2D gas temperature distribution from ALMA observations of the optically thick CO J=2-1 line. Values are given in Table 1.

The vertical distribution of gas is self-consistently derived from the imposed temperature law. However, to account for dust settling, we assume grains of a given size follow a simple Gaussian vertical profile, whose scale height is simply related to the gas hydrostatic scale at the disk mid-plane temperature according to a simple prescription (see Appendix A.2). Our model is therefore not fully consistent, since very small grains should follow the vertical profile of the gas, but should be adequate for the larger grains observed in disks. To compute the settling, we assume an α viscosity of 0.01 and a Schmidt number of $S_c = 1$. Although often assumed in disk modelling, these values are somewhat arbitrary, and observations with ALMA are not yet accurate enough to allow for a quantitative description of dust settling.

Figure 2 is a 2D representation of the disk structure in density and in temperature for the gas and for the dust (multi-grain model with settling).

2.2. Radiation fields and dust temperature

In this new approach, we use the dust radiative transfer code to calculate throughout the disk the UV field and the dust temperature for each of the 16 grain sizes, in each cell of the disk (in

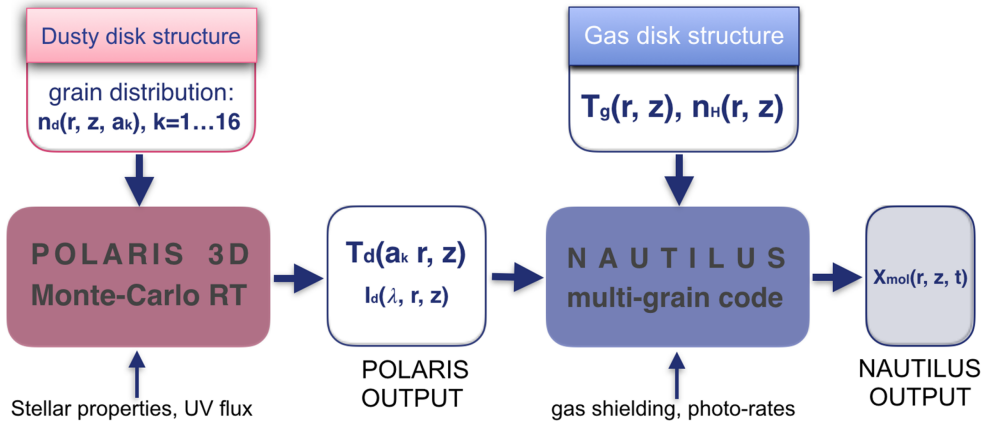

Fig. 1: Multi-grain model: Coupling scheme between NAUTILUS and POLARIS.

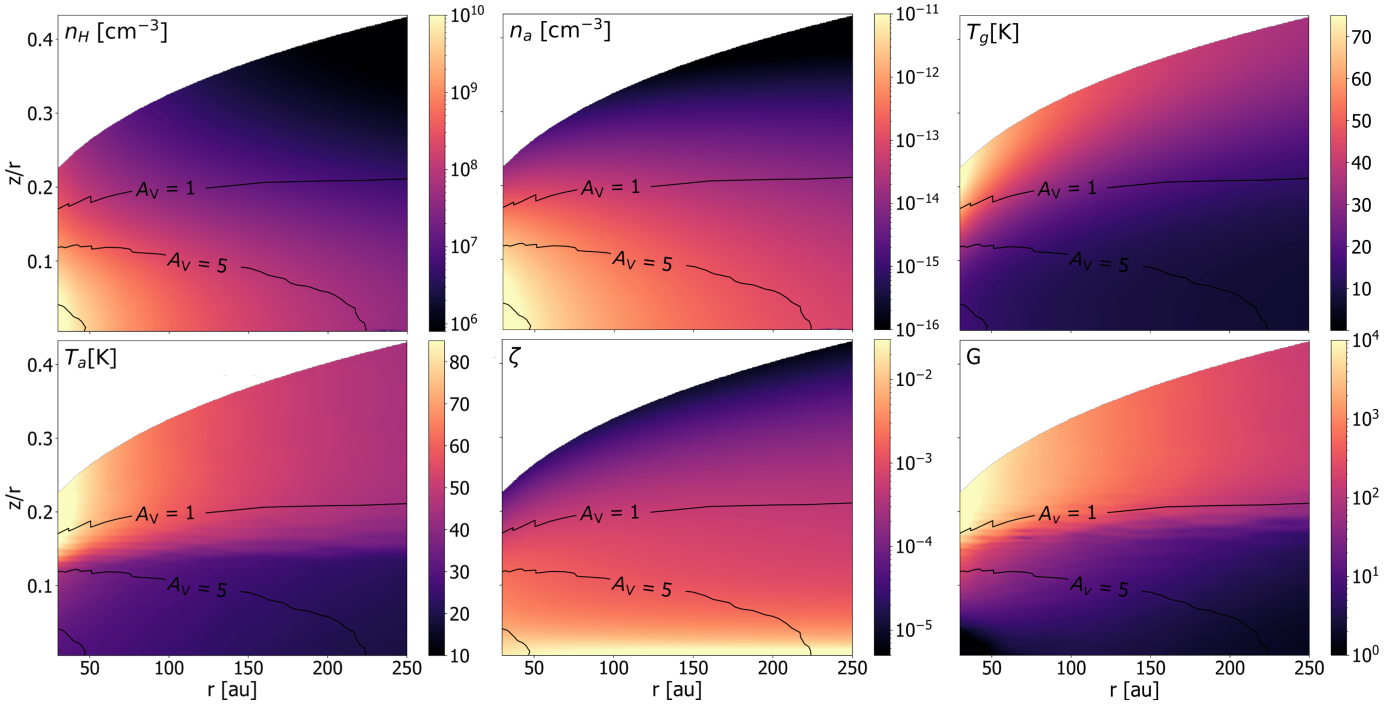

Fig. 2: Physical structure of the multi-grain models incorporating a full dust distribution. T_g is the gas temperature, n_H is the gas number density, G is the local stellar and interstellar field in the case of the HUV models (see Section A), ζ is the dust to gas mass ratio, T_a (Eq.1) is the area-weighted dust temperature, and n_a is the area-weighted grain number density. A_V is the visual extinction counted from disk surface towards the disk mid-plane.

radius and altitude). The dust temperatures are then used to compute the chemistry with NAUTILUS.

However, the UV field derived above only accounts for dust extinction and scattering. A proper account for self and mutual shielding of molecules and atoms is required to handle the photochemical processes.

2.2.1. Radiation sources

As the central heating source we assume a low-mass pre-main sequence star with a mass of $M_\star = 0.58$ M$_\odot$, which radiates as a black body with an effective temperature of $T_{\star,\mathrm{eff}} = 3900$ K and a luminosity $L_\star = 0.75$ L$_\odot$. Additionally, we consider the interstellar radiation field (ISRF) with a spectral energy distribution (SED) from Draine (1978) between 91.2 nm and 200 nm and the extension of van Dishoeck & Black (1982) for longer wavelengths. Besides the stellar radiation field, TTauri stars exhibit a significant UV excess coming from the inner disk boundary and accretion shocks on the stellar surface. This contribution is highly wavelength-dependent, with spectral lines like Lyman α having substantial intensities (France et al. 2014). As concerns the thermal balance of dust, the frequency dependence is largely irrelevant, and can be absorbed by ensuring that the luminosity used in the model contains the UV excess contribution. However, photo-processes being wavelength dependent, the details of the UV spectrum shape strongly affect the chemistry. For this reason, we take as stellar input spectrum for our radiative transfer and chemical model the sum of the stellar black body spectrum and the UV excess typically found in the in TTauri stars. Further details about the radiation fields are given in Section 3.1.

Table 1: Overview of the disk model parameters

Disk Parameters	
$T_{\star,\mathrm{eff}}$ (star temperature)	3900 K
$L_\star$ (star luminosity)	0.75 $L_\odot$
$M_\star$ (star mass)	0.58 $M_\odot$
ISRF	DRAINE
$\Sigma_{g,0}$ (gas (H + H_2) surface density at R_0)	0.335 g.cm^{-2}
p (surface density exponent)	1.5
R_{in} (innermost radius)	1 au
R_{out} (outermost radius)	250 au
R_0 (reference radius)	100 au
ζ (dust to gas mass ratio)	0.01
$T_{\mathrm{mid},0}$ (observed T_{mid} at R_0)	10 K
$T_{\mathrm{atm},0}$ (observed T_{atm} at R_0)	50 K
σ (stiffness of the vertical T profile)	2
q (radial T profile exponent)	0.4
S_c (Schmidt number)	1
α (viscosity coefficient)	0.01
d (grain size distribution exponent)	3.5
a_{min} (smallest grain radius)	5 nm
a_{max} (biggest grain radius)	1 mm
number of bins	16
ρ_{grain} (material density of dust)	2.5 g.cm^{-3}
M_{disk} (total disk mass)	7.5.10^{-3} $M_\odot$

2.2.2. Radiative transfer simulations

The radiation field is computed using the 3D Monte-Carlo continuum and line radiative transfer code POLARIS (Reissl et al. 2016). As in Heese et al. (2017), we calculate the dust temperature distribution of 16 grain size intervals (see Fig. 5). We assume spherical grains with a size independent composition consisting of a homogeneous mixture of 62.5 % silicate and 37.5 % graphite. Optical properties from Draine & Lee (1984) and Laor & Draine (1993) are used to calculate the scattering and absorption coefficients based on Mie scattering (Mie 1908) using the MIEX code (Wolf & Voshchinnikov 2004). The radiative transfer is solved using 100 wavelengths logarithmically spaced between 50 nm and 2 mm. The spatial grid involves 300 radii, logarithmically spaced by a factor 1.05 between 1 and 300 au, and 181 angles with the same factor between 0 and π.

The temperature in the upper optically thin disk layers strongly depends on the grain size (Fig. 5, middle panel). The dust temperature increases with grain size for sizes in the range 0.007 μm to 0.070 μm, then decreases for sizes in range 0.32 μm to 15 μm, and increases again, although only slightly, with larger grain sizes. As explained in Heese et al. (2017), this can be understood by looking at the ratios of the absorption cross-section for wavelengths at which the star radiates ($\approx$ 1 μm) and the absorption cross-section for wavelengths at which the dust emits ($\approx$ 20 μm, Fig. 4). The ratio increases up to grain sizes of 0.07 μm, meaning that the ratio of absorbed to emitted radiation increases, leading to higher grain temperatures. For larger grain sizes, the behavior is reversed until grains become larger than about 15 μm. Using these radiative transfer simulations we can obtain a distribution of dust temperatures $T_d(a_i, r, z)$ that fully depend on the size and location of the grains. To compare our set of models with those consisting of a single grain size (see Section 3.1.1), it is also convenient to introduce an area-weighted temperature defined as:

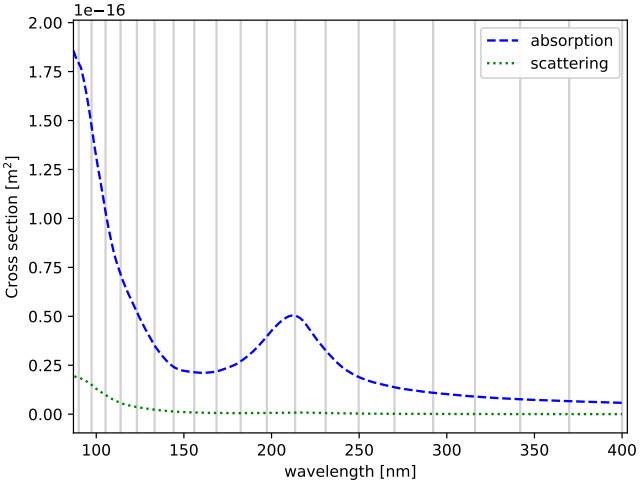

Fig. 3: Absorption (*blue dashed line*) and scattering cross-sections (*green dotted line*) for the first grain size bin (7 nm). The vertical grey lines mark the wavelengths for which the radiation fields are simulated.

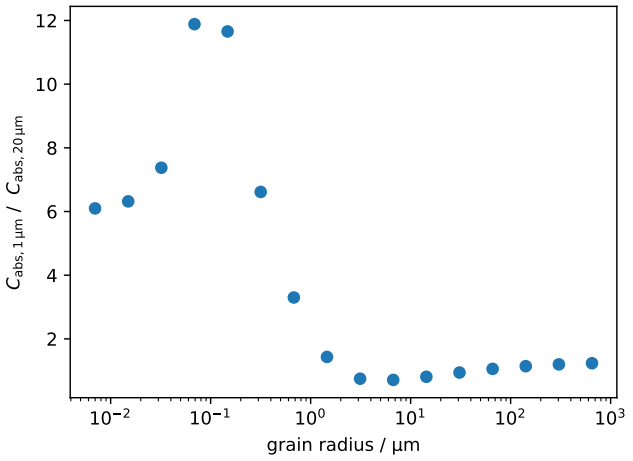

Fig. 4: Ratio of the absorption cross-sections for wavelengths characteristic for stellar radiation ($C_{\mathrm{abs},1\mu\mathrm{m}}$) and dust emission ($C_{\mathrm{abs},20\mu\mathrm{m}}$).

$$T_a(r,z) = \frac{\sum_i a_i^2 T_d(a_i,r,z) n_d(a_i,r,z)}{\sum_i a_i^2 n_d(a_i,r,z)}. \quad (1)$$

We note that the area-weighted dust density $n_{\mathrm{a}}(r,z)$ (Fig. 2) is defined by an equation of the same form. Figure 6 shows the dust temperature profiles at 100 au used by all our different models.

Our disk model is less massive than that used by Heese et al. (2017), leading to smaller opacities, and thus the temperature differences between grains of different sizes is much larger in Figs.5 and 6 than in that previous work.

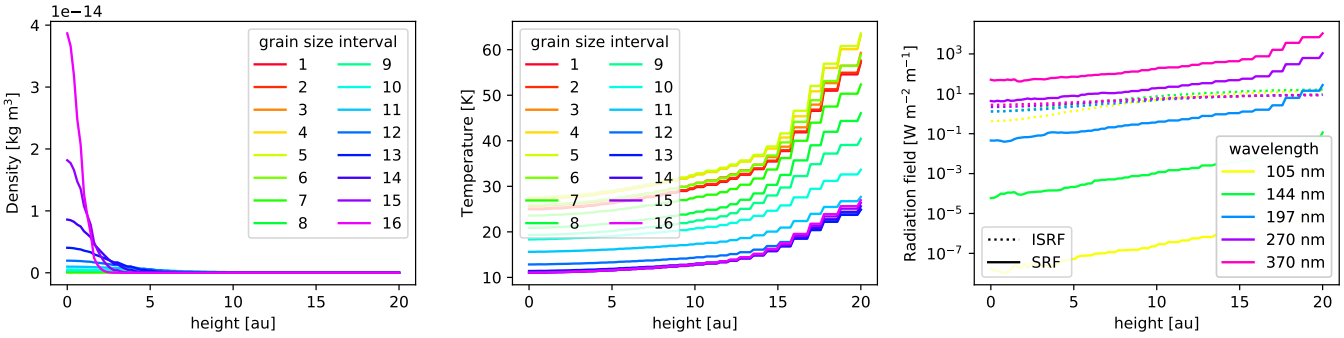

Fig. 5: Results of the radiative transfer simulation in vertical direction at a disk radius of $r = 100$ au. *Left:* Dust density distribution for the 16 grain size intervals as described in Appendix A.2.2 and A.2.3. *Middle:* Dust temperature of the 16 grain size intervals. *Right:* Stellar (solid lines) and interstellar radiation field (dotted lines).

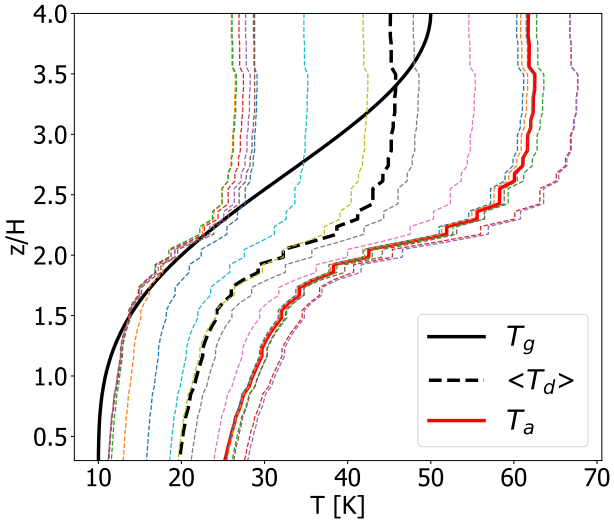

Fig. 6: Vertical profiles of temperatures at 100 au. The thick black line is the gas vertical temperature profile in Kelvin. The dotted colored lines are temperatures of each grain population and the thick red line is the area-weighted temperature T_a. We see that temperatures are roughly constant for $z/H < 1.5$ and for $z/H > 2.5$. Between these two altitudes the temperatures exhibit a strong transition.

2.2.3. Dust extinction, self and mutual shielding

The radiation field is a contribution of both the interstellar radiation field (ISRF) and the stellar radiation field (SRF). Radiation from these two sources encounters molecular or atomic gas and dust grains that affects its propagation through extinction and scattering. The effect of the dust is computed by the 3D Monte-Carlo continuum and line radiative transfer code POLARIS as described in Sec. 2.2.2 (Fig.3 shows the sampling in the 90 to 400 nm wavelengths range relevant for photo-processes). Figure 5 shows results at a disk radius of $r = 100$ au.

In chemical codes, the effect of extinction due to gas, known as self and mutual shielding, is often estimated using empirical attenuation factors as a function of line-of-sight visual extinction (e.g. Lee et al. 1996, for a discussion). The situation for disks is more complex, due to the two sources of UV radiation (stellar neighbourhood and ISRF) and varying dust properties. Empirical attenuation factors have been derived for disks (see for example Visser et al. 2009; Heays et al. 2017). They are in general used in a 1+1D approach, where the two sources of radiation are treated independently and scattering is neglected. Furthermore, they depend implicitely on the dust settling that was assumed during their derivation, as well as on the shape of the incident UV field.

For better consistency, we use here a procedure that builds on our knowledge of the dust-attenuated UV field. The extinction produced by the gas requires to know the opacity generated by the molecules through which the radiation travels from outside the disk to the local cell.

We show in Appendix B that a first order approximation for self and mutual shielding is obtained by applying the attenuation of the vertical opacity due to molecules to the radiation field computed with dust only by the POLARIS code:

$$I_L(\lambda, r, z) = e^{-\tau_m^V} I_d(\lambda, r, z) \quad (2)$$

where $I_d(\lambda, r, z)$ is the radiation field given by POLARIS, which explicitly includes the impact of dust scattering, and τ_m^V is the total opacity due to molecules from the (r, z) point to $(r, +\infty)$.

2.3. Chemistry simulations

The NAUTILUS gas-grain code (Ruaud et al. 2016) is used to perform chemistry simulations. NAUTILUS is dedicated to computing chemical evolution in different interstellar environments and uses the rate equation approach (Hasegawa et al. 1992; Hasegawa & Herbst 1993) to calculate the abundance as a function of time. The NAUTILUS gas-grain code is a 3-phase model (Ruaud et al. 2016) that includes gas-phase chemistry and chemically active grain surfaces and mantles. Thus, aside from the gas-phase chemistry, NAUTILUS covers the physisorption of neutral species on the surface, the diffusion of these species and their reactions, desorption of species from the surface and repopulation of the surface by species from the mantle as the species on the surface evaporate. The latest version of NAUTILUS, the Nautilus Multi Grain Code (NMGC) 0D model (Iqbal & Wakelam 2018), can perform simulations using a full grain distribution in size. Each grain size bin is treated independently of the others, and only interact with gas. Compared to the single-grain model (model using a single grain size), a multi-grain model changes chemical rates in two ways. First, accretion rates of species depend on grain population. In a multi-grain model, accretion rates vary on different grain sizes according to their total

surface area (iTable A.1 shows the relative surface areas as function of grain sizes). Second, dust temperature depends on its size (see Fig. 5). Species have higher reaction rates on grains which are hotter due to higher hopping and desorption rates. In general, grains which are hotter have lower abundances of lighter species such as CN, CH_2, CO, etc. and more of heavier species such as H_2O, CH_3OH, etc... (see Iqbal & Wakelam 2018, for details). In our current work, we generalize this multi-grain capability to a 1D situation to represent a protoplanetary disk as described in previous Sections. NMGC computes chemistry in all cells given in cylindrical coordinates (r, z) where we provide as input the gas temperature (Eq. A.5), the local radiation field $I_d(\lambda, r, z)$ and dust temperatures $T_d(a_i, r, z)$ given by the radiative transfer simulations, and the number density of each dust population $n_d(a_i, r, z)$ in order to compute the local grain abundances relative to the number density of Hydrogen nuclei $n_H(r, z)$:

$$AB_d(a_i, r, z) = \frac{n_d(a_i, r, z)}{n_H(r, z)}. \quad (3)$$

The z direction is treated as in Hersant et al. (2009), but using 64 points.

2.4. Photorates

Radiations in the UV range have a critical impact on the disk chemistry since UV photons have the necessary energy to photoionize or photodissociate molecules in the disk. For this reason, characterizing the photorates [s^{-1}] at which molecules are dissociated or ionized is of high importance in chemistry models and necessary for a full interpretation of observations.

We evaluate the photoprocess rate as in Heays et al. (2017):

$$k_p(X, r, z) = \int_\lambda \sigma_p(X, \lambda) I_L(\lambda, r, z) d\lambda \quad (4)$$

where $\sigma_p(X, \lambda)$ is the photoprocess cross-section of species X at wavelength λ and $I_L(\lambda, r, z)$ is the local UV radiation. The index p equals i when it stands for ionization and equal d when it stands for dissociation. We perform our integration over the 91.2 to 400 nm wavelength range. To evaluate the rate at each point in the disk, we thus need the local UV radiation field and the (space-independent) cross-sections. Following Section 2.2.3, the UV field is derived using Eq. 2.

The molecular cross-sections used in this study are extracted from the Leiden University website[1] (Heays et al. 2017). They are collected from experimental and theoretical studies. Eighty molecules are treated in this way. The photorates are recomputed at each explicit time step of the chemical evolution.

For all other gas constituents (atoms or molecules unavailable in Heays et al. 2017), we use approximate shielding factors from Visser et al. (2009).

2.5. Molecular Hydrogen formation at the disk surface

2.5.1. The atomic H problem

The NAUTILUS code initially implemented the H_2 formation through the Langmuir-Hinshelwood (LH) mechanism that considers physisorption on grain surfaces. The LH mechanism is efficient only over a relatively narrow temperature range (5-15 K on flat surfaces Katz et al. 1999; Vidali et al. 2004, 2005).

[1] https://home.strw.leidenuniv.nl/~ewine/photo/index.php?file=cross_sections.php

Small grains illuminated by the UV field from the star can get warmer at the disk surface, and this H_2 formation mechanism becomes inefficient, leading to much smaller H_2 formation rate than in the case of a single, larger, equivalent-area, grain size. The low formation rate of H_2 leaves a significant amount of atomic Hydrogen that can severely affect the chemical balance in the disk upper layer (see Section 4 for a more detailed discussion).

However, observations of H_2 in unshielded regions (Habart et al. 2004, 2011) where dust can reach high temperatures (≥ 20 K) show that the column density can be significantly higher than what is expected by simple equilibrium rate equation and PDR model predictions. This implies that the formation mechanisms of H_2 can be efficient in a wider domain than predicted by the LH mechanism.

Several studies proposed more sophisticated mechanisms that theoretically produce comparable H_2 column densities to those derived by observations (e.g. Duley 1996; Cazaux & Tielens 2004; Cuppen & Herbst 2005; Iqbal et al. 2012, 2014; Thi et al. 2020). We follow here the approach of Bron et al. (2014), hereafter B14, which is based on temperature fluctuations of small grains.

2.5.2. Effects of temperature fluctuations

Small grains (≤ 0.01 μm), given their very small heat capacity, have their temperature fluctuating widely even when a relatively small quantity of energy is absorbed. In typical unshielded regions, a small grain can absorb UV-photons originated from the interstellar field with a rather high probability, causing a sudden spike in temperature. If the interval of time between UV-photon absorptions is sufficiently long, the grain which has undergone transient heating has the time to cool down to temperatures smaller than the equilibrium temperature, giving the opportunity for H_2 to form on the surface. Then, the rapid heating of the grain by the absorption of a UV-photon will thermally desorb most species on the surface, releasing H_2 molecules to the gas phase.

Bron et al. (2014) have studied the effect of these temperature fluctuations on the formation of H_2 in PDRs and high UV radiation regions using a statistical approach. By numerically solving the master equation (Le Bourlot et al. 2012), they show (Bron et al. 2014, see their Fig.6) that the LH mechanism alone is sufficient to reach the typical H_2 formation rates observed in PDRs when the temperature fluctuations of small grains are accounted for.

2.5.3. Implementing the H_2 formation rates

The investigation of B14 lies in a domain of gas temperature (100 K) and gas density (10^0 to 10^6 cm^{-3}) distinct from our study but this difference can easily be corrected as both temperature and gas density only affect the results through the collision rate of atomic Hydrogen with the grains, which scales as $n_H \sqrt{T_g}$. Thus, we can estimate the rate for a given density n_H and a given temperature T_g by extracting or interpolating from B14's data the value corresponding to an equivalent gas density n_{eq} equal to:

$$n_{eq} = n_H \sqrt{\frac{T_g}{100\,\mathrm{K}}} \frac{s(T_g)}{s(100\,\mathrm{K})} \quad (5)$$

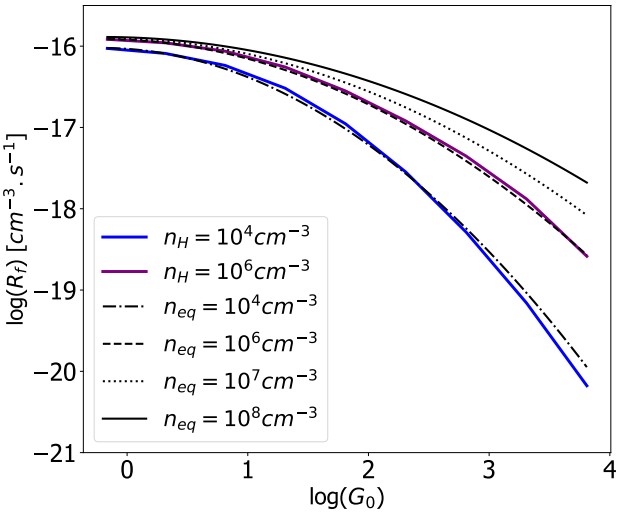

Fig. 7: H_2 formation rate as a function of the UV field intensity (in units of the Habing interstellar field) for various proton number density. Data adapted from Fig. 6 of Bron et al. (2014) are the blue (10^4 cm^{-3}) and purple (10^6 cm^{-3}) solid lines while black lines correspond to our analytic fit for four different number densities (10^4, 10^6, 10^7, 10^8 cm^{-3}).

where s(T_g) is the sticking coefficient at temperature T_g as defined by Le Bourlot et al. (2012):

$$s(T) = \left(1 + \frac{T}{T_2}^{\beta}\right)^{-1} \quad (6)$$

with $T_2 = 464$ K and $\beta = 1.5$, which approximately gives the same result as in Sternberg & Dalgarno (1995).

We interpolated B14 data as a function of proton density and UV field intensity using an analytic polylogarithmic function. The interpolation results are displayed in Fig.7. The PDR layers of protoplanetary disks are dense, typically above $10^6 - -10^8$ cm^{-3} so that essentially the upper curves in Fig.7 apply to our case.

It should be noted that the B14 calculations assume a power-law size distribution from 1 nm to 300 nm composed of only carbonaceous grains. Changing the composition and/or size distribution would affect the precise values of the rates and of the fitted coefficients. However, the asymptotic behaviors of the rates should remain similar. The rate is proportional to the density at low densities, and progressively saturates for larger densities as the fraction of atomic H decreases because the UV flux is insufficient to dissociate H_2. As a function of UV field intensity, the (unsaturated) rate is expected to decrease as $1/G$ since the time spent by any grain in the relevant temperature range where the LH formation is efficient is inversely proportional to the UV photon flux.

3. Model parameters and results

3.1. Detailed description of models

We implement a set of ten different models (see Table 3). All models share a common set of disk structure and physical parameters (see Fig. 2) as described in Table 1, but differ for a limited number of assumptions on grain sizes and temperatures, UV field or H_2 formation mechanism.

The set is divided into two groups, i.e. the single-grain models and the multi-grain models. We describe their specific characteristics in detail in Section 3.1.1 and 3.1.2. As mentioned in Section 2.2.1, the excess of UV radiation exhibited by typical TTauri stars, given the strong wavelength-dependence of photo-processes, inevitably impacts the chemistry of the disk. In order to have a broad view on how our chemical models react to different intensities of UV flux, we adopt two regimes of radiation. One regime uses the spectrum of a relatively high-UV emitting TTauri star and another uses the spectrum of a relatively low-UV emitting one, hereafter called HUV and LUV, respectively. For the HUV regime we use the spectrum of TW Hya (Heays et al. 2017) while for the LUV we use the one of DM Tau. Both FUV spectra are provided in the CTTS FUV spectra database[2] (France et al. 2014). The blue solid line in Fig. B.3 exhibits the spectrum of TW Hya as provided by France et al. (2014) before it is attenuated by the disk.

The chemical abundances in the disk are calculated using the time-dependent equation embedded in NAUTILUS. We use atomic initial abundances described in Table B.1 and all the chemical output are extracted after an integration time of 5.10^6 yrs. All models incorporate the same chemical network and chemical processes described in Section 2.3. In the following, x in model names is either H for high or L for low.

3.1.1. Single-grain models

We use single-grain models as a comparison to our more sophisticated multi-grain models described in Section 3.1.2. These models are treated as in Wakelam et al. (2016), in particular with respect to the UV field penetration and photo-processes (see Hersant et al. 2009). We use the same gas density distribution and same overall gas-to-dust ratio (and hence the same dust mass) as in the multi-grain models. All single-grain models have a single dust size of 0.1 μm. The grains are settled toward the mid-plane assuming a dust scale height as defined in Equation A.20. However, 0.1 μm grains exhibit little settling, as it can be seen from Fig.A.1 and such models are virtually equivalent to non-settled dust models (Wakelam et al. 2016).

Model 1: xUV-LH-T$_g$ The dust temperature (T_d) profile follows that of the gas (T_g) which is given by the solid black line in Fig. 6), T_d is equal to T_g everywhere in the disk. Model 1 is either HUV-LH-T$_g$ or LUV-LH-T$_g$, depending on whether the stellar UV field is high (HUV) or low (LUV). The differences are detailed in Section 3.1.

Model 2: xUV-LH-T$_a$ Model 2 is similar to Model 1, except for the dust temperature. In Model 2, the grain temperature is given by Eq. 1 and shown in Fig. 6 (red solid line). The temperature T_d is hence the area-weighted temperature from the grain size distribution of the multi-grain models and it is called T_a. As T_a is significantly higher than T_g, we expect depletion to occur at lower elevations than in Model 1.

Model 3: xUV-B14-T$_a$ In Model 3, the prescription of Bron et al. (2014) as described in Section 2.5 is used to form H_2. The

[2] https://cos.colorado.edu/~kevinf/ctts_fuvfield.html

Table 2: List of figures.

Models	Figures
single, HUV	8, 9, 12, 13, 15, 16, C.1
single, LUV	D.1, D.2, D.3
multi, HUV	8, 9, 11, 12, 14, 15, 17, 18, 19, 20, C.2
multi, LUV	D.1, D.4

expected effect is a higher production of H_2 in the PDRs region of the disk than in the other models.

3.1.2. Multi-grain models

Multi-grain models, as opposed to single-grain ones, include the full grain distribution detailed in Table A.1 where each grain population has a specific temperature (Fig. 6), a specific settling factor and is chemically active. For all multi-grain models, we use a size range of [5 mm, 1 mm] with a size exponent $d = -3.5$ (Eq. A.16) and divide the grain size interval into 16 logarithmically distributed subintervals using Eq. A.19. An overview of the grain size interval with their respective relative dust mass and surface area is given in Table A.1 while Fig. A.1 shows the scale height of each 16 grain size population as a function of the radius. Multi-grain models are composed of two categories.

Model 4: M-xUV-LH Either called M-HUV-LH or M-LUV-LH depending on the flux, they use the classical LH mechanisms for H_2 formation without considering small grains temperature fluctuation.

Model 5: M-xUV-B14 We add the H_2 formation mechanisms prescribed in B14 (see Section 2.5). These models, with grain growth, dust settling, one temperature per grain size and H_2 formation derived from Bron et al. (2014) are the most complex model and we use them as reference.

Table 3 summarizes the various models. Table 2 lists the different figures in the text in relation with their respective models. A few figures relevant of the HUV cases are presented in Appendix C, while all figures for the LUV cases appear in Appendix D.

3.2. Results

We present here some general issues about the UV field, the dust temperature and the H_2 formation. A more thorough discussion of the chemistry is done in the next section.

3.2.1. Impact of UV field

A comparison between Tables 4 and D.1 shows that, for a given model, the integrated column densities (or molecular surface densities) have about the same order of magnitude whether the flux is high (HUV) or low (LUV). Unlike in the PDR layer, the mid-plane chemistry is not dependent on the UV flux regime. The dust opacity is such that the UV flux is sufficiently attenuated in the HUV and LUV models for the chemistry to be similar in both cases.

Figures C.1, C.2, D.3, and D.4 show that the chemistry is nearly the same for all models from the mid-plane to roughly $1.5\,H$. We observe more H_2, CO, CS and CN above 3 scale-heights in the LUV models than in the HUV ones because a high UV flux implies more efficient photodissociation. Near the mid-plane, the UV field is similarly attenuated and the radiation field intensities are about the same in all models. As a consequence, the only parameter that impacts the chemistry is the dust temperature T_d and this applies both to the single-grain models and the multi-grain models.

3.2.2. Impact of dust temperature on H_2 formation and chemistry

A first effect of the adopted grain temperature is related to the formation of H_2 and the remaining amount of H, which is very important for the gas-phase chemistry. Adopting the formalism of Bron et al. (2014) to form H_2 produces, as expected, more H_2. In these cases, Figures C.1 and C.2 show a shift in the H/H_2 transition toward the disk surface which implies less gas-phase H and more H_2 in the upper layers.

For single-grain models, the gas temperature we take is relatively low. Table 4 shows that when $T_d = T_g$, the remaining amount of H is still reasonably low (intermediate), contrary to the case where $T_d = T_a$ (HUV-LH-T_a) which exhibits the highest amount of H, together with the multi-grain model M-HUV-LH. Using only the LH mechanism to form H_2 on grains with high temperatures reduces significantly the amount of H_2 above two scale heights. This is particularly true for the M-HUV-LH Model, where the grain temperature depends on the grain size: the reservoir of "cold" grains is not large enough to allow for an efficient H_2 formation on grains in the upper disk layer.

On the contrary, near the mid-plane, in most models the grain temperature is always low enough for the LH mechanism to efficiently form H_2 and regulate the atomic H abundance.

4. Discussion

We first discuss (Sec.4.1) the vertical variations of abundances for CO, CN and CS. We then investigate the C,N and O reservoirs and surface chemistry (Sec.4.2-4.3) before discussing the formation of water and complex organic molecules (Sec.4.4-4.5). We also discuss some possible implications of our results on planet formation and embryos compositions. We focus the discussion that follows (except for Section 4.1) on the HUV case (corresponding to the UV flux received by the TW Hya disk) because we have seen that most of the analysis of HUV models can be considered valid for LUV models. Figures relevant to the LUV case (similar to what is expected for the DM Tau disk) are presented in Appendix D. All results are presented at the final stage of time evolution i.e. 5.10^6 yrs.

4.1. Vertical distribution of abundant (easily observed) molecules

4.1.1. Column densities

Figure 8 shows the molecular surface densities of a few popular species detected in TTauri disks. Table 4 and D.1 present the column densities at a radius of 100 au for the most abundant species such as CO, CN and CS. These tables reveal that there is no specific trend for a given model, although there can be variations of up to 2.5 orders of magnitude in the column densities. An analysis of Figures 9, C.1 and C.2, which provide the vertical profile

Table 3: Description of models

	bins	sizes (μm)	T_d	HUV	LUV	H_2 formation
HUV-LH-T_g	1	0.1	T_g	✓		LH
HUV-LH-T_a	1	0.1	T_a	✓		LH
HUV-B14-T_a	1	0.1	T_a	✓		B14
LUV-LH-T_g	1	0.1	T_g		✓	LH
LUV-LH-T_a	1	0.1	T_a		✓	LH
LUV-B14-T_a	1	0.1	T_a		✓	B14
M-HUV-LH	16	$[5.10^{-3} - 10^3]$	$T_{i\ \{i=1...16\}}$	✓		LH
M-HUV-B14	16	$[5.10^{-3} - 10^3]$	$T_{i\ \{i=1...16\}}$	✓		B14
M-LUV-LH	16	$[5.10^{-3} - 10^3]$	$T_{i\ \{i=1...16\}}$		✓	LH
M-LUV-B14	16	$[5.10^{-3} - 10^3]$	$T_{i\ \{i=1...16\}}$		✓	B14

Notes. HUV stands for high UV field and LUV for low UV field. LH is for the classical traitement of the Langmuir-Hinshelwood mechanism and B14 when the prescription of Bron et al. (2014) is used instead. T_g means that the dust temperature equals to that of the gas, T_a is the weighted-area dust temperature as defined by Eq. 1. T_i is the temperature of i^{th} grain population. M stands for multigrain model. As an example, the model M-HUV-B14 is a multi-grain model computed using the B14 method with a high UV field.

of molecular densities at 100 au, is required to understand the origin of these variations.

For the column density of CO it shall be noted that 1) CO is formed in the gas phase and 2) is sensitive to photodissociation. The model that produces the most CO is thus LUV-B14-T_a because this model combines both a low UV flux, a large column density of H_2 that shields CO from the UV and a high grain temperature that prevents CO from being adsorbed. The second model producing the most CO is M-LUV-B14: the CO column density is slightly lower than in LUV-B14-T_a because in multi-grain models a fraction of the grains is significantly settled, involving a more effective UV penetration. In that sense, it is not surprising that M-HUV-LH is the model that produces the smallest column density: this model combines a high UV flux, more penetration due to settling and a small production of H_2 which decreases the shielding.

For the column densities of CS and CN, Table 4 shows that using predicted molecular surface densities is not enough to derive general trends. Nevertheless, we can note that M-HUV-B14 is the model that produces the most CS and CN. On the other hand, HUV-B14-T_a produces the smallest column density of CS while HUV-LH-T_a is the model that produces the smallest column density of CN. This suggests routes of formation which do not simply depend on the grain temperature.

In the case of the single-grain models (see Figs. C.1 and D.3), all models using the same grain temperature ($T_d = T_g$ or T_a) have the same vertical profile at altitudes $z < 1.5H$ regardless of the flux regime. Similarly, since all multi-grain models use exactly the same grain temperature and size distribution, they all exhibit the same vertical density profile at altitudes $z < 1.5H$ (for a given species) regardless of the incident flux and of the assumed H_2 formation mechanism (see for example, the CO abundance profiles for the two multi-grain models in Figure C.2, middle panels of columns b-c). Accordingly, in this relatively high mass disk, differences in column densities (Tab. 4) result from what happens above $z = 1.5H$.

4.1.2. Vertical variations

CO Gas-phase CO abundance is both influenced by grain temperature and by abundance of H_2. For multi-grain models, the flux penetration is larger than in single-grain models, so that CO column densities appear to be globally smaller than in single-grain models (Fig. 8). In M-HUV-LH, the CO abundance remains low above $z \sim 3H$ (see Fig. C.2). On the other hand, M-HUV-B14 produces more H_2 allowing CO to survive at higher altitudes. The resulting CO column density is of the same order than in HUV-LH-T_a and HUV-B14-T_a. Although this has little impact on the total column density, the abundance of CO at $z \leq 1H$ is much higher in multi-grain models than in single-grain ones. In single-grain models, the single grain temperature becomes low enough for CO to freeze out efficiently while in multi-grain models there is always a fraction of abundant small grains whose temperature remains high enough to prevent CO from being depleted as efficiently as in single-grain models.

CN and Nitrogen bearing Species For all models, the main reactions that create CN in the upper layers at 100 au are bimolecular reactions in the gas-phase: $N + C_2 \rightarrow C + CN$ (69%) and $N + CH \rightarrow H + CN$ (22%). Note that CH is mostly destroyed by the reaction $H + CH \rightarrow C + H_2$. Therefore, more atomic H in the upper layers implies less CH available to form CN. The effect is clearly visible for the single-grain models (Fig.C.1) where HUV-B14-T_a produces more CN above 3.5H because H_2 is more abundant compared to HUV-LH-T_a. The effect is less obvious in the multi-grain models (C.2). Below $z = 1.5\,H$, all the single-grain models exhibit roughly the same abundance, including HUV-LH-T_g, which suggests a low sensitivity of CN due to the dust temperature in this range of values.

CS The main formation proceess of CS in the upper layers is a sequence of a bimolecular reaction and a dissociative recombination reaction: $H_2 + CS^+ \rightarrow H + HCS^+$ and $HCS^+ + e^- \rightarrow H + CS$. The sequence shows that the production of CS is dependent on H_2. As a consequence, forcing the formation of H_2 leads to the formation of CS, providing that the ionization fraction is the same (as it is the case here).

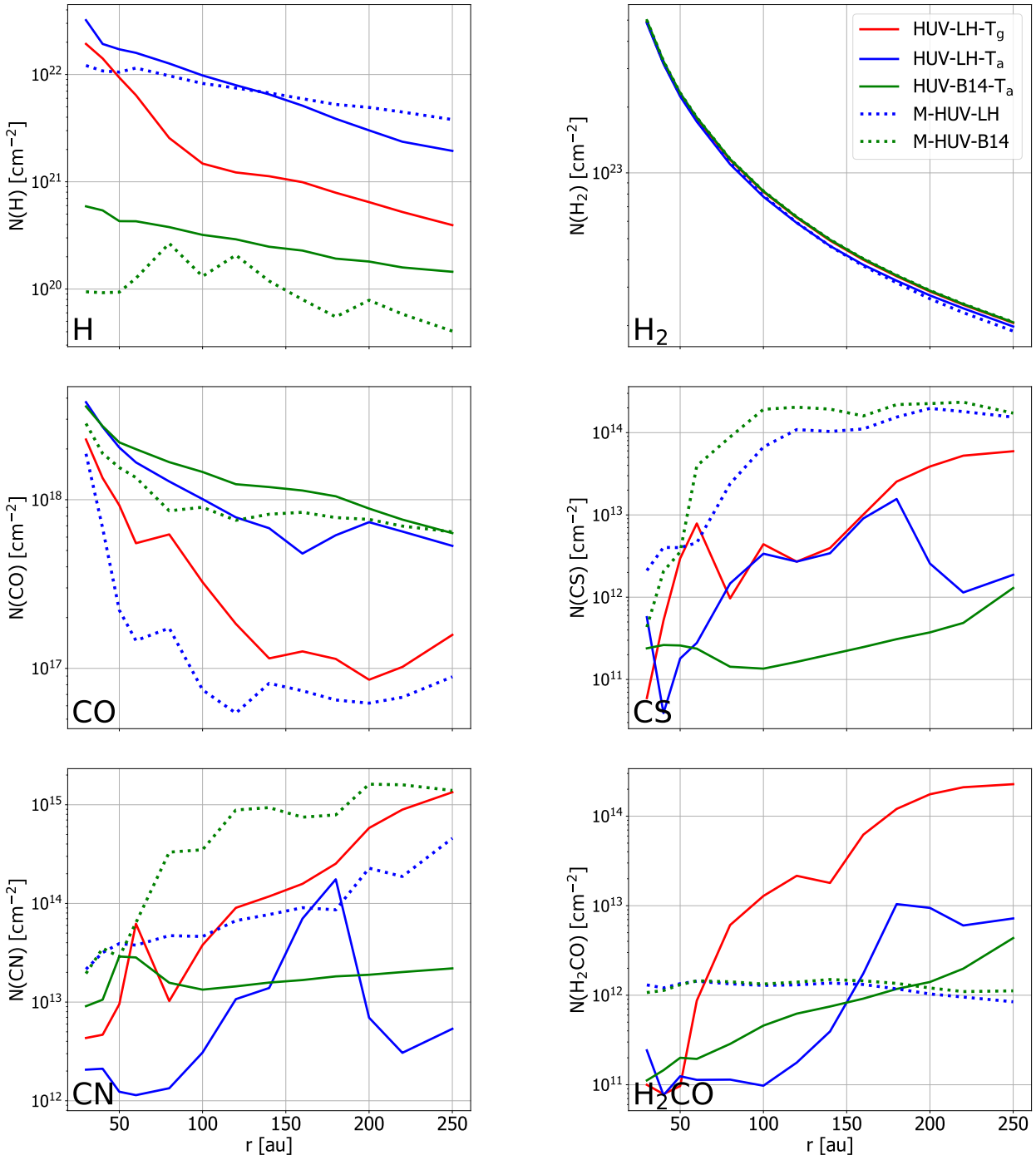

Fig. 8: Surface densities of the single-grain models (solid lines) and multi-grain models (dotted lines) as a function of the radius in high UV flux regime.

For single-grain models, the grain temperature is higher in HUV-LH-T_a than in HUV-LH-T_g. The production of H_2 being more efficient in the latter model at high elevation, the peak of CS in HUV-LH-T_g (Fig. C.1) is broader ($\sim$ 2 to 3 H). In the meantime, CS also tends to undergo sticking processes on surfaces higher in the disk, competing with its production in the gas-phase. This explains the dramatic drop of CS density below 2 H. As regards HUV-LH-T_a, the production of H_2 starts to be efficient at a lower scale height ($\sim$ 2 versus 3 H). Then, CS abundance dramatically increases at $\sim$ 1.8 H (because of the steep temperature slope) before rapidly decreasing as temperature is low enough for CS to deplete on the grains, resulting in a very narrow peak. In HUV-B14-T_a, the production of H_2 is efficient even in the upper layers and CS starts to form higher in the disk, explaining why the CS abundance is two orders of magnitude larger than in HUV-LH-T_g and HUV-LH-T_a at 4 H (Fig.C.1).

For multi-grain models, we find larger CS column density but the location of the peak of abundance is lower in altitude (Fig. 9 (c)) because of the relatively low visual extinction. Just as for the single-grain models, the surface density is larger in the

Table 4: Column densities [cm^{-2}] of main molecules at 100 au for HUV models. Last three columns summarize the main properties of the model with respect to the H_2 formation and grains (% of grains, in sites, with a temperature above 20 K between 0 and 1.5H and 1.5 and 2.5H).

	H	H_2	CO	CS	CN	H_2 formation	0 to 1.5H	1.5 to 2.5H
HUV-LH-T_g	$1.48.10^{21}$	$8.19.10^{22}$	$3.24.10^{17}$	$4.40.10^{12}$	$3.79.10^{13}$	"cold" grains	0%	25%
HUV-LH-T_a	$9.80.10^{21}$	$7.78.10^{22}$	$1.01.10^{18}$	$3.38.10^{12}$	$3.08.10^{12}$	more H	100%	100%
HUV-B14-T_a	$3.20.10^{20}$	$8.25.10^{22}$	$1.46.10^{18}$	$1.35.10^{11}$	$1.34.10^{13}$	less H	100%	100%
M-HUV-LH	$8.26.10^{21}$	$7.86.10^{22}$	$7.46.10^{16}$	$6.69.10^{13}$	$4.62.10^{13}$	more H	96%	99%
M-HUV-B14	$1.31.10^{20}$	$8.26.10^{22}$	$9.02.10^{17}$	$1.92.10^{14}$	$3.49.10^{14}$	less H	96%	99%

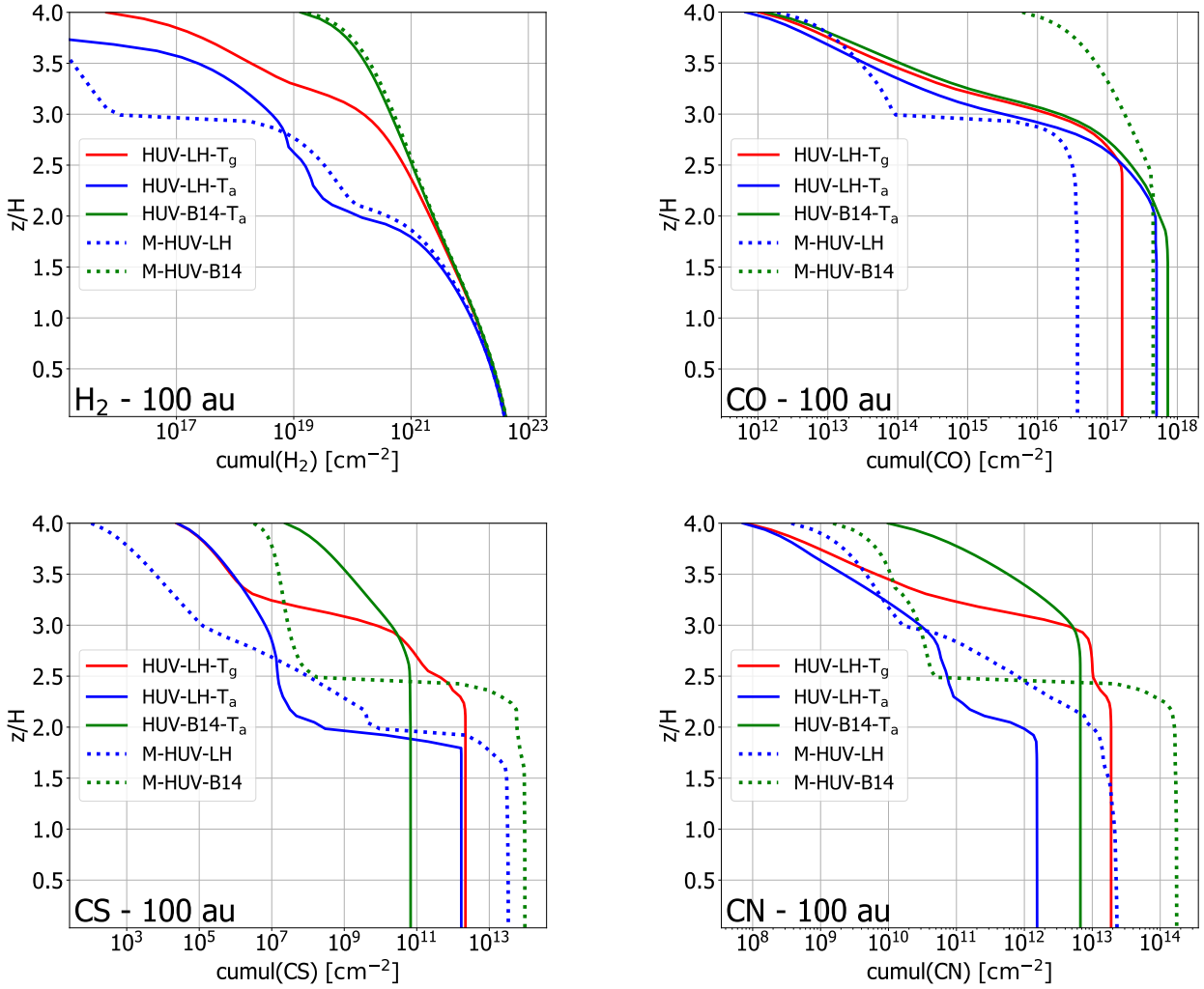

Fig. 9: Vertical cumulative surface density [cm^{-2}] of H_2, CO, CS and CN at 100 au from the star in the HUV models.

case of M-HUV-B14 because the formation of H_2 is more efficient and the quantity of H lower. Below $z = 1.5\,H$, the difference in abundance is strictly dependent on T_d and as expected, the hot-grain models (HUV-LH-T_a and HUV-B14-T_a) produce more CS in the gas-phase than the cold-grain model HUV-LH-T_g, whereas all multi-grain models exhibit the same vertical profile.

4.2. Element reservoirs: C, N, O in the cold mid-plane

The relative importance of reservoirs appearing roughly constant along the distance from the star, we decide to study the reservoirs at 100 au. All species that have been investigated represent at least 0.5 % of the total quantity of carbon, nitrogen or oxygen. As previously seen, the chemistry below $z = 1.5\,H$ only depends on the grain temperature. Therefore, it turns out to be sufficient to discuss HUV-LH-T_g, HUV-LH-T_a and M-HUV-LH only.

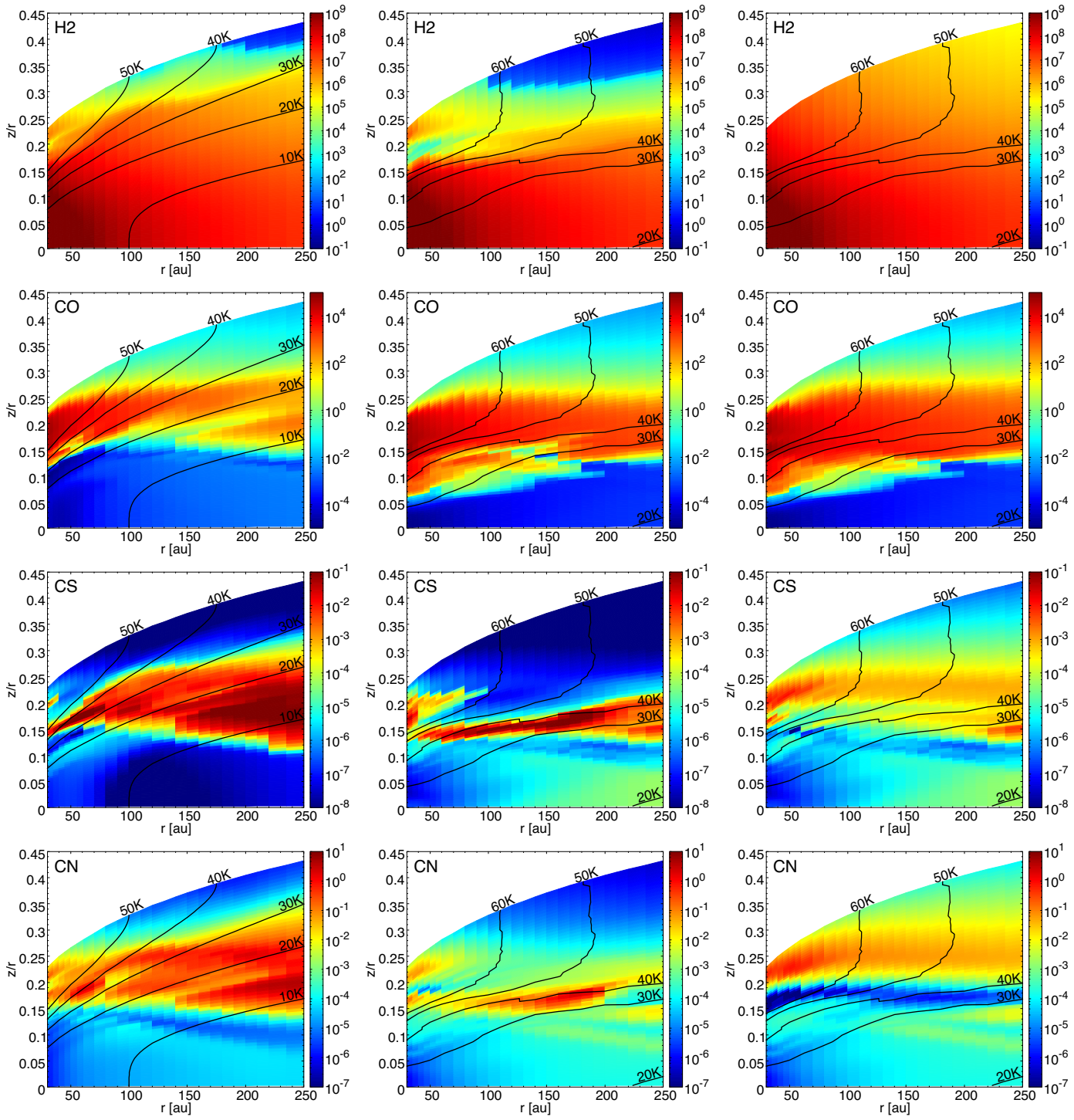

(a) HUV-LH-T_g (b) HUV-LH-T_a (c) HUV-B14-T_a

Fig. 10: Density [cm^{-3}] of H_2, CO, CS and CN in the gas-phase of the single-grain models in HUV regime. Left column is the HUV-LH-T_g models, middle one is HUV-LH-T_a and right one is HUV-B14-T_a.

Carbon bearing species Figure 12 (top) shows that frozen CO_2 is the main carrier of carbon, both in HUV-LH-T_a and M-HUV-LH with 58.1% and 51.3% of elemental carbon, respectively, while the quantity of CO_2 is negligible in comparison to the other species in HUV-LH-T_g. The dust temperature appears too high in these two models to allow for a large quantity of hydrogen to successively hydrogenate the frozen atomic oxygen to form water. Instead, the atomic oxygen easily diffuses on the surface and the relatively high temperature allows to overcome the activation barrier to rapidly form CO_2 by reacting with the frozen CO. In HUV-LH-T_g, on the other hand, Fig. 12 (top) shows that the main carrier of carbon is CH_4 with 49.1%. In this colder dust temperature model, CO is initially formed in the gas before being efficiently and rapidly adsorbed onto the grain surfaces, just like in hot-grain models. However, once on the surface, CO is channeled to s-CH_3OH through hydrogenation sequences. The photo-

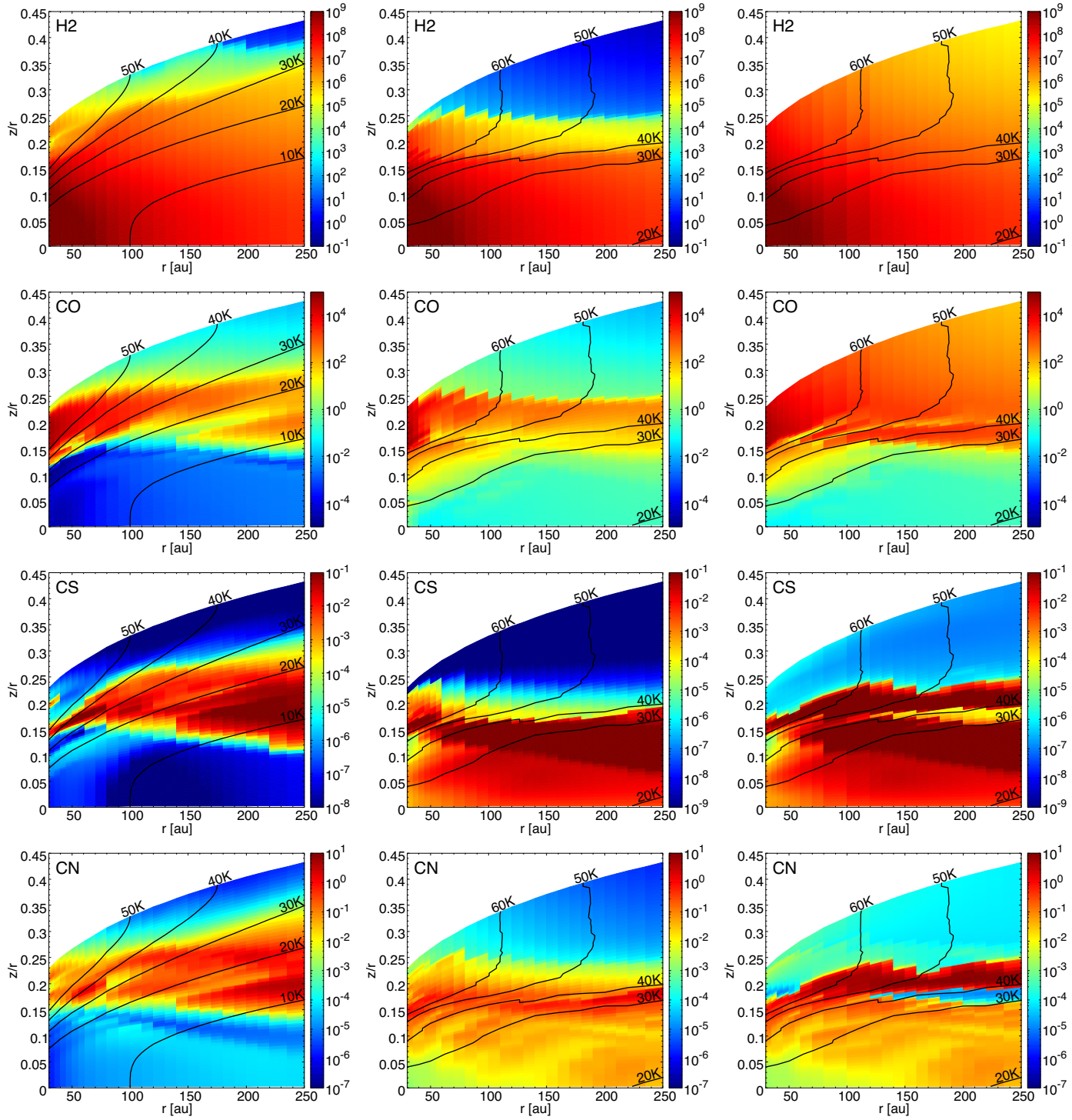

(a) HUV-LH-T_g (b) M-HUV-LH (c) M-HUV-B14

Fig. 11: Density [cm^{-3}] of H_2, CO, CS and CN in the gas-phase of HUV-LH-T_g (left column) and of the multi-grain models in HUV regime.

dissociation of CH_3OH then leads to CH_4 formation. Hence, in the mid-plane, disks with colder grains will produce more CH_4 while warmer disks will produce more CO_2. The other main carrier is the complex organic species CH_3OH, which holds about 10% of carbon in M-HUV-LH and HUV-LH-T_g.

Oxygen bearing species CO_2 ice is the main carrier of oxygen in HUV-LH-T_a and M-HUV-LH with 82.0% and 72.5%, respectively (Fig. 12, bottom). The temperature of the grains in these two models is too high (T_a = 24.6 K) to allow for a large quantity of atomic hydrogen to remain on the grains and hydrogenate the atomic oxygen to form water. As described above, atomic oxygen easily diffuses and also combines with CO to form CO_2. In HUV-LH-T_g, H_2O is by far the largest carrier of oxygen with

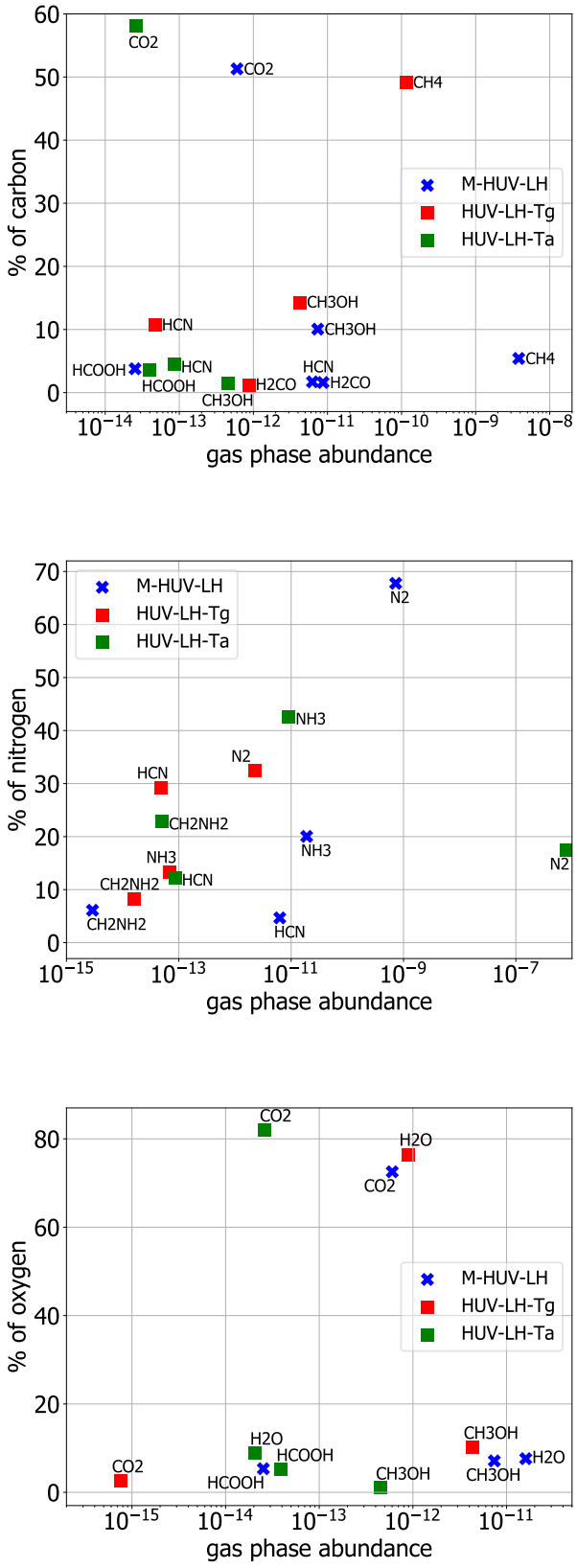

Fig. 12: Species that contains at least 0.5% of elemental carbon (top), nitrogen (middle) and oxygen (bottom) in the mid-plane at 100 au: percentage of the carbon/nitrogen/oxygen locked in the species as a function of the gas-phase species abundance.

76.4%. Disks with colder grains will produce more H_2O while disks with warmer grains will produce more CO_2. CH_3OH is, again, an important carrier and holds about 10% of oxygen in HUV-LH-T_g.

Nitrogen bearing species Nitrogen is mostly in the form of N_2 in M-HUV-LH (67.8%) and in HUV-LH-T_g (32.4%) (Fig. 12, middle). Moreover, in all models, the gas-phase abundance of N_2 is noticeably larger than the one of the other species. The reason for that is a combined effect of the faster conversion of atomic nitrogen into N_2 in the gas-phase compared to the depletion of N and the high grain temperature that prevents N_2 from depleting onto the surfaces. Indeed, The binding energy of N_2 ($E_b(N_2)$ = 1100 K on amorphous water ice surface) is smaller than most of the other molecules and slightly smaller than that of CO (Minissale et al. 2016; Wakelam et al. 2017) so that N_2 is retained more efficiently in the gas. We note that, given the low dust temperature, the gas-phase abundance of N_2 in HUV-LH-T_g is the smallest of all models. In HUV-LH-T_a, N_2 is still the main carrier of nitrogen but remains in the gas-phase because of the large dust temperatures. On the grains, NH_3 is the main carrier of nitrogen with 42.7% of the elemental nitrogen. Therefore N_2 is expected to be the carrier of nitrogen in the disk mid-plane but remains mostly in the gas-phase in hot-grain models. The other main carriers of nitrogen are HCN (29.2% in HUV-LH-T_g, 12.3% in HUV-LH-T_a) and CH_2NH_2 (22.9% in HUV-LH-T_a, 8.3% in HUV-LH-T_g).

4.3. Surface chemistry in the mid-plane

One important conclusion of Section 4.2 is that disks with colder grains will produce in the mid-plane more CH_4 and H_2O while warmer disks will produce more CO_2. This clearly demonstrates the major role of the grain temperature on the surface chemistry. We investigate here more deeply the mid-plane surface chemistry of a few key molecules for the same three models i.e. HUV-LH-T_g, HUV-LH-T_a and M-HUV-LH.

Figures 13 and 14 present maps of number density for H_2, CO, CS and CN locked on grain surfaces in the case of single-grain and multi-grain models, respectively. Figure 15 presents the surface abundance per total atomic hydrogen for various molecules as a function of the grain radius a and their temperature in the mid-plane of the disk. The crosses, the square markers, and the round markers stand for the multi-grain model at 30 au, 100 au and 200 au respectively. The triangle pointing upward represents the surface abundance in the single-grain model HUV-LH-T_g and the triangle pointing downward represents the abundance in the single-grain model HUV-LH-T_a, both at 100 au.

4.3.1. Carbon and oxygen-bearing molecules: CO, CO_2 and CH_4

CO is formed in the gas-phase prior to being accreted on small grains during the first 10^6 yrs of the simulation. However, because of its small binding energy (E_b(CO) = 1300 K Wakelam et al. 2017), it is rapidly thermally desorbed from the hot ($T_g > 20$ K) smaller grains and gets accreted by large cold grains ($T_g < 20$ K), where it remains locked until the simulation is stopped. Considering this mechanism, CO is distributed according to the grain population and Fig. 15 (top left panel) shows two regimes of abundance, accounting for the desorption bar-

rier, where CO ice tends to stay locked on grains of size $\gtrsim 1\ \mu$m at all radii.

For the single-grain models, the same mechanism is at play. However, rather than involving a distribution of CO on various grain populations, this simply results in a small (gas-phase) abundance in the hot-grain model HUV-LH-T_a and a high abundance in the cold-grain model HUV-LH-T_g.

As for CO_2, its binding energy is relatively high ($E_b(CO_2)$ = 2600 K Wakelam et al. 2017). As a consequence the abundance of CO_2 ice depends very little on the dust temperature. In multi-grain models, s-CO_2 is efficiently formed through

$$\text{s-O} + \text{s-CO} \rightarrow \text{s-CO}_2\ (\text{E}_\text{A} = 1000\,\text{K}) \quad (7)$$

$$\text{s-OH} + \text{s-CO} \rightarrow \text{s-CO}_2 + \text{s-H}. \quad (8)$$

CO_2 is more abundant on the smaller grains because their temperature allows to overcome the activation barrier of reaction 7 and the drop in abundance on large grains at 200 au (and further) originates from the grain temperature getting too low for reaction 7 to be activated. Therefore, the outer disk forms fewer CO_2 ice.

In cold-grain models, CH_4 is the largest carrier of carbon (see Section 4.2). As expected, Figure 15 (Bottom-left) shows that s-CH_4 is more abundant on cold grains ($T_g < 20$ K). s-CH_4 is formed via the hydrogenation of s-CH_3. The latter is formed through the following two sequences:

$$\text{s-CO} + \text{h}\nu \rightarrow \text{s-C} + \text{s-O} \quad (9)$$

$$\text{s-H}_2 + \text{s-C} \rightarrow \text{s-CH}_2 \quad (10)$$

$$\text{s-H}_2 + \text{s-CH}_2 \rightarrow \text{s-CH}_3 + \text{s-H} \quad (11)$$

and

$$\text{s-CH}_3\text{OH} + \text{h}\nu \rightarrow \text{s-OH} + \text{s-CH}_3. \quad (12)$$

In view of the above, CH_3OH is formed on the grains prior to being photo-dissociated (if the computation domain is sufficiently extended). Then the released atomic carbon (Reaction 9) and s-CH_3 (Reaction 12) lead to s-CH_4 formation. Consequently, the formation of CH_4 is more efficient on large cold grains since 1) CO must be adsorbed and 2) hydrogenation is needed to create CH_3OH. CH_4 ice is thus found to be more abundant on large grains and in the outer disk.

4.3.2. Sulfur-bearing species: H_2S

In the gas phase, H_2S has been identified in dense cloud cores, cometary comae and Phuong et al. (2018) reported the first detection of H_2S in the cold and dense ring about the TTauri star GG Tau A. The low H_2S column densities observed in GG Tau A and in dense molecular clouds are assumed to be the result of a strong sulfur depletion (Hudson & Gerakines 2018; Phuong et al. 2018).

We investigate here the formation routes of S-H bonds and more specifically the simple S-bearing molecule Hydrogen sulfide, H_2S, in the mid-plane icy mantles of our multi-grain models. Figure 15 (second row, right column) shows the abundance of icy H_2S as a function of the grain size. There is a strong anti-correlation with grain temperatures. The smallest H_2S abundances are located on the hottest grains ($T_d \sim 27$ K) while the largest abundances are found on large colder grains ($T_d \lessapprox 15$ K). This anti-correlation is observed at all radii. The abundances on the large grains ($> 10\mu$m) are independent of the radius. For the small grains, however, the inner disk exhibits larger abundances than the outer disk because of higher collision rates in the inner regions. The strong anti-correlation with temperature is directly related to the main formation pathways of H_2S that implies hydrogenation sequences:

$$\text{s-S} \xrightarrow{\text{s-H}} \text{s-HS} \xrightarrow{\text{s-H}} \text{s-H}_2\text{S} \quad (13)$$

$$\text{s-CH}_3\text{SH} \xrightarrow{\text{s-H}} \text{s-CH}_3 + \text{s-H}_2\text{S}. \quad (14)$$

We note that the channels to s-CH_3SH also involve successive hydrogenations (of s-CS, mainly). Reaction 13 occurs on grains of all sizes but is more effective on the large cold grains ($T_d \lessapprox 15$ K) and Reaction 14 is only found to be effective on the colder grains.

4.3.3. Nitrogen-bearing species: NH_3

The main nitrogen-bearing icy species in the mid-plane are NH_3, HCN, N_2 and CN at all radii. In the multi-grain models, as seen in Fig. 15, the abundance of sNH_3 is inversely proportional to the grain size until $\approx 1\mu$m where the abundance stops decreasing. The abundances of NH_3 ice are roughly the same at 100 and 200 au but not at 30 au.

The main pathway to sNH_3 originates from the accretion of N at the surface of the grains and its successive hydrogenations to form sNH_3 (see Aikawa et al. 2015; Eistrup et al. 2018; Ruaud & Gorti 2019). Such hydrogenation reactions are efficient on cold surfaces ($T_d \lessapprox 15$ K), which explains why the surface abundance of NH_3 does not keep dropping when grain temperatures are low. As for the small warmer grain surfaces, their high quantity implies a high collision rate with NH_3 which stays on their surface given its binding energy ($E_b(NH_3)$ = 5500 K). As the disk evolves, a large fraction of nitrogen-bearing species are transformed into complex molecules and other routes become effective such as the destructive hydrogenation of NH_2CO:

$$\text{s-NH}_2\text{CO} \xrightarrow{\text{s-H}} \text{s-NH}_3 + \text{s-CO}. \quad (15)$$

4.4. Water

The formation of water is key to explain the evolution of protoplanetary disks and formation of comets, both decisive elements to understand the delivery of water to planetary surfaces. Spectral lines of H_2O in the gas-phase of inner disk regions have now been widely detected in disks around TTauri stars using near- and mid-infrared (Carr & Najita 2008; Pontoppidan et al. 2010) or far-infrared observations (Riviere-Marichalar et al. 2012). Cold water in the outer disk regions, on the other hand, is harder to detect due to low excitation lines.

It is assumed (Dominik et al. 2005; Lecar et al. 2006; Podio et al. 2013; Du & Bergin 2014) that water on grain surfaces cannot exist inside the snow-line ($T_d \gtrsim 150$ K), which represents radii smaller than a few to ten au around T Tauri stars. The innermost radius computed by our models is 30 au, which is beyond the radial ice line of water. Therefore, we do not discuss the radial location of the water ice line.

4.4.1. Gas-phase

Three main parameters control the abundance of water in gas-phase, the photo-desorption by FUV photons and cosmic rays, the dust temperature and the chemical reactions in the gas-phase, in particular:

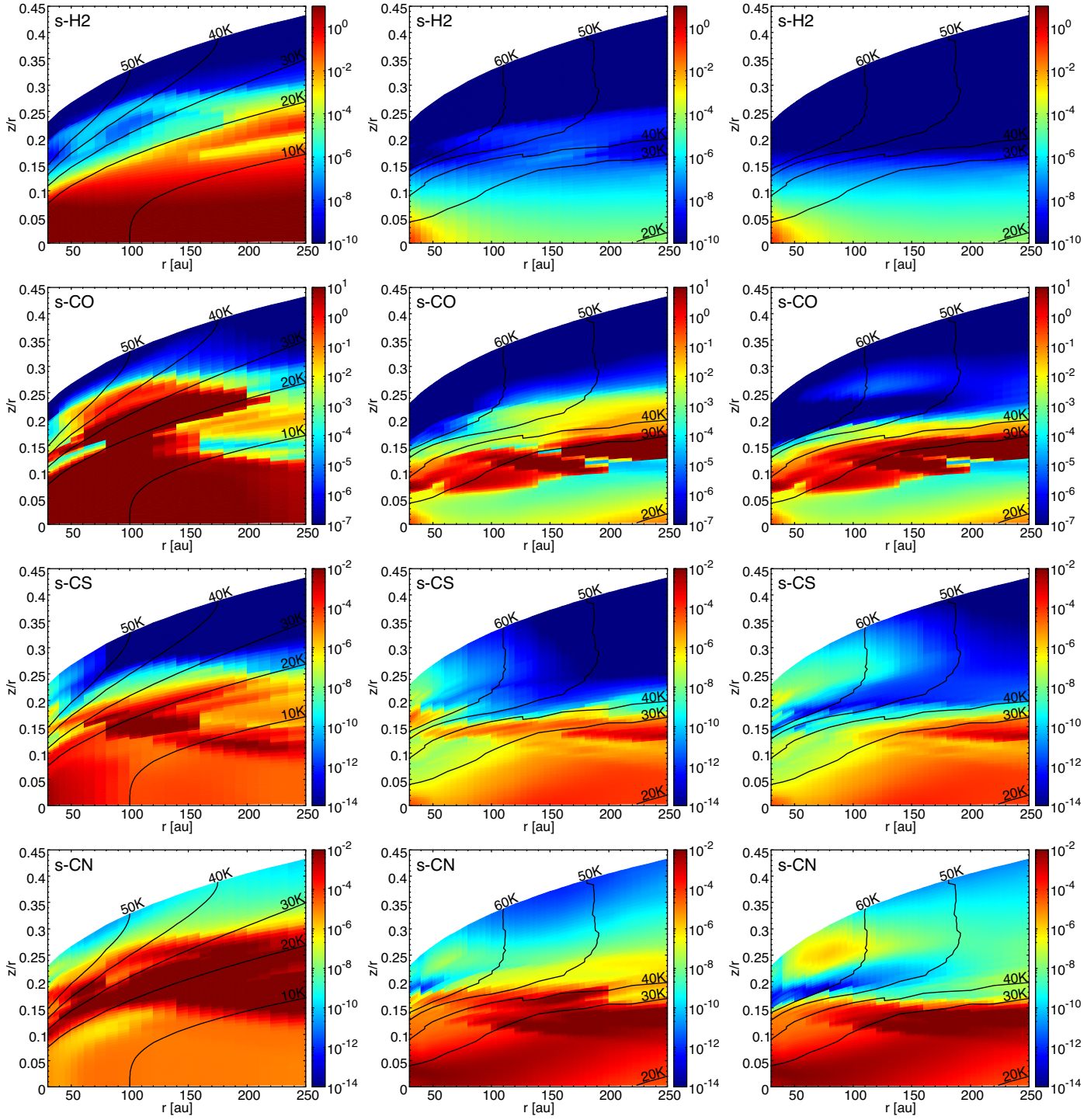

(a) HUV-LH-T_g (b) HUV-LH-T_a (c) HUV-B14-T_a

Fig. 13: Density [cm^{-3}] of H_2, CO, CS and CN in the gas-phase of the single-grain models in HUV regime. Left column is the HUV-LH-T_g models, middle one is HUV-LH-T_a and right one is HUV-B14-T_a.

$$H_2 + OH^+ \rightarrow H + H_2O^+ \quad (16)$$
$$H_2O^+ + H_2 \rightarrow H + H_3O^+ \quad (17)$$
$$H_3O^+ + e^- \rightarrow H + H_2O \quad (18)$$

Thus H_2 and OH^+ are the main precursors for H_2O. Whether H_2 or OH^+ is the limiting factor is determined by this other sequence:

$$H_2 + CR \rightarrow H_2^+ + e^- \quad (19)$$
$$H_2^+ + H_2 \rightarrow H_3^+ + H \quad (20)$$
$$H_3^+ + O \rightarrow OH^+ + H_2. \quad (21)$$

These two sequences show that H_2O formation depends on H_2 and OH^+ but the latter also depends on H_2. Therefore, this is the

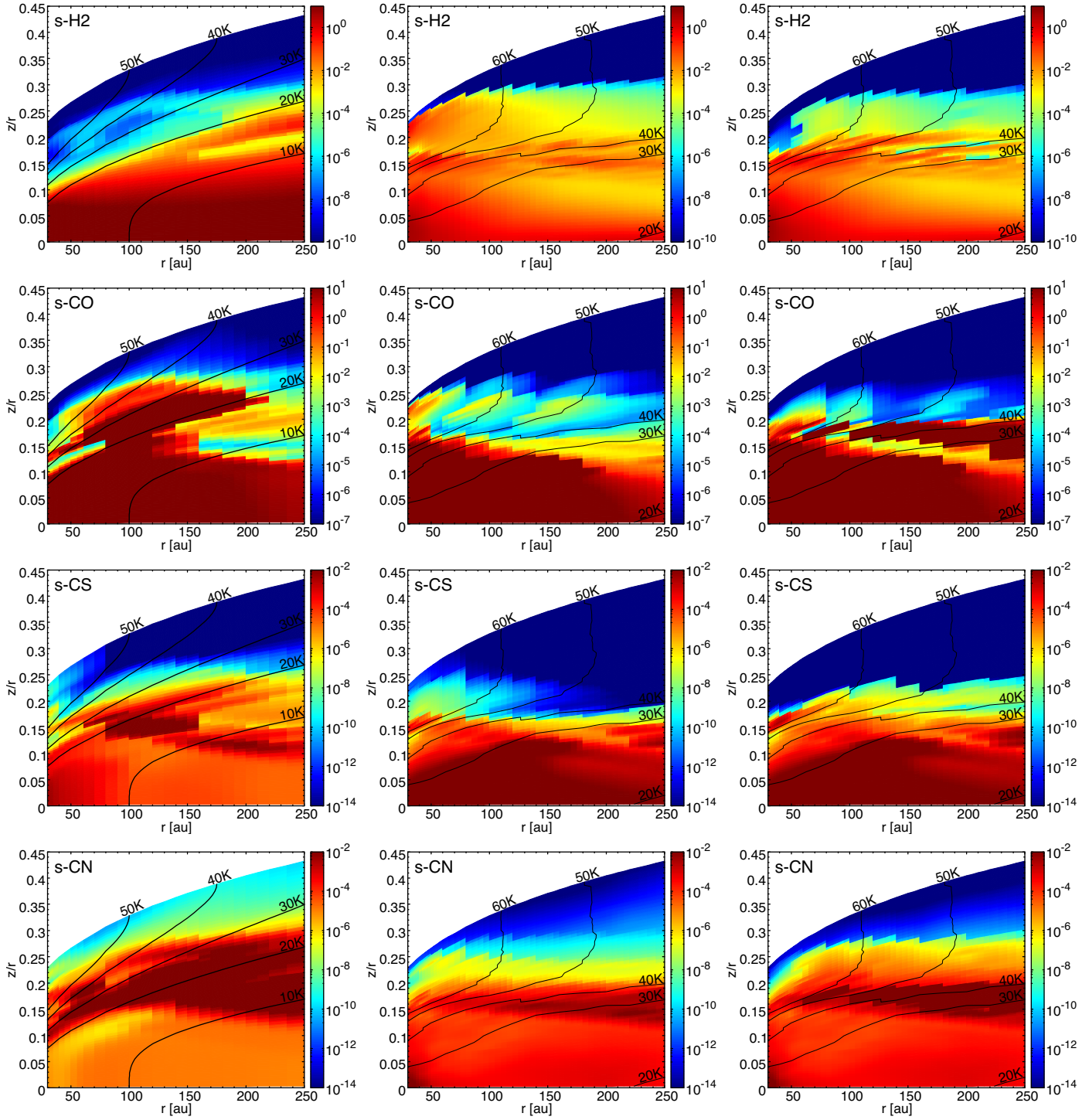

(a) HUV-LH-T_g (b) M-HUV-LH (c) M-HUV-B14

Fig. 14: Density [cm^{-3}] of H_2, CO, CS and CN in the gas-phase of HUV-LH-T_g (left column) and of the multi-grain models in HUV regime.

H_2 abundance that sets the gas-phase formation of water and accounts for the difference between the models (not cosmic-rays or OH^+). However, the gas-phase formation of H_2O only represents a small fraction of all H_2O molecules formed as most H_2O are formed on grain surfaces. The abundance of gas-phase water is thus mainly governed by both the formation rate of icy water and by the photo-desorption rate. Thermal-desorption is ineffective in most parts of the disk because the binding energy of water is high. The formation rate depends on the grain temperature while the photo-desorption rate depends on the FUV flux and cosmic-rays. The analysis of the results herein (Figs. 16 and 17) shows that the dust temperature plays the major role in the production of gas-phase water.

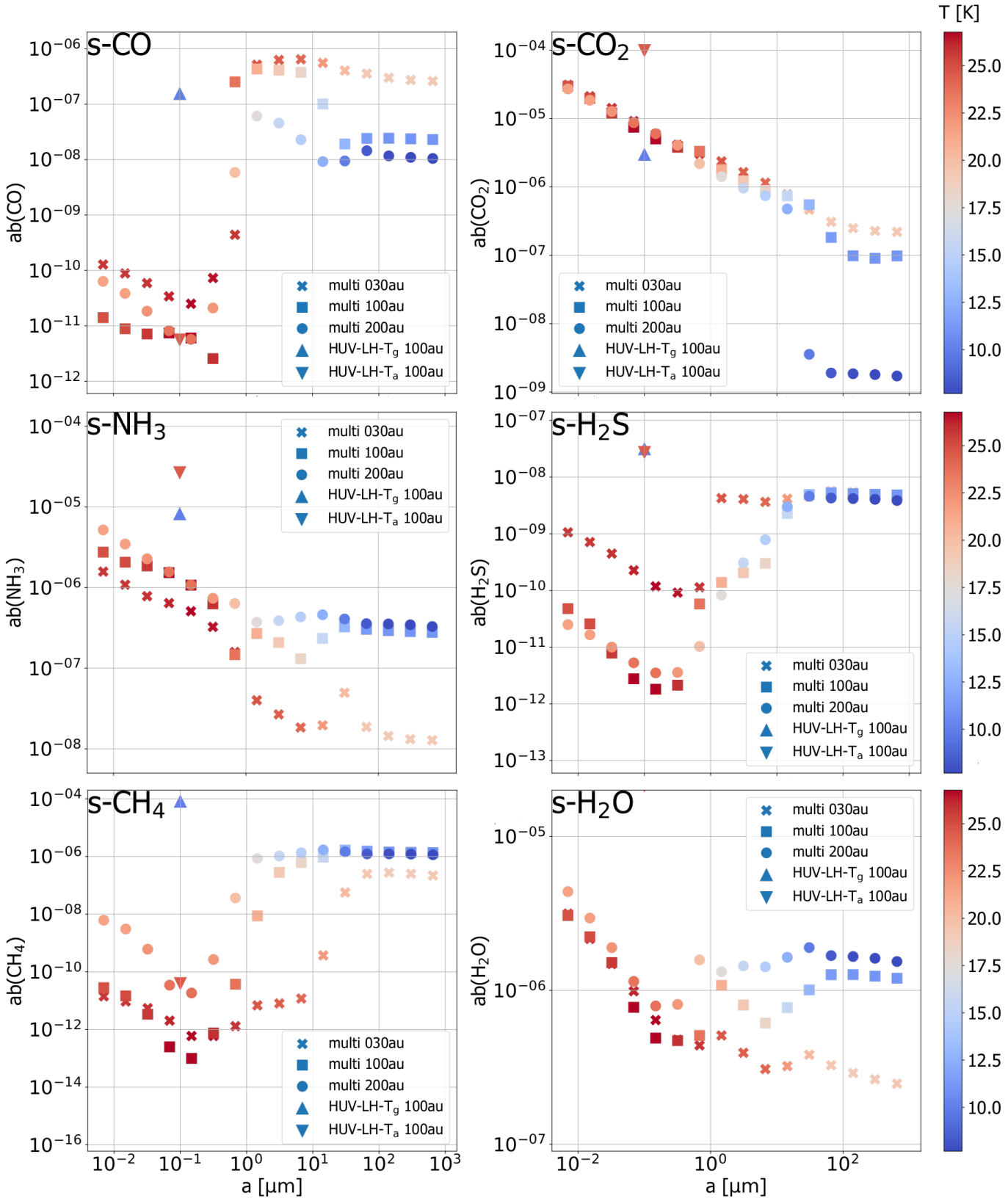

Fig. 15: Grain surface abundance per total atomic hydrogen for various molecules at the final stage of integration i.e. 5 10^6 yrs as a function of the grain radius a in relation to the grain temperatures. Cross markers stand for the multi-grain model at 30 au, the square markers stand for the multi-grain model at 100 au and the round markers stand for 200 au. The triangles pointing upward represent the surface abundance in the single-grain model HUV-LH-T_g (grains of size 0.1 μm) and the triangle pointing downward represents the abundance in the single-grain model HUV-LH-T_a, both at 100 au.

Single-grain models The vertical snow-line forms a clear boundary between high and low gas-phase H_2O abundance at $z/r \sim 0.15$ (Fig. 16) and we see that HUV-B14-T_a produces the most distinct boundary of all three models. The snow-line corresponds roughly to the abrupt drop in the UV flux as shown in Fig. 2 (bottom-right panel). The cold-grain model HUV-LH-T_g produces substantially more water in the upper layers than the other single-grain models, because low dust temperature increase the hydrogenation rates on the grain surfaces. The photo-desorption rates are approximately equal in the three models (same flux) but since HUV-LH-T_g produces a larger water abundance on grain surfaces the final gas-phase abundance is much larger. It results in a column density of water about a factor 10 larger in HUV-LH-T_g than in the other two models. On the other hand, the B14's prescription increases only marginally the column density of gas-phase water.

Multi-grain models The vertical snow-line is far less apparent (Fig. 17, top row, middle and right column). Both models have approximately the same distribution of abundance. because both have the same dust temperature distribution and same UV. We notice, however, that B14's prescription in M-HUV-B14 produces marginally more water in the upper layer of the disk than in M-HUV-LH, due to the gas-phase formation of water via the two sequences presented above.

4.4.2. Water ice

Single-grain models The vertical snow-line location is clearly defined (see Fig. 16, bottom row), although we note the presence of a notable band around $z = 3\,H$ ($z = 2\,H$) in HUV-LH-T_g (resp. HUV-LH-T_a). The reason is the following activated hydrogenation reaction:

$$\text{s-H} + \text{s-HOOH} \rightarrow \text{s-}H_2O + \text{s-OH}\ (E_A = 1400\,\text{K}). \quad (22)$$

Indeed, the band illustrates the location in the disk where this reaction is activated. Below the band, the reaction is not activated and water ice is mostly photo-desorbed while above the band the photo-desorption rates competes with the formation rate and the abundance drops. In HUV-LH-T_a (Fig. 16, middle column), Reaction 22 is activated at smaller altitudes in the disk since the dust temperature is globally higher, resulting in a peak in abundance at around 2 scale heights. In contrast, HUV-B14-T_a does not exhibit such a peak near $z = 2\,H$ since a large fraction of atomic hydrogen on surfaces is used to create molecular hydrogen. This dramatically decreases the quantity of available H atoms necessary to form water.

Multi-grain models The same mechanisms are at work (see middle and right columns of Fig.17). Yet, the dust temperature distribution involves that we find both hot (up to $\sim$ 95 K) and cold (as low as $\sim$ 7 K) grains nearly everywhere in the disk. Consequently, Reaction 22 is activated at lower altitudes and the formation of s-H_2O through hydrogenation can occur at higher altitudes on cold medium- and large-sized grains so that the snow-line is located at a higher altitude.

Around the mid-plane In all models, water is found in the form of ice around the mid-plane, where the desorption by UV flux and cosmic-rays is limited and where hydrogenation is effective. For single-grain models, the width of the region where water is on the icy mantles is larger in HUV-LH-T_g than in the two others because, again, the dust temperature is smaller. As presented in Fig. 15 (bottom right panel), we see that the abundance is inversely proportional to the grain size at 30 au. The reason is the combination of the large binding energy of water and the high density of small grains. At 100 and 200 au, however, the abundance on large grains (size $> 0.1\ \mu m$) is larger because the grain temperature is low enough to allow for effective hydrogenation.

4.5. COMs

Complex organic molecules (COMs), supposedly constituting the crucial bond between simple ISM molecules and prebiotic chemistry, are hard to detect due to their low abundance and weak emission lines originating from their molecular complexity. This is especially true for objects with small spatial extensions like disks. Simple organic molecules have been regularly detected over the last decades such as H_2CO (Dutrey et al. 1997; Aikawa et al. 2003; Öberg et al. 2011), HC_3N (Chapillon et al. 2012), CH_3CN (Öberg et al. 2015) and CH_3OH (Walsh et al. 2016). We investigate here the effectiveness of our models to synthesize COMs from surfaces or gas-phase when given sufficient time (5×10^6 yrs).

4.5.1. Methyl Cyanide (CH_3CN)

C-N bonded species are very important for the synthesis of Glycine (Goldman et al. 2010). Öberg et al. (2015) have observed methyl cyanide (CH_3CN) in the disk around the Herbig Ae star MWC 480, a star exhibiting a stronger UV flux and a warmer disk than a TTauri star.

CH_3CN to HCN abundance ratio To facilitate comparisons, we discuss the abundance of CH_3CN relative to HCN, as practiced in cometary studies (Mumma & Charnley 2011; Öberg et al. 2015). The model that produces the largest CH_3CN/HCN ratio is the single-grain model HUV-LH-T_g with $\sim$ 14% (vertically integrated) at 100, 120 and 140 au while the other single-grain models produce nearly more than $\sim$ 1% at these radii. The outer regions (200-250 au) produce a larger ratio (up to 9%) than the inner disk regions in the warm grain single-models, whereas the peak is in the region around 100 au in HUV-LH-T_g. In multi-grain models, the gas-phase abundance ratio never exceeds 1%. However, it never goes below 0.1%, implying a rather uniform production of CH_3CN along the radius as compared to the single-grain models. M-HUV-B14 produces slightly more CH_3CN than M-HUV-LH. The model HUV-LH-T_g (with the coldest grains overall) is the one that globally produces the largest CH_3CN/HCN ratio.

CH_3CN in gas-phase In the upper regions, the main known pathways to form gas-phase CH_3CN are the reaction of HCN with CH_3^+ and the photo-desorption of icy CH_3CN (thermal desorption is not effective because of the large binding energy of CH_3CN). Results show that the reaction between HCN and CH_3^+ is the most effective route in M-HUV-B14 while only photo-desorption is effective in M-HUV-LH. The reason is straightforward since the production of CH_3^+ requires the presence of molecular hydrogen:

$$C^+ \xrightarrow{H_2} CH_2^+ \xrightarrow{H_2} H + CH_3^+ \quad (23)$$

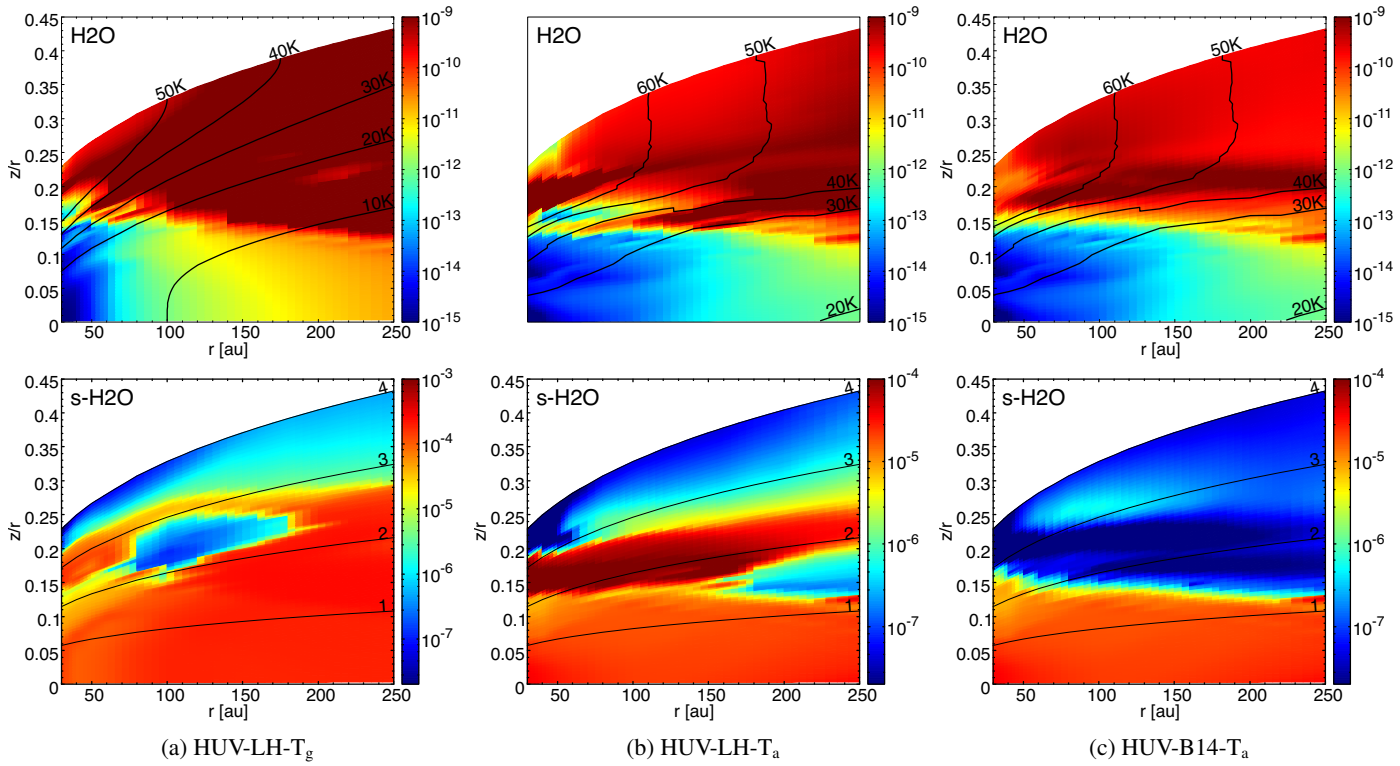

(a) HUV-LH-T_g (b) HUV-LH-T_a (c) HUV-B14-T_a

Fig. 16: Water abundance in the gas-phase (top) and on the grain surfaces (bottom) of the single-grain models. Left column shows the abundances in HUV-LH-T_g, middle in HUV-LH-T_a and right one in HUV-B14-T_a. In the top row, the solid black lines show the dust temperature iso-contours, in the bottom row they denote iso-contours of scale heights.

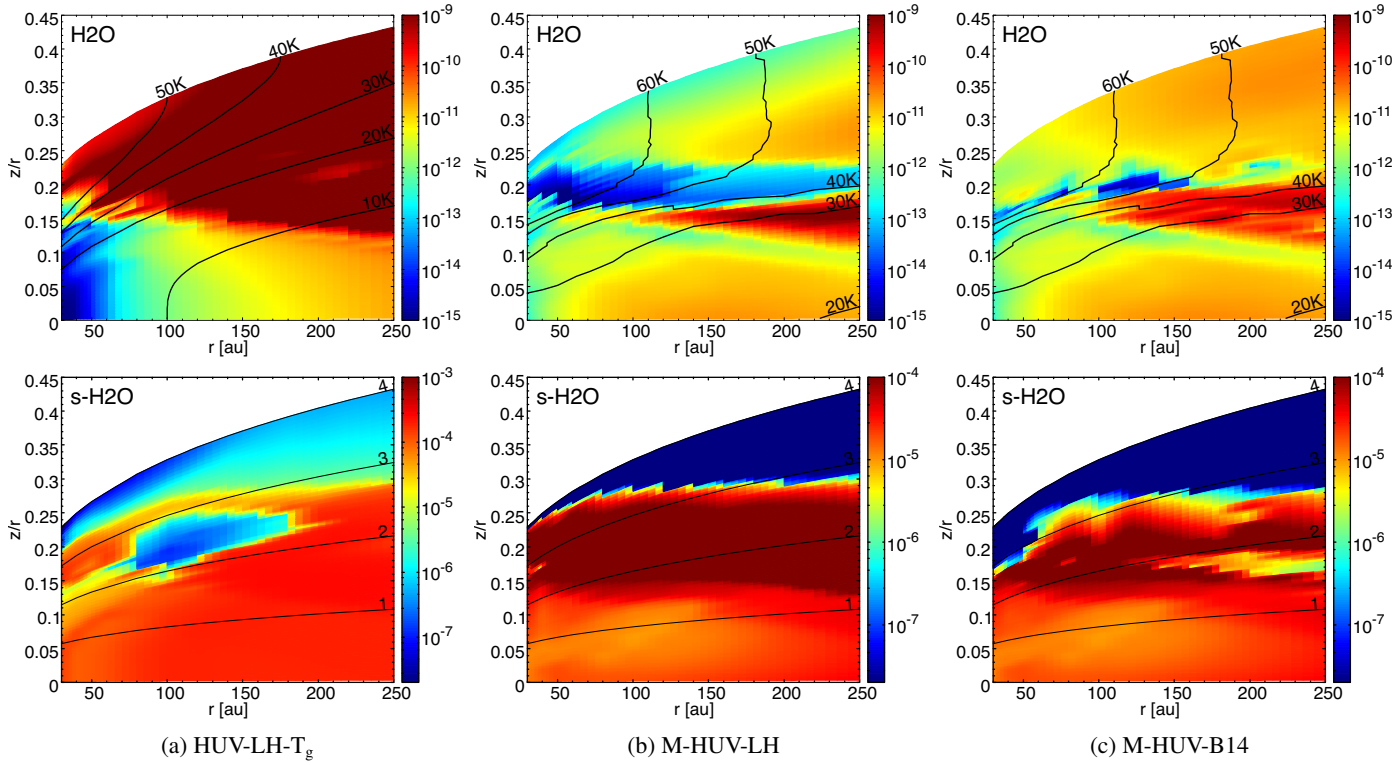

(a) HUV-LH-T_g (b) M-HUV-LH (c) M-HUV-B14

Fig. 17: Water abundance in the gas-phase (top) and on the grain surfaces (bottom). Left column shows the abundances in HUV-LH-T_g and middle and right column in the multi-grain models. In the top row, the solid black lines show the dust temperature iso-contours, in the bottom row they denote iso-contours of scale heights.

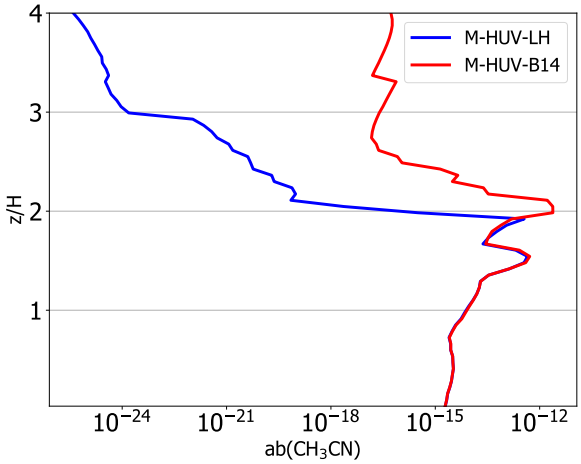

Fig. 18: Altitude above the mid-plane as a function of the abundance relative to H of CH_3CN at 100 au. Blue line shows the abundance produced by model M-HUV-LH, red line shows the abundance produced by model M-HUV-B14. We see that the abundance dramatically drops above $\sim$ 2 scale heights in M-HUV-LH while M-HUV-B14 keeps a rather high abundance at high altitudes. This is due to the available quantity of gas-phase H_2 in M-HUV-B14, which enhances the production of CH_3^+.

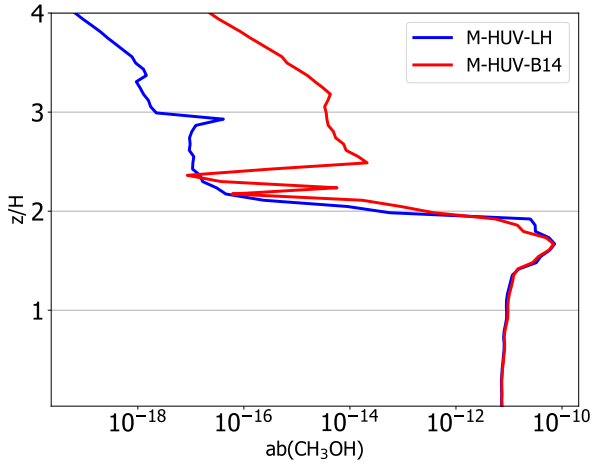

Fig. 19: Altitude above the mid-plane as a function of the abundance relative to H of CH_3OH at 100 au. Blue line shows the abundance produced by model M-HUV-LH, red line shows the abundance produced by model M-HUV-B14. We see that the abundance dramatically drops at $\sim$ 2 scale heights in both models, although M-HUV-B14 maintains a larger abundance than M-HUV-LH at high altitudes.

and H_2 is much more abundant in M-HUV-B14 in the upper layers. At 100 au, the abundance of CH_3^+ in M-HUV-LH is very low ($\sim 10^{-20}$) as compared to the abundance in M-HUV-B14 ($\sim 10^{-10}$). It follows that, as seen in Fig. 18, M-HUV-B14 produces much more CH_3CN than in M-HUV-LH. Therefore, the presence of H_2 appears to be decisive for the production of gas-phase CH_3CN in the upper regions of the disk. However, this difference between the two models does not significantly impact the total column density of CH_3CN as most of it is produced near the mid-plane.

CH_3CN ices Figure 20 (bottom) shows the abundance of CH_3CN ices in the mid-plane relative to the grain size as a function of the radius. CH_3CN mostly stays on warm small grains while there is a large drop in abundance around grain populations of size $\sim$ 0.317 μm. The results show that the two main reactions that lead to icy CH_3CN are the adsorption of gas-phase CH_3CN onto the surfaces and the following surface reaction:

$$\text{s-CH}_3 + \text{s-CN} \rightarrow \text{s-CH}_3\text{CN}. \quad (24)$$

CH_3CN is more abundant on small grains because of three main reasons. The first reason is the large number density of small grains that implies large collision rates with 1) gas-phase produced CH_3CN and 2) with CH_3 that, despite a low binding energy, will briefly stick and quickly react with s-CN (see reaction 24). The second reason is the high binding energy of CH_3CN ($E_b(CH_3CN)$ = 4680 K Wakelam et al. 2017) and of the precursors (s-CN) so that they stay on small grain surfaces. Moreover, the temperature of small grains is sufficiently high to allow precursors to diffuse on the surface and increase reaction rates. The last reason is that even if CH_3CN ices can be formed on large grain surfaces, photo-desorption rates are large enough for CH_3CN to be desorbed from large grains and seed small grains as the disk evolves.

4.5.2. Methanol and formaldehyde

CH_3OH in gas-phase For multi-grain models, Fig. 19 shows that the vertical profile of gas-phase CH_3OH is divided into two layers separated by an abrupt drop in abundance at $\sim 2\,H$, which corresponds roughly to the dust temperature transition (Fig. 6). There is a peak in gas-phase CH_3OH at $\sim 1.8\,H$ in both models. This corresponds to the location where dust temperature is low enough for adsorbed CO to be hydrogenated and where the UV flux is high enough to efficiently photo-dissociate a significant fraction of newly formed methanol. The lower layer ($<$ 2 H) contains most of CH_3OH column density. In the upper layer, M-HUV-B14 produces more CH_3OH than M-HUV-LH.

CH_3OH to H_2CO abundance ratio In multi-grain models, the ratio CH_3OH/H_2CO increases by a factor of $\sim$ 2 to 3 in the outermost region ($\geq$ 200 au) between 10^6 and 5×10^6 years while it remains stable in the inner region ($<$ 100 au). In M-HUV-B14, after 10^6 years, the averaged ratio in the region 80 - 120 au is equal to 1.3. This appears to be consistent with the observed ratio in TW Hya (Walsh et al. 2016; Carney et al. 2019). In M-HUV-LH, the averaged ratio is equal to 2.4. The difference is due to a more efficient pathway to form H_2CO in the upper disk regions of M-HUV-B14. Gas-phase H_2CO is efficiently formed through the following sequence:

$$H_2 + CH_3^+ \rightarrow CH_5+ \quad (25)$$
$$CH_5^+ + e^- \rightarrow H + H + CH_3/H_2 + CH_3 \quad (26)$$
$$O + CH_3 \rightarrow H + H_2CO. \quad (27)$$

This shows that molecular hydrogen is a key element in the formation process of gas-phase formaldehyde and M-HUV-B14 provides much more H_2 than M-HUV-LH.

Grain size dependence of surface chemistry for CH_3OH Figure 20 gives a set of maps of ice abundance in the mid-plane with

grain sizes as a function of the computed radii. Top left panel is the grain temperature which allows to analyse the surface abundance in view of the surface temperature. We have same results for both multi-grain models. On icy mantles, both s-H_2CO and s-CH_3OH are formed via the same hydrogenation sequence:

$$\text{s-CO} \xrightarrow{\text{H}} \text{s-HCO} \xrightarrow{\text{H}} \text{s-H}_2\text{CO} \xrightarrow{\text{H}} \text{s-CH}_3\text{O} \xrightarrow{\text{H}} \text{s-CH}_3\text{OH}. \quad (28)$$

However, we note that H_2CO is mainly formed in the gas-phase. As seen in Fig. 20 (top right), CO tends to be efficiently adsorbed onto cold surfaces ($T_d \lessapprox 17$ K). The map of H_2CO (bottom left) grossly follows the same distribution although the trend is globally less pronounced. CH_3OH, on the other hand, exhibits a totally different distribution and tend to concentrate on small grain surfaces (bottom right). The main reason comes from the fact that the binding energy increases as the molecules become more complex (e.g., E_b(CO) ~1200 K, E_b(H_2CO) ~3200 K, E_b(CH_3OH) ~5500 K Minissale et al. 2016; Noble et al. 2012; Collings et al. 2004) and that the hydrogenation of H_2CO (which leads to CH_3OH) has an activation barrier and cannot efficiently occur on cold grain surfaces.

4.6. Impact for planet formation

Planet formation is strongly linked to grain growth and dust disk evolution. Our study reveals some interesting trends which should influence it.

For a T Tauri disk of a few Myr, radial changes of the millimeter spectral index (e.g. Birnstiel et al. 2010) reveal that, after settling, large grains have drifted towards the central star. Typically, grains larger than a few 0.1- 1 mm are located inside a radius of 50-80 au. Beyond this, dust disks have a spectral index which is similar to that observed in the ISM, suggesting a similar size distribution, even if settling still occurs with larger grains residing onto the mid-plane. As a consequence, towards the mid-plane, one expects to observe different icy layers on grains in the inner (large cold grains) and outer disk (warmer smaller grains). We have seen in the previous section that CH_4 and H_2O are preferentially located on large grains while CO_2 remains on smaller ones (Fig. 15). This implies also a different chemical coupling between the gas and solid phase. Moreover, we have seen that complex molecules tend to stick and remain on small warmer grains ($\leq \sim 0.1$ μm), which are less likely to drift toward the inner disk. The outer disk (r $\geq$ 80 au) is therefore assumed to support rich chemistry on small grains which are probable precursors to cometary nuclei. On the other hand, as larger grains drift efficiently toward the inner region, their surface temperature is likely to vary during the journey which can allow for the growing chemical complexity to occur until the less refractory molecules become vaporized when sufficiently close to the star. Therefore, rich chemistry of the inner disk region can be assumed to come from the gas-phase which is later accreted by planetary embryos, while rich chemistry of the outer disk region occurs on the small grain surfaces and then seeds the inner region through planet-cometary collision in later phases of the disk.

Grain-grain collisions may modify this picture. The characteristic timescale (the time for a large grain to encounter small grains of equivalent area) around 100 au is of order 10^4–10^5 years. However, while large grains may accrete the smaller ones, and inherit part of their surface composition while growing, small grains are re-created by disruptive events that may severely affect their surface layer and ice mantles. The outcome of the surface state during such grain-grain collisions remains to be studied.

Nevertheless, in all cases, the grain size distribution, because it results in a spread of dust temperature, allows for a faster depletion of C and O, that are converted to s-CO_2 on the colder grains in the disk mid-plane, but also a more active surface chemistry leading to formation of COMs on the warmer grains in the upper layer. Such a behaviour cannot be reproduced by a single grain temperature chemical model, because the formation processes are highly non-linear, since the mobility and evaporation efficiency depend exponentially on dust temperature.

The range in dust temperatures also spreads out spatially the snow-lines that become fuzzy. The spatial extent of these "snow bands" will depend on the specific dust properties and disk mass. The temperature spread is larger for less massive disks.

As disks evolve, the amount of dust (and gas) decreases until they reach the optically thin, debris disk phase. A less massive dust disk necessarily implies a warmer dust disk, which should affect the composition of the icy layers at the grain surface in evolved disks. Recent surveys of 5-40 Myr old disks suggest the existence of an intermediate phase (at least for Herbig Ae stars) between debris and proto-planetary disks (e.g. Kóspál et al. 2013; Péricaud et al. 2017). The so-called hybrid disks share dust properties similar to those observed around debris disks, while the amount of gas is still significant, and a larger than standard gas-to-dust-ratio is observed. For instance, in HD141569, Di Folco et al. (2020) observed a CO surface density which is only a factor 10 lower than in a typical protoplanetary HAe disk, whereas the amount of millimeter grains is a factor 50 times smaller than in typical young disks. The reduced amount of grains, and in some cases at least possible changes in the grain size distribution (e.g. Hughes et al. 2018), should affect the grain surface chemistry during the late phases of disk evolution. More simulations of older, gas-rich disks with a small amount of dust and a larger gas-to-dust ratio are needed to quantify the impact on chemistry and planet formation.

5. Summary

We presented here a new chemical model of proto-planetary disks that consistently accounts for the impact of grain sizes on the dust temperatures and UV penetration. Representative results were obtained for a typical disk around T Tauri stars, using parameters derived from the Flying Saucer observations (Dutrey et al. 2017). We coupled the chemical code NAUTILUS and radiative transfer code POLARIS to use a consistent distribution of grain sizes and temperatures, accounting for size-dependent dust settling. We implemented in NAUTILUS a new method to account for self and mutual shielding of molecules in photo processes, method that accounts for the frequency dependence of photo-rates. The outputs of multi-grain models are compared to those of single grain size, using two different assumptions for the single-grain temperature: equal to the (assumed) gas temperature, or to the area-weighted mean temperature of the multi-grain models.

– We identify the formation of H_2 through Langmuir-Hinshelwood mechanism as inefficient for a grain size distribution, and the amount of atomic H as critical for the chemistry of the upper layers (2-4 H). The parametric method of Bron et al. (2014), that accounts for temperature fluctuations for small grains, appears more appropriate to produce enough H_2.

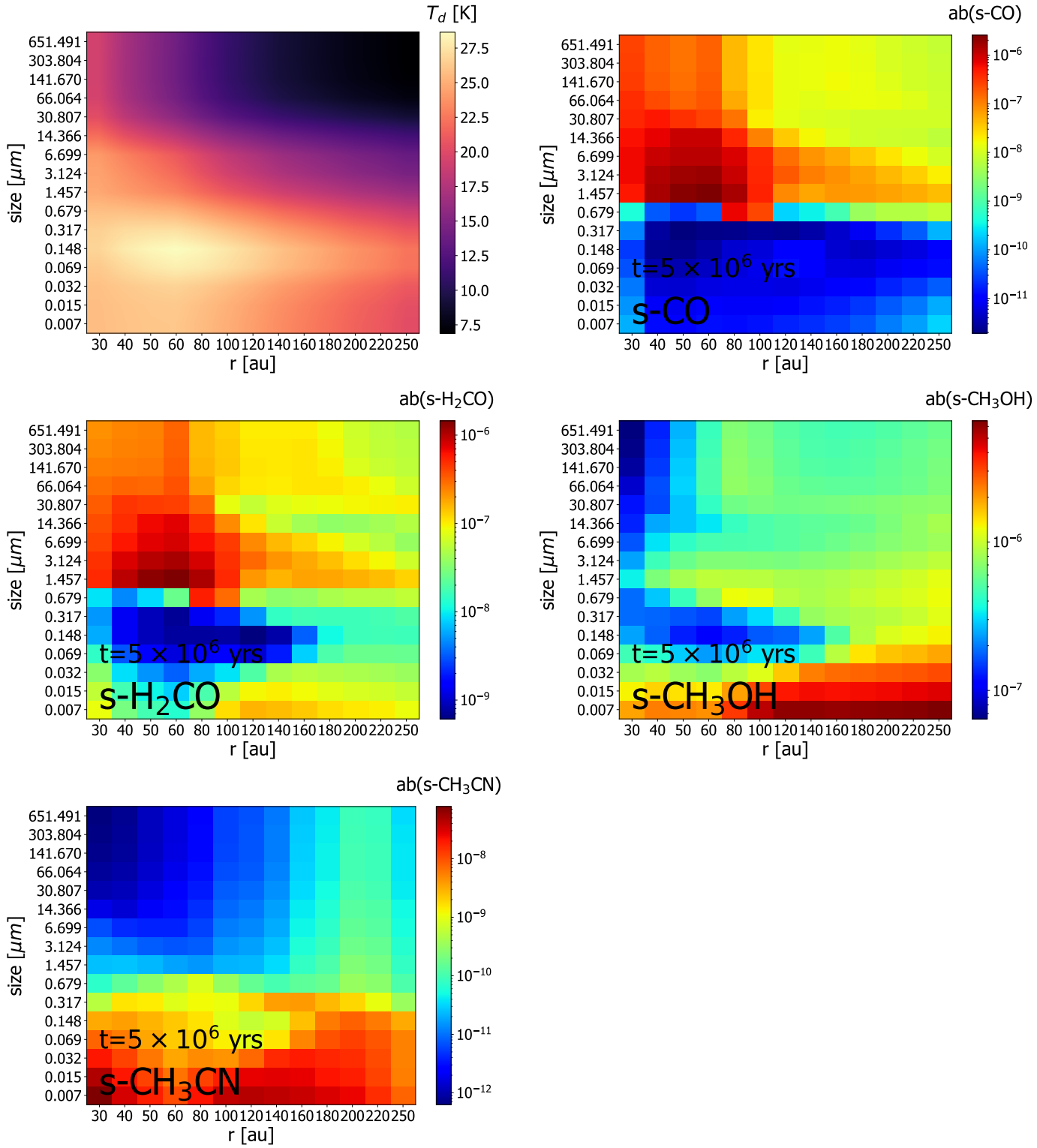

Fig. 20: multi-grain models: Maps of ice abundance relative to H in the mid-plane, with grain sizes as a function of the radius. Top left panel is the distribution in grain temperature. We see that the hottest region is located at around 60 au from the star on grains of size 0.148 μm.

- Comparisons between the models reveal differences of more than 1-2 orders of magnitudes for some abundant gas-phase species. Most of these differences arise from above $1.5H$, despite the larger UV penetration in multi-grain models.
- The location of the H_2O vertical snow-line is partly regulated by the UV penetration but also by the amount of H_2. In the upper disk layers, the amount of H_2 also regulates the formation of H_2CO, although this molecule is mostly formed, like CH_3OH, on grain surfaces.
- CH_3CN, like CH_3OH to a lesser extent, is preferentially formed on warmer grains that allow for a larger diffusivity of precursors on the grain surface.

- At 100 au, in the mid-plane, disks with colder dust produce more H_2O and CH_4 while those with warmer dust produce more CO_2 on grain surfaces.
- As soon as CO is locked onto large (hence colder) grains ($a > 1\mu$m), it remains trapped until the end of the simulated evolution.
- The spread of temperatures available with grain size distributions simultaneously provides surface chemistry for cold and warm grains that cannot be mimicked by a unique dust temperature. In particular, it allows depletion of C and O to proceed efficiently (by conversion to CO_2 or CH_4 and H_2O on colder grains), while the COMs production is boosted on the warmer grains.
- Another direct consequence of having different dust temperatures at the same location is a spatial spread-out of the snow-lines.

Our results clearly show that the chemistry of protoplanetary disks cannot simply be represented by a single grain size and temperature.

Finally, our disk model assumes a relatively high dust mass (i.e. an optically thick dust disk). An optically thinner dust disk would impact the UV penetration and dust temperature, changing the chemistry at play even on the mid-plane. This remains to be investigated to determine how it can affect the grain surfaces and then the composition of planetesimals and embryos.

Acknowledgements. We thank E.Bron for fruitful discussions about the H_2 formation in PDRs and M.Ruaud for a detailed reading of the article. This work was supported by the "Programme National de Physique Chimie du Milieu Interstellaire" (PCMI) from INSU/CNRS. J.K. acknowledges support from the DFG grants WO 857/13-1, WO 857/15-1, and WO 857/17-1.

References

Acharyya, K., Hassel, G. E., & Herbst, E. 2011, ApJ, 732, 73
Aikawa, Y., Furuya, K., Nomura, H., & Qi, C. 2015, ApJ, 807, 120
Aikawa, Y., Momose, M., Thi, W.-F., et al. 2003, PASJ, 55, 11
Aikawa, Y. & Nomura, H. 2006, ApJ, 642, 1152
Akimkin, V., Zhukovska, S., Wiebe, D., et al. 2013, ApJ, 766, 8
Birnstiel, T., Dullemond, C. P., & Brauer, F. 2010, A&A, 513, A79
Boehler, Y., Dutrey, A., Guilloteau, S., & Piétu, V. 2013, MNRAS, 431, 1573
Bron, E., Le Bourlot, J., & Le Petit, F. 2014, A&A, 569, A100
Carney, M. T., Hogerheijde, M. R., Guzmán, V. V., et al. 2019, A&A, 623, A124
Carr, J. S. & Najita, J. R. 2008, Science, 319, 1504
Cazaux, S. & Tielens, A. G. G. M. 2004, ApJ, 604, 222
Chapillon, E., Dutrey, A., Guilloteau, S., et al. 2012, ApJ, 756, 58
Chapillon, E., Guilloteau, S., Dutrey, A., & Piétu, V. 2008, A&A, 488, 565
Collings, M. P., Anderson, M. A., Chen, R., et al. 2004, MNRAS, 354, 1133
Cuppen, H. M. & Herbst, E. 2005, MNRAS, 361, 565
Dartois, E., Dutrey, A., & Guilloteau, S. 2003, A&A, 399, 773
de Gregorio-Monsalvo, I., Ménard, F., Dent, W., et al. 2013, A&A, 557, A133
Di Folco, E., Péricaud, J., Dutrey, A., et al. 2020, A&A, 635, A94
Dominik, C., Ceccarelli, C., Hollenbach, D., & Kaufman, M. 2005, ApJ, 635, L85
Dong, R., Zhu, Z., & Whitney, B. 2015, ApJ, 809, 93
Draine, B. T. 1978, ApJS, 36, 595
Draine, B. T. & Lee, H. M. 1984, ApJ, 285, 89
Du, F. & Bergin, E. A. 2014, ApJ, 792, 2
Duley, W. W. 1996, MNRAS, 279, 591
Dutrey, A., Guilloteau, S., & Guelin, M. 1997, A&A, 317, L55
Dutrey, A., Guilloteau, S., Piétu, V., et al. 2017, A&A, 607, A130
Eistrup, C., Walsh, C., & van Dishoeck, E. F. 2018, in IAU Symposium, Vol. 332, IAU Symposium, ed. M. Cunningham, T. Millar, & Y. Aikawa, 69–72
France, K., Schindhelm, E., Bergin, E. A., Roueff, E., & Abgrall, H. 2014, ApJ, 784, 127
Fromang, S. & Nelson, R. P. 2009, A&A, 496, 597
Garaud, P. & Lin, D. N. C. 2004, ApJ, 608, 1050
Ge, J. X., He, J. H., & Li, A. 2016, MNRAS, 460, L50
Goldman, N., Reed, E. J., Fried, L. E., William Kuo, I. F., & Maiti, A. 2010, Nature Chemistry, 2, 949
Gorti, U., Hollenbach, D., Najita, J., & Pascucci, I. 2011, ApJ, 735, 90
Habart, E., Abergel, A., Boulanger, F., et al. 2011, A&A, 527, A122
Habart, E., Boulanger, F., Verstraete, L., Walmsley, C. M., & Pineau des Forêts, G. 2004, A&A, 414, 531
Hasegawa, T. I. & Herbst, E. 1993, MNRAS, 263, 589
Hasegawa, T. I., Herbst, E., & Leung, C. M. 1992, ApJS, 82, 167
Heays, A. N., Bosman, A. D., & van Dishoeck, E. F. 2017, A&A, 602, A105
Heese, S., Wolf, S., Dutrey, A., & Guilloteau, S. 2017, A&A, 604, A5
Hersant, F., Wakelam, V., Dutrey, A., Guilloteau, S., & Herbst, E. 2009, A&A, 493, L49
Hollenbach, D. & Gorti, U. 2009, ApJ, 703, 1203
Hudson, R. L. & Gerakines, P. A. 2018, ApJ, 867, 138
Hughes, A. M., Duchêne, G., & Matthews, B. C. 2018, ARA&A, 56, 541
Iqbal, W., Acharyya, K., & Herbst, E. 2012, ApJ, 751, 58
Iqbal, W., Acharyya, K., & Herbst, E. 2014, ApJ, 784, 139
Iqbal, W. & Wakelam, V. 2018, A&A, 615, A20
Katz, N., Furman, I., Biham, O., Pirronello, V., & Vidali, G. 1999, ApJ, 522, 305
Kóspál, Á., Moór, A., Juhász, A., et al. 2013, ApJ, 776, 77
Laor, A. & Draine, B. T. 1993, ApJ, 402, 441
Le Bourlot, J., Le Petit, F., Pinto, C., Roueff, E., & Roy, F. 2012, A&A, 541, A76
Lecar, M., Podolak, M., Sasselov, D., & Chiang, E. 2006, ApJ, 640, 1115
Lee, H. H., Herbst, E., Pineau des Forets, G., Roueff, E., & Le Bourlot, J. 1996, A&A, 311, 690
Mie, G. 1908, Annalen der Physik, 330, 377
Minissale, M., Moudens, A., Baouche, S., Chaabouni, H., & Dulieu, F. 2016, MNRAS, 458, 2953
Mumma, M. J. & Charnley, S. B. 2011, ARA&A, 49, 471
Noble, J. A., Theule, P., Mispelaer, F., et al. 2012, A&A, 543, A5
Ober, F., Wolf, S., Uribe, A. L., & Klahr, H. H. 2015, A&A, 579, A105
Öberg, K. I., Guzmán, V. V., Furuya, K., et al. 2015, Nature, 520, 198
Öberg, K. I., Qi, C., Fogel, J. K. J., et al. 2011, ApJ, 734, 98
Pauly, T. & Garrod, R. T. 2016, ApJ, 817, 146
Péricaud, J., Di Folco, E., Dutrey, A., Guilloteau, S., & Piétu, V. 2017, A&A, 600, A62
Phuong, N. T., Chapillon, E., Majumdar, L., et al. 2018, A&A, 616, L5
Podio, L., Kamp, I., Codella, C., et al. 2013, ApJ, 766, L5
Pontoppidan, K. M., Salyk, C., Blake, G. A., et al. 2010, ApJ, 720, 887
Reissl, S., Wolf, S., & Brauer, R. 2016, A&A, 593, A87
Riviere-Marichalar, P., Ménard, F., Thi, W. F., et al. 2012, A&A, 538, L3
Ruaud, M. & Gorti, U. 2019, ApJ, 885, 146
Ruaud, M., Wakelam, V., & Hersant, F. 2016, MNRAS, 459, 3756
Semenov, D. & Wiebe, D. 2011, ApJS, 196, 25
Sternberg, A. & Dalgarno, A. 1995, ApJS, 99, 565
Thi, W. F., Hocuk, S., Kamp, I., et al. 2020, A&A, 634, A42
van Dishoeck, E. F. & Black, J. H. 1982, ApJ, 258, 533
Vidali, G., Roser, J., Manicó, G., et al. 2005, in Journal of Physics Conference Series, Vol. 6, Journal of Physics Conference Series, 36–58
Vidali, G., Roser, J. E., Manicó, G., & Pirronello, V. 2004, Journal of Geophysical Research (Planets), 109, E07S14
Visser, R., van Dishoeck, E. F., & Black, J. H. 2009, A&A, 503, 323
Wakelam, V., Chapillon, E., Dutrey, A., et al. 2019, MNRAS, 484, 1563
Wakelam, V., Loison, J. C., Mereau, R., & Ruaud, M. 2017, Molecular Astrophysics, 6, 22
Wakelam, V., Ruaud, M., Hersant, F., et al. 2016, A&A, 594, A35
Walsh, C., Loomis, R. A., Öberg, K. I., et al. 2016, ApJ, 823, L10
Walsh, C., Millar, T. J., Nomura, H., et al. 2014, A&A, 563, A33
Williams, J. P. & Best, W. M. J. 2014, ApJ, 788, 59
Woitke, P., Kamp, I., Antonellini, S., et al. 2019, PASP, 131, 064301
Woitke, P., Kamp, I., & Thi, W. F. 2009, A&A, 501, 383
Wolf, S. 2003, ApJ, 582, 859
Wolf, S. & Voshchinnikov, N. V. 2004, Computer Physics Communications, 162, 113

Appendix A: Formal description of the model

Unless otherwise specified, we use subscript g for gas quantities and subscript d for dust. Subscript 0 is used for reference values.

Appendix A.1: Gas disk structure

We describe here the gas temperature and disk structure.

We neglect gas pressure and disk self-gravity, and thus assume that the disk is in Keplerian rotation around the host star:

$$v_g(r) = \sqrt{\frac{GM_*}{r}} \iff \Omega_g(r) = \sqrt{\frac{GM_*}{r^3}} \tag{A.1}$$

where r is the radius.

The gas surface density $\Sigma_g(r)$ also follows a power law:

$$\Sigma_g(r) = \Sigma_{g,0}\left(\frac{r}{R_0}\right)^{-p}. \tag{A.2}$$

and, by integration, the gas surface density $\Sigma_{g,0}$ at the reference radius R_0 for $p \neq 2$ is related to the gas disk mass by:

$$\Sigma_{g,0} = \frac{M_g R_0^{-p}\,(2-p)}{2\pi\left(R_{\rm out}^{2-p} - R_{\rm in}^{2-p}\right)}, \tag{A.3}$$

where $R_{\rm in}$ and $R_{\rm out}$ are the inner and outer radii of the disk.

The gas temperature is not self-consistently derived from the dust temperature distribution but imposed by analytical laws. The kinetic temperature T_k in the mid-plane is given by

$$T_k(r, z=0) = T_{\rm mid,0}\left(\frac{r}{R_0}\right)^{-q} \tag{A.4}$$

Following Dartois et al. (2003), we allow for a warmer disk atmosphere using the formulation of Williams & Best (2014)

$$T_{\rm g}(r,z) = T_{\rm mid}(r) + (T_{\rm atm}(r) - T_{\rm mid}(r))\sin\left(\frac{\pi z}{2 z_{\rm atm}}\right)^{2\sigma} \tag{A.5}$$

where σ is the siffness of the vertical temperature profile and $z_{\rm atm}$ is the altitude at the upper boundary of our disk model (4 scale heights H), meaning that the temperature above $4\,H$ is constant. The atmosphere temperature is also given by a power law with the same exponent as that of the mid-plane temperature:

$$T_{\rm atm}(r) = T_{\rm atm,0}\left(\frac{r}{R_0}\right)^{-q} \tag{A.6}$$

Isothermal case: If the gas temperature is vertically isothermal, we can derive the vertical density structure by assuming hydrostatic equilibrium at the mid-plane temperature. Consequently the gas vertical mass distribution follows a Gaussian profile :

$$\rho_g(r,z) = \rho_{g,mid}(r)\exp\left(-\frac{z^2}{2\,H_{\rm g}(r)^2}\right) \tag{A.7}$$

where $\rho_{\rm g,mid}$(r) is the density in the mid-plane, that is related to the surface density by

$$\rho_{g,mid}(r) = \frac{\Sigma_g(r)}{\sqrt{2\pi}H_g(r)} \tag{A.8}$$

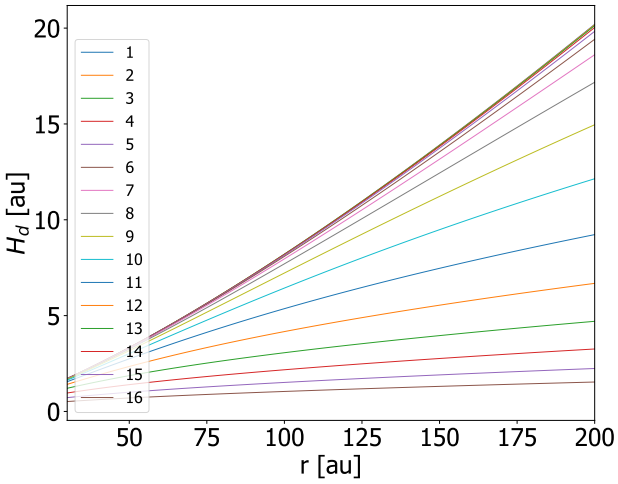

Fig. A.1: Scale heights of the grain distribution for the 16 different grain sizes as a function of the radius. The grain averaged size interval ranges from 0.007 to 651 μm. Small grains scale heights (size < 0.317 μm) practically follow the gas scale height. For larger grains the settling factor (Eq. A.21) becomes significant and the dust scale height decreases.

The scale height $H_g(r)$ is given by

$$H_g(r) = \frac{C_s(r)}{\Omega_g(r)} \tag{A.9}$$

and using the definition of the temperature law from Eq.A.4

$$H_{g,0} = \frac{C_s\,(R_0)}{\Omega\,(R_0)} = \sqrt{\frac{k_{\rm b} T_{\rm mid,0} R_0^3}{\mu_{\rm m}\, m_H\, GM_*}} \tag{A.10}$$

where $\mu_{\rm m}$ is the mean molecular weight, and $m_{\rm H}$ the Hydrogen mass. The temperature and velocity being power laws, the scale height $H(r)$ also follows a power law:

$$H_g(r) = H_{g,0}\left(\frac{r}{R_0}\right)^{\frac{3}{2}-\frac{q}{2}} \tag{A.11}$$

Vertical temperature gradient: With a vertical temperature gradient, the vertical gas profile deviates from a Gaussian profile. In Nautilus, we compute the gas density for each vertical cell z_i at a given r by solving out locally the equation as in Hersant et al. (2009):

$$ln(\rho_g(z_i) = ln(\rho_g(z_i - 1)) - (\Omega^2 \frac{\mu m_H}{k_B T_g(z_i)} + (ln(T_g(z_i)) - ln(T_g(z_{i-i}))) \tag{A.12}$$

Appendix A.2: Dust distribution and properties

Appendix A.2.1: Dust material

We assume that the grains are made of an homogeneous mixture of a population of silicate grains (62.5%) and graphite grains (37.5%). This composition is used both for radiative transfer and chemical modelling. This leads to a material specific mass density for dust grains in all this study equal to $\rho_{\rm m} = 2.5$ g.cm^{-3}. The grain temperatures are defined for each grain sizes using radiative transfer simulations as described in Section 2.2.2.

Appendix A.2.2: Size distribution

We consider a size dependent grain population. Overall, this grain population is derived assuming no radial drift, but accounting for dust settling as a function of height. The surface density of a grain population of size a is thus given by

$$\sigma_d(r,a) = \sigma_{d,0}(a)\left(\frac{r}{R_0}\right)^{-p}. \tag{A.13}$$

where $\sigma_{d,0}(a)$ is the surface density of grains of size a at reference radius. Eq. A.13 implies that the total dust surface density is:

$$\Sigma_d(r) = \int_a \sigma_d(r,a)da, \tag{A.14}$$

which we associate to the overall (vertically integrated, equivalently disk averaged) dust-to-gas mass ratio ζ through $\Sigma_d(r) = \zeta\Sigma_g(r)$. The mass fraction of grains of size $[a, a+da]$ is given by

$$x_a da = \frac{m(a)dn(a)}{\int_{a_{min}}^{a_{max}} m(a)dn(a)} = \frac{m(a)dn(a)}{m_{dust}} \tag{A.15}$$

where the size distribution in number $dn(a)$ is assumed to follow a power law of exponent d:

$$dn(a) = Ca^{-d}da \tag{A.16}$$

where C is a normalisation constant. C is related to the dust mass by simply integrating over the size as follows:

$$m_{dust} = \int_{a_{\rm min}}^{a_{\rm max}} m(a)dn(a) = \int_{a_{\rm min}}^{a_{\rm max}} \frac{4\pi}{3}\rho_m C a^{3-d}da \tag{A.17}$$

where $\rho_{\rm m}$ is the specific mass density defined in the previous section. Using Eq.A.15 and the definition of ζ yields

$$\sigma_d(r,a) = x_a\zeta\Sigma_g(r) = \frac{\zeta\Sigma_g(r)a^{3-d}}{\int_{a_{\rm min}}^{a_{\rm max}} a^{3-d}da} \tag{A.18}$$

For radiative transfer and chemistry simulations the grain size distribution is discretized into several logarithmically distributed subranges with relative dust masses of the i$^{\rm th}$ grain size interval:

$$\frac{m_{d,i}}{m_d} = \frac{\int_{a_{{\rm min},i}}^{a_{{\rm max},i}} \frac{4}{3}\pi\rho_{\rm grain}a^3 n(a){\rm d}a}{\int_{a_{\rm min}}^{a_{\rm max}} \frac{4}{3}\pi\rho_{\rm grain}a^3 n(a){\rm d}a} = \frac{a_{{\rm max},i}^{4-d} - a_{{\rm min},i}^{4-d}}{a_{\rm max}^{4-d} - a_{\rm min}^{4-d}}. \tag{A.19}$$

The relative dust mass per bin and the relative area per bin (which also quantifies the number of chemical sites) are given in Table A.1.

Appendix A.2.3: Dust settling

To account for size-dependent dust settling, we assume that the vertical profile for a given grain size has a Gaussian shape:

$$\rho_d(r,z,a) = \frac{\sigma_d(r,a)}{\sqrt{2\pi}H_d(r,a)}\exp\left(-\frac{z^2}{2\,H_d(r,a)^2}\right). \tag{A.20}$$

Because dust grains do not react to pressure forces in the same way as gas, the dust scale height will differ from that of the gas. Following Boehler et al. (2013), we define the settling factor,

Table A.1: Overview of the grain size intervals

bin	averaged size (μm)	relative dust mass	relative area
1	0.007	0.10 %	30.5 %
2	0.015	0.15 %	20.8 %
3	0.032	0.22 %	14.2 %
4	0.069	0.33 %	9.73 %
5	0.15	0.48 %	6.67 %
6	0.32	0.70 %	4.59 %
7	0.68	1.03 %	3.19 %
8	1.46	1.50 %	2.25 %
9	3.13	2.20 %	1.64 %
10	6.69	3.22 %	1.25 %
11	14.4	4.72 %	1.03 %
12	31.0	6.91 %	0.90 %
13	66.0	10.1 %	0.84 %
14	142	14.8 %	0.80 %
15	304	21.7 %	0.78 %
16	651	31.8 %	0.76 %

that is the ratio between $H_d(r,a)$ and the gas scale height near the mid-plane $H_g(r)$

$$s(a,r) = \frac{H_d(a,r)}{H_g(r)} \tag{A.21}$$

that can be related to the dust properties through the stopping time. The stopping time of a dust particle τ_s is the characteristic time for a dust particle initially at rest to reach the local gas velocity. We use the dimensionless stopping time $T_s(r,z)$ defined as the product of τ_s and the Keplerian angular momentum $\Omega(r)$ which is a way to compare the stopping time to the dynamical time in the disk. Garaud & Lin (2004) showed that dust friction with gas in protoplanetary disks is well described by the Epstein regime, in which the dimensionless stopping time is given by:

$$T_s(r,z) = \tau_s\Omega_g(r) = \frac{a\rho_m}{\rho_g(r,z)C_s}\Omega(r) \tag{A.22}$$

The stopping time depends linearly on the grain size. Using Eq. A.9 we can write:

$$T_s(r,z) = \frac{a\rho_m}{\rho_g(r,z)H_g(r)} = \frac{\sqrt{2\pi}a\rho_m}{\Sigma_g(r)}\exp\left(-\frac{z^2}{2H_g(r)^2}\right). \tag{A.23}$$

The settling factor is given by the approximation of Dong et al. (2015):

$$s(a,r) = \frac{H_d(a,r)}{H_g(r)} = \frac{1}{\sqrt{1+T_{s,mid}\frac{S_c}{\alpha}}} \tag{A.24}$$

where α is the α viscosity coefficient,

$$T_{s,mid} = \frac{\sqrt{2\pi}a\rho_m}{\Sigma_g(r)} \tag{A.25}$$

is the dimensionless stopping time in the mid-plane, and S_c is the Schmidt number. The Schmidt number is a dimensionless number defined by the ratio between the turbulent viscosity ν_t and the turbulent diffusion D_t:

$$S_c = \frac{\nu_t}{D_t}. \tag{A.26}$$

Figure A.2 shows the settling factor at the reference radius as defined in Dong et al. (2015) compared to the asymptotic behavior used by Boehler et al. (2013) and the values from the numerical simulations of Fromang & Nelson (2009).

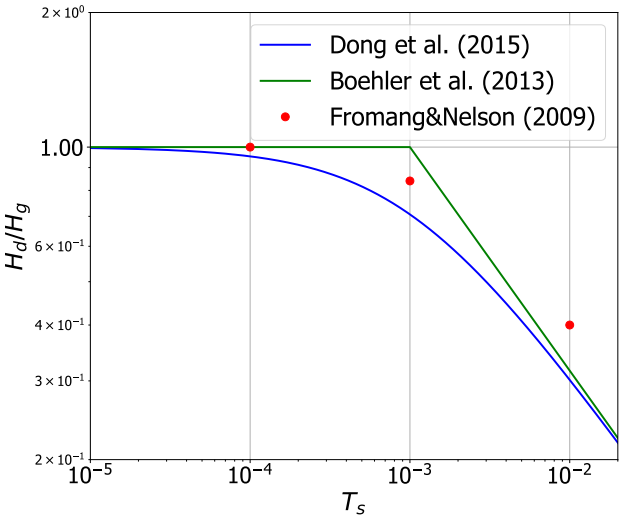

Fig. A.2: Settling factor as a function of the dimensionless stopping time at R_0. In green the model given by Boehler et al. (2013), the red dots show the simulation values of Fromang & Nelson (2009) and the blue curve is the model of Dong et al. (2015) that we use.

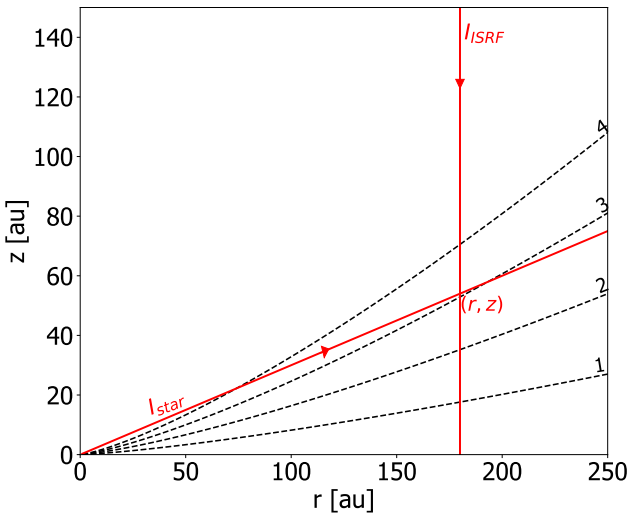

Fig. B.1: Elevation above the midplane as a function of the radius. The dotted black lines are scale heights of the gas (1 H, 2 H, 3 H and 4 H). The red lines are radiation emitted from the central star and from the interstellar radiation field (ISRF). The coordinates (r, z) represent a point at where both fields cross.

Table B.1: Adopted elemental initial abundances relative to H.

Element	abundance (relative to H)	mass (amu)
He	9.0(-2)	4.00
C	1.7(-4)	12.00
N	6.2(-5)	14.00
O	2.4(-4)	16.00
Si	8.0(-9)	28.00
S	8.0(-8)	32.00
Fe	3.0(-9)	56.00
Na	2.0(-9)	23.00
Mg	7.0(-9)	24.00
Cl	1.0(-9)	35.00
P	2.0(-10)	31.00
F	6.7(-9)	19.00

Appendix B: Self and Mutual Shielding

The local UV flux in the disk is not a simple sum of the attenuated stellar and interstellar fields because of scattering by dust grains. Scattering can be significant near the disk mid-plane, where the optical depths are large. However, molecular shielding is most important only in the upper layers, when dust optical depth remains low while molecular optical depth can be significant.

Thus, at first order, to evaluate the impact of self-shielding, we neglect scattering in our analysis by writing in a simple form the local flux I in the cell of coordinates (r, z) as follows:

$$I(\lambda, r, z) \approx I_{ISRF} e^{-\tau^V} + I_*(r, z) e^{-\tau^R} \tag{B.1}$$

where I_{ISRF} is the incident flux from the ISRF, $I_*(r, z)$ is the spatially diluted, unattenuated, incident flux from the central star, τ^V is the vertical opacity generated by the disk matter above the local point (r, z) and τ^R is the radial opacity generated by the matter between the central star and the local point. As the opacities are a contribution of both dust and gas, we write:

$$\begin{aligned} \tau^V &= \tau^V_m + \tau^V_d \\ \tau^R &= \tau^R_m + \tau^R_d \end{aligned} \tag{B.2}$$

where m stands for molecules and d for dust. So the local expression becomes:

$$I(\lambda, r, z) \approx I_{ISRF} e^{-(\tau^V_d + \tau^V_m)} + I_* e^{-(\tau^R_d + \tau^R_m)} \tag{B.3}$$

The local flux weighted by the dust only I_d can also be approximated by:

$$I_d(\lambda, r, z) \approx I_{ISRF} e^{-\tau^V_d} + I_* e^{-\tau^R_d} \tag{B.4}$$

POLARIS treats consistently scattering by dust and this simple expression was checked to be a reasonable approximation in the upper layers where molecular shielding is important.

At a given wavelength, the molecular opacity is defined as follows:

$$\tau_m(\lambda, r, z) = \sum_X \int_{l=f(r,z)} n(X, r, z) \sigma(X, \lambda) dl \tag{B.5}$$

where X includes all molecules for which we have cross-sections (including H_2O), $n(X, r, z)$ is the number density [cm^{-3}] of species X at coordinates (r, z) and $\sigma(X, \lambda)$ is the sum of the absorption, dissociation and ionization cross-sections of species X at wavelength λ. Depending on whether the radiation is from the interstellar medium or from the central star, the line l over which we integrate is either the altitude z above the cell of coordinates (r, z) or the radial distance $\sqrt{r^2 + z^2}$ between the central star and the considered cell, respectively.

Figure B.2 shows the vertical opacities generated both by the dust (dotted lines) and the molecules (solid lines). The opacities are given for different altitudes at 100 au. **H_2, CO and N_2 are the main contributors to the line opacity.**

As shown in Figs. B.2, at all wavelengths where H_2 contributes to the attenuation ($\lambda \lesssim 115$ nm), its opacity is in all parts of the disk always substantially larger than the dust opacity.

While calculating the vertical molecular opacity τ_m^V is trivial, characterizing the radial molecular opacity τ_m^R is more difficult as it couples different radii and thus their chemical evolution together. Given the significant computing time involved in the multi-grain model, we show below that we can reasonably simplify the problem through a simple approximation.

Self or mutual shielding is only relevant for high molecular opacities, because frequencies where molecular shielding occurs cover a limited fraction of the UV domain. In regard to Figure B.1, we introduce the ratio between the radial and vertical molecular optical depths as follows:

$$RV = \frac{\tau_m^R}{\tau_m^V} \tag{B.6}$$

and Eq. B.3 can be rewritten as:

$$I(\lambda, r, z) \approx e^{-\tau_m^V}\left(I_{ISRF}e^{-\tau_d^V} + I_* e^{-\tau_d^R} e^{-\tau_m^V (RV-1)}\right) \tag{B.7}$$

Strictly speaking, RV is position and frequency dependent, since the radial and vertical distribution of molecules differ.

The geometry shown in Figure B.1 indicates that RV should be ≥ 1 and we approximate Eq. B.7 by:

$$I(\lambda, r, z) \approx e^{-\tau_m^V}\left(I_{ISRF}e^{-\tau_d^V} + I_* e^{-\tau_d^R}\right) \approx e^{-\tau_m^V} I_d(\lambda, r, z) \tag{B.8}$$

This approximation may underestimate the molecular shielding when τ_m^V is $\lesssim 1$, while τ_m^R is substantially larger than 1, impacting thus the details of the H_2 formation layer and more generally the physico-chemistry in the upper disk atmosphere. Studying the disk upper layer is out of the scope of our paper (and would require the use of a PDR code). In fact, our approximation becomes reasonable as soon as dust attenuation is significant, a situation which happens at $z/H < 3.5 - 3.8$ in our dust disk model (which has a relatively high dust mass), and does not affect our results on the molecular layer and below.

In summary, everywhere in the disk, self and mutual shielding are considered by applying the attenuation by the vertical opacity due to molecules to the radiation field computed with dust only by the POLARIS code:

$$I(\lambda, r, z) = e^{-\tau_m^V} I_d(\lambda, r, z) \tag{B.9}$$

where $I_d(\lambda, r, z)$ explicitly includes the impact of dust scattering that is handled by POLARIS.

It is important to mention that compared to empirical, precomputed factors as a function of visual extinction and H_2 column densities (or also CO and N_2 for self-shielding), this approach has the advantage to take consistently the dust extinction into account for the specific dust properties and distribution.

Consequently, we use Eq. B.9 to compute the photorates and the vertical molecular opacities are computed using Eq. B.5 in all our simulations. Figure B.3 gives the flux as a function of the wavelength in the mid-plane and in the upper atmosphere (4 H) at 100 au for the disk whose parameters are given in Table 1. It shows a comparison between the flux as given by the radiative transfer simulation (dotted lines) and the flux as given by Eq. 2 which takes into account the molecular contribution to the opacity (solid line). The attenuation by spectral lines, especially those of H_2, is clearly visible. The contribution of the molecules to the opacity occurs in a limited range of the UV domain. Although our chemical code (Section 2.3) computes other molecular species that contribute to the UV opacity, their abundance relative to H_2 remains small and limit their contribution.

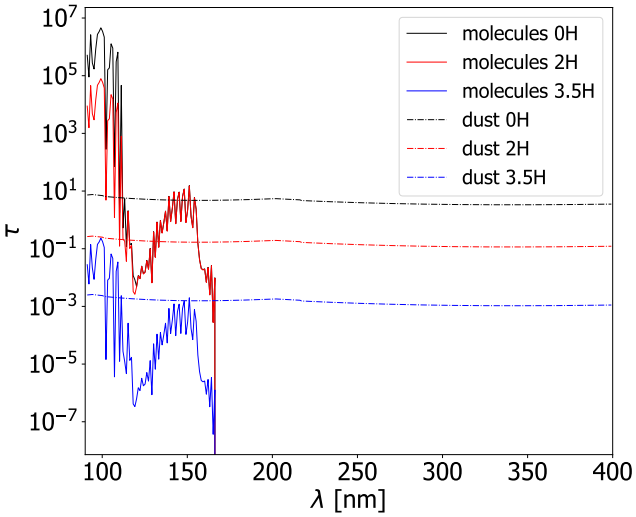

Fig. B.2: Vertical optical depth as a function of wavelengths given at different scale heights H_g (0 H, 2 H, 4 H) of a disk at 100 au away from the star. Solid lines are molecular opacities, dotted lines are dust opacities.

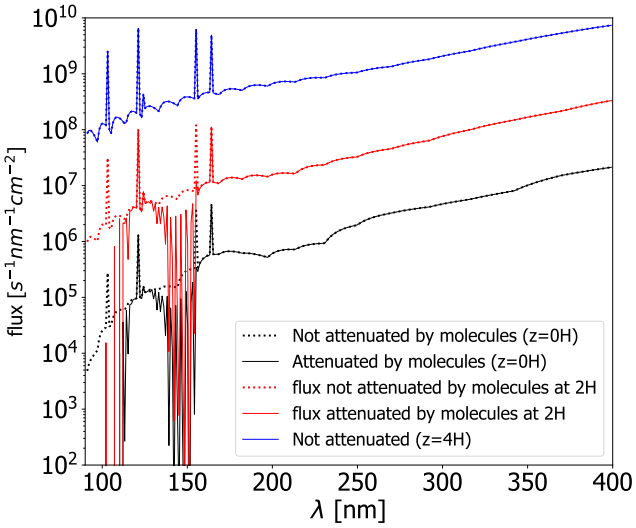

Fig. B.3: Flux as a function of the wavelength in the midplane (black lines), at 2 H (red lines) and at 4 H (blue lines) at 100 au. The unattenuated UV spectrum is derived from France et al. (2014) with spectral resampling preserving the equivalent widths of the lines..

Appendix C: HUV cases

In Figs.C.1 and C.2 we present the vertical profiles at 100 au of the fractional abundances and number densities of gas-phase H,

H_2, CO, CS and CN in HUV single-grain models and multi-grain models, respectively.

Appendix D: LUV cases

In Figure D.1 we present vertical cumulative column density of H_2, CO, CS and CN at 100 au from the LUV models. The profiles are very similar to that of the HUV models below $z \sim 2H$ (see Fig. 9). We shall note a few noticeable differences. The model M-LUV-LH produces a larger column density of CS than M-HUV-LH. As for CN, it is clear that M-HUV-B14 produces a larger column density than M-HUV-LH. In the case of LUV multi-grain models, the difference is far less pronounced and M-LUV-LH produces a slightly larger column density than M-LUV-B14. These different results are mostly due to the lower UV penetration in the case of the LUV models than in the HUV models.

In Figure D.2 we present maps of number density for H_2, CO, CS and CN in the case of LUV single-grain models. Again, the similarity with HUV models is clear. The profiles around the mid-plane are identical between LUV and HUV. The impact of the different flux on the upper layers is visible. The peak of CO, CS and CN are located at higher altitudes and are globally wider in LUV models. We note one major difference for CN between LUV and HUV models. HUV-LH-T_a exhibits a clear spike of CN density around $2H$ while, conversely, LUV-LH-T_a exhibits a drop at the same location.

Figs. D.3 and D.4 show the vertical profiles at 100 au of the fractional abundances and number densities of gas-phase H, H_2, CO, CS and CN in LUV single-grain models and multi-grain models, respectively.

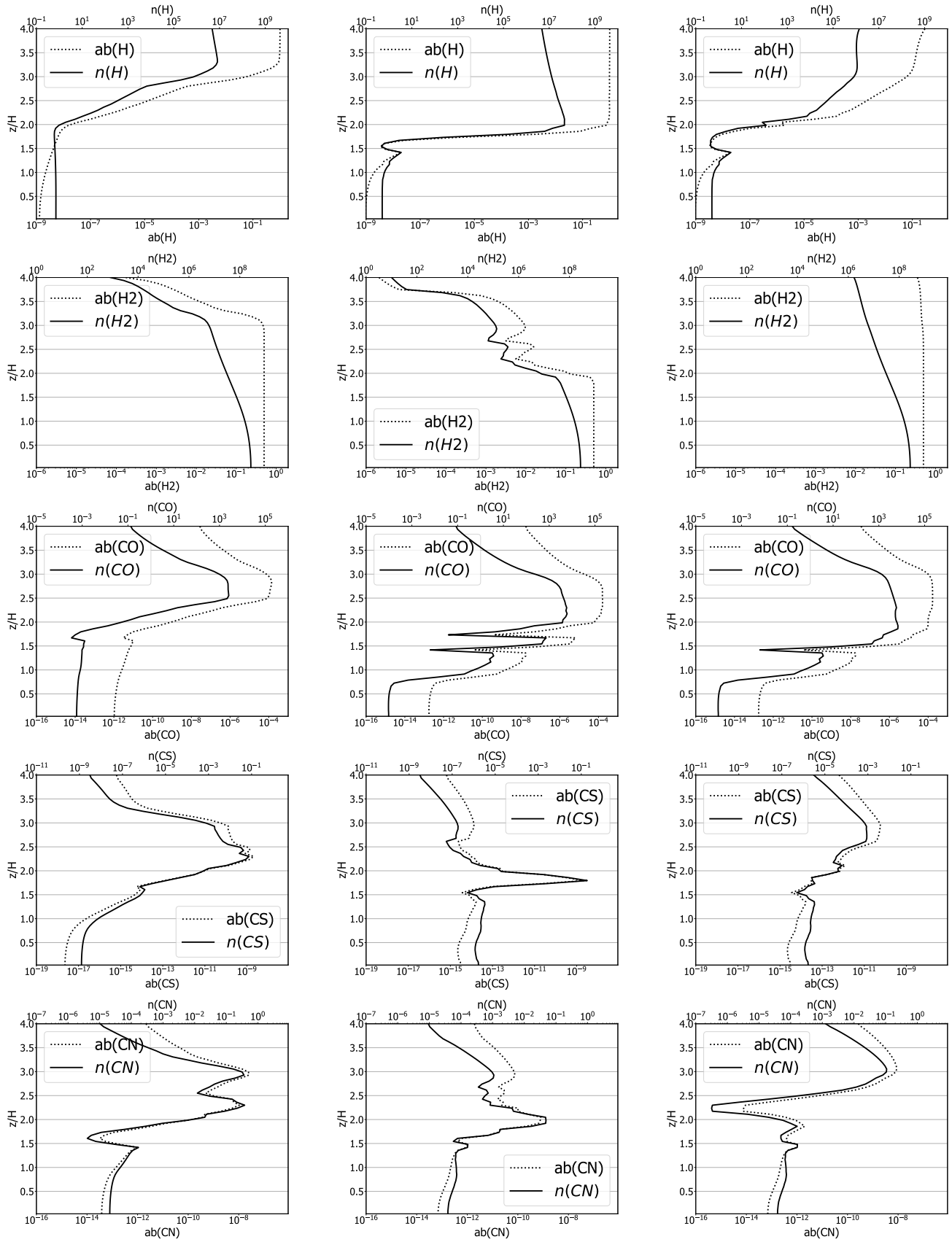

(a) HUV-LH-T_{gas} (b) HUV-LH-T_a (c) HUV-B14-T_a

Fig. C.1: Vertical profiles of H, H_2, CO, CS and CN at 100 au from the star of the HUV single-grain models. The dotted line is the abundance relative to H and the solid line is the density [cm^{-3}].

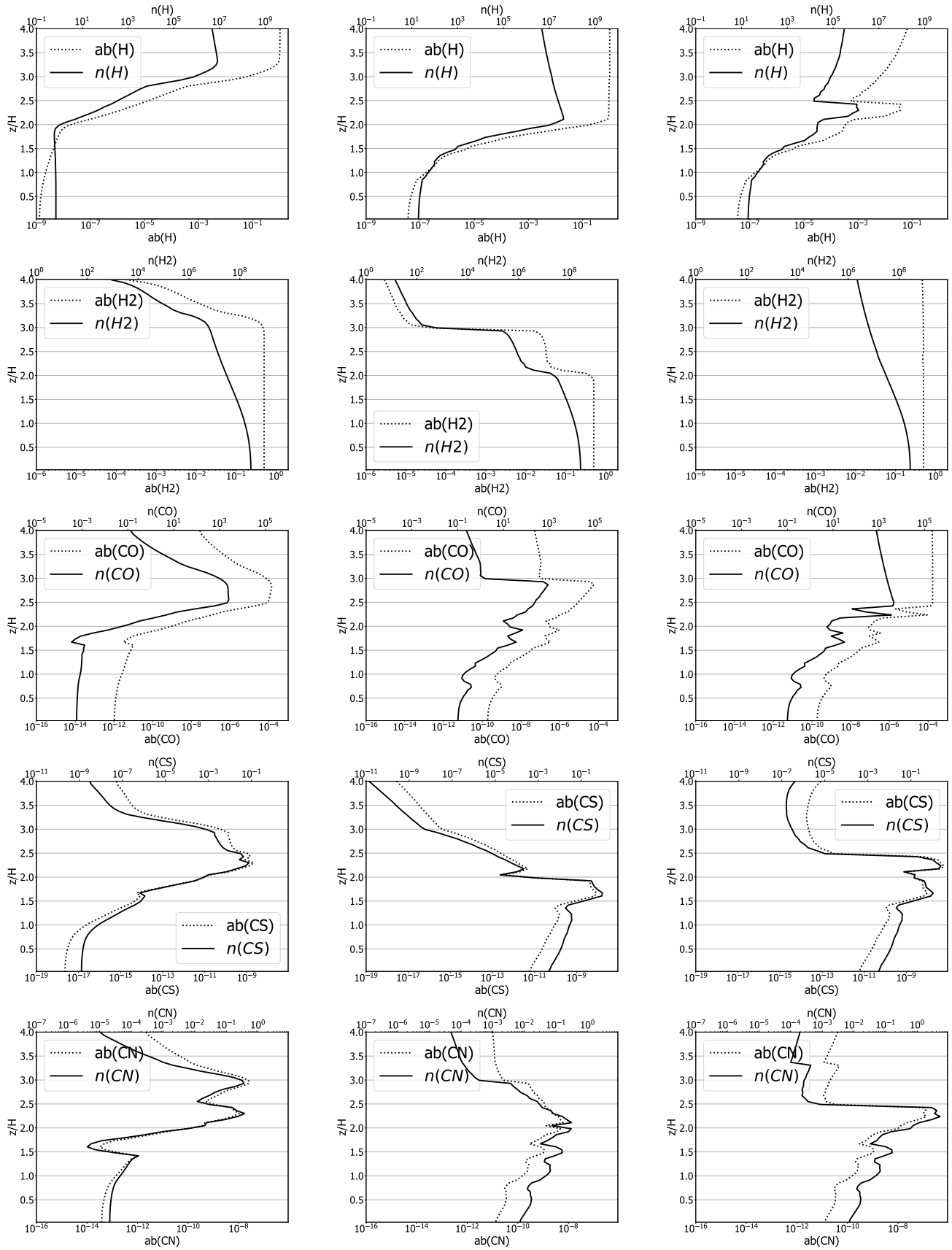

(a) HUV-LH-T_{gas} (b) M-HUV-LH (c) M-HUV-B14

Fig. C.2: Vertical profiles of H, H_2, CO, CS and CN at 100 au from the star of the HUV single-grain model HUV-LH-T_g on the left column, and multi-grain models on middle and right columns. The dotted line is the abundance relative to H and the solid line is the density $[cm^{-3}]$.

Table D.1: LUV cases: column densities of different species at 100 au all models..

	H	H_2	CO	CS	CN
LUV-LH-Tg	$9.70.10^{20}$	$8.22.10^{22}$	$4.11.10^{17}$	$2.34.10^{12}$	$1.01.10^{13}$
LUV-HL-Ta	$7.89.10^{21}$	$7.87.10^{22}$	$1.21.10^{18}$	$3.75.10^{12}$	$1.87.10^{12}$
LUV-B14-Ta	$9.68.10^{19}$	$8.26.10^{22}$	$1.47.10^{18}$	$2.96.10^{11}$	$2.25.10^{13}$
M-LUV-LH	$6.70.10^{21}$	$7.93.10^{22}$	$1.79.10^{17}$	$3.55.10^{13}$	$5.87.10^{13}$
M-LUV-B14	$1.34.10^{19}$	$8.27.10^{22}$	$1.15.10^{18}$	$1.33.10^{13}$	$4.67.10^{13}$

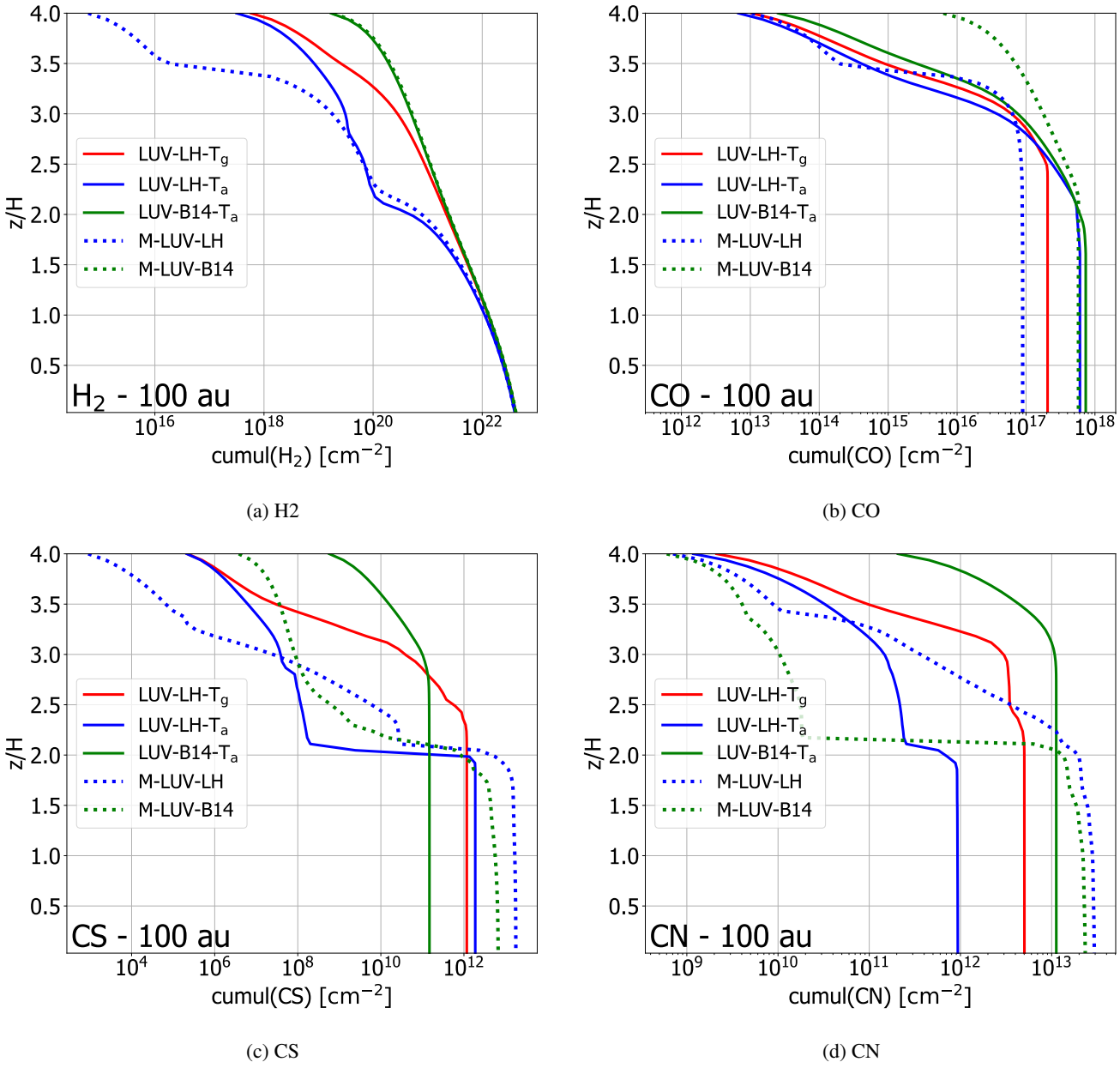

(a) H2

(b) CO

(c) CS

(d) CN

Fig. D.1: Vertical cumulative surface density [cm^{-2}] of H_2, CO, CS and CN at 100 au from the star of the LUV models.

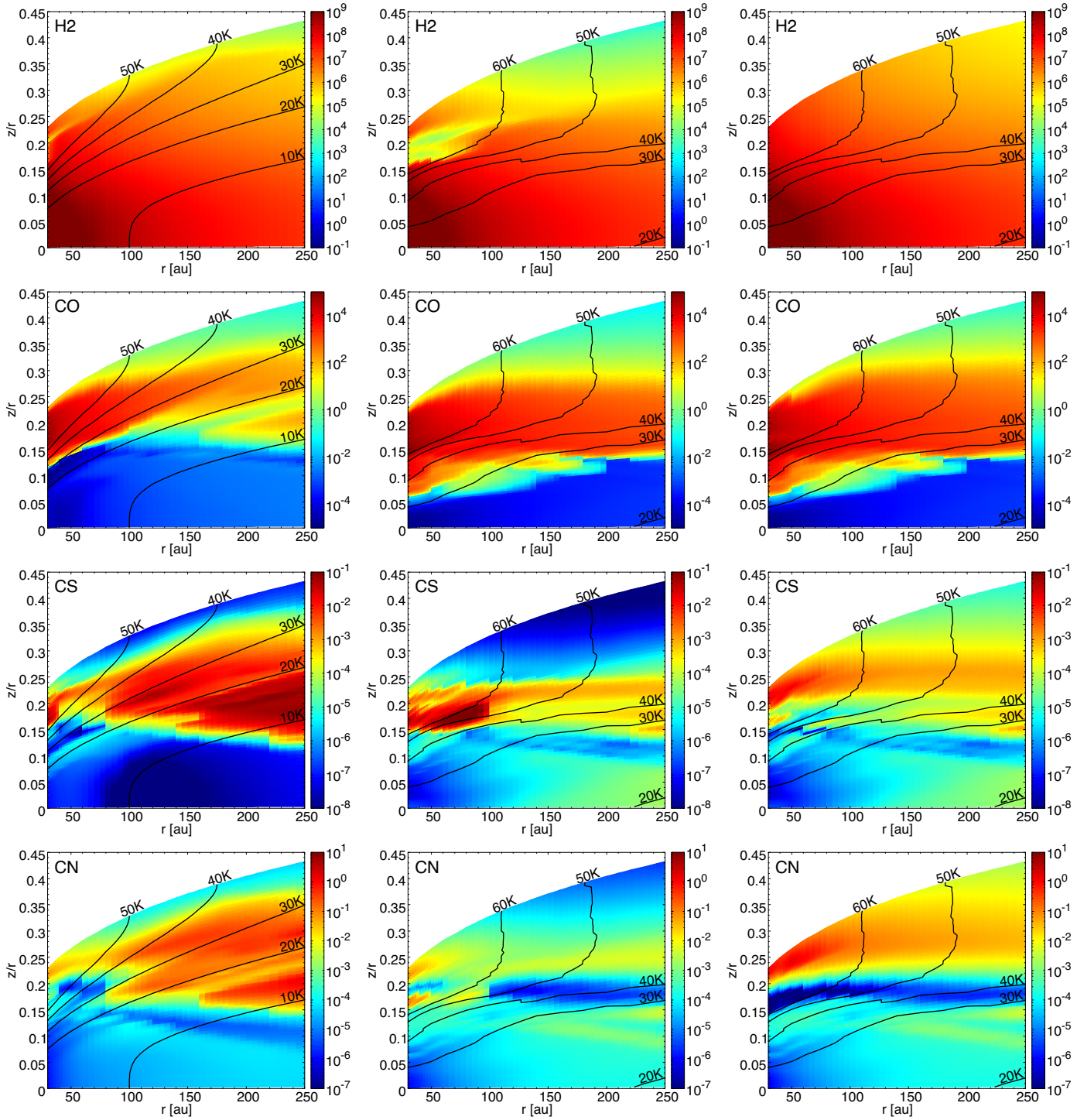

(a) LUV-LH-T_g (b) LUV-LH-T_{eff} (c) LUV-B14-T_{eff}

Fig. D.2: Density [cm^{-3}] of H2, CO, CS and CN in the gas phase of the single-grain models in LUV regime. Left column shows the results of LUV-LH-T_g, middle column is the results of LUV-LH-T_a and right column is the results of LUV-B14-T_a.

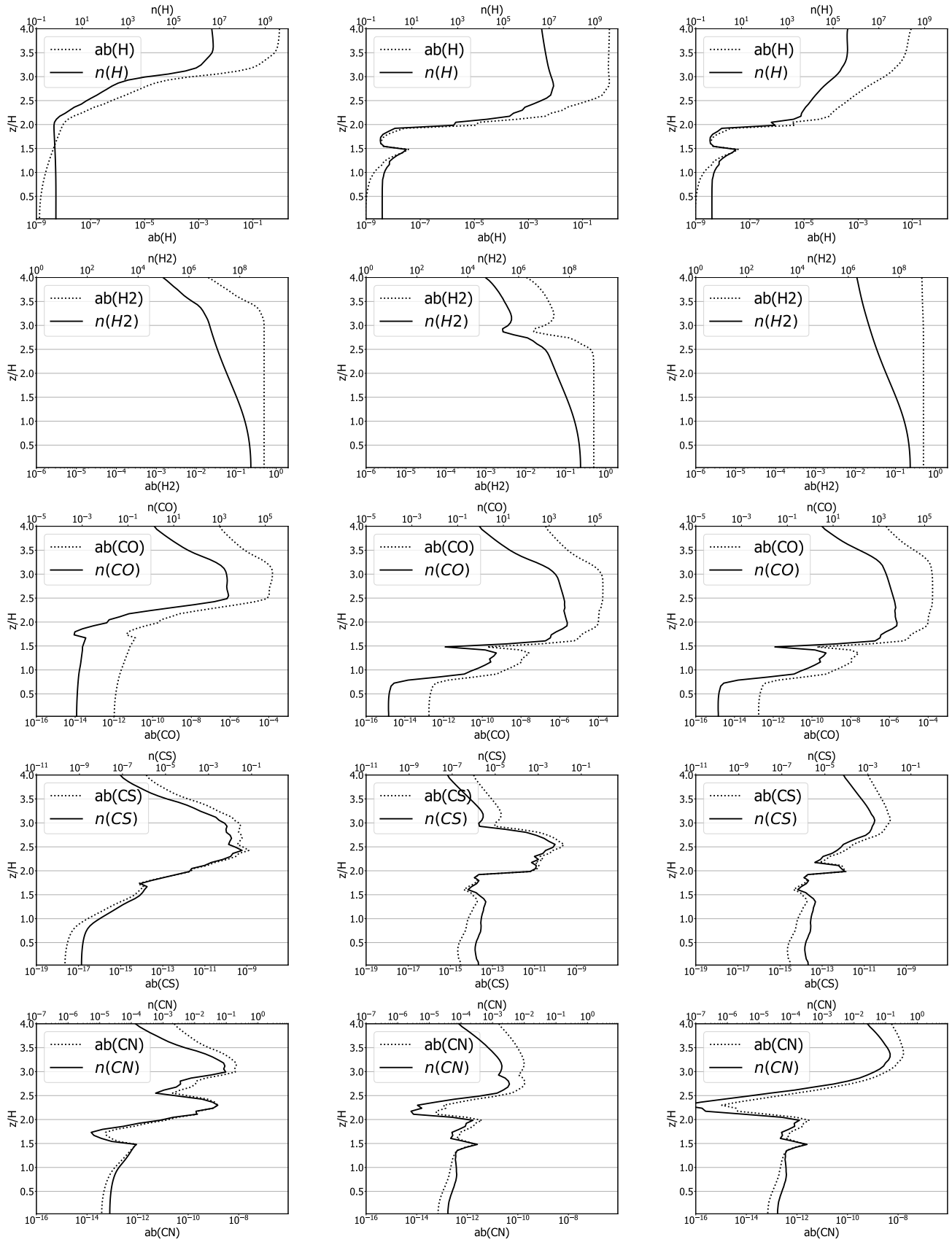

(a) LUV-LH-T_{gas} (b) LUV-LH-T_{eff} (c) LUV-B14-T_{eff}

Fig. D.3: Vertical profiles of H, H_2, CO, CS and CN at 100 au from the star of the LUV single-grain models. The dotted line is the abundance relative to H and the solid line is the density [cm^{-3}].

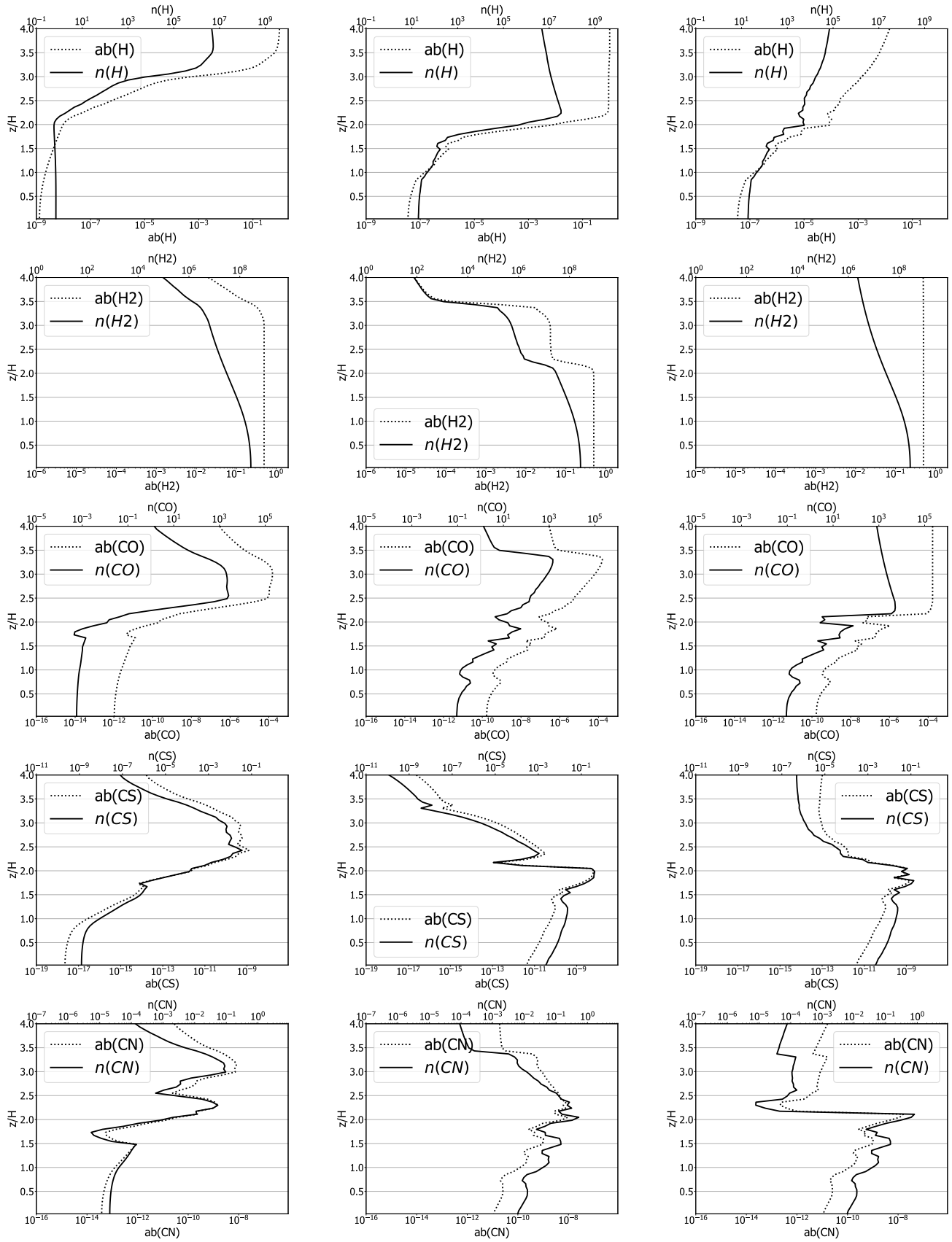

(a) LUV-LH-T_{gas} (b) M-LUV-LH (c) M-LUV-B14

Fig. D.4: Vertical profiles of H, H_2, CO, CS and CN at 100 au from the star of the LUV single-grain model HUV-LH-T_g on the left column, and multi-grain models on middle and right columns. The dotted line is the abundance relative to H and the solid line is the density $[cm^{-3}]$.